Autonomous Exploration of Small Near-Earth Asteroids

by

Shota Takahashi

B.S., Keio University, Tokyo, Japan, 2017

M.S., University of Colorado Boulder, Boulder, CO, 2019

A thesis submitted to the

Faculty of the Graduate School of the

University of Colorado in partial fulfillment

of the requirements for the degree of

Doctor of Philosophy

Department of Aerospace Engineering Sciences

2022

Committee Members:

Daniel Scheeres, Chair

Jay McMahon

Nisar Ahmed

Zachary Sunberg

Christopher D'Souza

Yuichi Tsuda

Takahashi, Shota (Ph.D., Aerospace Engineering)

Autonomous Exploration of Small Near-Earth Asteroids

Thesis directed by Prof. Daniel Scheeres

The capability to autonomously explore a small near-Earth asteroid (NEA) could be a pivotal element in realizing future asteroid missions where cost-effective small spacecraft are distributed to various targets for increased scientific and engineering returns. Recent missions to NEAs such as Hayabusa-2 and OSIRIS-REx have identified feasible operational modes for asteroid exploration, such as initial characterization, near-inertial hovering, orbiting, and slow flybys. These operations currently rely heavily on support from the ground stations for navigation and orbit control, which could be costly. To overcome the limitation, we propose and study the feasibility of an onboard navigation scheme that incorporates optical information and delta-v measurements based on on-board accelerometers. Aside from navigation, onboard orbit control strategies are studied. For an orbital phase, approaches to efficiently define more stable frozen orbits under various perturbations are studied, leveraging the analytical insight of the underlying averaged dynamics. For a close hovering phase, we study the application of reinforcement learning, combined with function approximation by neural networks, to obtain an offline policy for global mapping under maneuver control noise. By performing the training in a simulation environment using various asteroid models, an adaptive policy that changes the behavior depending on the target asteroid is obtained. The robustness of the onboard global mapping policy is tested by performing end-to-end numerical simulations that combine both onboard navigation and control, which shows that the approach is robust. The research suggests that these techniques could be used in future asteroid exploration missions, potentially lowering the cost of such missions and bringing richer scientific and engineering returns.

Acknowledgements

First of all, I would like to express my deepest appreciation to my advisor Professor Scheeres for his generous support throughout the course of my Ph.D. Whenever I struggled with my research, he kindly and patiently guided me with helpful advice backed by his great insight into astrodynamics problems and long teaching experience. I would like to also thank him for helping me connect with people in the aerospace field. Without him, my Ph.D. would have been impossible.

I am extremely grateful to all the committee members for their support. Courses by Dr. McMahon, Dr. Ahmed, and Dr. Sunberg at CU were essential for my research, and discussions with them were invaluable. I also greatly appreciate Dr. D'Souza for a detailed review of the dissertation. Special thanks to Tsuda-sensei for joining my defense presentation early in the morning and providing valuable feedback.

I'd like to thank members of CSML for making my Ph.D. life fruitful both academically and socially. I really appreciate getting to know everyone in the lab and I've learned a lot from them.

Also, I'd like to extend my gratitude to Karman+ for providing me an opportunity to get involved in an exciting project for future asteroid in-situ resource utilization missions. Especially, I'd like to thank Daynan Crull for assisting me during the collaboration.

I would also like to acknowledge the Nakajima Foundation for its incredible support through the fellowship. It is an honor to be chosen as a fellow, and all of the study and research were possible because of the fellowship.

Finally, I am deeply indebted to my parents in Japan, my wife Megumi, and her parents in Colorado for mentally supporting me during my Ph.D. and helping me stay sane.

Contents

Chapter

Bibliography   **169**

Appendix

Tables

Table

Figures

Figure

Chapter 1

Introduction

1.1   Exploration of Near-Earth Asteroids

Small solar system bodies are remnants of the early stage of planetary formation, and studying their orbital evolution, surface morphology, internal structures, and chemical compositions can give us a clue to better understand the formation and evolution of our solar system and other planetary systems. Unlike massive planets, small bodies are believed to have experienced little or only partial differentiation, which constrains the model of the solar system formation. Furthermore, small bodies are considered to be the source of water on Earth and thus provide us critical information to decipher the origin of life [2, 3].

A class of small bodies that is of particular interest is near-Earth asteroids (NEAs), whose perihelion distance is less than 1.3 astronomical units (AU). NEAs are part of a larger group that includes both asteroids and comets, referred to as near-Earth objects (NEOs). Comets are characterized by their coma, and exploration of such bodies requires additional precaution. Thus, the current work limits its focus on NEAs. Besides, the fact that the vast majority of NEOs are NEAs justifies the exclusion of comets.

One interesting aspect of NEA studies is planetary defense. Due to their proximity to Earth, NEAs have non-zero probabilities of Earth impact, which can cause destructive events. NEAs are categorized as potentially hazardous asteroids (PHAs) when they have a minimum distance from the Earth orbit of 0.05 AU or less and have an absolute magnitude of 22 or less [4, 5]. These bodies are large enough to cause catastrophic events upon Earth impact. As of June 20, 2022,

there are 29,131 NEAs discovered, with 2,270 of them being PHAs, and the discovery is still in progress through several surveys [6]. Information such as a PHA's ephemeris, bulk density, shape, and porosity is all critical in assessing the risks posed by PHAs and in studying the feasibility of asteroid deflection techniques. The observations by spacecraft provide us with great details of these bodies for further understanding [7].

From an economic viewpoint, there is an interest in NEAs for in-situ resource utilization (ISRU), owing to their greater accessibility from Earth. Some fractions of NEAs are considered to contain hydrated minerals, and extracting water from such materials could lower the cost of space exploration [8, 9]. The extracted water could be used as a propellant or as a resource to support human activities in space. There are a number of proposed architectures aimed at mining asteroids [10, 11, 12, 13].

The reasons described above easily motivate scientists and engineers to design missions to send probes to NEAs for detailed characterization, and there have been several rendezvous missions to NEAs to date [14, 15, 16, 17]. In a conventional mission operation, the observation data acquired on board are sent to ground stations to obtain a navigation solution, which in turn is used for maneuver planning. The spacecraft then receives control commands and performs the orbit control. While it has been demonstrated that a precise measurement of an asteroid's physical properties is possible through such an approach, frequent communications between the spacecraft and ground stations could be costly.

The capability of spacecraft to autonomously operate in proximity to asteroids could open up a new approach to NEA exploration. Along with the recent advances in small satellite missions, the autonomy in proximity operation could enable us to distribute multiple cost-effective satellites to a wide range of small bodies [18]. In this study, the feasibility of removing the ground in the loop based on onboard optical navigation and other measurements is evaluated in a rendezvous mission to a small NEA. Additionally, the onboard guidance and control algorithms in various phases of a proximity operation are of interest. For orbital phases, strategies to insert a spacecraft into more stable orbits are investigated analytically. Also, the application of reinforcement learning

(RL) for the design of autonomous guidance algorithms is studied. As an example, a controller design in a close reconnaissance phase for surface imaging using RL is presented. Given the end-to-end architecture of the proximity operation, the operational load could be reduced significantly. The capability to navigate and guide the spacecraft without ground intervention could also reduce operational margins for safety as the spacecraft could respond to contingencies with more agility. Such benefits may be a key to realizing future asteroid missions, where a fleet of small satellites is distributed to various NEAs more frequently.

1.2   Research Overview

Proximity operations at asteroids can be divided into a few different phases. This section highlights the specific phases we focus on for autonomous capabilities and presents an overview of the research. Some common assumptions we make regarding the target bodies throughout the research are also summarized herein.

1.2.1   Operational modes

Recent missions to NEAs have identified several distinctive phases in proximity operations, each corresponding to unique mission objectives. These phases include an approach from the end of an interplanetary trajectory, multiple slow hyperbolic flybys, near-inertial or body-fixed hovering, orbiting, and interaction with the asteroid's surface. Each phase has different dynamical constraints, and the level of complexity required for automation varies [18]. In this study, the focuses are on the fundamental operations that are likely to be required by many asteroid missions, leaving out the more challenging operations such as surface interaction. The specific phases considered here are approach after arrival at the target body, near-inertial hovering for reconnaissance at various observation geometries, mass estimation with a gradual descent to lower altitudes, and orbit insertion.

The hovering-oriented approach used herein is based on the approach employed by the Hayabusa2 mission, where a robotic probe rendezvoused with (162173) Ryugu, a carbonaceous

NEA, whose diameter is about 900 m [19]. The Hayabusa2 spacecraft was nominally placed at its home position, a point 20 km above the asteroid on the sub-Earth line on the Sun side [16]. Whenever a critical operation occurs, the spacecraft departs from the home position and transitions to a different operational mode, such as gravity field estimation, rover deployment, and surface sampling. The success of the Hayabusa-2 mission motivates our use of it as a template for developing a fully autonomous algorithm.

The insertion phase into a stable orbit is motivated by the OSIRIS-REx mission's use of such orbits. The OSIRIS-REx spacecraft visited a 500-meter-sized NEA (101955) Bennu, and after the initial characterization, the spacecraft stayed on stable Sun-synchronous orbits, called terminator orbits, for the majority of its proximity phase. Because of its stability, the final phase of an exploration mission to an asteroid is likely a long-term observation from such an orbital platform, and thus considering such operation will be beneficial [20, 21].

In these phases, it is convenient to define a spacecraft's position relative to the Sun-asteroid fixed rotating frame, as the direction of the sunlight, which causes strong perturbing force, becomes constant. Thus, throughout the study, the Hill frame is used to describe the asteroid-relative motion of the spacecraft. The Hill frame is centered on an asteroid's mass center, and its x-axis and z-axis are in the direction of the Sun-asteroid vector and the asteroid orbit's angular momentum vector, respectively. The y-axis is defined to form a right-handed system.

The following is a typical motion of a spacecraft assumed in this study. After arrival at an asteroid, the spacecraft is delivered to a position about 1000 km away from the asteroid on the Sun side. Then, the probe approaches the asteroid, moving along the Sun-asteroid line while properly performing orbit controls to reach a distance of several dozens of km as shown in Fig. 1.1. Spacecraft then performs various scientific observations such as mass estimation and surface imaging from multiple phase angles. Then, it is inserted into a stable orbit for long-term monitoring.
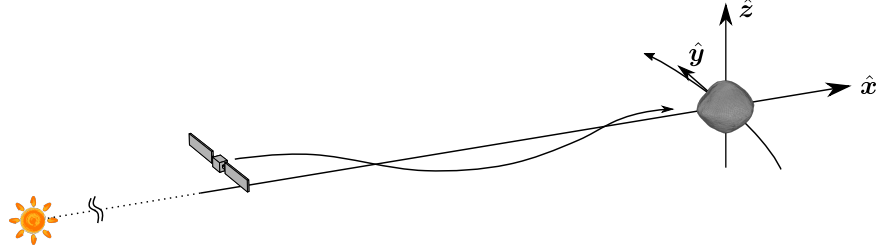
Figure 1.1: Schematic of a spacecraft approaching an asteroid.
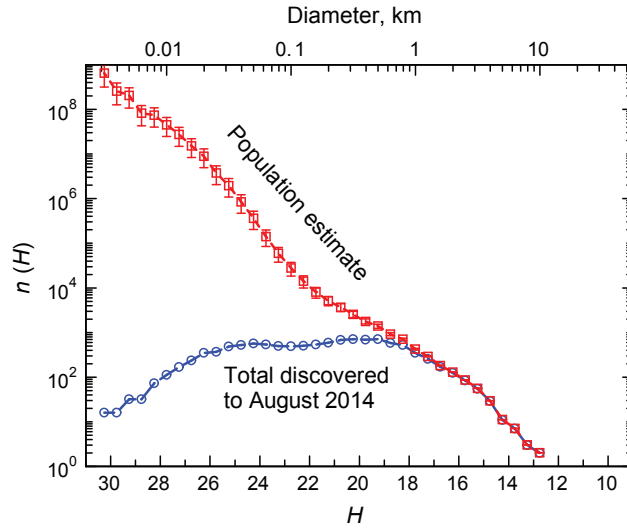
Figure 1.2: The estimated and discovered number of NEAs as a function of absolute magnitude H or equivalently diameter, assuming an albedo of 0.14. The figure is taken from [1].

1.2.2   Target body assumptions

The size distribution of NEAs is widespread. Figure 1.2 shows the estimated number of NEAs as well as the number of discovered NEAs as of August 2014 for different absolute magnitudes, which is converted to diameter assuming an albedo of 0.14 [1]. Because appropriate modes of proximity operations change significantly depending on the target body size, it is important to clarify assumed targets. It should be reasonable to limit the target size range to 100 m to 1 km, in accordance with the Hayabusa2 and OSIRIS-REx missions that this study uses as templates. For larger NEAs, hovering oriented approach may not be feasible in terms of fuel consumption. Even with the size limit, there are plenty of target asteroids, substantiating the original motivation for autonomous exploration.

1.2.3   Thesis Statement

Autonomous navigation and guidance capabilities in proximity operations at small near-Earth asteroids are enabling technologies to realize future asteroid missions where cost-effective satellites are distributed to a wide range of targets, providing increased opportunities for scientific and engineering returns. To that end, it is necessary to understand the limitations and improve the robustness of autonomous algorithms in various modes of operation.

1.2.4   Research goals

In this study, four different research goals are defined as follows.

- Goal 1: Study of Frozen Orbit Design at Small Bodies

- Goal 2: Design of an Adaptive Policy via Reinforcement Learning

- Goal 3: Covariance Analysis of Onboard Navigation

- Goal 4: End-to-End Simulation of Autonomous Navigation and Trajectory Control

The first research focus is the frozen orbit design at small asteroids. A conventional solution to specify a terminator orbit suffers the effect of perturbing forces that are not necessarily captured in its formulation when the orbit size is too small or too large. When the orbit size is small, the contributions from the higher-order gravity field must be taken into consideration. When the orbit size is large, the relatively stronger SRP causes a large short-period oscillation. Analytical corrections to resolve these issues have been studied.

The second goal is to study the application of reinforcement learning (RL) to design an offline feedback policy for trajectory control. Specifically, the study focuses on the hovering trajectory controller for the surface global imaging task. The poor a priori information of the target body means that an autonomous spacecraft needs to adaptively change its behavior after asteroid arrival rather than sticking to a predefined nominal trajectory. Besides, the control of the spacecraft is usually noisy, and the spacecraft needs to take it into consideration. The design of such an adaptive policy is studied by formulating the global mapping task as a continuous sequential decision-making problem and by training the agent with various asteroid models.

The third focus is the navigation analysis, where the information content of various measurement types is investigated. Specifically, navigation capability with onboard optical and accelerometer-based Delta-V measurements is of interest. The core concept is to study how well the Delta-V measurements can address the issue of scale invariance inherent to the optical measurements. Covariance analyses have been performed using simpler dynamics models for the approach, home position hovering, and gravity estimation phases. This simplified analysis helps us understand the limitations of different measurement types and the benefit of combining different measurements to observe the system accurately.

The fourth goal is to perform higher fidelity numerical simulations of end-to-end autonomous operations that incorporate both onboard navigation and guidance algorithms. The feasibility and robustness of the proposed onboard navigation and guidance algorithms are evaluated by introducing realistic errors in the dynamical models. This goal encompasses the results from the other research focuses, and the overall performance of the autonomous exploration scheme is studied.

As part of the analysis, the application of the proposed navigation and guidance scheme for much smaller asteroids whose diameters are smaller than the assumed nominal range of 100 m - 1 km is studied as well.

The thesis first explains the dynamical models used throughout the study. Then, each of the research goals 1-4 is described in detail, namely, frozen orbit design, RL-based hovering controller design, covariance analysis with simple dynamics, and end-to-end numerical study. The concluding remarks are made at the end, summarizing the findings and potential future work.

1.3   Publications

Over the course of the Ph.D., the author published the following journal and conference papers. The thesis is based on these publications.

(1) S. Takahashi and D. J. Scheeres, "Autonomous Reconnaissance Trajectory Controller Design at Small NEAs via Reinforcement Learning," Journal of Guidance, Control, and Dynamics, 2022, Under Review.

(2) S. Takahashi and D. J. Scheeres, "Autonomous Exploration of a Small Near-Earth Asteroid," Journal of Guidance, Control, and Dynamics, Vol. 44, No. 4, 2021, pp. 701-718, `https://doi.org/10.2514/1.G005733`.

(3) S. Takahashi and D. J. Scheeres, "Higher-Order Corrections for Frozen Terminator Orbit Design," Journal of Guidance, Control, and Dynamics, Vol. 43, No. 9, 2020, pp. 1642-1655, `https://doi.org/10.2514/1.G004901`.

(4) S. Takahashi and D. J. Scheeres, "Autonomous Rendezvous with Small Temporarily Captured Orbiters, "AAS/AIAA Astrodynamics Specialist Conference, Charlotte, North Carolina, 2022, AAS 22-700.

(5) S. Takahashi and D. J. Scheeres, "Autonomous Proximity Operations at Small NEAs," 33rd International Symposium on Space Technology and Science, C000520, Online, 2022.

(6) S. Takahashi and D. J. Scheeres, "Autonomous Reconnaissance Trajectory Guidance at Small Near-Earth Asteroids using Reinforcement Learning," 72nd International Astronautical Congress, Dubai, United Arab Emirates, 2021, IAC21,C1,3,1,x6432.

(7) S. Takahashi and D. J. Scheeres, "Autonomous Navigation and Exploration of a Samll Near-Earth Asteroid," AAS/AIAA Astrodynamics Specialist Conference, Lake Tahoe, California, 2020, Paper AAS 20-514.

(8) S. Takahashi and D. J. Scheeres, "Autonomous Characterization of an Asteroid from a Hovering Trajectory,"AAS/AIAA Astrodynamics Specialist Conference, Portland, Maine, 2019, AAS 19-850.

(9) S. Takahashi and D. J. Scheeres, "Effect of Shifted Origin on the J2 Perturbed Terminator Orbit," 32nd International Symposium on Space Technology and Science, Fukui, Japan, 2019.

(10) S. Takahashi and D. J. Scheeres, "The Effect of a Shifted Origin on the Osculating Orbital Elements of a Terminator Orbit," AAS/AIAA Space Flight Mechanics Meeting, Ka'anapali, Hawaii, 2019, Paper AAS 19-450.

Chapter 2

Dynamical Models

2.1   Equations of Motion

With the assumption of a small NEA, solar radiation pressure (SRP) tends to have a signifi-cant impact on a spacecraft's motion. A natural choice of frame to describe the motion in such an environment is the Sun-relative orbit fixed frame, as the direction of the SRP force is fixed. The origin is at the mass center of the asteroid. The x-axis is aligned with the direction from the Sun to the asteroid, and the z-axis is in the direction of the asteroid's orbit normal. The y-axis is defined to form a right-handed system. The most general form of the equations of motion in the orbit fixed frame is given as follows.

$$\ddot{\boldsymbol{r}} + \ddot{F}\tilde{\hat{\boldsymbol{z}}} \cdot \boldsymbol{r} + 2\dot{F}\tilde{\hat{\boldsymbol{z}}} \cdot \dot{\boldsymbol{r}} + \dot{F}^2\tilde{\hat{\boldsymbol{z}}} \cdot \tilde{\hat{\boldsymbol{z}}} \cdot \boldsymbol{r} = \frac{\partial U_g}{\partial \boldsymbol{r}} + \frac{\partial U_s}{\partial \boldsymbol{r}} + C_{\text{SRP}}\boldsymbol{a}_{\text{SRP}} + \sum_i \boldsymbol{\Delta V}_i\, \delta(t - \tau_i) \tag{2.1}$$

Throughout the thesis, bold letters are used to represent vectors. The single and double dot notation is used for first and second time derivatives. The dot products represent products with a contraction such as $(a \cdot b)_{ik} = \sum_j a_{ij}b_{jk}$, while the products without dots indicate outer products such as $(ab)_{ijkl} = a_{ij}b_{kl}$. A spacecraft's position vector is represented by $\boldsymbol{r}$. The hat over a vector represents a unit vector. The tilde over a vector forms a skew-symmetric matrix for cross-product operation such that $\tilde{\hat{\boldsymbol{z}}} \cdot \boldsymbol{r} = \hat{\boldsymbol{z}} \times \boldsymbol{r}$. F is the true anomaly of the asteroid's orbit and its first and second derivatives are functions of F.

$$\dot{F} = \sqrt{\mu_s/[A(1 - E^2)]^3}(1 + E\cos F)^2 \tag{2.2}$$

$$\ddot{F} = -2E\sqrt{\mu_s/[A(1 - E^2)]^3}\sin F(1 + E\cos F)\dot{F} \tag{2.3}$$

where μ_s is the gravitational parameter of the Sun. A and E are the semimajor axis and eccentricity of the asteroid's orbit, respectively, and Kepler's equation is solved at each time step to compute the true anomaly. In Eq. (2.1), U_g is the asteroid's gravitational potential, and the potential U_s is the Sun's third body effect. The vector $\boldsymbol{a}_{\mathrm{SRP}}$ is the SRP acceleration acting on the spacecraft, and C_{SRP} is its scaling coefficient. The vector $\boldsymbol{\Delta V}_i$ represents an instantaneous velocity change that occurs at $t = \tau_i$. Because the velocity change is modeled as impulsive, its corresponding acceleration is defined by the Dirac delta $\delta(t - \tau_i)$. In general, there are multiple maneuvers during a mission period, and the subscript i is used as a label for each maneuver.

Different parts of the analysis in this thesis use dynamics models with different complexity. As for the gravity from the asteroid, the gravitational field expressed by spherical harmonics is the most detailed model used in this study.

$$U_g = \frac{\mu}{r} \sum_{n=0}^{5} \sum_{m=0}^{n} P_{nm}(\sin\phi) \left[C_{nm} \cos(m\lambda) + S_{nm} \sin(m\lambda) \right] \qquad (2.4)$$

where ϕ and λ are the latitude and longitude of the spacecraft's position as seen in the asteroid's body frame respectively, r is the norm of $\boldsymbol{r}$, μ is the gravitational parameter of the asteroid, and P_{nm} is the associated Legendre polynomials. For the computation of its partial derivatives, recursive structures of P_{nm} are used [22, 23]. We assume the asteroid's pole orientation and orbital elements are given relative to J2000 Earth Ecliptic frame, which is denoted as N-frame. The attitude of the asteroid's body frame (B-frame) relative to N-frame is computed by the direction cosine matrix (DCM): $R_{[BN]} = R_3(\dot{\theta}_p t + \theta_0) \cdot R_1(\pi/2 - \delta_p) \cdot R_3(\pi/2 + \alpha_p)$ where $R_i(\theta)$ is a DCM for i-th axis rotation by angle θ. The relationship between the body and inertial frames is shown in Fig. 2.1. By computing the DCM of the orbit frame (O-frame) relative to the inertial frame ($R_{[ON]}$) by a similar 3-1-3 Euler angle rotation, relative attitude between the body and orbit frames can be computed as $R_{[BO]} = R_{[BN]} \cdot R_{[ON]}^T$. The initial phase angle of the body frame θ_0 and the asteroid's true anomaly are both set to zero at $t = 0$. When a simple gravity model suffices, the point mass gravity model is used, namely,

$$U_g = \mu/r \qquad (2.5)$$
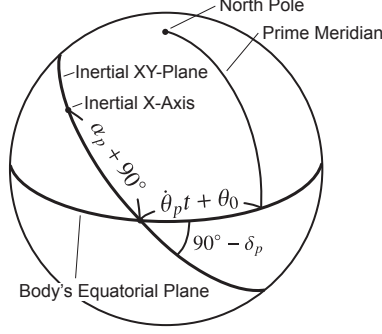
Figure 2.1: Relationship between the body frame and ecliptic frame.

As for the third body acceleration, the Hill approximation is made in this study assuming that the distance between the Sun and asteroid is much larger than the distance between the spacecraft and asteroid [24]. Thus,

$$U_s = \frac{\mu_s}{2d^3} r^2 \left(3(\hat{\boldsymbol{r}} \cdot \hat{\boldsymbol{d}})^2 - 1 \right) \tag{2.6}$$

$$\frac{\partial U_s}{\partial \boldsymbol{r}} = \frac{\mu_s}{d^3} (3\hat{\boldsymbol{d}}\hat{\boldsymbol{d}} - I) \cdot \boldsymbol{r} \tag{2.7}$$

where $\boldsymbol{d}$ is a vector pointing from the asteroid to the Sun and I is an identity matrix. The Sun-asteroid distance is given by $d = A(1 - E^2)/(1 + E\cos(F))$.

Accurate modeling of the complex interaction between the incident solar photons and the spacecraft's surface is nontrivial and not addressed in this work. However, it is interesting to study the performance of the overall navigation and orbit control algorithms when there are modeling errors in SRP. Therefore, in some cases, the SRP acceleration is computed as a combination of the flat-plate model and the cannonball model. When a simple model is sufficient, the cannonball model is used, where the area-to-mass ratio is assumed constant regardless of the attitude. The complex SRP model is used to simulate a trajectory that is treated as truth in the end-to-end numerical study. The cannonball SRP acceleration is given by

$$\boldsymbol{a}_{\text{SRP, CB}} = \frac{P_0(1 + \rho)(1\text{AU})^2 A_{\text{SC}}}{M_{\text{SC}}} \frac{\boldsymbol{r} - \boldsymbol{d}}{|\boldsymbol{r} - \boldsymbol{d}|^3} \tag{2.8}$$

where ρ is the surface reflectivity. $P_0 = 4.56 \times 10^{-6}\,\text{Nm}^{-2}$ is the SRP at 1 AU [25, 23, 24]. A_{SC} is the area of the spacecraft's surface, and M_{SC} is the total mass of the spacecraft. Assuming that

$r << d$, the expression can be further simplified [24].

$$\boldsymbol{a}_{\text{SRP, CB}} = \frac{P_0(1+\rho)A_{\text{SC}}}{M_{\text{SC}}}\frac{(1\text{AU})^2}{d^2}\hat{\boldsymbol{x}} \tag{2.9}$$

where $\hat{\boldsymbol{x}}$ points from the Sun to the asteroid as defined earlier. For the flat-plate components, the acceleration is computed by

$$\boldsymbol{a}_{\text{SRP, FP}} = \frac{P_0}{M_{\text{SC}}}\frac{(1\text{AU})^2}{d^2}\sum_i A_{\text{SC},i}(\hat{\boldsymbol{n}}_i \cdot \hat{\boldsymbol{u}})\left(\rho\left(\frac{2}{3}(1-s) - 2s(\hat{\boldsymbol{n}}_i \cdot \hat{\boldsymbol{u}})\right)\hat{\boldsymbol{n}}_i - (1-\rho s)\hat{\boldsymbol{u}}\right) \tag{2.10}$$

where $\hat{\boldsymbol{n}}_i$ and $A_{\text{SC},i}$ are a surface normal vector and area for the i-th surface [25]. The vector $\hat{\boldsymbol{u}}$ represents the direction of the incident light, pointing from the Sun to the spacecraft. The parameter s is the fraction of specular reflection out of the reflected light. Details about the used model parameters are provided in each chapter.

Finally, the simplest dynamics model is derived by setting E to zero, which is true when the asteroid's orbit about the Sun is circular. In this case, the dynamics can be represented as the following Hill three-body model with SRP.

$$\ddot{\boldsymbol{r}} = -2n\tilde{\hat{\boldsymbol{z}}} \cdot \dot{\boldsymbol{r}} + n^2\left(3\hat{\boldsymbol{x}}\hat{\boldsymbol{x}} - \hat{\boldsymbol{z}}\hat{\boldsymbol{z}}\right) \cdot \boldsymbol{r} - \mu\frac{\boldsymbol{r}}{r^3} + C_{\text{SRP}}a_{\text{SRP}}\,\hat{\boldsymbol{x}} \tag{2.11}$$

where $n = \dot{F}$ is no longer time-varying. As the Sun-asteroid distance is constant, a_{SRP} is also constant.

2.2   Linearized Dynamics

A state transition matrix (STM) describes the evolution of a small deviation from a reference trajectory. The STM $\Phi(t;t_0) = \partial\boldsymbol{X}(t)/\partial\boldsymbol{X}(t_0)$ linearly maps a state deviation at time t_0 to the state deviation at time t, where $\boldsymbol{X} = [\boldsymbol{r};\dot{\boldsymbol{r}}]$. The STM is used in the navigation filters and in the computation of orbit transfers. The STM can be obtained by numerically integrating the following set of differential equations.

$$\dot{\Phi}(t;t_0) = \frac{\partial\dot{\boldsymbol{X}}(t)}{\partial\boldsymbol{X}} \cdot \Phi(t;t_0) \tag{2.12}$$

$$\Phi(t_0;t_0) = I \tag{2.13}$$

The partial derivative can be computed as follows.

$$\frac{\partial \dot{\boldsymbol{X}}(t)}{\partial \boldsymbol{X}} = \begin{bmatrix} 0_{3\text{x}3} & I_{3\text{x}3} \\ \partial \ddot{\boldsymbol{r}}/\partial \boldsymbol{r} & \partial \ddot{\boldsymbol{r}}/\partial \dot{\boldsymbol{r}} \end{bmatrix} \tag{2.14}$$

With the general form of the spacecraft's dynamics in Eq. (2.1), the derivatives can be given by

$$\frac{\partial \ddot{\boldsymbol{r}}}{\partial \boldsymbol{r}} = -\ddot{F}\tilde{\boldsymbol{z}} - \dot{F}^2 \tilde{\boldsymbol{z}} \cdot \tilde{\boldsymbol{z}} + \frac{\partial^2 U_g}{\partial \boldsymbol{r}^2} + \frac{\partial^2 U_s}{\partial \boldsymbol{r}^2} + C_{\text{SRP}} \frac{\partial \boldsymbol{a}_{\text{SRP}}}{\partial \boldsymbol{r}} \tag{2.15}$$

$$\frac{\partial \ddot{\boldsymbol{r}}}{\partial \dot{\boldsymbol{r}}} = -2\dot{F}\tilde{\boldsymbol{z}} \tag{2.16}$$

The second partial derivative of the point-mass gravity potential is given by

$$\frac{\partial^2 U_g}{\partial \boldsymbol{r}^2} = \frac{\mu}{r^3} \left(3\hat{\boldsymbol{r}}\hat{\boldsymbol{r}} - I\right) \tag{2.17}$$

The current study does not use the spherical harmonics gravity model in the navigation filter or guidance algorithms. The spherical harmonics model is only used to simulate truth trajectories. Thus, the computation of the second-order partials for the spherical harmonics gravity potential is omitted.

The partial derivative for the third-body acceleration after the Hill approximation can be readily obtained from Eq. (2.7) as

$$\frac{\partial^2 U_s}{\partial \boldsymbol{r}^2} = \frac{\mu_s}{d^3}(3\hat{\boldsymbol{d}}\hat{\boldsymbol{d}} - I) \tag{2.18}$$

As for the SRP acceleration, the partial derivatives are nonzero when the acceleration is computed by Eq. (2.8). The partial derivative is given by

$$\frac{\partial \boldsymbol{a}_{\text{SRP, CB}}}{\partial \boldsymbol{r}} = \frac{P_0(1+\rho)(1\text{AU})^2 A_{\text{SC}}}{M_{\text{SC}}} \left(I - 3\frac{\boldsymbol{r}-\boldsymbol{d}}{|\boldsymbol{r}-\boldsymbol{d}|}\frac{\boldsymbol{r}-\boldsymbol{d}}{|\boldsymbol{r}-\boldsymbol{d}|}\right) \tag{2.19}$$

2.3 Two-Point Boundary Value Problem

The trajectory control in this study is based on the solution of the two-point boundary value problems (TPBVPs). In TPBPVs, the goal is to find an initial velocity $\boldsymbol{v}_0$ such that the final

position reaches a given target position $\boldsymbol{r}_f$ for a given transfer time T starting from an initial position $\boldsymbol{r}_0$. Thus, we need to find the root of

$$\boldsymbol{G}(\boldsymbol{v}_0; \boldsymbol{p}) \equiv \boldsymbol{r}_T(\boldsymbol{r}_0, \boldsymbol{v}_0; \boldsymbol{p}) - \boldsymbol{r}_f = \boldsymbol{0} \tag{2.20}$$

where $\boldsymbol{p}$ is a set of parameters for the dynamics and could be used for continuation as explained shortly; $\boldsymbol{r}_T$ is a position vector obtained by propagating $\boldsymbol{r}_0$ and $\boldsymbol{v}_0$ with $\boldsymbol{p}$ for a given transfer time T.

Assuming there is an initial guess of $\boldsymbol{v}_0$, the solution to Eq. (2.20) can be obtained by the Newton-Raphson method with a given tolerance. In this method, a correction to a guess is computed based on linearization, and the correction is applied iteratively to the guess until the solution $\boldsymbol{v}_0 = \boldsymbol{v}_0^*$ is found. If a correction $\boldsymbol{\delta v}$ to a guess $\boldsymbol{v}_0 = \hat{\boldsymbol{v}}_0$ solves the problem, then $\boldsymbol{r}_T(\boldsymbol{r}_0, \hat{\boldsymbol{v}}_0 + \boldsymbol{\delta v}; \boldsymbol{p}) - \boldsymbol{r}_f = \boldsymbol{0}$ holds true. Linearizing this equation gives

$$\left(\frac{\partial \boldsymbol{r}_T}{\partial \boldsymbol{v}_0} \right) \Big|_{\boldsymbol{v}_0 = \hat{\boldsymbol{v}}_0} \cdot \boldsymbol{\delta v} = -\boldsymbol{G}(\hat{\boldsymbol{v}}_0; \boldsymbol{p}) \tag{2.21}$$

where $\partial \boldsymbol{r}_T / \partial \boldsymbol{v}_0$ is obtained by numerically integrating the STM for the guessed trajectory. From the equation, a necessary correction $\boldsymbol{\delta v}$ is computed. Because the correction is based on the linear approximation, update of the guess ($\hat{\boldsymbol{v}}_0 \leftarrow \hat{\boldsymbol{v}}_0 + \boldsymbol{\delta v}$) must be repeated until $\hat{\boldsymbol{v}}_0 \simeq \boldsymbol{v}_0^*$.

Once a solution of Eq. (2.20) is obtained for a set of parameter values, a neighboring solution with slightly different parameter values can be computed as well. Assuming $\boldsymbol{r}_T(\boldsymbol{r}_0, \boldsymbol{v}_0; \boldsymbol{p})$ and $\boldsymbol{r}_T(\boldsymbol{r}_0, \boldsymbol{v}_0 + \boldsymbol{\delta v}; \boldsymbol{p} + \boldsymbol{\delta p})$ both satisfy $\boldsymbol{G} = \boldsymbol{0}$, a necessary correction is

$$\boldsymbol{\delta v} = -\left(\frac{\partial \boldsymbol{r}_T}{\partial \boldsymbol{v}_0} \right)^{-1} \cdot \left(\frac{\partial \boldsymbol{r}_T}{\partial \boldsymbol{p}} \right) \cdot \boldsymbol{\delta p} \tag{2.22}$$

If we can compute a solution to the TPBPV when $\boldsymbol{p} = \boldsymbol{0}$, then an initial guess of a solution with a small perturbation $\boldsymbol{\delta p}$ can be found by Eq. (2.22). The desired solution is then computed through the iterative Newton-Raphson updates, which is again used to find a solution with a slightly larger perturbation. This study uses such a continuation scheme to find a solution $\boldsymbol{v}_0^*$ of a TPBVP with the desired parameter value $\boldsymbol{p}$ for the simplest form of the relative motion dynamics for heliocentric asteroid rendezvous defined in Eq. (2.11) with SRP defined by Eq. (2.9).

For the SRP augmented Hill three-body problems in Eq. (2.11), there are two approaches to compute the solution of the TPBPV for given parameter values. When the spacecraft is far away from the target asteroid, the gravitational attraction of the asteroid may be ignored. In such a case, the equations of motion become linear, and the closed-form solution to the TPBPVs can be computed. In this case, the continuation parameter is $p = \mu$. When $p = 0$, by variation of parameters, the solution is obtained as

$$\boldsymbol{X}(t) = \Phi(t; 0) \cdot \boldsymbol{X}(0) + \Phi(t; 0) \cdot \int_0^{t'} \Phi(t'; 0)^{-1} dt' \cdot \boldsymbol{c} \tag{2.23}$$

where $\boldsymbol{X} = [\boldsymbol{r}, \boldsymbol{v}]$ and $\boldsymbol{c} = [\boldsymbol{0}_3, a_{\mathrm{SRP}}, 0, 0]$. Here, Φ is an STM for the homogeneous Clohessy–Wiltshire (CW) equations, and it is computed analytically. Given initial and final positions, the necessary velocity vector for the transfer is obtained as

$$\boldsymbol{v}_0 = \Phi_{rv}^{-1} \cdot (\boldsymbol{r}_f - \Phi_{rr} \cdot \boldsymbol{r}_0 - \boldsymbol{c}_r') \tag{2.24}$$

where $\boldsymbol{c}_r'$ is the position components of the second term in the right-hand side of Eq. (2.23).

When the spacecraft is so close to the target asteroid that the gravitational attraction from the asteroid is stronger than SRP, then the solutions of the TPBVPs can be found by setting $\boldsymbol{p} = [n, C_{\mathrm{SRP}}]$. When $\boldsymbol{p} = \boldsymbol{0}$, the spacecraft follows the simple two-body equations of motion. The solution to this problem is obtained by solving Lambert's problem. Then, the effects of SRP, third-body, and frame rotation are gradually introduced to the dynamics. As for the Lambert solver, Gooding's algorithm is used because it can find a solution even for a rectilinear motion, which is necessary for hovering at a fixed position [26].

2.4 Relative Motion Dynamics for TCO Rendezvous

The current work also studies the feasibility of autonomous rendezvous with small temporarily captured orbiters (TCOs), while the main focus is the rendezvous with heliocentric asteroids. This section describes the dynamical models and some observations about the spacecraft's relative motion for a TCO rendezvous scenario. TCOs are a group of asteroids that move on Earth-like orbits and

are captured by the gravitational attraction of Earth for a short period. Granvik et al. define a TCO as an object that makes at least one revolution around Earth in a co-rotating frame and estimate that there is at least one TCO whose diameter is larger than one meter at any given time [27]. The proximity of TCOs to Earth provides a great opportunity for a detailed investigation of these bodies. TCOs are of interest as potential targets for retrieval missions and for in-situ extraction of resources [28]. Even when the size of a target TCO is small and thus the project is less profitable, rendezvous missions with TCOs could pave the way for future retrieval and extraction missions by serving as technological demonstrations and by giving us a deeper insight into the distribution of valuable resources [29].

In general, the target TCOs for rendezvous missions are much smaller than the heliocentric asteroids considered in this study. This study uses asteroids Bennu and Itokawa as hypothetical targets of the heliocentric asteroid exploration missions, and they are several hundred meters in diameter. We assume target TCOs are a few orders of magnitude smaller. Specifically, this study uses a know TCO, 2006 RH120, whose diameter is a few meters [28]. A primary goal is to understand the behavior of the navigation solutions when the target is a few orders of magnitude smaller than Bennu. In addition, unlike rendezvous missions with a larger asteroid on a simple heliocentric orbit, the asteroid and a nearby spacecraft are under the strong influence of Earth's gravity. Thus, the dynamical modeling is not as simple, which necessitates further analysis.

This section first describes dynamical models to propagate the trajectories of an asteroid and spacecraft. The effect of an asteroid's ephemeris errors is discussed. Then, hovering control and the dynamics are discussed.

2.4.1   Equations of Motion

This study assumes the motion of the TCO in the vicinity of the Earth can be modeled by the Hill three-body equations. Unlike Eq. (2.11), the contribution of SRP on the TCO's trajectory is ignored as the area-to-mass ratio is small. The equations of motion of objects flying in the vicinity

of the Earth are given by

$$\ddot{\boldsymbol{r}}^* = -2n\dot{\tilde{\boldsymbol{z}}} \cdot \dot{\boldsymbol{r}}^* + n^2(3\hat{\boldsymbol{x}}\hat{\boldsymbol{x}} - \hat{\boldsymbol{z}}\hat{\boldsymbol{z}}) \cdot \boldsymbol{r}^* - \frac{\mu_e}{r^{*3}}\boldsymbol{r}^* \tag{2.25}$$

where $\hat{\boldsymbol{r}}^*$ is the position vector of the asteroid wrt. Earth; μ_e is the gravitational parameter of Earth; n is the mean motion of the Earth's orbit. We note that for TCO analyses, the Hill frame is defined for the Earth's orbit around the Sun and that the origin of the coordinate frame is at the Earth. This model only considers the gravity of the Sun and Earth. According to [28], the lunar gravity cannot be ignored if we wish to reproduce the trajectory of 2006 RH120 accurately. However, in this study, lunar gravity is ignored for the sake of simplicity.

The current TCO rendezvous analysis uses 2006 October 1, 0:00:00 UTC as an initial epoch. The initial position and velocity of 2006 RH120 at this epoch are retrieved from the JPL Horizons system [30]. Figure 2.2 shows the trajectories of 2006 RH120 and a nearby spacecraft propagated by our model for 360 days. The spacecraft is placed 10 km away from the asteroid on the Sun side with zero asteroid-relative velocity. The spacecraft dynamics additionally have a simple Solar Radiation Pressure (SRP) acceleration in Eq. (2.9). The mass-to-area ratio is set to $M_{\text{SC}}/A_{\text{SC}} = 50$ kg/m^2.

The relative trajectory of the spacecraft with respect to the asteroid can be constructed by looking at the difference between the trajectories of the TCO and the spacecraft propagated for 360 days. Figure 2.3 shows the resulting relative position. It is evident that the spacecraft moves away from the target without any control.

Instead of looking at the difference in the position vectors of the asteroid and spacecraft relative to Earth to construct the relative trajectory, we can directly define the relative motion dynamics. The assumption here is that we have access to the nominal position of the asteroid, or the ephemeris. In this study, a prepropagated trajectory of 2006 RH120 using the models explained earlier is used as the ephemeris. If we take the difference in the accelerations between two objects
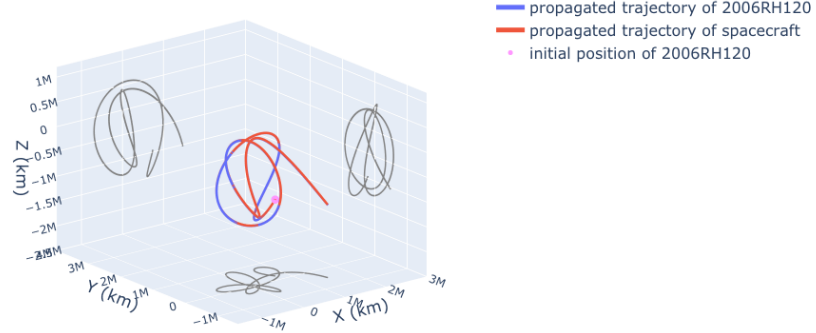
Figure 2.2: Trajectories of 2006 RH120 and nearby spacecraft propagated by the simplified models.

that follow Eq. (2.25), we get

$$
\begin{aligned}
\ddot{\boldsymbol{r}} &= \ddot{\boldsymbol{r}}_{\mathrm{s/c}} - \ddot{\boldsymbol{r}}^* \\
&= -2n\tilde{\hat{\boldsymbol{z}}} \cdot \dot{\boldsymbol{r}} + n^2(3\hat{\boldsymbol{x}}\hat{\boldsymbol{x}} - \hat{\boldsymbol{z}}\hat{\boldsymbol{z}}) \cdot \boldsymbol{r} - \frac{\mu_e}{r_{\mathrm{s/c}}^3}\boldsymbol{r}_{\mathrm{s/c}} + \frac{\mu_e}{r^{*3}}\boldsymbol{r}^*
\end{aligned}
\tag{2.26}
$$

where $\boldsymbol{r} = \boldsymbol{r}_{\mathrm{s/c}} - \boldsymbol{r}^*$ is the relative position of the spacecraft as seen from the asteroid. Assuming $\mathcal{O}(|\boldsymbol{r}|) << \mathcal{O}(|\boldsymbol{r}^*|)$, the position vector of the spacecraft can be expanded around $\boldsymbol{r}^*$. Ignoring the higher order terms, the gravity gradient can be linearized as

$$
-\mu_e \left(\frac{\boldsymbol{r}^* + \boldsymbol{r}}{|\boldsymbol{r}^* + \boldsymbol{r}|^3} - \frac{\boldsymbol{r}^*}{|\boldsymbol{r}^*|^3} \right) = -\frac{\mu_e}{|\boldsymbol{r}^*|^3} \left(I - 3\hat{\boldsymbol{r}}^*\hat{\boldsymbol{r}}^* \right) \cdot \boldsymbol{r} + \mathcal{O}((r/r^*)^2)
\tag{2.27}
$$

The spacecraft also experiences SRP acceleration. Furthermore, we can add the gravitational attraction of the asteroid experienced by the spacecraft. Also, we allow the spacecraft to perform impulsive maneuvers. Thus, the generic form of the relative motion dynamics can be written as

$$
\begin{aligned}
\ddot{\boldsymbol{r}} = &-2n\tilde{\hat{\boldsymbol{z}}} \cdot \dot{\boldsymbol{r}} + n^2(3\hat{\boldsymbol{x}}\hat{\boldsymbol{x}} - \hat{\boldsymbol{z}}\hat{\boldsymbol{z}}) \cdot \boldsymbol{r} - \frac{\mu_e}{|\boldsymbol{r}^*|^3} \left(I - 3\hat{\boldsymbol{r}}^*\hat{\boldsymbol{r}}^* \right) \cdot \boldsymbol{r} \\
&+ C_{\mathrm{SRP}} a_{\mathrm{SRP}} \hat{\boldsymbol{x}} - \frac{\mu}{r^3}\boldsymbol{r} + \boldsymbol{\Delta V}_i \delta(t - \tau_i)
\end{aligned}
\tag{2.28}
$$

where C_{SRP} is the SRP coefficient; $\boldsymbol{r}^*$ comes from the known ephemeris; μ is the gravitational parameter of the asteroid. One thing to note is that apart from the asteroid's gravity and Delta-
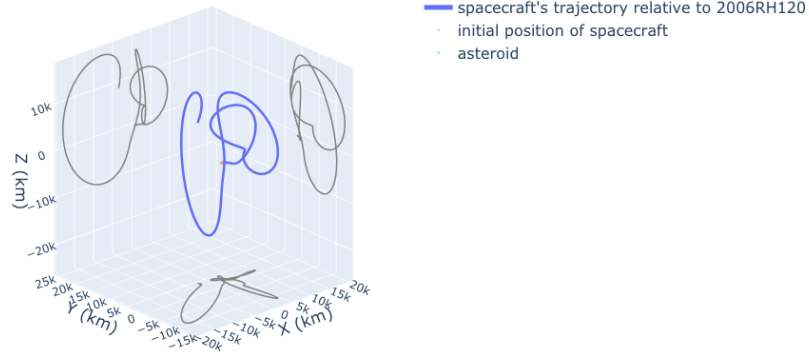
Figure 2.3: Relative position of the spacecraft as seen from 2006 RH120.

Vs, the model has linear dynamics. As for the asteroid's mass parameter, $\mu = 8.7366 \times 10^{-15}$ km^3/s^2 is used, assuming a density of 2.0 g/cm^3.

Figure 2.4 shows the relative trajectory propagated by the relative motion dynamics. The spacecraft's relative state is initially set to $\boldsymbol{r} = [-10, 0, 0]$. There are no maneuvers. We can confirm that the resulting trajectory matches Figure 2.3.

It is of interest to study the orders of magnitude of different accelerations experienced by the spacecraft. Figure 2.5 shows the different accelerations (solar tide, Earth's gravity gradient, SRP, and asteroid's gravity) at different altitudes throughout the asteroid's orbit around Earth. The solar tide effect is labeled as "Hill (solar gravity)" in Fig. 2.5, and it corresponds to the following acceleration

$$n^2(3\hat{\boldsymbol{x}}\hat{\boldsymbol{x}} - \hat{\boldsymbol{z}}\hat{\boldsymbol{z}}) \cdot \boldsymbol{r} \tag{2.29}$$

The spacecraft is assumed to be stationary relative to the asteroid. In general, the gravity gradient and solar tide become stronger when the spacecraft-asteroid distance is larger. On the other hand, the gravitational attraction from the asteroid becomes stronger at a shorter distance. SRP is constant. We can confirm that at a distance greater than 10 km, the gravity gradient is the major acceleration acting on the spacecraft. At 1 km, SRP becomes the dominant acceleration. At 10 meters, the gravity from the asteroid becomes comparable with SRP. Thus, the study tells us that
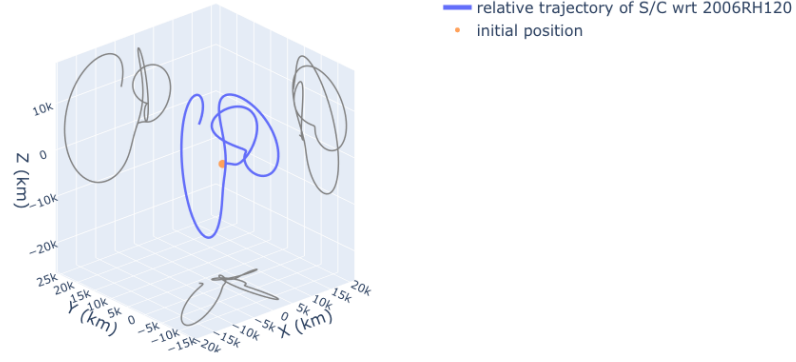
Figure 2.4: TCO-relative trajectory generated by the relative motion dynamics

the asteroid's gravity is mostly negligible for navigation and orbit control unless the spacecraft is as close as 10 meters to the asteroid.

2.4.2   TCO Ephemeris Error Effect

Another aspect of interest is the effect of the ephemeris errors. With the relative motion dynamics, it is possible to compute the covariance matrix of the relative acceleration given the covariance matrix of the asteroid's position.

$$
\begin{aligned}
C_{\ddot{\boldsymbol{r}}} &= \mathbb{E}[\delta\ddot{\boldsymbol{r}}\delta\ddot{\boldsymbol{r}}] \\
&= \frac{\partial\ddot{\boldsymbol{r}}}{\partial\boldsymbol{r}^*} \cdot \mathbb{E}[\delta\boldsymbol{r}^*\delta\boldsymbol{r}^*] \cdot \left(\frac{\partial\ddot{\boldsymbol{r}}}{\partial\boldsymbol{r}^*}\right)^T \\
&= \frac{\partial\ddot{\boldsymbol{r}}}{\partial\boldsymbol{r}^*} \cdot C_{\boldsymbol{r}^*} \cdot \left(\frac{\partial\ddot{\boldsymbol{r}}}{\partial\boldsymbol{r}^*}\right)^T
\end{aligned}
\tag{2.30}
$$

where $C_{\boldsymbol{r}^*}$ is the covariance matrix of the asteroid's position; $\mathbb{E}$ is the expectation operator. If we assume the position error is constant and is a spherical Gaussian, then $C_{\boldsymbol{r}^*} = \sigma_{\boldsymbol{r}^*}^2 I$. Thus, the acceleration error covariance is defined as follows.

$$
C_{\ddot{\boldsymbol{r}}} = \sigma_{\boldsymbol{r}^*}^2 \left(\frac{\partial\ddot{\boldsymbol{r}}}{\partial\boldsymbol{r}^*}\right) \cdot \left(\frac{\partial\ddot{\boldsymbol{r}}}{\partial\boldsymbol{r}^*}\right)^T
\tag{2.31}
$$

The partial derivative can be derived as follows. We use indices to represent an element of a

tensor and use Einstein's summation convention.

$$
\begin{aligned}
\left(\frac{\partial \ddot{\boldsymbol{r}}}{\partial \boldsymbol{r}^*}\right)_{ij} &= \frac{\partial}{\partial r_j^*}\left[-\frac{\mu_e}{r^{*3}}(\delta_{ik} - 3\hat{r}_i^*\hat{r}_k^*)r_k\right] \\
&= 3\frac{\mu_e}{r^{*4}}\hat{r}_j^*(\delta_{ik} - 3\hat{r}_i^*\hat{r}_k^*)r_k + 3\frac{\mu_e}{r^{*3}}\left(\frac{\partial \hat{r}_i^*}{\partial r_j^*}\hat{r}_k^* + \hat{r}_i^*\frac{\partial \hat{r}_k^*}{\partial r_j^*}\right)r_k
\end{aligned}
\tag{2.32}
$$

Note that δ_{ij} is Kronecker's delta. If we use the following relationship

$$
\frac{\partial \hat{r}_i^*}{\partial r_j^*} = \frac{1}{r^*}(\delta_{ij} - \hat{r}_i^*\hat{r}_j^*)
\tag{2.33}
$$

then,

$$
\left(\frac{\partial \ddot{\boldsymbol{r}}}{\partial \boldsymbol{r}^*}\right)_{ij} = 3\frac{\mu_e}{r^{*4}}\left(\hat{r}_i\hat{r}_j^* - 5\hat{r}_i^*\hat{r}_j^*\hat{r}_k^*\hat{r}_k + \delta_{ij}\hat{r}_k^*\hat{r}_k + \hat{r}_i^*\hat{r}_j\right)r
\tag{2.34}
$$

where $r = |\boldsymbol{r}|$. Therefore,

$$
\frac{\partial \ddot{\boldsymbol{r}}}{\partial \boldsymbol{r}^*} = 3\frac{\mu_e}{r^{*4}}r\left[\hat{\boldsymbol{r}}\hat{\boldsymbol{r}}^* - 5(\hat{\boldsymbol{r}} \cdot \hat{\boldsymbol{r}}^*)\hat{\boldsymbol{r}}^*\hat{\boldsymbol{r}}^* + (\hat{\boldsymbol{r}} \cdot \hat{\boldsymbol{r}}^*)I + \hat{\boldsymbol{r}}^*\hat{\boldsymbol{r}}\right]
\tag{2.35}
$$

From Eqs. (2.31) and (2.35), we can show that the acceleration noise is parameterized by a single value $r\sigma_{\boldsymbol{r}^*}$. Figure 2.6 shows the acceleration errors computed by Eq. (2.31). At each time, $\sigma_{\ddot{\boldsymbol{r}}} = \sqrt{C_{\ddot{\boldsymbol{r}},1,1} + C_{\ddot{\boldsymbol{r}},2,2} + C_{\ddot{\boldsymbol{r}},3,3}}$ is plotted, which is the net acceleration error. The plot also has 100%, 10%, and 1% of nominal SRP as references. For example, we can see that if $r\sigma_{\boldsymbol{r}}^* = 1e5$ km, namely, $r = 100$ km and $\sigma_{\boldsymbol{r}^*} = 1,000$ km or $r = 1,000$ km and $\sigma_{\boldsymbol{r}^*} = 100$ km and so on, then the acceleration errors are mostly less than 10% of the nominal SRP. The end-to-end simulations in this study nominally use a process noise covariance whose $1 - \sigma$ value is about 10% of the nominal SRP. Thus, the noise due to the ephemeris errors up to 1,000 km should not change the result of the study here, assuming the hovering occurs at less than 100 km distance. To further assess the impact of the ephemeris errors, we need to actively include the ephemeris errors and perform covariance analyses. If the ephemeris errors are larger or the spacecraft's distance is larger, then we might be able to estimate the ephemeris itself by leveraging the information in the gravity gradient acceleration.

2.4.3   TCO Hovering Dynamics

As shown in the earlier sections, the spacecraft moves away from the target asteroid if no control is applied. The study first analyzes a simple box-based trajectory control scheme, where the direction of the relative velocity is corrected such that the spacecraft moves towards the center of the box every time the spacecraft is about to move outside a predefined control box in Cartesian position space. This approach can suffer from the issue of chattering, but it gives us a conservative bound on the necessary ΔV budget to track the target asteroid. Another approach is to solve TPBVPs to compute a ΔV that connects two position vectors in a given transfer time. To solve such a TPBVP, a numerically integrated state transition matrix (STM) of the relative motion dynamics can be used.

2.4.3.1   Box-based hovering for TCO tracking

First, a simple hovering control scheme is studied to understand the motion of the spacecraft performing hovering and to estimate the required ΔV. In this approach, a cubic box centered at a nominal hovering position is defined, and every time the spacecraft reaches the box's boundaries, a maneuver is performed. The maneuver is applied such that the post-maneuver velocity points toward the center of the box. Three different cases are illustrated in this section: 100 km hovering, 10 km hovering, and 1 km hovering. The hovering occurs on the Sun side in all cases. The hovering distance, box size, number of maneuvers, and total ΔV for the 10-month tracking for each of these cases are shown in Table 2.1. Figure 2.7 shows the resulting trajectories for these cases.

Table 2.1: 10-month box-control simulation conditions and results for TCO tracking

Case	hovering distance (km)	box size (km)	number of maneuvers	total ΔV (m/s)
1	100	1	277	8.8295
2	10	1	215	4.5857
3	1	0.1	678	4.5861

When the hovering distance is short, most of the acceleration comes from SRP. The nominal SRP is 1.2768×10^{-10} km/s^2, thus, by multiplying the duration of the hovering period by the SRP

acceleration, we can estimate that the required ΔV is about 3.3095 m/s. Thus, the box-based control seems to give us a reasonable estimate of the total ΔV, although it is slightly higher than the expected total ΔV. Also, from the results, we can confirm that we will need to perform more maneuvers to control the spacecraft in a smaller control box. When the hovering is performed at a 100 km distance, the resulting total ΔV is significantly larger. The large ΔV would be required to counteract the additional acceleration of the gravity gradient.

2.4.3.2   TPBVP-based hovering for TCO tracking

If we ignore the contribution of the asteroid's gravity, the relative motion dynamics becomes a non-homogeneous linear time-varying (LTV) system.

$$\ddot{\boldsymbol{r}} = -2n\tilde{\hat{\boldsymbol{z}}} \cdot \dot{\boldsymbol{r}} + n^2(3\hat{\boldsymbol{x}}\hat{\boldsymbol{x}} - \hat{\boldsymbol{z}}\hat{\boldsymbol{z}}) \cdot \boldsymbol{r} - \frac{\mu_e}{|\boldsymbol{r}^*|^3}\left(I - 3\hat{\boldsymbol{r}}^*\hat{\boldsymbol{r}}^*\right) \cdot \boldsymbol{r} + C_{\mathrm{SRP}}a_{\mathrm{SRP}}\hat{\boldsymbol{x}} \tag{2.36}$$

We can solve a TPBVP using a numerically integrated STM of the LTV dynamics. Given $\boldsymbol{r}_0$ at $t = t_0$ and a target position $\boldsymbol{r}_{\mathrm{tgt}}$ at $t = \Delta t$, the solution of the TPBVP $\boldsymbol{v}_0$ can be obtained as follows. The numerical integration gives us the expected position $\boldsymbol{r}(t_0 + \Delta t)$ at $t = t_0 + \Delta t$ when no control is applied, as well as an STM $\Phi_{rv}(t_0 + \Delta t; t_0)$. By definition, the STM is $\partial \boldsymbol{r}(t_0 + \Delta t)/\partial \boldsymbol{v}(t_0)$. Since the dynamics are a linear system, the solution is simply obtained as

$$\Delta\boldsymbol{v} = \Phi_{rv}^{-1}(t_0 + \Delta t) \cdot (\boldsymbol{r}_{\mathrm{tgt}} - \boldsymbol{r}_0) \tag{2.37}$$

Figures 2.8 and 2.9 show the resulting relative trajectory for 10 km hovering and 100 km hovering respectively. Maneuvers are applied every two days. We can see that the solutions from the TPBVP solver keep bringing the spacecraft back to the target position. Another thing to note is that the gravity gradient becomes stronger when the hovering distance is farther away from the asteroid. At 100 km hovering, the transfer arc changes its direction depending on where Earth is located relative to the asteroid. In contrast, at 10 km hovering, the major acceleration is SRP. Thus, the maneuver is applied to push the spacecraft away from the asteroid along the x-axis. The shift in the acceleration direction would benefit the operation during an approach phase because the

spacecraft's motion becomes more predictable as the spacecraft gets closer to the target. In both cases, we observe the off x-axis motion around 100 days, 175 days, and 255 days. This behavior is also caused by the stronger gravity gradient acceleration as the asteroid travels closer to Earth, which can be confirmed by looking at Figure 2.5. For 10-month hovering at 10 km, the total ΔV is 3.368 m/s. The total ΔV for 100 km hovering is 4.869 m/s. Thus, the approach based on the TPBVP solver is more efficient than the simple box-based control as there is no issue of chattering.
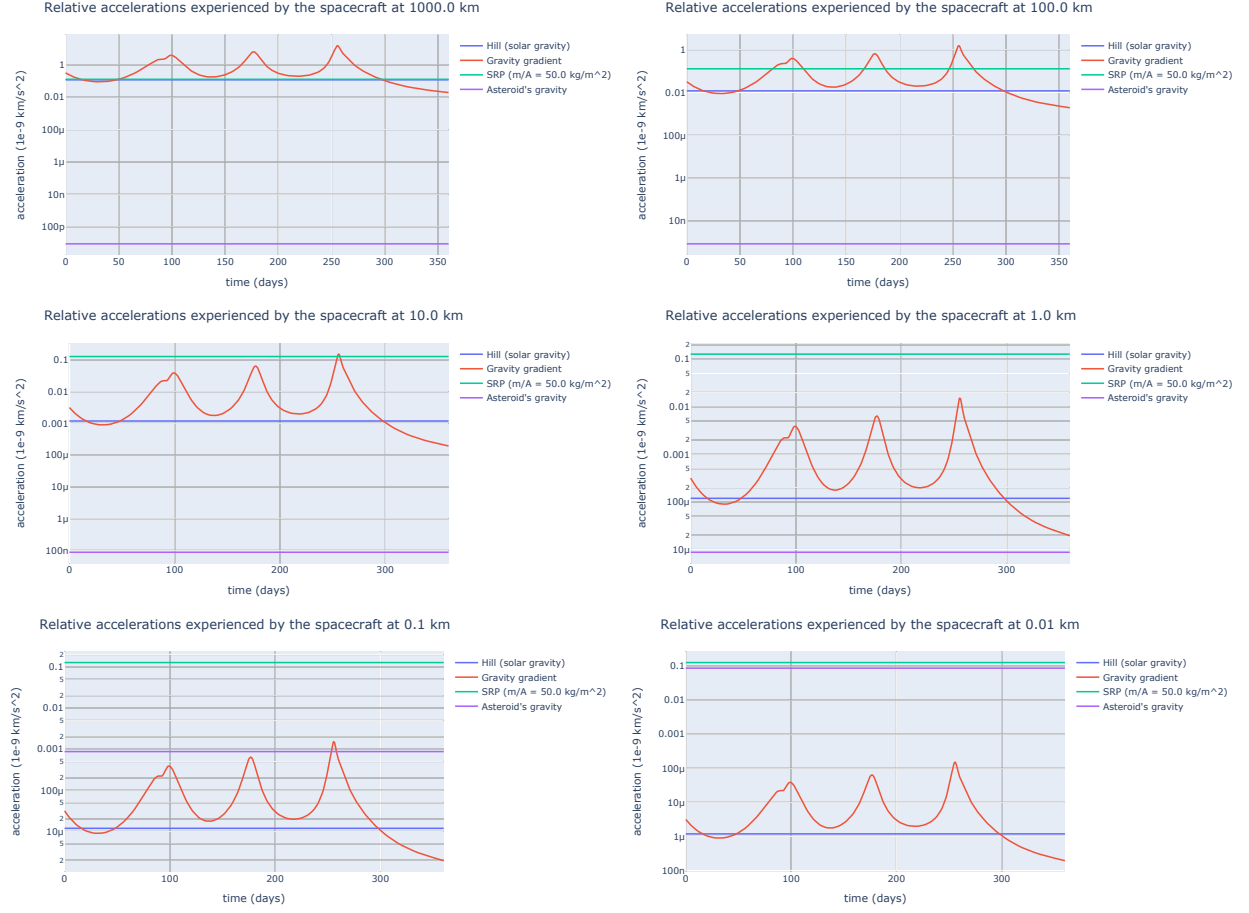
Figure 2.5: Relative accelerations experienced by the spacecraft at different distances from the TCO. (1000 km, 100 km, 10 km, 1 km, 0.1 km, 0.01 km).

Figure 2.6: Acceleration errors given the TCO's ephemeris errors.

Case 1: 100 km hovering, 1 km box.

Case 2: 10 km hovering, 1 km box.

Case 3: 1 km hovering, 0.1 km box.
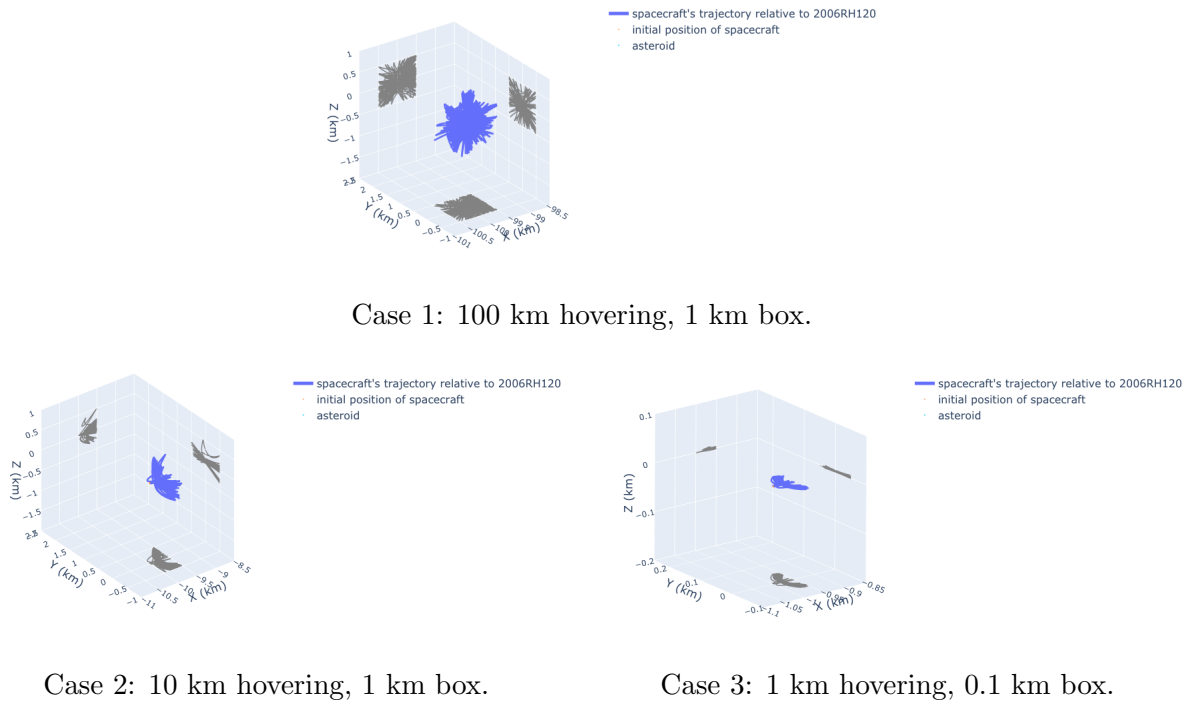
Figure 2.7: 3D plots of trajectories for the 10-month box-based control.

3D plot of trajectory

position time history
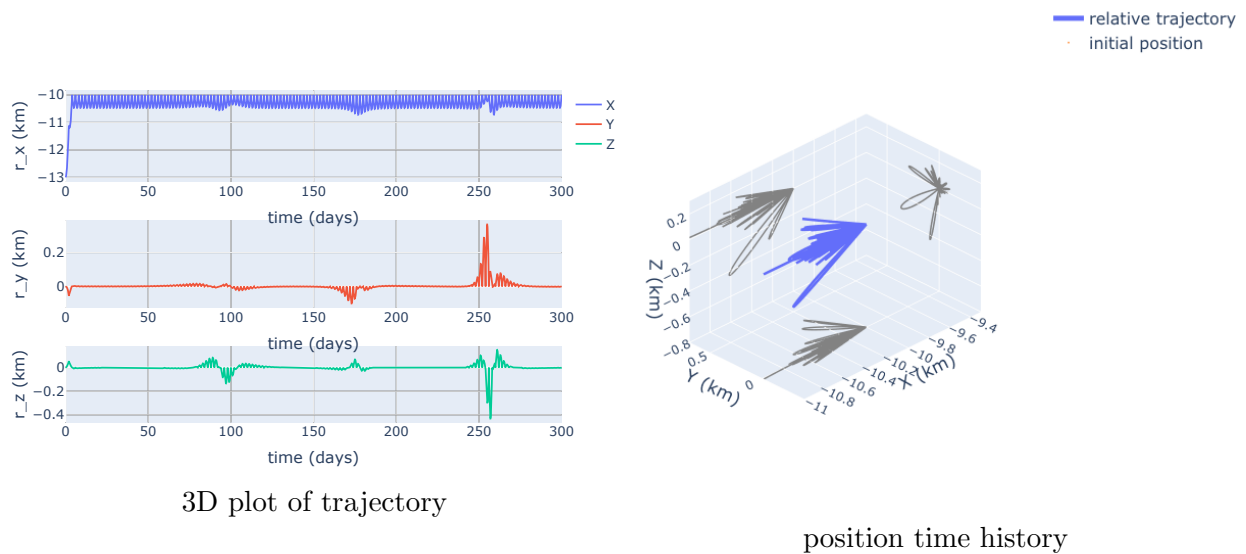
Figure 2.8: 10 km hovering trajectory for 10 months obtained using a numerical STM to solve TPBVP.

3D plot of trajectory

position time history
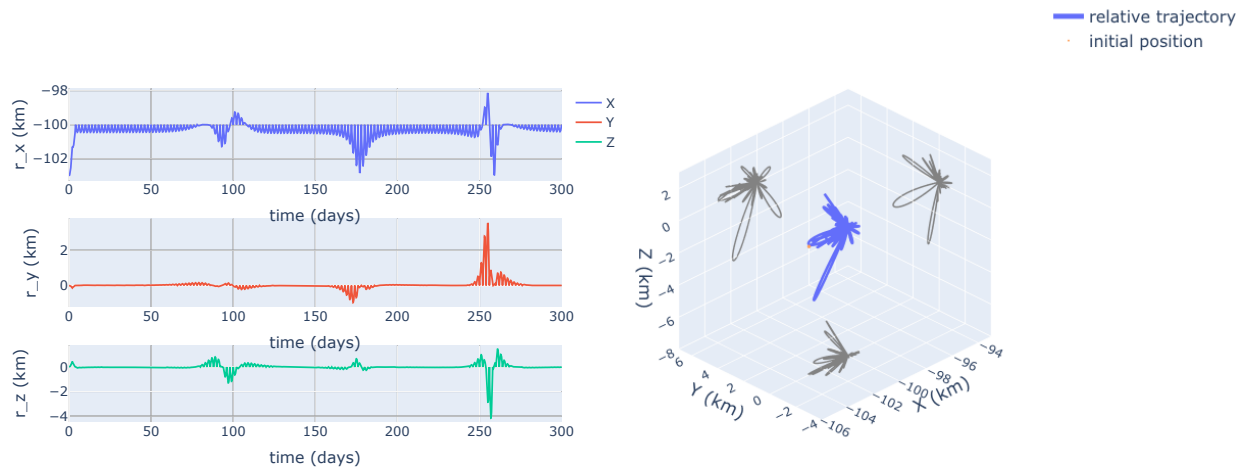
Figure 2.9: 100 km hovering trajectory for 10 months obtained using a numerical STM to solve TPBVP.

Chapter 3

Frozen Orbit Design

Several useful orbits around an asteroid have been identified to date through two different approaches. The first approach is to compute periodic and quasi-periodic orbits in the framework of the Hill three-body problem with the addition of SRP [31, 32]. The wide variety of orbit geometries provided by these types of orbits can be beneficial for global mapping. However, designing such orbits requires iterative numerical computation. The focus of this study is the second approach, where perturbed Keplerian orbits are considered, and a specific orbit geometry that cancels out perturbations on average is studied. Conditions to realize such a frozen orbit are investigated analytically through averaged planetary equations; therefore, resulting orbits are specified by a set of mean orbital elements. With the analytical approach, we can immediately understand how a designed orbit depends on various parameters and evaluate how sensitive the orbit is to the change in these parameters. The capability to define desired orbits analytically is advantageous for onboard guidance and orbit correction in that the computation is simple and robust, as opposed to a numerical approach that requires larger computational resources and might not necessarily converge. Also, the solution from the analytical calculation can be used as an initial guess for the predictor-corrector algorithm to improve the convergence if there is a need for computing a periodic orbit.

A class of orbits found by the averaged analysis is terminator orbits, near-circular polar orbits that exist when there is a strong SRP perturbation. Its orbit normal points toward or away from the Sun; namely, the orbit lies in the terminator plane of an asteroid. The orbits are stable, although

there exists an upper bound on the possible orbit size [33, 34, 35]. When point mass gravity is assumed along with the SRP force, secular dynamics are integrable, which gives us closed-form frozen orbit conditions [36, 37, 38, 24].

This chapter addresses two kinds of corrections to the conventional frozen conditions for terminator orbits. The first correction accounts for the irregular gravity effect. As the orbit size becomes smaller, the point mass assumption starts to break down. We focus on the zonal terms of the asteroid's gravity field to derive analytical corrections, assuming the asteroid's rotation is fast enough to average out the longitudinal dependence. In this study, we specifically consider the contribution of J_2 and J_3. Furthermore, a common assumption is made that the rotation pole of the asteroid is aligned with the asteroid's orbit normal, which helps simplify the problem. For small asteroids whose diameters are less than 10km, thermal re-emission and scattering of the sunlight at the surface have been considered to affect the spin state significantly, which is known as the YORP effect. Research to date indicates that YORP is responsible for driving the obliquity to $0°$, $90°$, and $180°$ [39, 40, 41]. The observations made by recent NEA exploration missions are consistent with the YORP models, and the asteroids Itokawa, Ryugu, and Bennu all have obliquities close to $180°$ [42, 43, 44]. In that the obliquity of $0°$ and $180°$ are asymptotic cases of the YORP models and that they are what we have physically observed, making this assumption is reasonable. The joint effects of J_2 and SRP have been analyzed in several studies. In [38], the fluctuation of orbital elements due to the J_2 perturbation when a spacecraft is nominally in a terminator orbit is evaluated. In [45] and [46], new frozen orbit conditions are investigated when SRP and J_2 are both present. While their work focuses on equatorial orbits called Heliotropic orbits, the terminator orbit solutions are also identified. Furthermore, in [47], a detailed linear stability analysis is performed for a terminator orbit, which explains the instability when SRP and J_2 have a coupled effect. One novel contribution of this study is the analysis of the J_3 effect. Unlike a J_2 only case, symmetry regarding frozen orbit conditions is broken, which necessitates a distinction between two possible terminator orbits. A recent study of the frozen orbits in small-body environments analyzes the contributions of additional zonal terms of the gravity field, and their findings are consistent with the current study

[48]. Another novelty is the formulation with the Milankovitch elements, which accomplishes a more comprehensive and simpler illustration of frozen orbit conditions. This formulation also enables us to derive a first-order approximation of the necessary correction to the original terminator orbit's mean orbital elements in a closed form.

The second correction stems from the fact that a terminator orbit has a geometric offset between mass and orbit centers as SRP pushes the orbit plane away from the Sun. Though a terminator orbit takes a simple near-circular shape, its orbital elements experience large variation over one orbit as the offset makes the motion non-Keplerian, as seen by the mass center. This large short-period variation leads to a significant bias between desired mean and initial values. Simply propagating the mean orbital elements that are obtained as a frozen orbit condition results in an orbit whose mean orbital elements are different from the target mean values. The offset effect becomes significant when the orbit size is large. A natural approach to eliminating the short-period variation is defining a set of orbital elements relative to the orbit center rather than the mass center. We generalize this idea and investigate the effect of shifting the origin at which we define orbital elements, moving it arbitrarily along the Sun-asteroid line.

Terminator orbits are an ideal option for long-term observation due to their stability, and thus it is of interest to study the long-term behavior of the orbits. Especially, studying the behavior of terminator orbits when the eccentricity of the asteroid's orbit is non-zero is meaningful. Leveraging the analytical insight of the problem, the effect of the asteroid orbit's eccentricity and the validity of the proposed offset corrections in such cases are studied.

In the first section of this chapter, we introduce models used to represent the dynamics. After reviewing the conventional terminator orbit, we address new frozen orbit conditions when the J_2 and J_3 perturbations are present. The thesis then describes two-dimensional maps that graphically show new frozen orbit conditions, followed by a discussion on analytical corrections for the original terminator orbit. The second part of the chapter focuses on the offset effect when SRP is the dominant perturbation. An optimal offset that minimizes the bias in the osculating orbital elements is derived from short-period analyses on the angular momentum vector. Additional

corrections to refine an initial condition when the offset effect is significant are further discussed, addressing the higher-order contribution of the offset. We then discuss applying both corrections to better define an initial condition of a terminator orbit for a wide range of orbit sizes. Finally, the long-term behavior of the terminator orbits for eccentric asteroid orbits and the offset corrections in such cases are described.

3.1   Dynamics

Insight into the evolution of a spacecraft's orbit is obtained by averaged planetary equations. While a set of desired orbital elements is derived from the averaged analysis, the results are based on the approximation that the change of the orbital elements is slow. For the purpose of verifying the averaged analysis, solutions of the numerically integrated equations of motion are used as a truth.

3.1.1   Perturbations

The study uses the Hill three-body model with SRP described in Chapter 2 to model the spacecraft's motion. Nominally, the eccentricity of the asteroid's orbit is assumed to be zero. Thus, the equations of motion have the form of Eq. (2.11). The contribution of the asteroid orbit's eccentricity is analyzed at the end of this chapter.

The current study additionally considers the contributions of zonal gravity field perturbations. The force potential for the zonal terms in the spherical harmonics gravity expansion is given by the following equations

$$U_{J_\ell}(\boldsymbol{r}, \hat{\boldsymbol{p}}) = \mu R_0^\ell C_{\ell 0} \sum_{i=0}^{\text{int}[\ell/2]} T_{\ell i} \cdot \frac{(\hat{\boldsymbol{r}} \cdot \hat{\boldsymbol{p}})^{\ell - 2i}}{r^{\ell + 1}} \tag{3.1}$$

$$T_{\ell i} = \frac{(-1)^i (2\ell - 2i)!}{2^\ell i! (\ell - i)! (\ell - 2i)!} \tag{3.2}$$

where R_0 is the reference radius and $\hat{\boldsymbol{p}}$ is a unit vector in the direction of the asteroid's spin pole

[24]. When $\ell = 2$ and 3, we get the following potential respectively.

$$U_{J_2} = \frac{-\mu R_0^2 C_{20}}{2r^3} \left[1 - 3(\hat{\bm{r}} \cdot \hat{\bm{p}})^2 \right] \tag{3.3}$$

$$U_{J_3} = \frac{\mu R_0^3 C_{30}}{2r^4} (\hat{\bm{r}} \cdot \hat{\bm{p}}) \left[5(\hat{\bm{r}} \cdot \hat{\bm{p}})^2 - 3 \right] \tag{3.4}$$

In numerical simulations, parameters listed in Table 3.1 are used, and the spin pole is assumed to satisfy $\hat{\bm{p}} = -\hat{\bm{z}}$. These values are closely aligned with the OSIRIS-REx spacecraft and asteroid Bennu [20, 49]. We note that these values do not reflect the best navigation solution to date; rather, they are used as a realistic reference.

Table 3.1: Parameters used for numerical computation of terminator orbits

Symbol	Unit	Description	Value
R_0	m	Reference radius	246
μ	m^3/s^2	GM of the asteroid	5.2
ρ	-	spacecraft's surface reflectivity	0.4
B	kg/m^2	spacecraft's mass-to-area ratio	62
A	AU	SMA of the asteroid's orbit	1.126
C_{20}	-	Unnormalized J_2 coefficient	-3.9156×10^{-2}
C_{30}	-	Unnormalized J_3 coefficient	1.4843×10^{-2}

3.1.2 Averaged Planetary Equations

A standard approach to describe the evolution of orbital elements is to use planetary equations. Lagrange Planetary Equations (LPEs) with averaged perturbing potentials are used to derive frozen orbit conditions where orbital elements stay constant on average. The LPEs are defined in terms of the Milankovitch elements. The advantage of using the Milankovitch elements is that it becomes easier to visualize the orbit geometry without assigning a particular frame, as they are vector elements. It turns out this property is helpful in considering frozen orbit conditions. Another benefit is that the averaged LPEs can be written in a simple form [50].

$$\dot{\bm{h}} = \tilde{\bm{h}} \cdot \frac{\partial \overline{U}^*}{\partial \bm{h}} + \tilde{\bm{e}} \cdot \frac{\partial \overline{U}^*}{\partial \bm{e}} \tag{3.5}$$

$$\dot{\bm{e}} = \tilde{\bm{e}} \cdot \frac{\partial \overline{U}^*}{\partial \bm{h}} + \tilde{\bm{h}} \cdot \frac{\partial \overline{U}^*}{\partial \bm{e}} \tag{3.6}$$

where $\boldsymbol{h}$ and $\boldsymbol{e}$ are mean values of angular momentum and eccentricity vectors respectively. The angular momentum vector is scaled by GM and semi-major axis such that

$$\boldsymbol{h} = \frac{\boldsymbol{H}}{\sqrt{\mu a}}. \tag{3.7}$$

Then the following condition holds true.

$$h^2 + e^2 = 1 \tag{3.8}$$

Similarly, an averaged perturbing potential $\overline{U}$ is scaled such that

$$\overline{U}^* = \frac{\overline{U}}{\sqrt{\mu a}}. \tag{3.9}$$

A perturbing potential is, in general, a function of mean anomaly M and a set of orbital elements $\boldsymbol{\alpha}$. The first-order averaging is performed by evaluating the following quadrature, which eliminates the explicit time dependence.

$$\overline{U}(\boldsymbol{\alpha}) = \frac{1}{2\pi} \int_0^{2\pi} U(\boldsymbol{\alpha}, M) dM \tag{3.10}$$

Although orbital elements are typically defined relative to an inertial frame, it turns out that studying orbit geometry with respect to the Sun-asteroid fixed rotating frame simplifies the problem, as the direction of the SRP acceleration becomes constant. A frozen orbit in the rotating frame thus becomes a Sun-synchronous orbit. We follow the approach taken in [37, 38] to study the evolution of the mean orbital elements, where we first ignore the solar gravity effect and consider the dynamics in an asteroid-centered inertial frame. Then, the aforementioned averaged LPEs can be defined for other perturbations, such as SRP and the higher-order gravity field of the asteroid in this frame. We can then derive the LPEs relative to the rotating frame by applying the transport theorem. One assumption is that the asteroid's orbital motion is slow enough compared to the spacecraft's orbit rate such that the same averaging results hold true. To have LPEs defined in the rotating frame, we only need to have additional terms of $-\dot{F}\tilde{\boldsymbol{z}} \cdot \boldsymbol{h}$ and $-\dot{F}\tilde{\boldsymbol{z}} \cdot \boldsymbol{e}$ in the right-hand sides of the original equations.

3.1.3   Regular Terminator Orbit

In the conventional case where point mass gravity is assumed, the main perturbation is SRP. The perturbing potential for SRP is given as

$$U_{\text{SRP}} = a_{\text{SRP}}\, \hat{\boldsymbol{x}} \cdot \boldsymbol{r} \tag{3.11}$$

and its average is found to be

$$\overline{U}_{\text{SRP}} = -\frac{3}{2}a \cdot a_{\text{SRP}}\hat{\boldsymbol{x}} \cdot \boldsymbol{e} \tag{3.12}$$

because the position vector $\boldsymbol{r}$ averages to $-3a\boldsymbol{e}/2$. With Eqs. (3.5) and (3.6), the LPEs for the SRP dominant case are obtained as follows.

$$\dot{\boldsymbol{h}} = -\dot{F}\tilde{\hat{\boldsymbol{z}}} \cdot \boldsymbol{h} + \frac{3}{2}a_{\text{SRP}}\sqrt{\frac{a}{\mu}}\tilde{\hat{\boldsymbol{x}}} \cdot \boldsymbol{e} \tag{3.13}$$

$$\dot{\boldsymbol{e}} = -\dot{F}\tilde{\hat{\boldsymbol{z}}} \cdot \boldsymbol{e} + \frac{3}{2}a_{\text{SRP}}\sqrt{\frac{a}{\mu}}\tilde{\hat{\boldsymbol{x}}} \cdot \boldsymbol{h} \tag{3.14}$$

The equations represent a simple linear time-invariant system, and its general solution can be analytically obtained. It is shown that changing the independent variable from time to the asteroid's true anomaly results in a similar linear system even when an elliptic asteroid orbit is considered [38, 24]. This result is owing to the fact that both $\dot{F}$ and a_{SRP} are proportional to $1/d^2$.

The secular SRP dynamics can be parameterized by a single parameter Λ, an angle indicating the relative strength of SRP. The parameter is defined by

$$\tan\Lambda = \frac{3(1+\rho)P_0(1\text{AU})^2}{2B}\sqrt{\frac{a}{\mu\mu_{\text{Sun}}A(1-E^2)}} \tag{3.15}$$

where E is the eccentricity of the asteroid's orbit. When SRP is weak, $\Lambda \to 0$, and when it is strong, $\Lambda \to \pi/2$. We note that Λ is a function of a, which suggests a stronger SRP effect when the orbit size is larger.

Detailed analysis of the null space of the linear secular dynamics reveals that there are two classes of frozen orbits: an equatorial family and a terminator plane family. Under a strong SRP environment, terminator orbits become preferable as the equatorial family becomes highly eccentric.

Besides, the equatorial orbits go through the asteroid's shadow, which complicates the trajectory design. The frozen orbit condition for a regular terminator orbit is summarized as

$$\hat{\boldsymbol{h}} = \pm\,\hat{\boldsymbol{x}} \tag{3.16}$$

$$\hat{\boldsymbol{e}} = \hat{\tilde{\boldsymbol{y}}} \cdot \hat{\boldsymbol{h}} \tag{3.17}$$

$$e = \cos\Lambda. \tag{3.18}$$

Depending on whether the angular momentum vector points toward or away from the Sun, two different terminator orbits geometries can exist. The eccentricity is the same for both of the orbits, and the orbit becomes more circular as the influence of SRP grows larger. When $\hat{\boldsymbol{h}}$ points toward the Sun, $\boldsymbol{e}$ points above the ecliptic plane, and when $\hat{\boldsymbol{h}}$ points away from the Sun, $\boldsymbol{e}$ points below the ecliptic plane.

3.2   New Frozen Orbits

This section discusses the necessary correction when the joint effect of SRP, J_2, and J_3 perturbations are considered. This correction becomes more important when the spacecraft's altitude is lower.

3.2.1   LPEs for J_2 and J_3

The contribution of J_2 and J_3 on the orbital elements are evaluated by averaging the original perturbing potentials defined in Eq. (3.1). The time dependence only shows up in the position vector. Thus we need to evaluate the following quadrature to find an averaged potential for a general J_ℓ perturbation.

$$\overline{\left(\frac{(\hat{\boldsymbol{r}} \cdot \hat{\boldsymbol{p}})^{\ell-2q}}{r^{\ell+1}}\right)} = \frac{(\sin i)^{\ell-2q}}{2\pi a^{\ell+1}(1-e^2)^{\ell-\frac{1}{2}}} \times \int_0^{2\pi} [\sin(\omega+f)]^{\ell-2q}\,(1+e\cos f)^{\ell-1}df \tag{3.19}$$

where a frame is assigned such that the third axis is aligned with $\hat{\boldsymbol{p}}$. Since the choice of the frame is arbitrary, we can recast the averaged potential in a frame-independent expression. After some

algebra, we obtain

$$\overline{U_{J_2}} = \frac{\mu R_0^2 C_{20}}{4a^3 h^3} \left[1 - 3(\hat{\boldsymbol{p}} \cdot \hat{\boldsymbol{h}})^2 \right] \tag{3.20}$$

and the averaged LPEs for the J_2 perturbation is

$$\dot{\boldsymbol{h}}_{J_2} = \frac{3n R_0^2 C_{20}}{2a^2 h^5} (\hat{\boldsymbol{p}} \cdot \boldsymbol{h}) \tilde{\hat{\boldsymbol{p}}} \cdot \boldsymbol{h} \tag{3.21}$$

$$\dot{\boldsymbol{e}}_{J2} = \frac{3n R_0^2 C_{20}}{4a^2 h^5} \left\{ \left[1 - \frac{5}{h^2} (\hat{\boldsymbol{p}} \cdot \boldsymbol{h})^2 \right] \tilde{\boldsymbol{h}} + 2(\hat{\boldsymbol{p}} \cdot \boldsymbol{h}) \tilde{\hat{\boldsymbol{p}}} \right\} \cdot \boldsymbol{e}. \tag{3.22}$$

Similarly, the averaged potential and LPEs for the J_3 perturbation are computed as

$$\overline{U_{J_3}} = \frac{3\mu R_0^3 C_{30}}{8a^4 h^5} \boldsymbol{e} \cdot \hat{\boldsymbol{p}} \left[1 - 5(\hat{\boldsymbol{p}} \cdot \hat{\boldsymbol{h}})^2 \right] \tag{3.23}$$

and

$$\dot{\boldsymbol{h}}_{J_3} = \frac{3n R_0^3 C_{30}}{4a^3 h^5} \left\{ \frac{5}{h^2} (\hat{\boldsymbol{p}} \cdot \boldsymbol{e})(\hat{\boldsymbol{p}} \cdot \boldsymbol{h}) \tilde{\hat{\boldsymbol{p}}} \cdot \boldsymbol{h} - \frac{1}{2} \left[1 - \frac{5}{h^2} (\hat{\boldsymbol{p}} \cdot \boldsymbol{h})^2 \right] \tilde{\hat{\boldsymbol{p}}} \cdot \boldsymbol{e} \right\} \tag{3.24}$$

$$\dot{\boldsymbol{e}}_{J_3} = \frac{3n R_0^3 C_{30}}{4a^3 h^5} \left\{ \frac{-5}{2h^2} (\hat{\boldsymbol{p}} \cdot \boldsymbol{e}) \left[1 - \frac{7}{h^2} (\hat{\boldsymbol{p}} \cdot \boldsymbol{h})^2 \right] \tilde{\boldsymbol{e}} \cdot \boldsymbol{h} + \right.$$

$$\left. \frac{5}{h^2} (\hat{\boldsymbol{p}} \cdot \boldsymbol{e})(\hat{\boldsymbol{p}} \cdot \boldsymbol{h}) \tilde{\hat{\boldsymbol{p}}} \cdot \boldsymbol{e} - \frac{1}{2} \left[1 - \frac{5}{h^2} (\hat{\boldsymbol{p}} \cdot \boldsymbol{h})^2 \right] \tilde{\hat{\boldsymbol{p}}} \cdot \boldsymbol{h} \right\} \tag{3.25}$$

While the derived LPEs for the J_2 and J_3 are valid for any $\hat{\boldsymbol{p}}$, we assume that $\hat{\boldsymbol{p}} = \pm \hat{\boldsymbol{z}}$ meaning the obliquity is either $0°$ or $180°$. The vector specifying the north pole is then written as

$$\hat{\boldsymbol{p}} = \sigma_p \hat{\boldsymbol{z}} \quad \text{where } \sigma_p = \pm 1. \tag{3.26}$$

If we combine Eqs. (3.13), (3.21), and (3.24) for $\boldsymbol{h}$ and Eqs. (3.14), (3.22), and (3.25) for $\boldsymbol{e}$, the averaged LPEs for the combined effect of SRP, J_2, and J_3 can be obtained. Our focus is to find equilibrium points of the full LPEs. As the resulting LPEs become complicated functions of $\boldsymbol{h}$ and $\boldsymbol{e}$ vectors, it is difficult to find all of the equilibrium points in a comprehensive manner. Instead, we focus on a specific group of frozen orbits that have common orbit geometry. If we look at the right-hand sides of the full LPEs, we notice that they are factored by several vector cross products, namely, $\tilde{\hat{\boldsymbol{z}}} \cdot \hat{\boldsymbol{h}}$, $\tilde{\hat{\boldsymbol{z}}} \cdot \hat{\boldsymbol{e}}$, $\tilde{\hat{\boldsymbol{x}}} \cdot \hat{\boldsymbol{h}}$, $\tilde{\hat{\boldsymbol{x}}} \cdot \hat{\boldsymbol{e}}$, $\tilde{\hat{\boldsymbol{e}}} \cdot \hat{\boldsymbol{h}}$, $\tilde{\hat{\boldsymbol{p}}} \cdot \hat{\boldsymbol{h}}$, and $\tilde{\hat{\boldsymbol{p}}} \cdot \hat{\boldsymbol{e}}$. When $\boldsymbol{h}$ and $\boldsymbol{e}$ lie in the x-z plane along with the assumption in Eq. (3.26), the differential equations on $\boldsymbol{h}$ and $\boldsymbol{e}$ only have non-zero

values along the $\hat{\boldsymbol{y}}$ direction. Thus, the first part of the frozen orbit conditions is to constrain the angular momentum and eccentricity vectors in the x-z plane. This condition is equivalent to setting the right ascension $\Omega = \pm\frac{\pi}{2}$ and the argument of periapsis $\omega = \pm\frac{\pi}{2}$ when the classical elements are used. The Heliotropic orbits and near-polar terminator orbits, which have been identified in other works, satisfy these conditions [45, 47]. A benefit of formulating the frozen orbit conditions in terms of the Milankovitch elements is that the orbit geometry is easier to visualize. Figure 3.1 shows the geometry of the Milankovitch elements in the x-z plane. The vectors $\boldsymbol{h}$ and $\boldsymbol{e}$ are not independent of each other. They must satisfy Eq. (3.8) and also $\hat{\boldsymbol{h}} \cdot \hat{\boldsymbol{e}} = 0$ by definition. After all, we only need two degrees of freedom to specify $\boldsymbol{h}$ and $\boldsymbol{e}$ in the x-z plane. We define a base vector

$$\hat{\boldsymbol{e}}_+ = \hat{\boldsymbol{y}} \times \hat{\boldsymbol{h}}. \tag{3.27}$$

Then the eccentricity vector is defined as $\boldsymbol{e} = e'\hat{\boldsymbol{e}}_+$ where e' is an augmented eccentricity. The augmented eccentricity is allowed to take negative values, and its norm is equivalent to the regular definition of eccentricity. Since the orbit is assumed to be bounded, $|e'| < 1$ must hold true. Another variable θ, which is similar to an inclination i, is introduced to specify $\hat{\boldsymbol{h}}$ vector. While an inclination only takes values between 0 and π, the variable θ takes values in $0 \le \theta < 2\pi$. Therefore, a set of variables (e', θ) can describe broader solution space than (e, i). The resulting differential equations for the $\hat{\boldsymbol{y}}$ components of the LPEs are given as follows.

$$\dot{\boldsymbol{h}}_y = \dot{F}\sqrt{1 - e'^2}\sin\theta - \frac{3}{2}a_{\text{SRP}}\sqrt{\frac{a}{\mu}}e'\sin\theta - \tag{3.28}$$

$$\frac{3nR_0^2 C_{20}}{2a^2(1 - e'^2)^{3/2}}\cos\theta\sin\theta +$$

$$\frac{3nR_0^3 C_{30}}{8a^3(1 - e'^2)^{5/2}}\sigma_p e'\cos\theta(15\cos^2\theta - 11)$$

$$\dot{\boldsymbol{e}}_y = -\dot{F}e'\cos\theta - \frac{3}{2}a_{\text{SRP}}\sqrt{\frac{a}{\mu}}\sqrt{1 - e'^2}\cos\theta + \tag{3.29}$$

$$\frac{3nR_0^2 C_{20}}{4a^2(1 - e'^2)^2}e'(1 - 3\cos^2\theta) +$$

$$\frac{3nR_0^3 C_{30}}{8a^3(1 - e'^2)^3}\sigma_p(1 + 4e'^2)(1 - 5\cos^2\theta)\sin\theta$$

The new frozen orbit conditions are found by solving $\dot{\boldsymbol{h}}_y = 0$ and $\dot{\boldsymbol{e}}_y = 0$ for e' and θ.
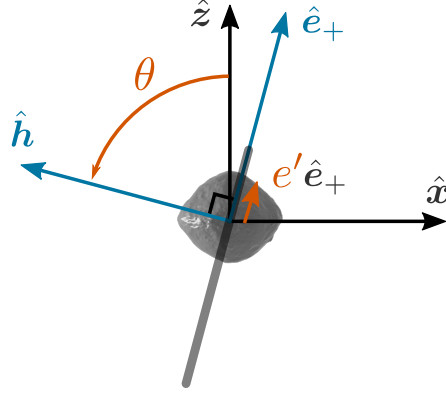
Figure 3.1: Geometry of the Milankovitch orbital elements confined in the x-z plane.

3.2.2 Frozen Condition in 2D Space

For a given value of semi-major axis, we can plot $\dot{\boldsymbol{h}}_y$ and $\dot{\boldsymbol{e}}_y$ over a grid of (e', θ), which enables us to graphically identify the frozen orbit conditions. As an example, Fig. 3.2 shows a contour plot for $\dot{\boldsymbol{h}}_y = 0$ and $\dot{\boldsymbol{e}}_y = 0$ when $a = 0.7$ km. The red dotted lines correspond to the location where the time rate becomes zero. A set of (e', θ) that results in a frozen condition can be found by overlaying the plots for $\dot{\boldsymbol{h}}_y = 0$ and $\dot{\boldsymbol{e}}_y = 0$. Figure 3.3 shows 2D maps that disclose the locations of frozen orbits in the (e', θ) space for $a = 0.8$ km (top), 0.6 km (middle), and 0.4 km (bottom). The plots on the right include both J_2 and J_3 effects, whereas the plots on the left do not. The solid blue lines indicate $\dot{\boldsymbol{h}}_y = 0$ and dotted red lines indicate $\dot{\boldsymbol{e}}_y = 0$. Frozen orbits exist at the intersections of the two lines, which are marked by circles. Lines for $e' = \cos\Lambda$ and $\theta = 90°, 270°$ are also drawn in gray. The intersections of the gray horizontal and vertical lines correspond to the original terminator orbits. We can see that modified terminator orbits exist, indicated as T.O. near the original frozen orbit locations, and the deviations become large when a is small in general. A family of equatorial orbits known as the Heliotropic orbits is also identified and indicated as H.O. Although the Heliotropic orbits have been typically discussed with the SRP and J_2 perturbations, similar orbits exist even when the J_3 effect is considered. The Heliotropic orbit under the J_3 effect is no longer a complete equatorial orbit. There are other frozen orbits identified, and the results are consistent with the analysis on the J_2 and SRP case [45]. However,

the other solutions have high eccentricities, and thus they may not be as useful as terminator orbits or heliotropic orbits for actual flight.
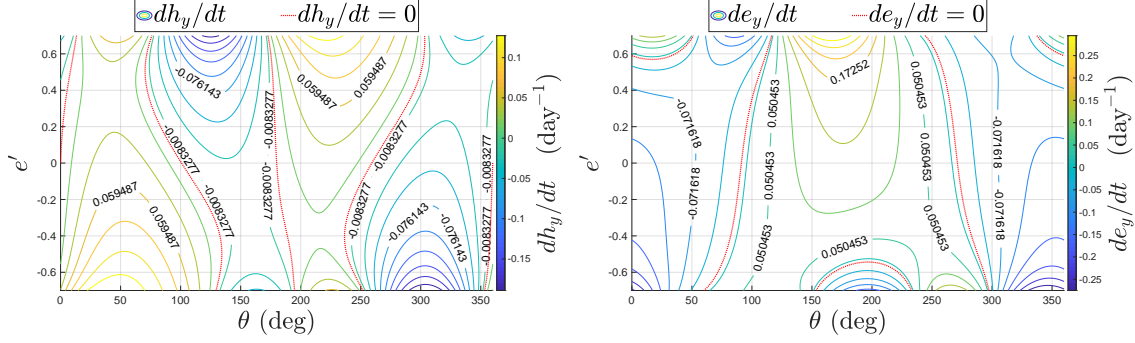
Figure 3.2: Time derivative of the angular momentum and eccentricity vectors' y components for $a = 0.7$ km.

An interesting point to note is that the symmetry of θ is broken once the J_3 term is included. This outcome can be confirmed by comparing the plots on the left and right in Fig. 3.3. With the simulated parameters, the terminator orbit with $\theta = 90°$ requires larger correction than the orbit with $\theta = 270°$. The difference becomes more evident if we look at Fig. 3.4 that shows the necessary corrections $(\delta e', \delta\theta)$ relative to the regular terminator orbit conditions $(\theta^* = 90°$ or $270°$ and $e'^* = \cos\Lambda)$ to account for the higher-order gravity effect. The left and right plots correspond to the J_2 only case and the $J_2 + J_3$ case, respectively. The circle and square markers each represent terminator orbits with $\theta = 90°$ and $\theta = 270°$. Each dot is for a different value of the semi-major axis. When J_3 is included, the corrections for the $\theta \simeq 90°$ family are larger than the J_2 only case. On the other hand, for $\theta \simeq 270°$, the corrections become smaller when J_3 is included. Thus, for one of the terminator orbit families, J_2 and J_3 perturbations jointly cause a larger disturbance than they individually do, and for another, they cancel out. We could argue that the orbit with $\theta^* = 270°$ is better in that it is less sensitive to the perturbations without correction. From the viewpoint of gravity field measurement, we could improve the observability of J_2 and J_3 if flight data from both terminator orbit geometries were combined. We note that this observation is based solely on the analysis without other harmonics terms, and they could also have a non-negligible effect. We can evaluate the J_2 and J_3 effect on the terminator orbit more quantitatively by evaluating $\dot{\boldsymbol{h}}$ and $\dot{\boldsymbol{e}}$ in
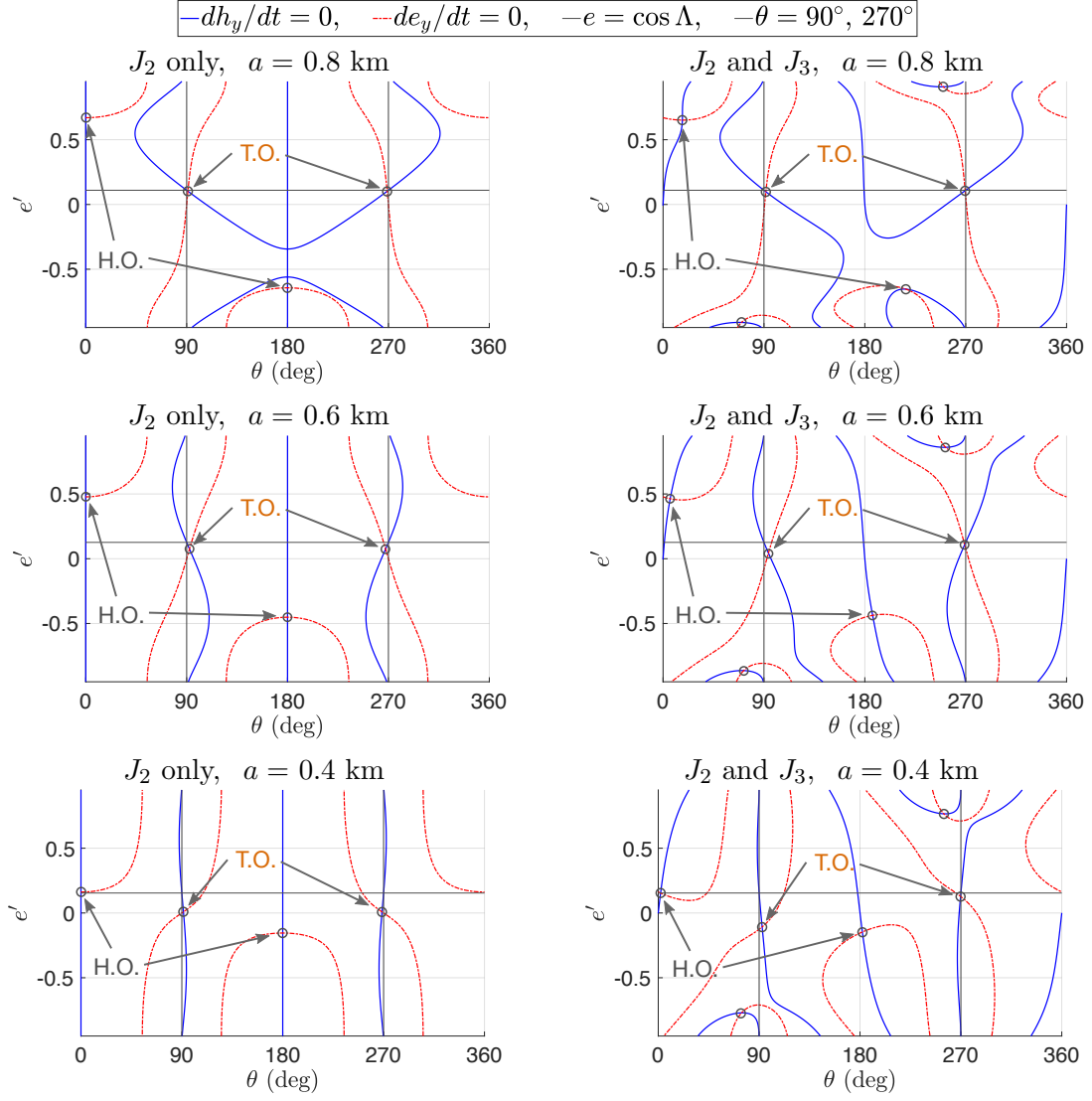
Figure 3.3: Locations of frozen orbits over e' and θ for three different semi-major axes.

the averaged LPEs.

$$\dot{\boldsymbol{h}}_y(e'^*, \theta^*) = 0 \tag{3.30}$$

$$\dot{\boldsymbol{e}}_y(e'^*, \theta^*) = \frac{3nR_0^2 C_{20}\cos\Lambda}{4a^2\sin^4\Lambda} + \frac{3nR_0^3 C_{30}\sigma_p\sigma_{\theta*}}{8a^3\sin^6\Lambda}(1 + 4\cos^2\Lambda) \tag{3.31}$$

where

$$\sigma_{\theta*} = \begin{cases} 1 & \text{if } \theta = 90° \\ -1 & \text{if } \theta = 270°. \end{cases} \tag{3.32}$$

Depending on the sign of C_{20}, C_{30}, and σ_p, there is a choice of $\sigma_{\theta*}$ that results in smaller $|\dot{\boldsymbol{e}}_y(e'^*, \theta^*)|$.
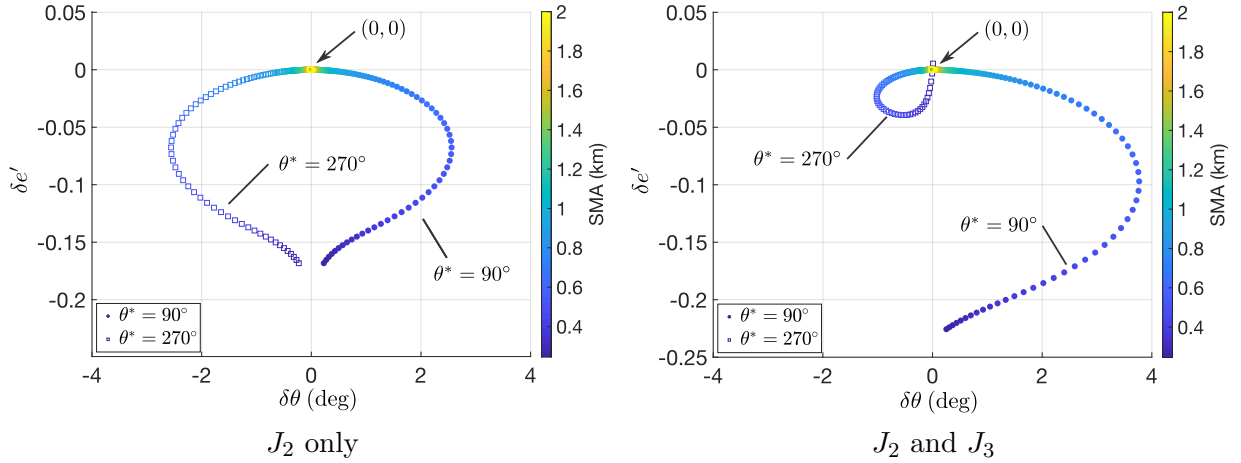
Figure 3.4: Required corrections to the terminator orbit families to account for the higher-order gravity field.

3.2.3 Linearization around Nominal Terminator Orbit

While it is possible to numerically find a frozen condition, it is convenient if we can construct an analytical approximation of the necessary correction for the original terminator orbit. Assuming the correction is small, we can linearize Eqs. (3.28) and (3.29) relative to nominal values. Denoting the nominal values as e'^* and θ^*, the necessary corrections $\delta e'$ and $\delta\theta$ satisfy

$$\dot{\boldsymbol{h}}_y(e'^* + \delta e', \theta^* + \delta\theta) = \dot{\boldsymbol{h}}_y(e'^*, \theta^*) + \frac{\partial\dot{\boldsymbol{h}}_y}{\partial e'}\bigg|_{e'^*,\theta^*}\delta e' + \frac{\partial\dot{\boldsymbol{h}}_y}{\partial\theta}\bigg|_{e'^*,\theta^*}\delta\theta = 0 \tag{3.33}$$

$$\dot{\boldsymbol{e}}_y(e'^* + \delta e', \theta^* + \delta\theta) = \dot{\boldsymbol{e}}_y(e'^*, \theta^*) + \frac{\partial\dot{\boldsymbol{e}}_y}{\partial e'}\bigg|_{e'^*,\theta^*}\delta e' + \frac{\partial\dot{\boldsymbol{e}}_y}{\partial\theta}\bigg|_{e'^*,\theta^*}\delta\theta = 0. \tag{3.34}$$

The zeroth order terms are defined as

$$b_1 \equiv \dot{\boldsymbol{h}}_y(e'^*, \theta^*) \tag{3.35}$$

$$b_2 \equiv \dot{\boldsymbol{e}}_y(e'^*, \theta^*). \tag{3.36}$$

The terms b_1 and b_2 are same as the right hand sides of Eqs. (3.30) and (3.31). The partial derivatives evaluated at the nominal orbits are obtained as follows.

$$a_{11} \equiv \left.\frac{\partial \dot{\boldsymbol{h}}_y}{\partial e'}\right|_{e'^*, \theta^*} = \frac{-\dot{F}\sigma_{\theta*}}{\sin\Lambda\cos\Lambda} \tag{3.37}$$

$$a_{12} \equiv \left.\frac{\partial \dot{\boldsymbol{h}}_y}{\partial \theta}\right|_{e'^*, \theta^*} = \frac{3nR_0^2 C_{20}}{2a^2\sin^3\Lambda} + \frac{33nR_0^3 C_{30}}{8a^3\sin^5\Lambda}\cos\Lambda\sigma_p\sigma_{\theta*} \tag{3.38}$$

$$a_{21} \equiv \left.\frac{\partial \dot{\boldsymbol{e}}_y}{\partial e'}\right|_{e'^*, \theta^*} = \frac{3nR_0^2 C_{20}(4 - 3\sin^2\Lambda)}{4a^2\sin^6\Lambda} + \frac{3nR_0^3 C_{30}(15 - 8\sin^2\Lambda)}{4a^3\sin^8\Lambda}\cos\Lambda\sigma_p\sigma_{\theta*} \tag{3.39}$$

$$a_{22} \equiv \left.\frac{\partial \dot{\boldsymbol{e}}_y}{\partial \theta}\right|_{e'^*, \theta^*} = \frac{\sigma_{\theta*}\dot{F}}{\cos\Lambda} \tag{3.40}$$

Then, an approximate correction is computed by

$$\delta e' = -\frac{a_{12}b_2}{a_{11}a_{22} - a_{12}a_{21}} \tag{3.41}$$

$$\delta\theta = \frac{a_{11}b_2}{a_{11}a_{22} - a_{12}a_{21}}. \tag{3.42}$$

The variables (e', θ) continuously define the entire orbit geometry where $\boldsymbol{h}$ and $\boldsymbol{e}$ are in the x-z plane. This property is helpful in linearization. For example, in Fig. 3.3, the plots on the right show that as the semi-major axis becomes smaller, the frozen terminator orbit with $\theta \simeq 90°$ has smaller e'. Eventually, e' becomes negative, which means the orbit flips the direction of periapsis. This transition is observed as a discontinuous change in the argument of periapsis from $\omega = \pi/2$ to $\omega = -\pi/2$ if the classical elements are used. With the current formulation, we can specify the frozen orbit simply with the deviation from the original terminator orbit, namely $(\delta e', \delta\theta)$, regardless of the periapsis flipping.

A numerical simulation is performed to validate the analytical correction. Figure 3.5 shows 3D plots of two trajectories. The propagation is performed using Eq. (2.11) with J2 and J3

perturbations in Eqs. (3.3) and (3.4). The trajectory on the left is generated by propagating the initial state obtained from the conventional terminator orbit conditions in Eqs. (3.16)-(3.18). The trajectory on the right is the result of applying the analytical correction. We note that no corrections are made to transform the mean orbital elements to the osculating orbital elements in both cases. The mean semi-major axis is 0.6 km, and the time of flight is 60 days. We can see that when the original condition is used, the orbit is no longer frozen and becomes gradually more eccentric. On the other hand, applying the correction keeps the orbit geometry more frozen. When the orbit size is smaller, errors due to the linearization become larger. However, errors originating from unmodeled gravity fields also become large in such a case, and trajectory design is challenging in the first place. Thus, finding an exact frozen orbit condition may not be essential. We note that the full dynamics only include the J_2 and J_3 perturbations; therefore, the simulation results do not show effects from other terms of spherical harmonics.

Without Correction   With Correction
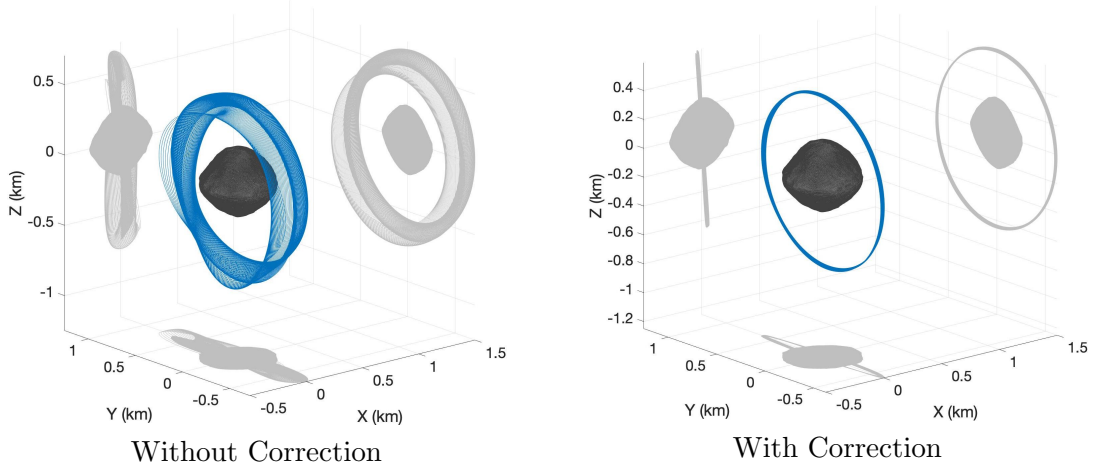
Figure 3.5: 3D plots of propagated example trajectories with and without the combined J_2 and J_3 correction.

3.3   Offset Effect

When the size of a terminator orbit is large, the point mass assumption is legitimate. However, the SRP effect becomes relatively stronger, which results in a larger geometric offset. The geometric offset, in turn, causes large short-period oscillation. Thus a correction for the offset is needed. We

first analyze the offset effect with LPEs and find an optimal value of the offset around which a set of orbital elements is defined. Then, corrections to further account for the higher-order offset effect are discussed, and two different approaches are presented to eliminate the bias caused by the short-period oscillation.

3.3.1   Orbital Elements Defined with Respect to an Offset
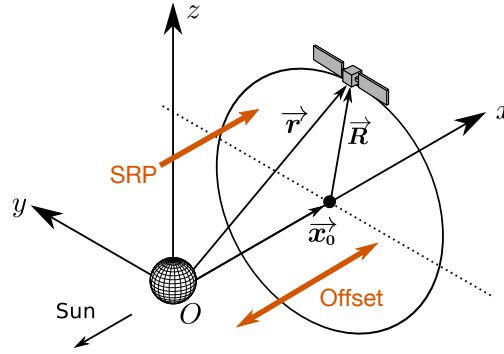
Figure 3.6: Asteroid centered coordinate frame and geometry of a position vector decomposed into an arbitrary offset and relative position vector.

We start from simple dynamics with point mass gravity and no rotation. The point mass gravity is employed throughout the section. The equations of motion are given by

$$\ddot{\boldsymbol{r}} = -\frac{\mu}{r^2}\hat{\boldsymbol{r}} + a_{\mathrm{SRP}}\hat{\boldsymbol{x}} \tag{3.43}$$

where $\hat{\boldsymbol{x}}$ is assumed to be inertially fixed. We then decompose the position vector into an arbitrary offset $x_0\hat{\boldsymbol{x}}$ and relative position vector $\boldsymbol{R}$. The definition of the frame considered here and the geometry of the position vector are shown in Fig. 3.6. With the decomposition, the original equations of motion can be expressed in terms of the relative position vector. The result is based on a series expansion of $\boldsymbol{r}$ about $\boldsymbol{R}$ assuming x_0 is small compared to R. The expansion is truncated

at the second order.

$$\boldsymbol{r} = x_0\hat{\boldsymbol{x}} + \boldsymbol{R} \tag{3.44}$$

$$\ddot{\boldsymbol{R}} = -\frac{\mu}{R^2}\hat{\boldsymbol{R}} + \underbrace{\frac{\mu}{R^3}\left(3\frac{\boldsymbol{R}\boldsymbol{R}}{R^2}\cdot\boldsymbol{x}_0 - \boldsymbol{x}_0\right) + a_{\mathrm{SRP}}\hat{\boldsymbol{x}} +}_{\equiv\boldsymbol{P}_1}$$

$$\underbrace{\frac{3\mu}{R^5}\left((\boldsymbol{x}_0\cdot\boldsymbol{R})\boldsymbol{x}_0 + \frac{1}{2}x_0^2\boldsymbol{R} - \frac{5}{2}\frac{(\boldsymbol{x}_0\cdot\boldsymbol{R})^2}{R^2}\boldsymbol{R}\right)}_{\equiv\boldsymbol{P}_2} + O((x_0/R)^3) \tag{3.45}$$

The term $\boldsymbol{P}_1$ includes the SRP perturbation and the first-order contribution of the offset. The term $\boldsymbol{P}_2$ represents the second-order effect of the offset.

Treating $\boldsymbol{P}_i$ as a perturbing force on the two-body problem with $\boldsymbol{R}$, we can define a perturbing potential U_i as follows.

$$U_1 = -\mu\frac{\boldsymbol{x}_0\cdot\boldsymbol{R}}{R^3} + a_{\mathrm{SRP}}(\boldsymbol{R}\cdot\hat{\boldsymbol{x}}) \tag{3.46}$$

$$U_2 = \frac{\mu}{2}\left(3\frac{(\boldsymbol{x}_0\cdot\boldsymbol{R})^2}{R^5} - \frac{x_0^2}{R^3}\right) \tag{3.47}$$

$$\text{where} \quad \boldsymbol{P}_i = \frac{\partial U_i}{\partial\boldsymbol{R}}$$

The averaged potentials can be computed as well following Eq. (3.10). We note that orbital elements are defined with the relative position vector $\boldsymbol{R}$, not with $\boldsymbol{r}$ while averaging.

$$\overline{U_1} = -\frac{3}{2}a\boldsymbol{a}_{\mathrm{SRP}}\cdot\boldsymbol{e} \tag{3.48}$$

$$\overline{U_2} = \frac{\mu x_0^2}{4a^3(1-e^2)^{3/2}}\left[1 - 3(\hat{\boldsymbol{x}}\cdot\hat{\boldsymbol{H}})^2\right] \tag{3.49}$$

The average of U_1 is exactly the same as U_{SRP} defined in Eq. (3.12). This result tells us that the orbital elements defined around an arbitrary offset follow the same secular evolution as the regular case where $x_0 = 0$ as long as the offset is small compared to the orbit size. This is true even when the rotation effect is incorporated. Therefore, the conditions for a frozen terminator orbit, namely Eqs. (3.16) - (3.18), are still valid. The second-order contribution is ignored in the subsequent derivation of the optimal offset. However, we will revisit the $\boldsymbol{P}_2$ contribution because the term turns out to have a non-negligible impact if the orbit is nominally in the terminator plane.

3.3.2   Optimal Offset
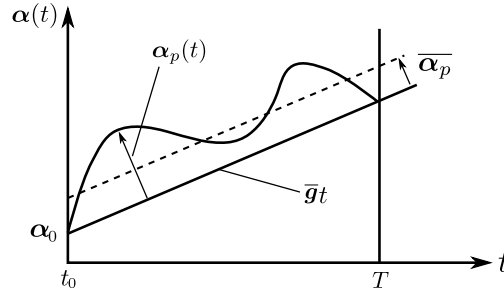
Figure 3.7: Schematic of osculating orbital elements' evolution over one orbit.

Even though the secular dynamics are invariant to the introduction of a small offset, short-period oscillation depends on the offset. A differential equation for the short-period term is derived as follows. If we generally denote a set of osculating orbital elements as $\boldsymbol{\alpha}(t)$, it can be broken down as

$$\boldsymbol{\alpha}(t) = \boldsymbol{\alpha}_0 + \overline{\boldsymbol{g}}t + \boldsymbol{\alpha}_p(t) \tag{3.50}$$

where $\boldsymbol{\alpha}_0$ is the initial value and $\overline{\boldsymbol{g}}$ is the secular rate. The term $\boldsymbol{\alpha}_p$ is the short-period term. Thus, the time rate of the full solution is

$$\boldsymbol{g}(\boldsymbol{\alpha}, t) = \overline{\boldsymbol{g}}(\boldsymbol{\alpha}) + \dot{\boldsymbol{\alpha}}_p(t). \tag{3.51}$$

Assuming an initial set of orbital elements defines the evolution of $\boldsymbol{\alpha}_p$ over one orbit, we have

$$\dot{\boldsymbol{\alpha}}_p(t) = \boldsymbol{g}(\boldsymbol{\alpha}_0, t) - \overline{\boldsymbol{g}}(\boldsymbol{\alpha}_0) \tag{3.52}$$

where the explicit time dependence in the differential equation comes from the change in the mean anomaly. The short-period term is zero at the initial time by definition. Since the short-period term does not contribute to the secular evolution, it is periodic over one orbit. However, it is possible that the mean of $\boldsymbol{\alpha}_p$ is nonzero. Figure 3.7 shows the relationship between a short-period term and secular evolution. Typically we have a set of desired mean orbital elements that we want to realize, as is the case with a frozen orbit. Simply propagating the desired orbital elements as an

initial condition will not result in the target mean orbital elements. Usually, there is a bias caused by the short-period term, namely $\overline{\boldsymbol{\alpha}_p} \neq \boldsymbol{0}$, and we have to subtract it from the desired mean orbital elements.

The short-period analysis aims to formulate $\overline{\boldsymbol{\alpha}}_p$ as a function of the offset x_0 and to find an optimal offset that minimizes the bias. The evolution of orbital elements can be described by LPEs or Gauss Planetary Equations (GPEs). The formulation with the LPEs has the benefit that we only need to evaluate the quadrature of a perturbing potential. However, we need to take partial derivatives of the integrated potential function with respect to a set of orbital elements. This process is non-trivial; thus, the LPEs are not considered here. In this work, GPEs are used instead for the short-period analysis. Specifically, we focus on the short-period term of an angular momentum vector $\boldsymbol{H}_p$ as it can be constructed relatively easily. The general form of GPEs is $\dot{\boldsymbol{\alpha}} = (\partial \boldsymbol{\alpha}/\partial \boldsymbol{v}) \cdot \boldsymbol{P}$ where $\boldsymbol{v}$ is a velocity vector and $\boldsymbol{P}$ is a perturbing acceleration. The differential equations for $\boldsymbol{H}_p$ are obtained following Eq. (3.52) as

$$
\begin{aligned}
\dot{\boldsymbol{H}}_p(t) &= \left. \left(\frac{\partial \boldsymbol{H}}{\partial \boldsymbol{v}} \cdot \boldsymbol{P}_1 \right) \right|_{\boldsymbol{\alpha}_0} - \left. \overline{\left(\frac{\partial \boldsymbol{H}}{\partial \boldsymbol{v}} \cdot \boldsymbol{P}_1 \right)} \right|_{\boldsymbol{\alpha}_0} \\
&= \left. \widetilde{\hat{\boldsymbol{x}}} \cdot \left[\mu x_0 \frac{\boldsymbol{R}}{R^3} - a_{\mathrm{SRP}} \left(\boldsymbol{R} + \frac{3a}{2} \boldsymbol{e} \right) \right] \right|_{\boldsymbol{\alpha}_0}.
\end{aligned}
\tag{3.53}
$$

The effect of the frame rotation does not appear because $\dot{F}\widetilde{\hat{\boldsymbol{z}}} \cdot \boldsymbol{H}_p(t_0) = \boldsymbol{0}$, as the initial value of the short-period term is zero. Therefore, there is no distinction between the rotating and non-rotating cases when a short-period term is considered. We can integrate Eq. (3.53) to find

$$
\boldsymbol{H}_p = \widetilde{\hat{\boldsymbol{x}}} \cdot \left[\mu x_0 \boldsymbol{Q}_1 - a_{\mathrm{SRP}} \boldsymbol{Q}_2 \right]
\tag{3.54}
$$

$$
\overline{\boldsymbol{H}}_p = \widetilde{\hat{\boldsymbol{x}}} \cdot \left[\mu x_0 \overline{\boldsymbol{Q}}_1 - a_{\mathrm{SRP}} \overline{\boldsymbol{Q}}_2 \right]
\tag{3.55}
$$

where $\boldsymbol{Q}_1$ and $\boldsymbol{Q}_2$ are time integrals of position dependent functions. The average of the short-period term is simply obtained by averaging $\boldsymbol{Q}_1$ and $\boldsymbol{Q}_2$. The terms $\boldsymbol{Q}_i$ and their averages are listed in Appendix A. The vectors $\boldsymbol{Q}_i$ and their averages are decomposed into two orthogonal unit vectors $\hat{\boldsymbol{e}}$ and $\hat{\boldsymbol{e}}_\perp$. The unit vector $\hat{\boldsymbol{e}}$ lies in the direction of an eccentricity vector and $\hat{\boldsymbol{e}}_\perp$ is in the direction of $\boldsymbol{H} \times \hat{\boldsymbol{e}}$. The mean value $\overline{\boldsymbol{H}_p}$ is parameterized by the offset x_0 and initial eccentric

anomaly E_0, which we can choose as free parameters. To have $\overline{\boldsymbol{H}_p} = \boldsymbol{0}$, both $\hat{\boldsymbol{e}}$ and $\hat{\boldsymbol{e}}_\perp$ components must be zero simultaneously . It turns out that with the following choice of x_0 and E_0, we can make the coefficients of $\hat{\boldsymbol{e}}$ and $\hat{\boldsymbol{e}}_\perp$ zero at the same time in the expression of $\overline{\boldsymbol{H}_p}$.

$$x_0^* = \begin{cases} \frac{a^3 a_{\text{SRP}}}{\mu} \left(1 - e\right) \left(1 + \frac{e}{4}\right) & \text{if} \quad E_0 = 0 \\ \frac{a^3 a_{\text{SRP}}}{\mu} \left(1 + e\right) \left(1 - \frac{e}{4}\right) & \text{if} \quad E_0 = \pi \end{cases} \tag{3.56}$$

If a frozen orbit is defined with the above offset values, we expect to find an orbit whose secular evolution is smaller than the regular case. As the bias in the angular momentum vector can be minimized with the optimal offset, the variation of the orbit plane can be suppressed. As detailed in the next sections, we numerically confirm that the obtained x_0^* is the optimal choice for a terminator orbit when the first-order offset contribution is considered.

3.3.3   Higher Order Correction for Offset

The discussion on the choice of the offset does not assume any particular orbit; the argument is indeed valid for any type of orbit. When a terminator orbit is considered in an SRP-dominant environment, it is possible to devise further orbit-specific corrections to remove the bias caused by the offset. In the derivation of the optimal offset, we only focused on $\overline{\boldsymbol{H}}_p$. Since an eccentricity vector is confined to a plane perpendicular to an angular momentum vector, the out-of-plane variation of the eccentricity vector should also become small if the optimal offset is used. However, the in-plane variation of the eccentricity vector is not necessarily minimized. Thus, a natural next step is to inspect the eccentricity vector defined with the optimal offset.

For a better understanding of a frozen terminator orbit in the rotating frame, it is instructive to review a terminator orbit in the non-rotating case. This is because the non-rotating case has an analytical solution, and a numerically computed periodic terminator orbit in the rotating case inherits its properties. The terminator orbit in the non-rotating case is a circular orbit with an

offset in the positive $x-$direction. The following relationships define the orbits.

$$x = \frac{r^3 a_{\text{SRP}}}{\mu} \tag{3.57}$$

$$R = \sqrt{r^2 - x^2} \tag{3.58}$$

$$v = R \sqrt{\frac{\mu}{r^3}} \tag{3.59}$$

The gravity and SRP forces along the x direction balance each other with these conditions. We recognize that the offset for this equilibrium solution is consistent with the optimal offset obtained from the short-period analysis. Once any of x, r, or R is specified, a circular orbit is defined. In this case, a position vector $\boldsymbol{R}$, which is measured from the offset, is perpendicular to $\hat{\boldsymbol{x}}$.

It turns out that applying a certain scaling results in a better conversion between a Cartesian state vector and an eccentricity vector. Let $\boldsymbol{R}' = R'\hat{\boldsymbol{R}}$ be a scaled relative position vector. Though its direction is the same as the $\boldsymbol{R}$ vector, its magnitude is different. The magnitude R' is determined such that the eccentricity becomes zero. If the eccentricity vector is defined with $\boldsymbol{R}'$, it becomes

$$\begin{aligned} \boldsymbol{e}' &= \frac{\boldsymbol{v} \times (\boldsymbol{R}' \times \boldsymbol{v})}{\mu} - \hat{\boldsymbol{R}} \\ &= \left(\frac{R'v^2}{\mu} - 1 \right) \hat{\boldsymbol{R}} \end{aligned} \tag{3.60}$$

and to have $\boldsymbol{e}' = \boldsymbol{0}$, the magnitude of $\boldsymbol{R}'$ must satisfy

$$R' = \frac{r^3}{R^2}. \tag{3.61}$$

The result suggests that if we redefine a position vector relative to an offset, the magnitude of the position vector must be modified to represent a frozen orbit. The necessity of the scaling comes from the fact that the angular velocity of the circular orbit is governed by r, whereas the radius of the orbit is R. If we use the scaled radius R' in the energy equation of the Keplerian motion, the corresponding semi-major axis satisfies

$$a' = R'. \tag{3.62}$$

Thus, scaling the position vector is equivalent to scaling the semi-major axis.

To understand the impact of shifting a position vector and scaling it in the rotating case, sets of classical orbital elements are computed for a periodic terminator orbit in the Hill three-body problem with SRP. Four different definitions of a position vector are used. Vectors $\boldsymbol{R}$ and $\boldsymbol{R}'$ point from the mean offset $\bar{x}\hat{\boldsymbol{x}}$ to the actual location of the spacecraft. Vectors $\boldsymbol{r}$ and $\boldsymbol{r}'$ point from the asteroid center to the spacecraft's position. Vectors with prime are scaled so that their lengths are r^3/R^2 at each time step. The motivation for the scaling comes from Eq. (3.61). Figure 3.8 shows the errors in numerically computed $\bar{x}$ and $\bar{r}^3 a_{\mathrm{SRP}}/\mu$. It is confirmed that the mean offset is almost identical to $\bar{r}^3 a_{\mathrm{SRP}}/\mu$. As an example, time histories of orbital elements for a periodic orbit with $a \simeq 2\mathrm{km}$ are shown in Fig. 3.9. The mean offset is about 125 m in this case. True anomaly f is zero at the initial time. In these plots, each line corresponds to a different definition of a position vector, while it represents the same periodic orbit. The plots of the inclination and right ascension show that the variation is smaller if the relative vectors $\boldsymbol{R}$ and $\boldsymbol{R}'$ are used as position vectors. Note that the right ascension is defined relative to the rotating frame. As for the eccentricity and argument of periapsis, using the scaled position vectors $\boldsymbol{R}'$ and $\boldsymbol{r}'$ results in smaller short-period variations. One interesting finding is that even when the scaled position vector is used, the mean of the eccentricity seems to match the frozen orbit conditions in Eq. (3.18), which is derived from the analysis of the secular dynamics. These observations suggest that the shifted and scaled position vector $\boldsymbol{R}'$ seems to be the most appropriate choice to represent a frozen terminator orbit, as the orbital elements stay nearly constant throughout the orbit.

The observation of Fig. 3.9 gives us a clue on two approaches to better define an initial condition for a frozen terminator orbit. The plot shows that the mean of the eccentricity is off from the initial value if the un-scaled position vectors are used. This is not the case for the argument of periapsis. Though the variation of the argument of periapsis is large if the un-scaled vectors are used, its mean and initial values are the same if $E_0 = 0$ or π. Thus, if we stick to the formulation with $\boldsymbol{R}$, there must be a correction to the initial eccentricity so that the mean value matches the frozen condition. Another approach is to take advantage of the scaling. We can use a scaled effective semi-major axis to define an initial condition.
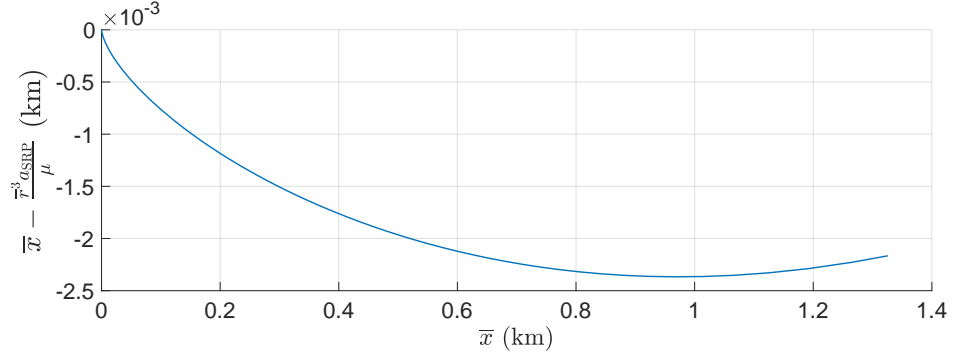
Figure 3.8: Difference between numerically averaged offset and predicted offset, computed from various periodic orbits.
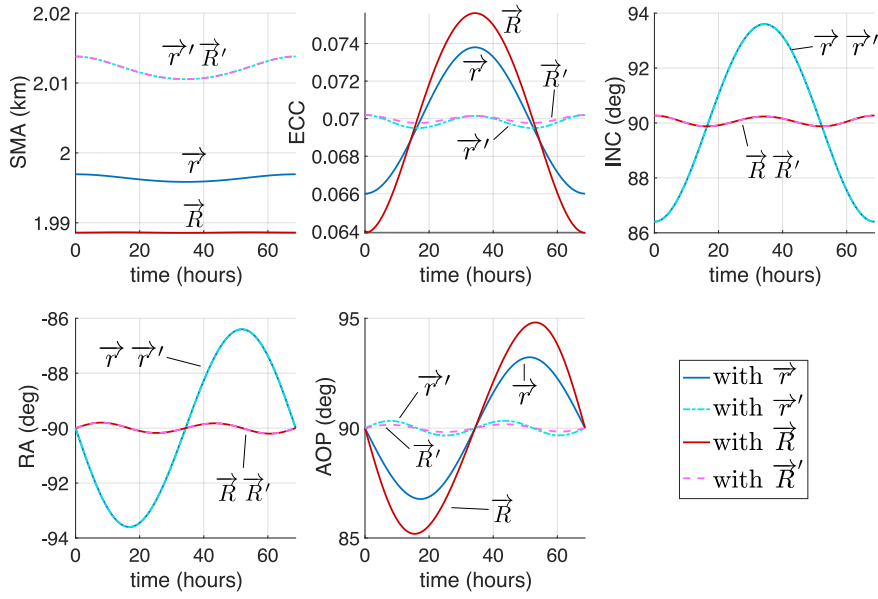
Figure 3.9: Time history of classical orbital elements with four different definitions of a position vector.

First, the method based on the short-period analysis of eccentricity is presented. The LPEs for an eccentricity are given by

$$\dot{e} = \frac{1}{na^2e} \left[(1-e^2)\frac{\partial U}{\partial \sigma} - \sqrt{1-e^2}\frac{\partial U}{\partial \omega} \right] \tag{3.63}$$

where $\sigma = -n\tau_0$ and n is the mean motion. τ_0 is the time of periapsis passage. In our notation, $U = U_1 + U_2$, and they are defined in Eqs. (3.46) and (3.47). We make an assumption that the terms with $\hat{\boldsymbol{R}} \cdot \hat{\boldsymbol{x}}$ is zero in the perturbing potential when the orbit is nominally in the terminator plane. Then, there is no contribution from U_1 and what remains is the second term in U_2. This means the large variation of the eccentricity is driven by the second-order offset effect. In other words, the optimal offset removes the bias associated with the first-order offset contribution. To obtain a differential equation for the short-period term, we simply need to replace U with $U - \overline{U}$ in the LPEs. After some simplification, the differential equation is obtained as

$$\dot{e}_p = \frac{(1-e^2)}{na^2e} \frac{\partial}{\partial \sigma} \left(-\frac{\mu}{2}\frac{x_0^2}{R^3} \right). \tag{3.64}$$

With the assumption that the orbit geometry stays constant while the mean anomaly changes from M_0 to $M_0 + 2\pi$, we can evaluate the quadrature twice using the orbit equation of the Kepler motion in place of R. Using an algebraic manipulator, the mean deviation is found as

$$\overline{e_p} = \begin{cases} -\frac{x_0^2}{2a^2} \frac{\left[1-\sqrt{1-e^2}-e\left(2-e+\sqrt{1-e^2}\,\right)\right]}{e(1-e)^2\sqrt{1-e^2}} & \text{if } E_0 = 0 \\ -\frac{x_0^2}{2a^2} \frac{\left[1-\sqrt{1-e^2}-e\left(2-e+\sqrt{1-e^2}\right)\right]}{e(-1+e)(1+e)^2} & \text{if } E_0 = \pi \end{cases} \tag{3.65}$$

where $0 < e < 1$ is assumed. To define an initial eccentricity for a frozen orbit, we need to subtract $\overline{e_p}$ from the target mean value of $\overline{e} = \cos\Lambda$. Once the correction is made, we can find $\boldsymbol{R}$ and $\boldsymbol{v}$ from the orbital element set. The complete initial condition is defined by introducing an offset x_0^* found in Eq. (3.56). The procedure to define an initial condition is summarized in Algorithm 1. The semi-major axis is considered to be a design parameter.

Next, an approach based on the idea of an effective semi-major axis is described. The scaling is introduced to better define an eccentricity such that the discrepancy between an orbit size and corresponding two-body energy is resolved. As seen in the LPE for the eccentricity in Eq. (3.65),

further correcting the eccentricity means accounting for the higher-order offset effect. Thus, the introduction of the scaling also serves as a correction to account for the higher-order offset effect. The scaled radius is given in Eq. (3.61), and it can be expanded as follows using Eq. (3.57) and (3.58).

$$R' = R\left(1 + \frac{x^2}{R^2}\right)^{3/2} \tag{3.66}$$

If we make an assumption that $x \simeq R^3 a_{\text{SRP}}/\mu$ in the above expression, then

$$R' = R\left(1 + \frac{R^4 a_{\text{SRP}}^2}{\mu^2}\right)^{3/2} \tag{3.67}$$

As long as e is small, $R \simeq a$ and we can define an effective semi-major axis in the same way as

$$a' = a\left(1 + \frac{a^4 a_{\text{SRP}}^2}{\mu^2}\right)^{3/2}. \tag{3.68}$$

The term multiplied by a on the right-hand side is the scaling factor that converts a geometric semi-major axis to an effective semi-major axis. We use the effective semi-major axis in this method to compute an effective position vector and velocity vector for a frozen terminator orbit. Then, we apply the re-scaling of the position vector and use it as the actual state vector. The position vector $\boldsymbol{r}$ is again obtained by using the optimal offset. This process is summarized in Algorithm 2.

Algorithm 1 Initial condition with $\overline{e_p}$

Require: a (geometric SMA)

get $\Lambda = \arctan\left(\frac{3P_0(1+\rho)(1\text{AU})^2}{2B}\sqrt{\frac{a}{\mu\mu_{\text{Sun}}A(1-E^2)}}\right)$

get $e = \cos\Lambda$

get $x_0 = x_0^*$ from Eq. (3.56)

get $\overline{e_p}$ from Eq. (3.65)

set $e = e - \overline{e_p}$

get $\boldsymbol{h} = \pm\sqrt{(1-e^2)}\hat{\boldsymbol{x}}, \quad \boldsymbol{e} = \mp e\hat{\boldsymbol{z}}, \quad f = 0 \text{ or } \pi$

get $\boldsymbol{R}$, $\boldsymbol{v}$ from orbital elements

get $\boldsymbol{r} = \boldsymbol{R} + x_0\hat{\boldsymbol{x}}$

3.3.4   Verification through Numerical Simulations

The validity of the short-period analysis is examined through numerical simulations. Also, the two methods' effectiveness in refining an initial condition for a frozen terminator orbit is inves-

---

Algorithm 2 Initial condition with effective SMA

Require: a (geometric SMA)

get $a' = a\left(1 + \frac{a^4 a_{\mathrm{SRP}}^2}{\mu^2}\right)^{\frac{3}{2}}$ (effective SMA)

get $\Lambda' = \arctan\left(\frac{3P_0(1+\rho)(1\mathrm{AU})^2}{2B}\sqrt{\frac{a'}{\mu\mu_{\mathrm{Sun}}A(1-E^2)}}\right)$

get $e = \cos\Lambda'$

get $\boldsymbol{h} = \pm\sqrt{(1-e^2)}\hat{\boldsymbol{x}}$, $\boldsymbol{e} = \mp e\hat{\boldsymbol{z}}$, $f = 0$ or π

get $\boldsymbol{R}'$, $\boldsymbol{v}'$ from orbital elements

get $\boldsymbol{R} = \boldsymbol{R}'\left(1 + \frac{a^4 a_{\mathrm{SRP}}^2}{\mu^2}\right)^{-\frac{3}{2}}$

get $x_0 = x_0^*$ from Eq. (3.56) with geometric SMA

get $\boldsymbol{r} = \boldsymbol{R} + x_0\hat{\boldsymbol{x}}$, $\quad \boldsymbol{v} = \boldsymbol{v}'$

---

tigated. First, to justify that analytically derived x_0^* in Eq. (3.56) is actually optimal, the initial condition for a frozen orbit, namely, $\boldsymbol{e} = \cos\Lambda\hat{\boldsymbol{z}}$, $\boldsymbol{h} = -\sqrt{1 - \cos^2\Lambda}\hat{\boldsymbol{x}}$, and $f = 0$ is propagated. No correction to the eccentricity is considered at this point. We tested five different values of x_0, including x_0^*. Figure 3.10 shows the time history of the classical orbital elements defined around each offset. Note that each set of orbital elements is computed with a different definition of a position vector $\boldsymbol{R}(t)$, each corresponding to a different value of x_0. Though the initial orbital elements are the same for each case of x_0, the actual state vectors in the asteroid-centered Cartesian frame are different since each point around which we define the set of orbital elements is different. The semi-major axis is a design parameter for a frozen orbit, and Fig. 3.10 corresponds to $a = 1$ km. The time of flight is about 10 orbit periods. In this case, $a^3 a_{\mathrm{SRP}}/\mu \simeq 15.6\,\mathrm{m}$ and $x_0^* \simeq 14.4\,\mathrm{m}$. First, it is evident that in all cases, there is a secular evolution in eccentricity. We can also confirm that using x_0^* results in the smallest drift, although the difference between the cases with $x_0 = a^3 a_{\mathrm{SRP}}/\mu$ and $x_0 = x_0^*$ is small. This trend is clear in the plot of the argument of periapsis. The conclusion stays the same when other values of the semi-major axis are tested or the correction to the initial eccentricity is applied. If the size of the orbit becomes large, the mismatch between the initial and mean eccentricity has a more significant influence than the slight difference in the offset choice.

In order to assess the performance of various ways to define an initial condition for a frozen orbit, four different cases are simulated. Case 1 is the most naive approach, where no offset or eccentricity correction is considered. In case 2, the initial orbital elements are defined around the
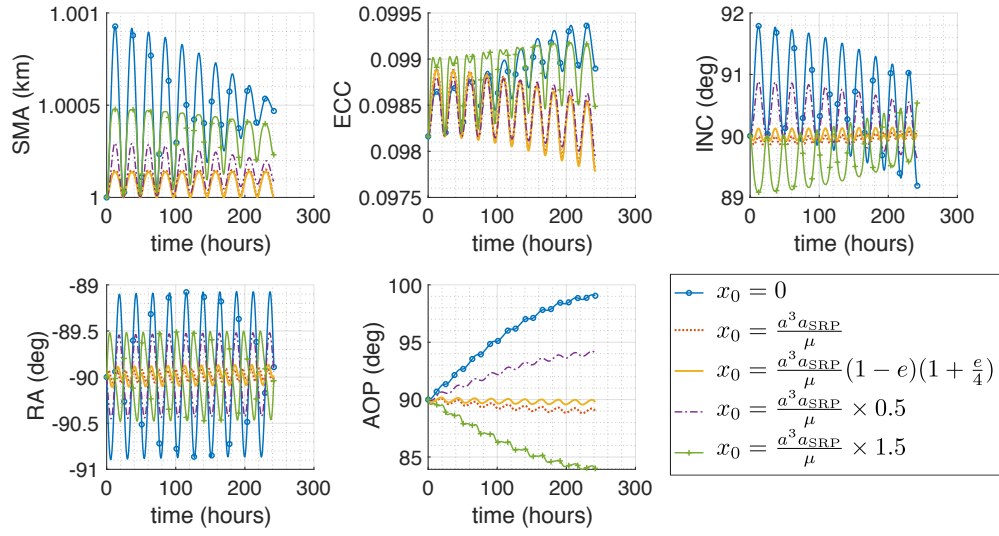
Figure 3.10: Time history of orbital elements defined with various offsets with $a = 1$km.

optimal offset x_0^*, but no correction to the eccentricity is made. Case 3 further incorporates the eccentricity correction using the result of the short-period analysis. Finally, the initial condition of case 4 is generated by the process summarized in Algorithm 2, where the optimal offset and concept of the effective semi-major axis are employed. Figure 3.11 shows 3D plots of the four trajectories. The top row is the XZ view, and the bottom row is the YZ view. Each column represents one of the four cases. The initial semi-major axis is 3km. In case 4, using $a = 3$ km to compute a' results in a slightly smaller final semi-major axis as the re-scaling is only applied to a position vector. Thus, a slightly larger value of $a = 3.12$km is used to have the resulting semi-major axis of 3 km when the orbital elements are defined with $\boldsymbol{R}$. The trajectories are propagated for about 10 orbits. It is evident that without the offset, the orbit wobbles a lot and the mean orbital elements have non-zero secular evolution. Since a terminator orbit in SRP dominant cases is stable, it does not diverge. However, if a larger semi-major axis is used to define an initial condition, the wobbling may cause an escape from the target body. The result from case 2 shows a more regular orbit, although we can still observe some variation in its orbit. When the initial eccentricity is modified by subtracting $\overline{e_p}$ from the desired mean along with the shift in the origin, the orbit becomes tighter. Nonetheless, a slight secular variation can be seen. The trajectory generated with the effective semi-major axis looks steadiest and is almost periodic. Figure 3.12 shows the time history of the orbital elements for cases 2 to 4. Plotted elements are the classical orbital elements computed with $\boldsymbol{R}$. We can confirm that case 3 results in a smaller variation than case 2. Whereas cases 2 and 3 have periodic secular trends, case 4 repeats almost identical orbital elements after one period.

3.3.5   Offset with the J_2 and J_3 Correction

As pointed out earlier, the offset and higher-order gravity effects inversely depend on the size of an orbit. Figure 3.13 shows the magnitude of the necessary corrections for different semi-major axes. The plots on the left and right are for eccentricity vector and angular momentum vector corrections, respectively. The yellow dash-dot lines indicate the correction to account for the offset. The solid blue and dashed red lines each indicate the J_2 and J_3 corrections for terminator orbits

	Case 1	Case 2	Case 3	Case 4
	$x_0 = 0$	$x_0 = x_0^*$	$x_0 = x_0^*$	$x_0 = x_0^*$
	No ECC correction	No ECC correction	ECC is corrected by $\overline{e_p}$	Effective SMA is used
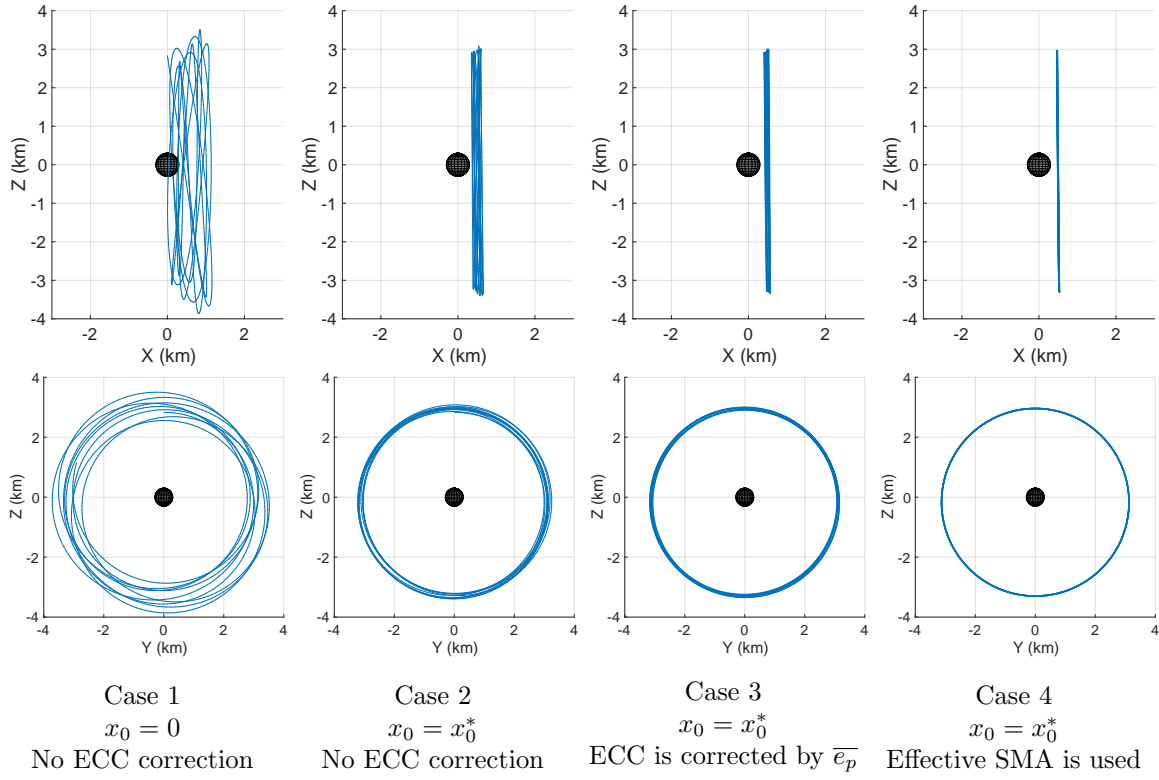
Figure 3.11: 3D plots of the propagated trajectories with XZ view at the top and YZ view at the bottom.
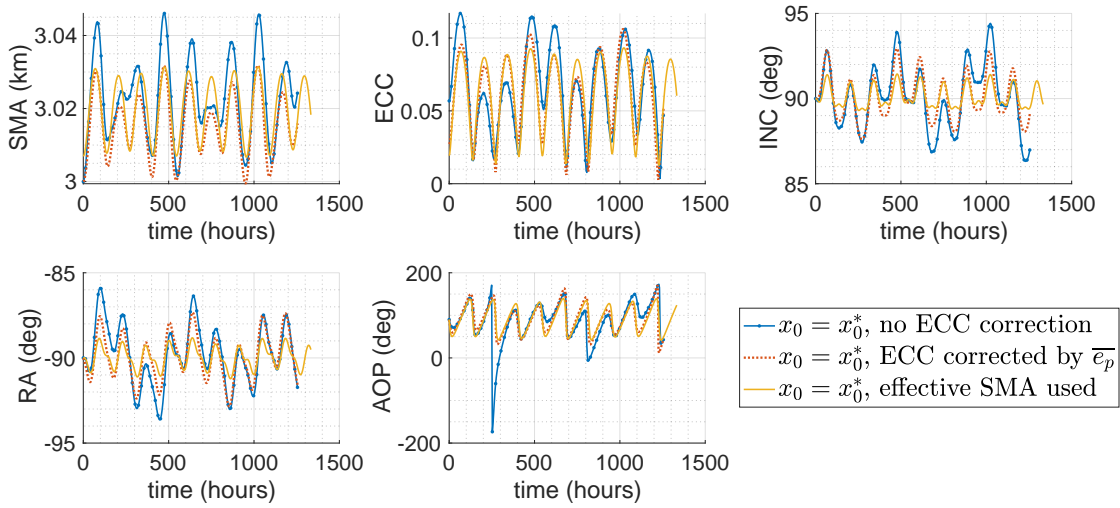
Figure 3.12: Time history of orbital elements for cases 2 to 4.

with their angular momentum vectors pointing toward the Sun ($\sigma_{\theta*} = 1$) and away from the Sun ($\sigma_{\theta*} = -1$). The negative correlation between the offset corrections and J_2, J_3 corrections is evident. Also, we can confirm terminator orbits with the Sun pointing angular momentum vector require larger corrections than their counterparts when J_2 and J_3 are considered. The offset correction and J_2 and J_3 correction have a similar magnitude around $a = 1$ km. We need to incorporate both corrections to better define an orbit with a semi-major axis around this value.

With SRP being the only perturbation, the secular dynamics are invariant to the introduction of an offset at first order, as explained earlier. Generally, this is not the case once J_2 and J_3 perturbations are included. However, it turns out that as long as a terminator orbit is concerned with $0°$ or $180°$ obliquity, the secular dynamics still do not depend on x_0 to first order. Indeed, the invariance can be confirmed by expanding the perturbing potentials for the J_2 and J_3 in terms of a relative position vector $\boldsymbol{R}$. The position-dependent term in U_{J_2} is expanded as follows:

$$\frac{1}{r^3}\left[1 - 3(\hat{\boldsymbol{r}} \cdot \hat{\boldsymbol{p}})^2\right] =$$
$$\frac{1}{R^3}\left[1 - 3(\hat{\boldsymbol{R}} \cdot \hat{\boldsymbol{p}})^2\right] + 3\frac{x_0}{R^4}\left\{\left[5(\hat{\boldsymbol{R}} \cdot \hat{\boldsymbol{p}})^2 - 1\right](\hat{\boldsymbol{R}} \cdot \hat{\boldsymbol{x}}) - 2(\hat{\boldsymbol{R}} \cdot \hat{\boldsymbol{p}})(\hat{\boldsymbol{x}} \cdot \hat{\boldsymbol{p}})\right\} + O((x_0/R)^2) \qquad (3.69)$$

Since we assume $\hat{\boldsymbol{R}} \cdot \hat{\boldsymbol{x}} = 0$ and $\hat{\boldsymbol{x}} \cdot \hat{\boldsymbol{p}} = 0$, we can argue that $[1 - 3(\hat{\boldsymbol{r}} \cdot \hat{\boldsymbol{p}})^2]/r^3 \simeq [1 - 3(\hat{\boldsymbol{R}} \cdot \hat{\boldsymbol{p}})^2]/R^3$. In the same way, the position dependent term in U_{J_3} can be expanded as

$$\frac{(\hat{\boldsymbol{r}} \cdot \hat{\boldsymbol{p}})}{r^4}\left[5(\hat{\boldsymbol{r}} \cdot \hat{\boldsymbol{p}})^2 - 3\right] =$$
$$\frac{(\hat{\boldsymbol{R}} \cdot \hat{\boldsymbol{p}})}{R^4}\left[5(\hat{\boldsymbol{R}} \cdot \hat{\boldsymbol{p}})^2 - 3\right] +$$
$$\frac{x_0}{R^5}\left\{5(\hat{\boldsymbol{R}} \cdot \hat{\boldsymbol{x}})(\hat{\boldsymbol{R}} \cdot \hat{\boldsymbol{p}})\left[3 - 7(\hat{\boldsymbol{R}} \cdot \hat{\boldsymbol{p}})^2\right] - 3(\hat{\boldsymbol{x}} \cdot \hat{\boldsymbol{p}})\left[1 - 5(\hat{\boldsymbol{R}} \cdot \hat{\boldsymbol{p}})^2\right]\right\} + O((x_0/R)^2). \qquad (3.70)$$

With the assumption of $\hat{\boldsymbol{R}} \cdot \hat{\boldsymbol{x}} = 0$ and $\hat{\boldsymbol{x}} \cdot \hat{\boldsymbol{p}} = 0$, we can conclude $(\hat{\boldsymbol{r}} \cdot \hat{\boldsymbol{p}})[5(\hat{\boldsymbol{r}} \cdot \hat{\boldsymbol{p}})^2 - 3]/r^4 \simeq (\hat{\boldsymbol{R}} \cdot \hat{\boldsymbol{p}})[5(\hat{\boldsymbol{R}} \cdot \hat{\boldsymbol{p}})^2 - 3]/R^4$.

Since the secular dynamics are not affected by the offset, the previous discussion of the new frozen orbit conditions is valid for orbital elements defined in terms of $\boldsymbol{R}$. These calculations justify an approach where we define orbital elements with the J_2 and J_3 corrections defined in Eqs. (3.41) and (3.42) around the optimal offset defined in Eq. (3.56). Figure 3.14 shows 3D plots and the

time history of orbital elements for two different terminator orbits. The angular momentum vector points towards the Sun, and the initial semi-major axis is set to 1 km. The initial orbital elements for both orbits are modified to account for the J_2 and J_3 perturbations. While the trajectory at the top does not incorporate the offset correction, the initial orbital elements for the bottom trajectory are defined around the optimal offset. We can confirm that including both corrections results in a more regular orbit. A detailed linear stability analysis shows that a terminator orbit becomes unstable at some threshold value of the semi-major axis due to the J_2 perturbation [47]. From the time histories of the orbital elements, we can confirm oscillatory growth as predicted by the linear stability analysis. The exponential growth is observed in both orbits; however, with the offset correction, the final oscillation amplitude is much smaller than the case without the offset. The numerical simulation verifies that introducing the offset still results in a set of mean orbital elements that is closer to the equilibrium point of the averaged LPEs even when the J_2 and J_3 perturbations are non-negligible. Since the orbit geometry stays constant for a longer time, introducing the offset is advantageous. With this approach, the short-period oscillation caused by SRP is addressed at the same time as the change in frozen orbit conditions caused by J_2 and J_3, resulting in more frozen orbits for a wide range of semi-major axes. We note that the offset becomes less significant when the orbit size is smaller. To further correct the initial condition with small semi-major axes, a formal short-period analysis may be necessary.
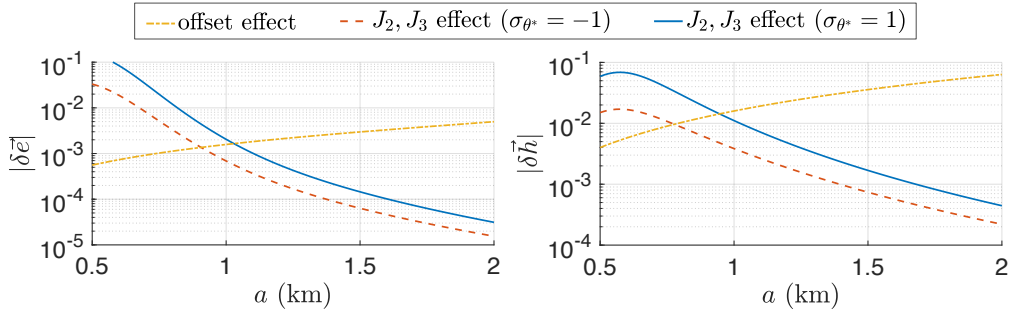
Figure 3.13: Magnitude of necessary corrections ($\delta \boldsymbol{e}, \delta \boldsymbol{h}$) to account for the offset and J_2 and J_3 perturbations as functions of semi-major axis.

Only with J_2 and J_3 correction.

With offset and J_2 and J_3 correction.
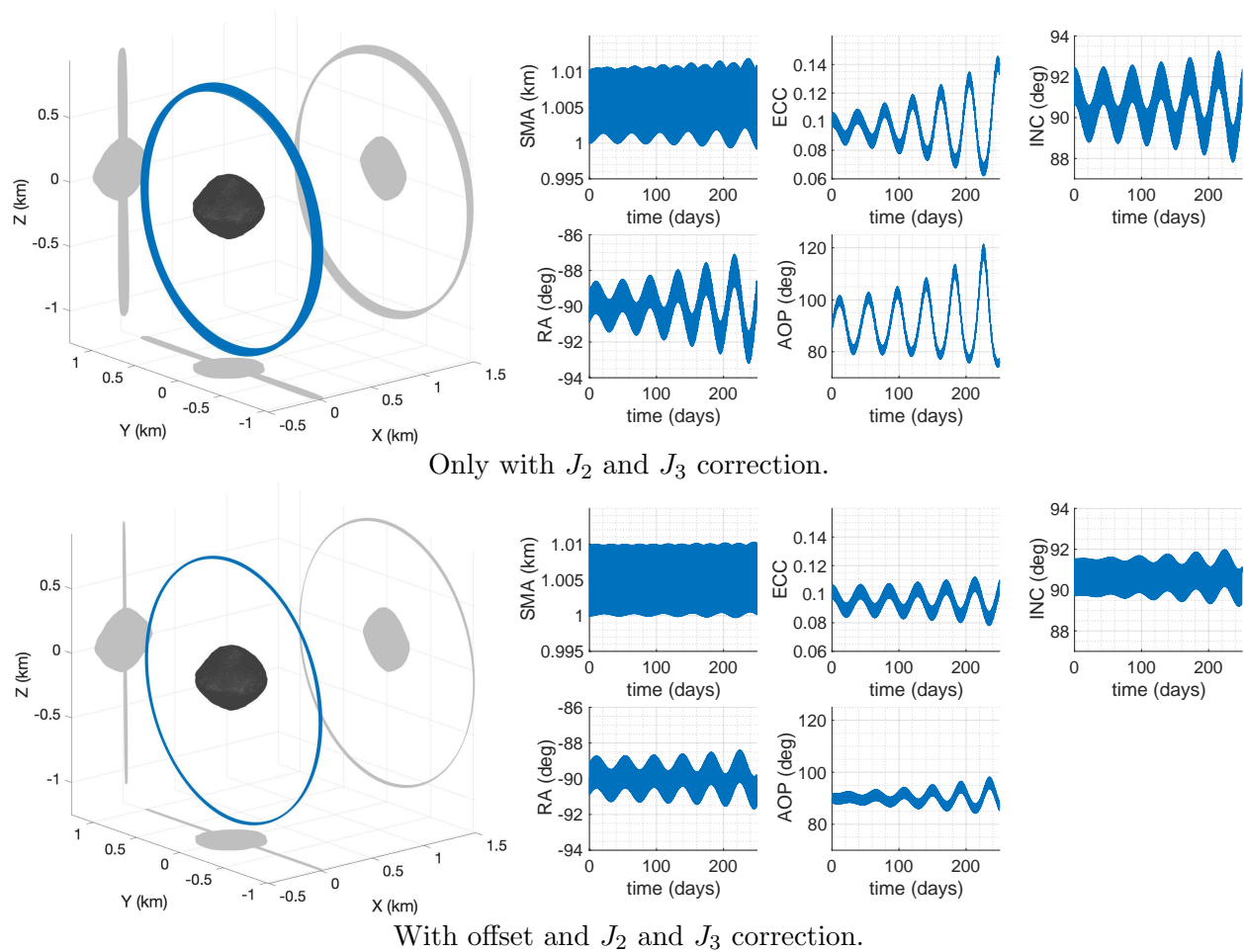
Figure 3.14: Comparison of two terminator orbits defined with and without offset correction.

3.3.6   Terminator Orbits with Eccentric Asteroid Orbits

Terminator orbits are good candidates for long-term observations due to their stability. The effects of the asteroid orbit's eccentricity may not be ignored for long-term dynamics. The magnitude of SRP varies as the asteroid moves around the Sun. In the derivation of the frozen orbit conditions in [24], it has been shown that frozen orbit conditions hold true with the nonzero asteroid's eccentricity. The frozen conditions do not depend on where the asteroid is along the heliotropic orbit because the time rates of change in the orbit plane due to SRP and frame rotation are both inversely proportional to the Sun-asteroid distance squared. However, the frozen conditions are derived in an averaged sense, and the effects of instantaneous dynamical evolutions are not studied. Thus, it is of interest to study the behavior of the long-term stable terminator orbits when the asteroid's orbit is eccentric more in detail and study the validity of the proposed offset corrections.

In order to study the effectiveness of the offset corrections to define a long-term stable terminator orbit when the asteroid's orbit is eccentric, numerical analyses are performed using an exaggerated eccentricity of $E = 0.6$. This analysis focuses on the SRP dominant case and ignores the effect of higher-order gravity terms. When the higher-order gravitational perturbations are nonnegligible, the orbits are unstable [48]. Thus, unless the SRP is dominant, terminator orbits may require station-keeping control. Such cases are outside the scope of the current analysis. Figure 3.15 shows terminator orbits propagated for one asteroid year. The initial conditions are defined either at perihelion ($F_0 = 0°$) or aphelion ($F_0 = 180°$), where F_0 is the initial asteroid orbit's true anomaly. The plots on the left were obtained by defining the initial conditions with offset corrections based on effective semi-major axes (Algorithm 2). No offset corrections were applied for the trajectories on the right. We confirm that the spacecraft can stay in the terminator orbits even with the varying SRP acceleration when the offset corrections are applied to define the initial conditions. The spacecraft can stay in the orbits when the offset corrections are not applied if $F_0 = 180°$. However, the spacecraft escapes without even making a single orbit around the target body when the initial conditions are defined without the offset corrections at perihelion. The offset

corrections, in essence, remove the bias between the osculating and mean orbital elements caused by the offset. At aphelion, the offset is small due to weaker SRP; thus, the offset corrections are smaller. On the other hand, the larger offset at perihelion means that the corrections are all the more important.

Although it's not clear, the plots of the propagated terminator orbits show that the orbit center moves along the $x-$axis. This behavior is highlighted more clearly in the time history of the terminator orbit's offset computed shown in Fig. 3.16. The plot corresponds to the terminator orbits computed with offset corrections for both $F_0 = 0°$ and $F_0 = 180°$. Offset values

$$x = a^3 a_{\text{SRP}}/\mu \tag{3.71}$$

are shown as well for different choices of position vectors used to compute the semi-major axis: regular position vector as measured from the mass center $\boldsymbol{r}$, shifted position vector $\boldsymbol{R}$, and shifted and scaled position vector $\boldsymbol{R}'$. One observation is that the terminator orbit naturally changes its orbit center as the SRP strength changes along with the asteroid's heliocentric motion. Also, the offset values computed by Eq. (3.71) represent the mean offset very well. At perihelion, the offset is so large that the difference between different definitions of the position vectors becomes evident. The offset in the non-rotating terminator orbit is defined in terms of r in Eq. (3.57). Thus, the semi-major axis computed with the original position vector $\boldsymbol{r}$ better predicts the offset. The scaling also enlarges the semi-major axis, and the resulting offset value closely matches the offset computed by r.

Figure 3.17 shows the time history of orbital elements computed with different position definitions, and larger plots of semi-major axes are shown in Fig. 3.18. The labels regular, shifted, and shifted + scaled correspond to $\boldsymbol{r}$, $\boldsymbol{R}$, and $\boldsymbol{R}'$ respectively. The label geometric indicates the case where the semi-major axis is rescaled to find the geometric semi-major axis after the orbital elements are computed with $\boldsymbol{R}'$. The plot for $F_0 = 0°$ is shown at the top, and the plot for $F_0 = 180°$ is shown at the bottom. Although some secular variations exist, the orbital elements stay constant on average except for the semi-major axis. As analyzed earlier, using a position vector defined
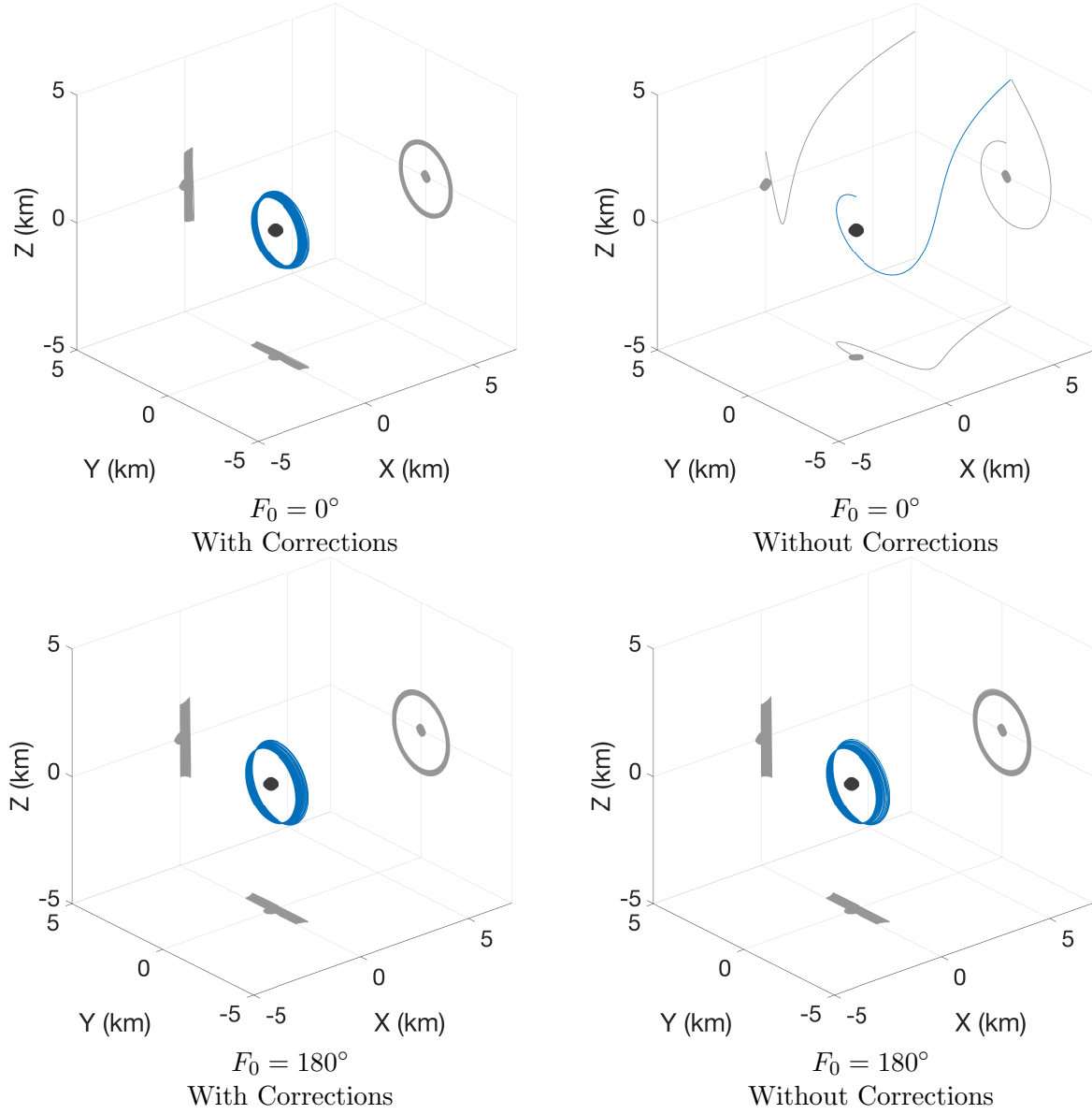
Figure 3.15: 3D plots of propagated terminator orbits with highly eccentric asteroid's orbit. Results with different initial asteroid's true anomalies are shown with and without the offset corrections. O.E. means orbital elements.

$$F_0 = 0°$$

$$F_0 = 180°$$
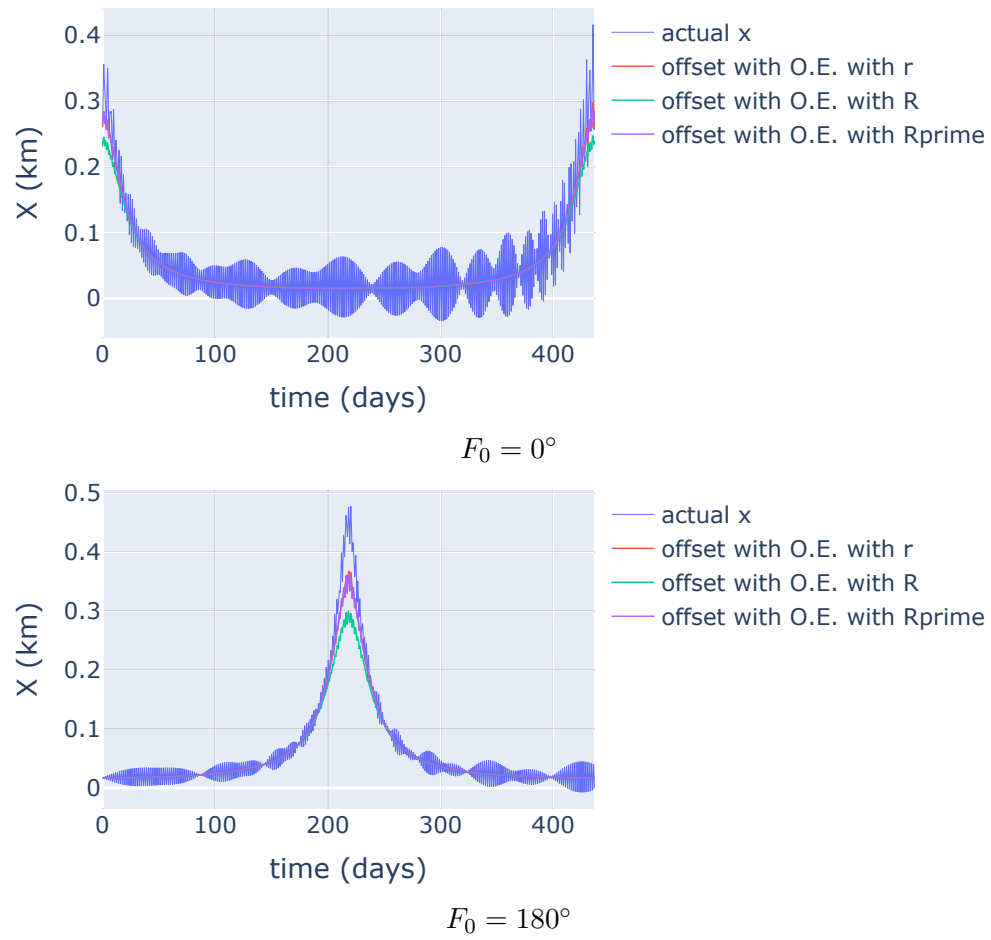
Figure 3.16: Time history of terminator orbits' offsets with highly eccentric asteroid's orbit computed with different position definitions. Results with different initial asteroid's true anomalies are shown. O.E. means orbital elements.

$F_0 = 0°$

$F_0 = 180°$
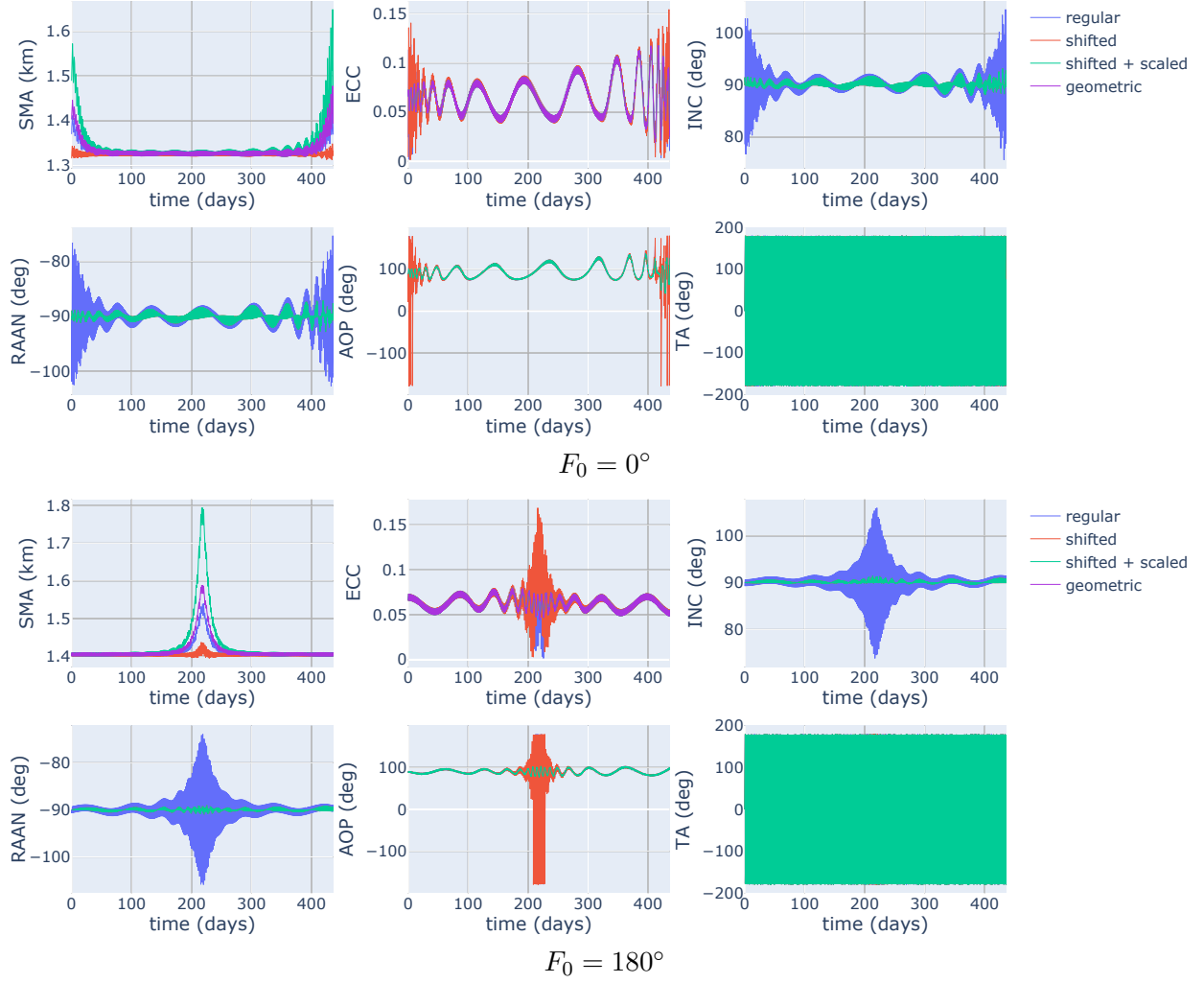
Figure 3.17: Time history of orbital elements for terminator orbits with highly eccentric asteroid's orbit. Results with different initial asteroid's true anomalies are shown with and without the offset corrections.
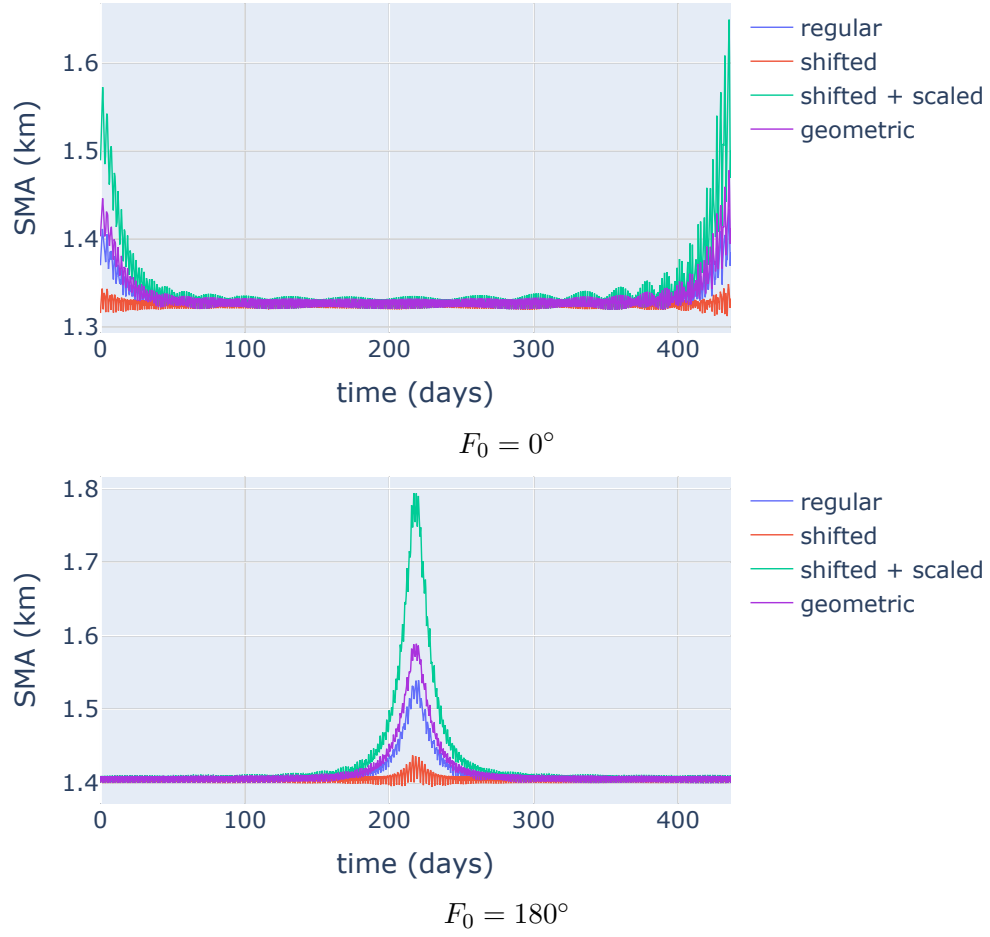
Figure 3.18: Time history of terminator orbits' semi-major axes with highly eccentric asteroid's orbit computed with different position definitions. Results with different initial asteroid's true anomalies are shown.

relative to the shifted orbit center to compute the orbital elements results in smaller orbit plane variations. The semi-major axis changes between perihelion and aphelion. The difference between the effective semi-major axis obtained with $\boldsymbol{R'}$ and the regular semi-major axis is significant at perihelion, whereas they are the same at aphelion. This observation also confirms that if one is defining initial conditions of terminator orbits at perihelion, the offset corrections are more important. Another thing to note is that the size of the orbit increases when SRP is stronger, as illustrated by the history of the geometric semi-major axis. The semi-major axis is assumed to be constant during the derivation of the frozen orbit conditions. The secular variation in the semi-major axis indicates that the change of SRP acceleration is fast enough, and the averaged dynamics cannot fully capture the effect. The plot also shows that the semi-major axis computed with $\boldsymbol{R}$ stays more or less constant.

The behavior of the semi-major axes can be explained by the energy equation and the properties of the terminator orbits. As explained earlier, the first-order effect of the offset can be given by the perturbing potential in Eq. (3.46). Thus, the evolution of $\boldsymbol{R}$ is determined by

$$\ddot{\boldsymbol{R}} = \partial U / \partial \boldsymbol{R} \tag{3.72}$$

$$U = \frac{\mu}{R} - \mu x_0 \frac{\boldsymbol{R} \cdot \hat{\boldsymbol{x}}}{R^3} + a_{\mathrm{SRP}}(\boldsymbol{R} \cdot \hat{\boldsymbol{x}}) \tag{3.73}$$

When the orbit is in the terminator plane, $\hat{\boldsymbol{R}} \cdot \hat{\boldsymbol{x}} \simeq 0$. Thus, the integral of motion $J = v^2/2 - U$ is approximated to be

$$J \simeq \frac{1}{2} v^2 - \frac{\mu}{R} \tag{3.74}$$

Therefore, we expect the semi-major axis defined in terms of $\boldsymbol{R}$ to stay constant. Further, if we assume the velocity is defined with Eq. (3.59), then,

$$v = R \sqrt{\frac{\mu}{(R^2 + x_0^2)^{3/2}}} \tag{3.75}$$

$$= \sqrt{\frac{\mu}{R}} \left(1 + \frac{x_0^2}{R^2} \right)^{-3/4} \tag{3.76}$$

Thus,

$$J \simeq \frac{\mu}{2R} \left(1 + \frac{x_0^2}{R^2} \right)^{-3/2} - \frac{\mu}{R} \tag{3.77}$$

$$\simeq -\frac{\mu}{2R} \left(1 + \frac{3x_0^2}{2R^2} \right) \tag{3.78}$$

assuming $x_0/R << 1$. In order for J to be constant when x_0 shifts, we need

$$\frac{\partial J}{\partial x_0} \delta x_0 + \frac{\partial J}{\partial R} \delta R = 0 \tag{3.79}$$

where

$$\frac{\partial J}{\partial x_0} = -\frac{3\mu x_0}{2R^3} < 0 \tag{3.80}$$

$$\frac{\partial J}{\partial R} = \frac{\mu}{2} \left(\frac{1}{R^2} + \frac{9x_0^2}{2R^4} \right) > 0 \tag{3.81}$$

We have

$$\delta R = - \left(\frac{\partial J}{\partial R} \right)^{-1} \left(\frac{\partial J}{\partial x_0} \right) \delta x_0 \tag{3.82}$$

$$\simeq \frac{6x_0/R}{2 + 9x_0^2/R^2} \delta x_0 \tag{3.83}$$

Thus, if $\delta x_0 > 0$, then $\delta R > 0$, which explains the increase in the orbit size when the terminator orbits are near perihelion. Between the perihelion and aphelion, the SRP acceleration change is

$$\Delta a_S = \pm a_{S,0} \left(\frac{1\text{AU}}{A} \right)^2 \frac{4E}{(1 - E^2)^2} \tag{3.84}$$

The rough estimate of ΔR computed from the above SRP change and Eq. (3.83) evaluated at perihelion is about -0.13 km. The shift in the geometric semi-major axis in Fig. 3.18 more or less matches this value.

3.3.7   Conclusions

This study proposes corrections to the conventional initial condition to define a terminator orbit. Two kinds of corrections are addressed. The first class of corrections accounts for shifts in frozen orbit conditions when the J_2 and J_3 perturbations are non-negligible. The second type

of correction is associated with a geometric offset and is necessary to eliminate the bias between initial and mean orbital elements.

The averaged LPEs defined in terms of the Milankovitch elements are used to analyze the joint effect of SRP, J_2, and J_3 on the secular evolution of orbital elements. With the assumption that the obliquity is $0°$ or $180°$, frozen orbits, including modified terminator orbits, can be identified over a two-dimensional grid of augmented eccentricity and inclination, namely (e', θ). As the two variables define a whole orbit geometry continuously, we can linearize the averaged LPEs around the original terminator orbit condition. This gives us a first-order approximation of the shift in the frozen orbit condition. This correction's efficacy is confirmed through numerical simulations. It is also demonstrated that one of the two terminator orbits is naturally less sensitive to J_2 and J_3 as they cancel each other.

The latter half of the study establishes an approach to define a set of orbital elements around an offset along the Sun-asteroid line rather than the mass center. An optimal offset is derived by analytically evaluating the short-period oscillation of an angular momentum vector under the SRP perturbation and the first-order offset effect. The bias between the initial osculating and mean orbital elements can be removed with the offset. Furthermore, approaches to address the short-period oscillation caused by the higher-order contribution of the offset are presented, assuming a terminator orbit as a nominal orbit. Numerical analyses support the analytical derivation. Then, the validity of defining a set of orbital elements for the new terminator orbit with J_2 and J_3 around the optimal offset is explained. With both the offset correction and J_2 and J_3 correction, orbits that stay close to the target frozen orbits for a longer period of time can be defined for a wide range of orbit sizes. Finally, the behavior of the terminator orbits in the SRP dominant case with the eccentric asteroid's heliocentric orbits is studied. It is found that the terminator orbits in such a case maintain the properties of the simpler terminator orbits in the non-rotating case. Thus, the offset corrections to define initial conditions are still valid and are more important at perihelion.

Chapter 4

Reinforcement Learning Policy for Global Mapping

One of the challenges in asteroid exploration missions is the poor a priori information of the target bodies. In conventional missions, detailed operational plans are determined after asteroid arrival by the operators on the ground. Thus, it may be impractical to design a nominal trajectory for the proximity phase ahead of time and make the spacecraft follow it. A fully autonomous spacecraft may need to make such operational plans on the fly, exploiting the latest knowledge of the environment obtained by the onboard navigation systems. Besides, the spacecraft's trajectory control is noisy in general, and the ability of the spacecraft to cope with the deviation from the predicted state is essential.

An approach to realize such responsive autonomous spacecraft trajectory control is a sampling-based approach proposed in [51]. They combined a receding horizon control scheme with a heuristic computation of the reachability regarding mission objectives of a target body's imaging in order to design impulsive maneuvers. While such an online planning approach could be more efficient than designing a general policy for all admissible states, the online generation of actions could be more computationally demanding, especially with a large state space. Also, the approach taken in [51] does not explicitly optimize a stochastic objective function, though the objective function has a heuristic constraint to account for state deviations.

As an alternative approach, we propose the application of reinforcement learning (RL) and function approximation by neural networks to design an offline guidance policy that is adaptive to environmental changes. In RL, the agent learns the policy through numerous interactions with

the environment, and this study performs the training in simulation environments. With RL, the stochastic objective function is directly optimized, allowing the policy to take the effect of maneuver noise into consideration. Global mapping tasks from hovering trajectories are formulated as a Markov decision process (MDP), a common framework of sequential decision-making problems, and the proximal policy optimization (PPO) [52] is used to obtain an adaptive policy.

While RL algorithms are sample inefficient during the training, they can potentially provide a good solution to MDPs that involve complex state transitions that are not necessarily tractable in a conventional approach. Besides, the training output is a policy network that maps an MDP state to an action, which could be evaluated efficiently on board. There is a growing interest in its application to astrodynamics problems. For example, in [53, 54], autonomous guidance design for body-fixed hovering at an asteroid is proposed, and in [55, 56], RL is applied for orbit transfers in a three-body environment.

The thesis first provides an overview of the relevant basic concepts in RL and the PPO algorithm used in this study. Then concrete MDP formulation for the hovering trajectory controller design is described. Then, the training results of the RL agent are provided along with hyperparameter studies and robustness analyses. Finally, concluding remarks for the chapter are made.

4.1   Basic Concepts for Reinforcement Learning

The goal of RL is to find the optimal policy for a sequential decision-making problem formulated as an MDP. In an MDP, an agent makes an observation of a current state $\boldsymbol{s}_t$ and takes an action $\boldsymbol{a}_t$ based on a policy π. Oftentimes, the policy is stochastic; the action is sampled from a distribution $\boldsymbol{a}_t \sim \pi(\boldsymbol{a}_t|\boldsymbol{s}_t)$. Given $\boldsymbol{s}_t$ and $\boldsymbol{a}_t$, the agent transitions to a next state $\boldsymbol{s}_{t+1}$ with some transition probability $p(\boldsymbol{s}_{t+1}|\boldsymbol{s}_t, \boldsymbol{a}_t)$ and receives a reward $r(\boldsymbol{s}_t, \boldsymbol{a}_t)$. The optimal policy π^* is a policy that maximizes the expectation of the return, or the discounted sum of future rewards,

given an initial state distribution $\boldsymbol{s}_0 \sim p(\boldsymbol{s}_0)$.

$$\pi^* = \arg \max_{\pi} E_{\pi} \left[\sum_{t=0}^{\infty} \gamma^t r_t \right] \tag{4.1}$$

where $0 < \gamma < 1$ is a discount factor. The discount factor determines how myopic the agent is. The expectation is taken over the distribution of state and action under the policy.

The objective function in Eq. (4.1) is referred to as a value function, which quantifies the expected return at a state $\boldsymbol{s}_t$ following a policy π.

$$V^{\pi}(\boldsymbol{s}_t) = E_{\pi} \left[\sum_{t'=t}^{\infty} \gamma^{t'-t} r_{t'} | \boldsymbol{s}_t \right] \tag{4.2}$$

The following state-action value is often used as a performance measure as well.

$$Q^{\pi}(\boldsymbol{s}_t, \boldsymbol{a}_t) = E_{\pi} \left[\sum_{t'=t}^{\infty} \gamma^{t'-t} r_{t'} | \boldsymbol{s}_t, \boldsymbol{a}_t \right] \tag{4.3}$$

which is the expected return of taking an arbitrary action $\boldsymbol{a}_t$ at $\boldsymbol{s}_t$ and following the policy π thereafter. The state value function is obtained by $V^{\pi}(\boldsymbol{s}_t) = E_{\boldsymbol{a}_t \sim \pi}[Q^{\pi}(\boldsymbol{s}_t, \boldsymbol{a}_t)]$.

In RL, an agent learns the optimal policy through numerous interactions with the environment. Typically function approximators such as neural networks are used to parameterize the policy or value function. The parameters are learned from the collected samples of $(\boldsymbol{s}_t, \boldsymbol{a}_t, r_t)$ in a simulation environment during the training.

The PPO algorithm used in this study is an actor-critic algorithm based on the policy gradient method [52]. Relevant key concepts are highlighted in the following subsections.

4.1.1   Policy Gradient

One popular approach in RL is the policy gradient method, where a parameterized policy is directly updated by taking the gradient steps so that the expected return is maximized. The gradient for the policy updates has the following general form

$$g = E_{\pi_\theta} \left[\Psi_t \nabla_\theta \log \pi_\theta(\boldsymbol{a}_t | \boldsymbol{s}_t) \right] \tag{4.4}$$

where θ is the policy parameters [57]. Ψ_t is a quantity that measures how good or bad the actual playout was. In the most naive case, Ψ_t is the return computed from the samples, which corresponds to the objective in Eq. (4.1). Setting Ψ_t as the return intuitively measns increasing the probability of a trajectory $(\boldsymbol{s}_0, \boldsymbol{a}_0, \boldsymbol{s}_1, \boldsymbol{a}_1, \cdots)$ that resulted in a larger return. In practice, the gradient estimate $\bar{g}$ is obtained by constructing the following objective function for a finite batch of samples and differentiating it with automatic differentiation software.

$$J^{\mathrm{PG}}(\theta) = \hat{E}_{\pi_\theta} \left[\Psi_t \log \pi_\theta(\boldsymbol{a}_t | \boldsymbol{s}_t) \right] \tag{4.5}$$

where $\hat{E}$ indicates an empirical average.

4.1.2 Actor-Critic Methods

A known issue of simply using $\Psi_t = \sum_{t=0}^{\infty} \gamma^t r_t$ is a large variance; namely, the returns from different trajectories are too diverse to perform stable learning. A common alternative is to parameterize the value function along with the policy and make use of the value estimate in the policy update [58, 57]. With the introduction of value estimates, the variance can be reduced.

The framework where both the policy (actor) and value (critic) are learned is known as an actor-critic method. The actor-critic method alleviates the issue of high variance in the naive policy gradient method and high bias in the value-based methods by fusing the two models. Figure

$$V_{\theta_c}^{\pi}(\boldsymbol{s}) \leftarrow E \left[\sum_{t=0}^{\infty} \gamma^t r_t \middle| \boldsymbol{s}_0 = \boldsymbol{s} \right]$$

$$\pi_{\theta_a} : \theta_a \leftarrow \theta_a + \alpha \nabla_{\theta_a} J(\theta_a)$$
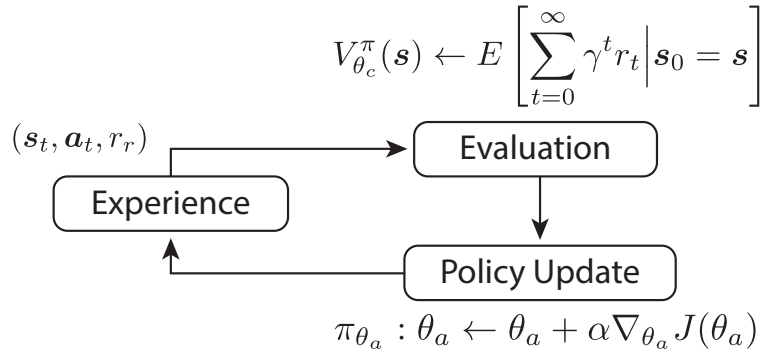
Figure 4.1: Schematic of the actor-critic algorithm.

4.1 shows the general learning process of the actor-critic methods. The parameters of the actor

and critic are each denoted as θ_a and θ_c. The agent first interacts with the environment using an initial policy and collects a batch of experience $(\boldsymbol{s}_t, \boldsymbol{a}_t, r_t)$. Then, the performance of the policy is evaluated by fitting the value function. With the value estimate, the policy is updated such that an action that results in a larger value is more likely to be chosen.

A common choice of Ψ_t in the actor-critic method is the advantage estimate $\overline{A}^\pi(\boldsymbol{s}_t, \boldsymbol{a}_t)$. The formal definition of the advantage is given by

$$A^\pi(\boldsymbol{s}_t, \boldsymbol{a}_t) = Q^\pi(\boldsymbol{s}_t, \boldsymbol{a}_t) - V^\pi(\boldsymbol{s}_t) \tag{4.6}$$

and it indicates how beneficial an $\boldsymbol{a}_t$ is at $\boldsymbol{s}_t$ with respect to the default behavior of the policy π.

For the computation of the advantage, generalized advantage estimation (GAE) is used [57, 52]. GAE controls the tradeoff between the bias and variance by introducing a parameter λ. The GAE is given by

$$\overline{A}^\pi(\boldsymbol{s}_t, \boldsymbol{a}_t) = \sum_{l=0}^{\infty} (\gamma\lambda)^l \delta_{t+l} \tag{4.7}$$

where

$$\delta_t = r_t + \gamma \overline{V}^\pi(\boldsymbol{s}_{t+1}) - \overline{V}^\pi(\boldsymbol{s}_t) \tag{4.8}$$

$\overline{V}^\pi$ is the estimated value for a policy π. If $\lambda = 0$, then $\overline{A}(\boldsymbol{s}_t, \boldsymbol{a}_t) = \delta_t$ and the estimate has low variance but high bias. If $\lambda = 1$, then $\overline{A}(\boldsymbol{s}_t, \boldsymbol{a}_t) = \sum_{l=0}^{\infty} \gamma^l r_{t+l} - \overline{V}(\boldsymbol{s}_t)$, which has high variance and low bias. The estimates with $0 < \lambda < 1$ balances the bias and variance.

While the definitions so far assumed an infinite horizon problem, in practice, the interaction of the agent is terminated if a terminal state or maximum time step is reached. An episode is the experience of an agent's interaction starting from an initial state through the termination. At the end of an episode, the advantage estimate is simply set to $r_t - \overline{V}(\boldsymbol{s}_t)$. The advantage at a non-terminal state is recursively computed as $\overline{A}^\pi(\boldsymbol{s}_t, \boldsymbol{a}_t) = \delta_t + \gamma\lambda\overline{A}^\pi(\boldsymbol{s}_{t+1}, \boldsymbol{a}_{t+1})$ looking at the trajectory backward in time.

4.1.3   Proximal Policy Optimization

In the policy gradient method, a slight change in the parameter space could degrade the performance of the policy. The Trust region policy optimization (TRPO) algorithm aims to prevent such a catastrophic update by keeping the policies before and after an update close. To be precise, TRPO solves the following constrained optimization problem [59].

$$\max_{\theta} \hat{E}_{\boldsymbol{s}_t, \boldsymbol{a}_t \sim \pi_{\theta_{\text{old}}}} \left[\frac{\pi_{\theta}(\boldsymbol{a}_t | \boldsymbol{s}_t)}{\pi_{\theta_{\text{old}}}(\boldsymbol{a}_t | \boldsymbol{s}_t)} \overline{A}^{\pi_{\theta_{\text{old}}}}(\boldsymbol{s}_t, \boldsymbol{a}_t) \right] \tag{4.9}$$

subject to

$$\hat{E}_{\boldsymbol{s}_t \sim \pi_{\theta_{\text{old}}}} \left[D_{\text{KL}}(\pi_{\theta_{\text{old}}}(\cdot | \boldsymbol{s}_t) || \pi_{\theta}(\cdot | \boldsymbol{s}_t)) \right] \leq \delta \tag{4.10}$$

where D_{KL} is the Kullback–Leibler (KL) divergence between the old and new policies. The objective function is obtained using importance sampling and an approximation to the state distribution in the original policy gradient objective.

PPO addresses the same goal as TRPO, i.e., improving the policy while preventing its drastic change during an update. Because PPO achieves stable policy improvement by a simple trick to clip the objective function, it is easier to implement. The objective function of PPO is defined as follows.

$$J^{\text{CLIP}}(\theta) = \hat{E}_{\pi_{\theta_{\text{old}}}} \left[\min \left\{ R_t(\theta) \overline{A}^{\pi_{\theta_{\text{old}}}}, \text{clip}(R_t(\theta), 1 - \epsilon_{\text{clip}}, 1 + \epsilon_{\text{clip}}) \overline{A}^{\pi_{\theta_{\text{old}}}} \right\} \right] \tag{4.11}$$

where $R_t(\theta) = \pi_{\theta}(\boldsymbol{a}_t | \boldsymbol{s}_t) / \pi_{\theta_{\text{old}}}(\boldsymbol{a}_t | \boldsymbol{s}_t)$ is the ratio of the action probability. If $\overline{A}^{\pi_{\theta_{\text{old}}}} > 0$ for an action $\boldsymbol{a}_t$ at $\boldsymbol{s}_t$, then we want to increase the likelihood of taking that action, which means θ is adjusted so that $R_t(\theta) > 1$. Because of the clipping, however, the objective function cannot be increased past $(1 + \epsilon_{\text{clip}}) \overline{A}^{\pi_{\theta_{\text{old}}}}$, demotivating further change in the policy. The same logic works for $\overline{A}^{\pi_{\theta_{\text{old}}}} < 0$.

4.1.4   PPO Implementation Details

Besides the PPO policy objective, two additional terms are defined to construct a combined loss function [52]. The first term is the value loss. In this study, an independent neural network is

trained to estimate the value function $V^{\pi_\theta}(\boldsymbol{s}_t)$. After samples $(\boldsymbol{s}_t, \boldsymbol{a}_t, r_t)$ are collected by executing the policy $\pi_{\theta_{\text{old}}}$, the advantage $A^{\pi_{\theta_{\text{old}}}}$ is computed by GAE algorithm. Then, the target value is computed as

$$V_{\text{targ}}^{\pi_{\theta_{\text{old}}}}(\boldsymbol{s}_t) = \overline{A}^{\pi_{\theta_{\text{old}}}}(\boldsymbol{s}_t, \boldsymbol{a}_t \sim \pi_{\theta_{\text{old}}}) + \overline{V}^{\pi_{\theta_{\text{old}}}}(\boldsymbol{s}_t) \tag{4.12}$$

The value function loss is defined as a mean squared error.

$$L^{\text{VF}}(\theta_c) = \frac{1}{n} \sum_i (\overline{V}_{\theta_c}(\boldsymbol{s}_i) - V_{\text{targ}}^{\pi_{\theta_{\text{old}}}}(\boldsymbol{s}_i))^2 \tag{4.13}$$

where $\boldsymbol{s}_i$ is a sampled state in the experience buffer. Based on the discussion in [60], the running mean and variance of the target values are computed during the training and used to normalize the value network. Thus, the value network predicts the normalized deviation $\overline{v}_{\theta_c}(\boldsymbol{s}_t)$ from the running mean such that

$$\overline{V}_{\theta_c}(\boldsymbol{s}_t) = \sigma_{\text{value}} \overline{v}_{\theta_c}(\boldsymbol{s}_t) + \mu_{\text{value}} \tag{4.14}$$

The running mean μ_{value} and variance σ_{value}^2 are updated in every epoch using every sample point $V_{\text{targ}}^{\pi_{\theta_{\text{old}}}}(\boldsymbol{s}_i)$.

Another term is the entropy bonus $S(\theta_a)$, which prevents the policy from becoming too deterministic in the early stage of the learning [52]. The entropy of the policy π_θ is computed for the state and action pairs sampled from $\pi_{\theta_{\text{old}}}$, and the sample average of the entropy is included in the loss. The combined loss function is defined as follows.

$$L^{\text{CLIP+VF+S}}(\theta_a, \theta_c) = \hat{E}_{\pi_{\theta_{\text{old}}}} \left[-J^{\text{CLIP}}(\theta_a) + w_1 L^{\text{VF}}(\theta_c) - w_2 S(\theta_a) \right] \tag{4.15}$$

where w_1 and w_2 are weights for the value and entropy losses. The stochastic gradient descent (SGD) algorithm is used to find parameters that minimize the combined loss function.

There are several hyperparameters in the SGD process. The PPO algorithm alternates between the sample collection and update process. Samples are collected by N_p parallel workers that execute the same policy; each agent collects N samples before the update. At the evaluation and update stage, $(N_p \times N)$ samples are randomly divided into M mini-batches or smaller sets of

samples. The minibatch size is $(N_p \times N)/M$. The gradient descent $L(\theta) \leftarrow L(\theta) - \alpha \nabla_\theta L(\theta)$ is sequentially performed using each minibatch, where α represents the learning rate. Updating the parameters M times using all mini-batches consists of an epoch. The number of epochs N_{epoch} is another hyperparameter. After N_{epoch}-th epoch, the algorithm goes back to collecting the samples with the updated policy. After each epoch, the advantage and target values are recomputed with the updated value estimate as recommended in [60]. The PPO algorithm implementation used in this study is based on v0.3.0 of ReinforcementLearning.jl package [61] with a few modifications by the authors to incorporate recommendations in [60].

As for the policy network, its outputs correspond to the mean $\boldsymbol{\mu}(\boldsymbol{s}_t)$ and standard deviation $\boldsymbol{\sigma}(\boldsymbol{s}_t)$ of a diagonal Gaussian distribution. If the dimension of the action is n_a, the output of the policy network is of size $2n_a$. The action is computed by $\boldsymbol{a}_t = \boldsymbol{\mu} + \boldsymbol{\sigma} \odot \boldsymbol{\xi}$ where $\odot$ is element-wise multiplication and $\boldsymbol{\xi}$ is a Gaussian random variable sampled from $\mathcal{N}(\boldsymbol{0}, I)$. The action is normalized and clipped to be in $[-1, 1]$. The mean is obtained by applying the hyperbolic tangent function tanh to the n_a outputs so that its element is in $[-1, 1]$. Following the recommendation in [60], the standard deviation is obtained by applying the softplus function $f(x) = \log(1 + e^x)$ elementwise to another n_a outputs, which guarantees $\sigma \geq 0$.

4.2 Reconnaissance Trajectory Guidance Design

The RL-based guidance algorithm aims to obtain an offline policy for global mapping tasks formulated as an MDP. The policy is made adaptive by including task context and parameters for the asteroid environment as part of the state and randomizing them during the training. In the global mapping task, the spacecraft maps an asteroid's surface from hovering trajectories as illustrated in Fig. 4.2. The motion of the spacecraft is described relative to the Sun-asteroid fixed rotating frame or the Hill frame. The spacecraft moves along the circumference of a circle at $r = 5R$ in the Hill frame, occasionally applying an impulsive velocity change. The spacecraft needs to observe all 50 target points distributed evenly on the sphere with radius R from the hovering trajectory with a set of observation criteria described in the subsequent sections. The number of

observation targets is a parameter of the MDP simulation environment, and the method described in this chapter can be applied to an environment with an arbitrary number of targets. Increasing the number of targets forces the spacecraft to cover more surface points. However, using more target points requires more computational resources as the MDP state becomes larger. Observation of the asteroid's surface with various lighting conditions is beneficial for the geophysical study of asteroids. Thus, we introduce the target azimuth angle as shown in Fig. 4.2 as a task context and allow the spacecraft to perform the observation from various phase angles. The target azimuth angle is fixed throughout an episode, which means that an observation campaign focuses on a single target azimuth angle at a time.

In this section, the dynamics models used to propagate the spacecraft's trajectory in the simulation environments for training and testing are described. Then the definition of the MDP is provided.
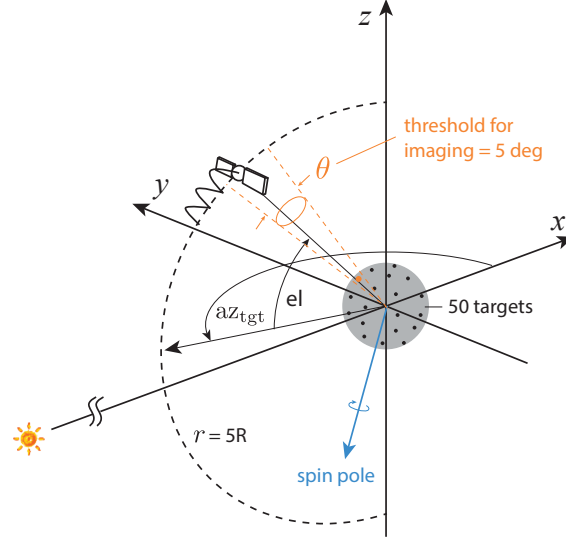
Figure 4.2: Schematic of global mapping hovering trajectory.

4.2.1 Dynamical Models

The Hill three-body models with the solar radiation pressure (SRP) are used to describe the trajectory of a spacecraft. The equations of motion are of the form in Eq. (2.11). However, the

dynamics are normalized to reduce the number of environmental parameters and to ensure that the policy can be applied to a range of asteroid parameters. The asteroid's radius is used as a unit length, and the reciprocal of the spacecraft's mean motion is used as a unit of time.

$$\text{(unit length)} = R \tag{4.16}$$

$$\text{(unit time)} = \sqrt{R^3/\mu} = \sqrt{3/(4\pi G \rho_d)} \tag{4.17}$$

where μ is an asteroid's mass parameter; ρ_d is its bulk density assuming a spherical asteroid; G is the gravitational constant. The normalization makes the mass parameter of the asteroid unity, resulting in the following equations of motion.

$$\ddot{r} = -2n\tilde{\hat{z}} \cdot \dot{r} + n^2(3\hat{x}\hat{x} - \hat{z}\hat{z}) \cdot r - r/r^3 + \beta\hat{x} + \Delta V \delta(t - \tau) \tag{4.18}$$

where r is the position of a spacecraft relative to an asteroid; β is a normalized SRP parameter; n is a normalized mean motion of the asteroid's orbit about the Sun.

The maneuver execution includes spherical Gaussian noise that is proportional to the ΔV magnitude. Thus, the trained policy needs to take the effect of the maneuver noise into account. The study uses $\sigma_{\Delta V} = 0.05\Delta V$ during the training.

As for the asteroid's spin state, single-axis rotation with a constant spin rate $\dot{\varphi}$ is assumed. The spin pole is not assumed to be perpendicular to the orbit plane. Thus, the spin pole in the Hill frame keeps moving and traces a circle at the same rate as the asteroid's mean motion.

To test the robustness of the policy, we defined a higher-fidelity test environment using the asteroids Bennu and Itokawa. The dynamical models in the test environment introduce additional unmodeled dynamical effects. First, the asteroid's point mass gravity model is replaced by the spherical harmonics gravity model using Eq. (2.4). The 5x5 harmonics coefficients obtained from [62] are used for Bennu. For Itokawa, 4x4 harmonics coefficients are used and obtained from [63]. The test dynamics further incorporate an elliptic asteroid's orbit. This change makes the equations non-autonomous, as they explicitly depend on the true anomaly F of the asteroid's orbit. The magnitude of the SRP force thus changes as the asteroid moves around the Sun. The SRP

acceleration is computed using the cannonball model in Eq. (2.8). Table 4.1 shows the asteroid's physical parameters used to define the test environment. The spacecraft's mass-to-area ratio is set to $M_{SC}/A_{SC} = 63$ kg/m^2 for the case of Bennu and to $M_{SC}/A_{SC} = 33$ kg/m^2 for the case of Itokawa. The surface reflectivity ρ_d is set to 0.4. The unit length and time depend only on the radius R and density ρ_d. Thus, given R and ρ_d, the equations of motion of the form in Eq. (2.1) can be normalized.

Table 4.1: Asteroids' parameters used for test environment

Symbol	Description	Unit	Bennu	Itokawa
R	Asteroid's radius	km	0.246	0.162
ρ_d	Asteroid's density	g/cm^3	1.26	1.98
A	Asteroid orbit's SMA	AU	1.126	1.324
E	Asteroid orbit's eccentricity	-	0.2	0.28
$\dot{\varphi}$	Asteroid's spin rate	rad/s	4.068E-4	1.439E-4

4.2.2 MDP Definition

In an MDP, the agent chooses an action based on the state at the decision-making step, which makes the agent transition to the next state. A hop on the hovering trajectory corresponds to a single decision-making step for our problem. Given the state and action, the resulting hovering trajectory is computed, which is then used to check the observation conditions. Each target point is marked as observed if the following conditions are met simultaneously along the trajectory; the angular separation between the spacecraft and target is less than $\theta_{\text{image}} = 5°$; the spacecraft's distance from the asteroid satisfies $3R < r < 7R$; the spacecraft's azimuth angle is within $5°$ from the target azimuth angle.

The state of the MDP is defined as follows and visualized in Fig. 4.3. The MDP state includes asteroid parameters, task context, the spacecraft's position and velocity, and observation status of the 50 angular points about the asteroid, which would be surveyed autonomously.

$$\boldsymbol{s}_t = [\beta, \dot{\varphi}, \text{az}_{\text{tgt}}, n, \cos(\alpha_p), \sin(\alpha_p), \varepsilon, \Delta r, \Delta\text{az}, \text{el}_H, \text{el}_B, \dot{\boldsymbol{r}}, \cos(\varphi), \sin(\varphi), \boldsymbol{b}_1, \boldsymbol{b}_2] \qquad (4.19)$$

where az_tgt is the target azimuth angle for the observation campaign; α_p is the azimuth angle of the spin pole in the Hill frame; ε is the obliquity; Δr is the deviation in the spacecraft's distance from the reference distance of $r = 5R$; Δaz is the deviation in the spacecraft position's azimuth angle relative to az_tgt; el_H is the spacecraft's elevation angle in the Hill frame; el_B is the spacecraft's elevation angle in the asteroid's body-fixed frame; φ is the spin pole's phase angle. We note that some elements of the state $\boldsymbol{s}_t$ are redundant if we are to compute the spacecraft's state and asteroid's spin state. For example, el_H can be computed from el_B given other state elements because we know how these quantities relate to each other. The RL agent might be able to identify such an underlying relationship and make a good decision without being explicitly told both el_B and el_H. However, we chose to show the RL agent both quantities, expecting that it would speed up the learning process. The same argument holds true for the binary vector $\boldsymbol{b}_2$, which can be computed from the other state elements. All the physical parameters are normalized using Eqs. (4.16) and (4.17). $\boldsymbol{b}_1$ and $\boldsymbol{b}_2$ are binary vectors with length 50, which are an abstract representation of the observation status of the distributed targets' angular locations. $\boldsymbol{b}_1$ represents observation progress and $\boldsymbol{b}_2$ indicates observability of each target. When a target has been successfully observed, the corresponding element of $\boldsymbol{b}_1$ is set to 1 and otherwise 0. When a target cannot be observed from the current phase angle, the corresponding element of $\boldsymbol{b}_2$ is marked as 1 and otherwise 0. The detail of the computation of the binary vector $\boldsymbol{b}_2$ is given in Appendix C. The binary vectors are ordered according to the target's elevation angle in the asteroid's body-fixed frame. The position of the spacecraft is determined by the elevation angle, deviation in the distance from $r = 5R$, and azimuth angle deviation from az_tgt. Asteroid parameters, namely, β, $\dot{\varphi}$, and ε and task context az_tgt are fixed throughout an episode.

During the training, the state needs to be reset to initial conditions. When the states are initialized, they are randomly sampled from a predefined distribution. We assume that the parameters of target asteroids fall within the following ranges; $R \in [0.25, 10.0]\,\text{km}$; $\rho_d \in [0.5, 4.0]\,\text{g/cm}^3$; $A \in [1.0, 1.5]\,\text{AU}$; (spin period) $\in [4.0, 12.0]\,\text{hours}$; ($a_\text{SRP}$ at 1 AU) $\in [0.5, 1.5]\,a_\text{SRP,0}$ where the base SRP of $a_\text{SRP,0} = 1.014 \times 10^{-10}\,\text{km/s}^3$ is computed assuming OSIRIS-REx spacecraft. Given

Figure 4.3: Schematic of global mapping hovering trajectory and MDP variables.

these parameter ranges, the upper and lower bounds of the normalized asteroid parameters are given as follows.

$$\beta \in [2.01 \times 10^{-6},\ 4.35 \times 10^{-3}] \tag{4.20}$$

$$\dot{\varphi} \in [0.138,\ 1.167] \tag{4.21}$$

$$n \in [1.025 \times 10^{-4},\ 5.325 \times 10^{-4}] \tag{4.22}$$

$$\varepsilon \in [165°,\ 180°] \tag{4.23}$$

These parameters are sampled from uniform distributions with the bounds listed above. Similarly, $\mathrm{az_{tgt}}$, α_p, el, and φ are sampled from a uniform distribution in $[\pi/2, 3\pi/2]$, $[-\pi, \pi]$, $[-\pi/2, \pi/2]$, and $[-\pi, \pi]$ respectively. Δr is sampled from a Gaussian distribution with zero mean and $\sigma = 0.1$. $\Delta\mathrm{az}$ is sampled from a Gaussian distribution with zero mean and $\sigma = 5°$. Each element of $\dot{\boldsymbol{r}}$ is sampled from a Gaussian distribution with zero mean and $\sigma = 0.01$. The vector $\boldsymbol{b}_1$ is set to zero and $\boldsymbol{b}_2$ is initialized based on other state values. We note that during the training, elements of the state are rescaled such that they are more or less in $[-1, 1]$ for improved feature representation.

The action that the agent chooses at every decision-making step is defined as follows.

$$\boldsymbol{a}_t = \begin{bmatrix} \Delta\mathrm{el} \\ \Delta t \end{bmatrix} \quad \text{where} \quad \begin{array}{c} -30° \leq \Delta\mathrm{el} \leq 30° \\ \pi \leq \Delta t \leq 6\pi \end{array} \tag{4.24}$$

The first element is the change in the spacecraft's elevation angle in the Hill frame, which defines the next target position of the hovering. The second component of the action is the transfer time to the target location. The transfer time is given in the normalized system. The policy network's output is normalized such that the action is in $[-1, 1]$. Thus, the action's upper and lower bounds are used to reconstruct actual Δt and Δt.

Given $\boldsymbol{s}_t$ and $\boldsymbol{a}_t$, the target $\boldsymbol{\Delta V}$ for the orbit transfer to the next target position can be computed by solving a TPBPV. The predictor-corrector algorithm described in section 2.3 is used to solve the TPBVPs. The upper bound of the transfer time is relatively short, and the TPBVP solver can easily find appropriate transfer trajectories that have no revolution around the asteroid. Thus, when a $\boldsymbol{\Delta V}$ is computed with the RL policy, only a single-step continuation is performed.

Namely, after the solution with a parameter $\boldsymbol{p} = \boldsymbol{0}$ is computed, the solution of the target parameter is directly computed. We introduce a Gaussian maneuver execution noise that is proportional to $|\boldsymbol{\Delta V}|$ during the training, and $\sigma = 0.05|\boldsymbol{\Delta V}|$ is used, which means the problem is optimization under aleatoric uncertainties. We assume the onboard navigation system can reconstruct the true trajectory once the maneuver is applied, which means the state is assumed to be fully observable. Along the spacecraft's trajectory, the observation condition is checked every 0.1 normalized time, which updates $\boldsymbol{b}_1$. Spacecraft's position and velocity and other time-varying quantities are updated as well.

There are two different classes of terminal states. The first terminal state corresponds to the end of a successful observation campaign. It is defined as the state where all of the observable targets have been observed, namely, $\boldsymbol{b}_{1,i} = 1 \, \forall_i$ unless $\boldsymbol{b}_{2,i} = 1$ and the spacecraft is near one of the poles, namely, $|\text{el}_H| \geq 70°$. The condition for the elevation angle drives the spacecraft to finish the observation campaign near the polar regions. Ideal locations to switch a target observation azimuth angle are near the polar regions because the change in the spacecraft's position is minimum. Thus, the condition allows the spacecraft to perform a sequence of observation campaigns from multiple target azimuth angles by simply running multiple episodes changing az_{tgt}. The second terminal state corresponds to the collision with the asteroid. This study considers $r < 2R$ to be a collision. The episode is also terminated if the agent does not reach a terminal state after the maximum horizon length, which is set to 200.

The reward the agent receives at each MDP time step is defined as follows.

$$
r_t = \begin{cases}
-1 + r_{\text{new}} - |\boldsymbol{\Delta V}| + p_{\text{altitude}} \\
\quad + p_{\text{elevation}} + \text{bonus}_1 + \text{bonus}_2 \\
p_{\text{collision}}
\end{cases}
\begin{aligned}
& \text{(if no collision)} \\
& \\
& \text{(otherwise)}
\end{aligned}
$$

where r_{new} is the number of newly observed targets; $p_{\text{altitude}} = 10 \cdot \min(r - 5R, 0)$ is the penalty for flying lower than the nominal hovering altitude; $p_{\text{elevation}}$ is a penalty that encourages the agent to move to polar regions by incentivizing the agent to have a large $|\text{el}_H|$ once the observation is complete. If there are remaining targets, $p_{\text{elevation}} = 0$ and otherwise $p_{\text{elevation}} = -(\pi/2 -$

$|\text{el}_H|)/(\pi/2)$. The first bonus term is a reward for achieving an intermediate goal, which is defined as follows. We divide the target locations into three groups: northern, southern, and others. The targets in the northern group have elevation angles in the body-fixed frame that are larger than $30°$, whereas in the southern group, they are smaller than $-30°$. When observable targets in the southern group are fully observed for the first time while no target in the northern group is observed, then $\text{bonus}_1 = 100$ and vice versa. This intermediate bonus term encourages the agent to stay in one of the hemispheres before moving to another. The second bonus term bonus_2 is set to 100 when the agent reaches the successful terminal state and 0 otherwise. $p_{\text{collision}} = -200$ is the penalty for collision, namely, $r < 2R$.

4.3   Performance of the PPO Policy

The adaptive offline policy for the onboard global mapping task under the maneuver execution noise is obtained by the PPO algorithm. This section first provides the analyses of the neural network model structures and other hyperparameters. Then, the analyses of the obtained policy's performance and robustness are presented.

4.3.1   Model Structure and Hyperparameters

First, the results of the hyperparameter study are presented. Although many hyperparameters affect the performance of the policy, we present the analyses on a few selected hyperparameters. Some nominal hyperparameters used in this study, whose analyses are not shown in this paper, such as learning rate, minibatch size, activation functions, etc., strongly influence the training outcome, and they have coupled effects on the training performance. They are selected based on trial and error. One observation is that since there are multiple paths that lead to a successful terminal state in the MDP, the policy often gets stuck at a local optimum. Thus, injecting large enough noises in the SGD process seems essential for the agent to escape these local optima by using a large learning rate or small minibatch size. Also, due to the discrete nature of the task progress as represented by the binary vectors, using rectified linear unit (relu) as activation functions resulted in a better

performance than other common alternatives such as tanh. Some other hyperparameters are simply set to values that result in stable learning without much investigation of the optimal choice.
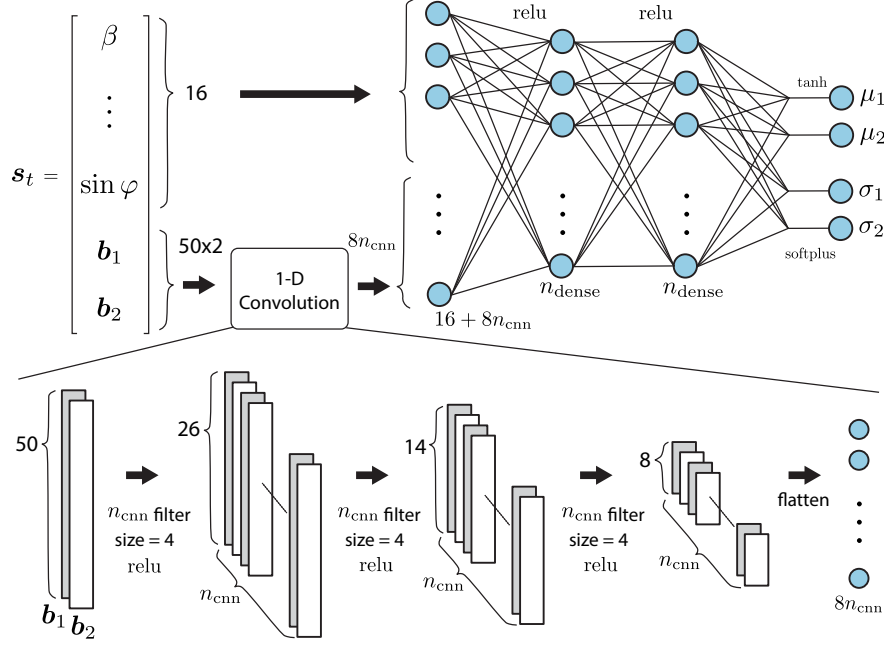
Figure 4.4: Neural network structure of the policy.

Feedforward neural networks are used to parameterize the policy and value functions. A part of the experiment is to study different parameterizations of the networks. However, for ease of analysis, we constrained the network structure. Figure 4.4 shows the general structure of the policy network. Since the binary vectors are ordered according to the target location's body-relative elevation angle, they exhibit spatial structures. For example, if a target is observed by taking action at a state, then neighboring targets are also likely to be observed. To exploit this spatial structure, nominally, the binary vectors $\boldsymbol{b}_1$ and $\boldsymbol{b}_2$ are processed by a 1-dimensional (1D) convolutional neural network (CNN) before they are passed to fully connected dense layers. The CNNs used in this study have three layers. In each layer, filters of size four are used. The zero paddings of size two are applied at the beginning and end of each convolution. The stride is set to two. The number of filters n_{cnn} is a hyperparameter. The two binary vectors in the input are treated as different channels. The output of the CNN is connected to the dense layers along with other elements of the

MDP state vector. The study fixes the number of hidden dense layers to two. The number of nodes in the dense layer, n_{dense} is another hyperparameter. The activation function in the convolutional and dense layers is relu. As for the policy, the hyperbolic tangent function (tanh) and softplus function are applied for the mean and standard deviation, respectively. The value network shares the same structure as the policy network. However, they are made independent; namely, no neural network parameters are shared. The final output of the value network is a single number computed without any activation functions. The study uses v0.12.10 of Flux.jl machine learning package to construct neural network models [64].

Table 4.2: PPO hyperparameters

N_p	32
N	2048
$(N_p \times N)/M$	512
N_{epoch}	10
α	3e-4
γ	0.99
λ (GAE)	0.9
ϵ_{clip}	0.2
w_1	1e-2
w_2	0.1
$\beta_{\text{adamw},1}$	0.9
$\beta_{\text{adamw},2}$	0.999
w_d	1e-5

The nominal PPO hyperparameters used in the study are shown in Table 4.2. The study uses the ADAMW optimizer. The exponential decay of the momentum estimates $\beta_{\text{adam},1}$ and $\beta_{\text{adam},2}$ and weight decay w_d for ADAMW are listed in the table as well [65, 64]. The weights of the policy and value networks are initialized with the uniform distribution proposed by Glorot and Bengio [66, 64]. Following the recommendation in [60], the policy network is initialized such that its outputs are 0 for the mean and 0.5 for the standard deviation. This initialization is done by setting the weights of the final dense layer 100 times smaller and by adding a bias $\log(e^{0.5} - 1)$ for the standard deviation. During the gradient descent step, the gradient is globally clipped so that the norm of the gradient does not exceed a threshold value for stable learning [67]. The threshold

value is set to 0.5. Also, the learning rate α is set to a smaller value of 1e-4 during the initial policy update iterations (for all N_{epoch} epochs) to stabilize the updates.

We first present the results of the hyperparameter study on the parameterization of the policy and value networks. The training is performed with different combinations of n_{cnn} and n_{dense}. We also performed the training without the convolution layers. In such a case, the two binary vectors in the MDP state are directly connected to the dense layers. When we perform a hyperparameter study, training is performed three times using a different random number seed for each set of hyperparameters. Figure 4.5 shows the history of average reward and Gaussian policy's entropy for different neural network models. The average reward is the sample average of the rewards obtained during the sample collection phase, computed using $N_p \times N$ samples. The entropy in the plot shows the average entropy of the last minibatch in the final epoch computed using $(N_p \times N)/M$ samples. The model name "cnnX_denseY" indicates a neural network with $n_{\text{cnn}} = X$ and $n_{\text{dense}} = Y$; the name "denseX" indicates that the network does not have convolutional layers and $n_{\text{dense}} = X$. Changing n_{cnn} results in a slight change in the final performance. However, the difference is not as significant as the performance change with and without a CNN. When there is no CNN, the agent performs poorly. Figure 4.6 shows the average reward and entropy at the end of training for wider combinations of n_{cnn} and n_{dense}. Every training is performed with a total of 4 million environmental steps. We note that throughout the thesis, the word "environmental step" is used to mean a single interaction of the RL agent with the simulation environment and a subsequent MDP state transition. The advantage of using a CNN is clearly highlighted, which allows the network to capture spatial structures the input binary vectors exhibit. Also, setting n_{dense} to a large value seems to hurt the performance. While the average rewards of "cnn8_dense128", "cnn16_dense64", and "cnn16_dense128" are more or less the same, the entropy of "cnn16_dense128" is slightly larger, which suggest that the policy of "cnn16_dense128" could outperform the other models if it is trained until it has the same level of policy entropy. Thus, $n_{\text{cnn}} = 16$ and $n_{\text{dense}} = 128$ are nominally used in this study. Table 4.3 shows the number of trainable parameters in the policy for different combinations of n_{cnn} and n_{dense}. The addition of a CNN does not significantly increase the number

of parameters, and we can confirm that the performance improvement is not simply due to the increase in the trainable parameters.
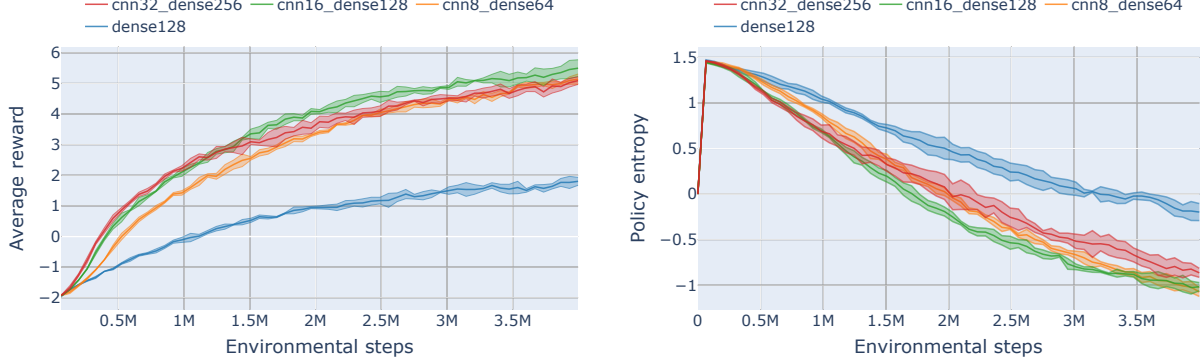
Figure 4.5: History of average reward and entropy during training with different neural network structures.

We also studied the impact of changing the weight decay. Figure 4.7 shows the training history with different weight decay values, and Fig. 4.8 shows the average reward and entropy at the end of training for different values of w_d. The neural network structure is fixed with $n_{\text{cnn}} = 16$ and $n_{\text{dense}} = 128$. It is confirmed that setting w_d too large (larger than $w_d = 10^{-4}$) hurts the performance. Otherwise, no significant performance change was observed. The study nominally uses $w_d = 1e\text{-}5$, expecting the model to generalize better with larger w_d as long as it does not degrade the policy.

Finally, experiments on different values N are performed. Because N_p is fixed, changing N is equivalent to changing the total number of environmental steps collected before updating the policy. It is reasonable to assume that the policy performs better when this buffer size is larger because the bias in the value loss can be reduced. However, a larger buffer size means that more training steps are required to perform the same number of policy update cycles. With the goal of obtaining a high-performing policy used in the end-to-end numerical study, training is performed with $N = 4096$, which doubles the buffer size. The neural network structure is fixed with $n_{\text{cnn}} = 16$ and $n_{\text{dense}} = 128$. The training is performed until the total environmental steps reach 16 million. Figure 4.9 shows the training history with $N = 2048$ and 4096. Figure 4.10 shows the average
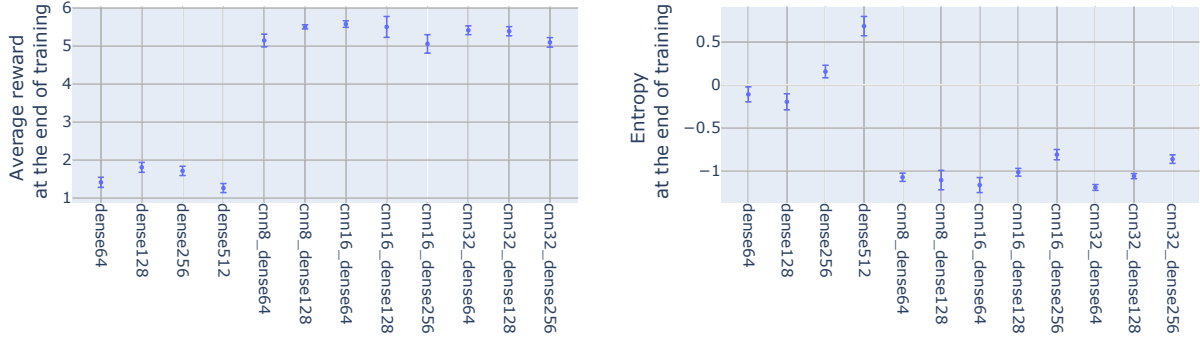
Figure 4.6: Comparison of average reward and entropy at the end of training with different neural network structures.

Table 4.3: Number of policy model parameters

n_{cnn}	n_{dense}	Number of parameters
-	64	11,908
-	128	32,004
-	256	96,772
-	512	324,612
8	64	10,204
8	128	27,996
16	64	15,924
16	128	37,812
16	256	106,164
32	64	30,436
32	128	60,516
32	256	145,252
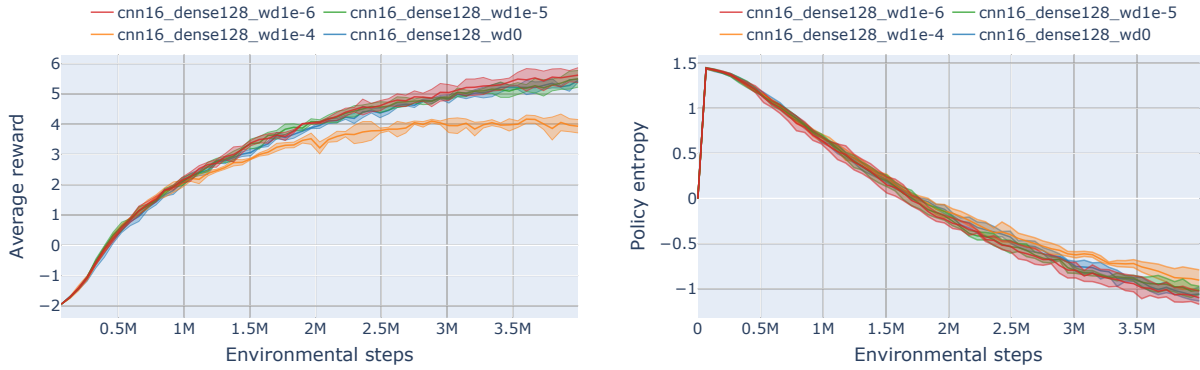
Figure 4.7: History of average reward and entropy during training with different values of w_d.
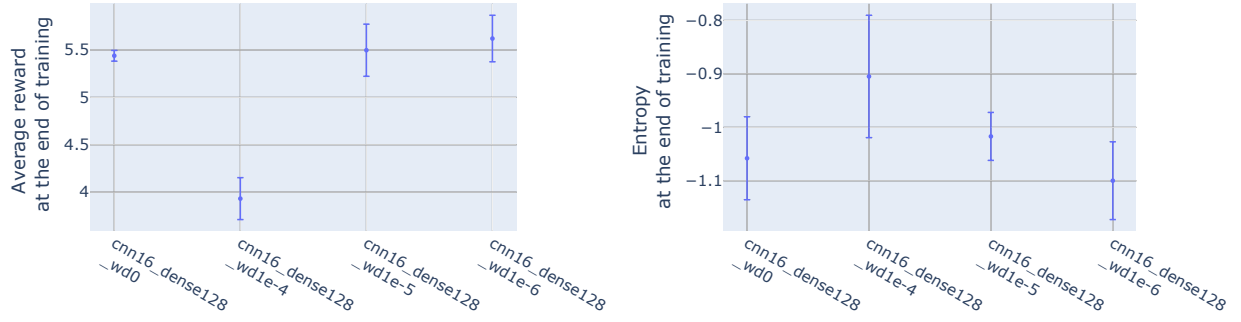
Figure 4.8: Comparison of average reward and entropy at the end of training with different values of w_d.
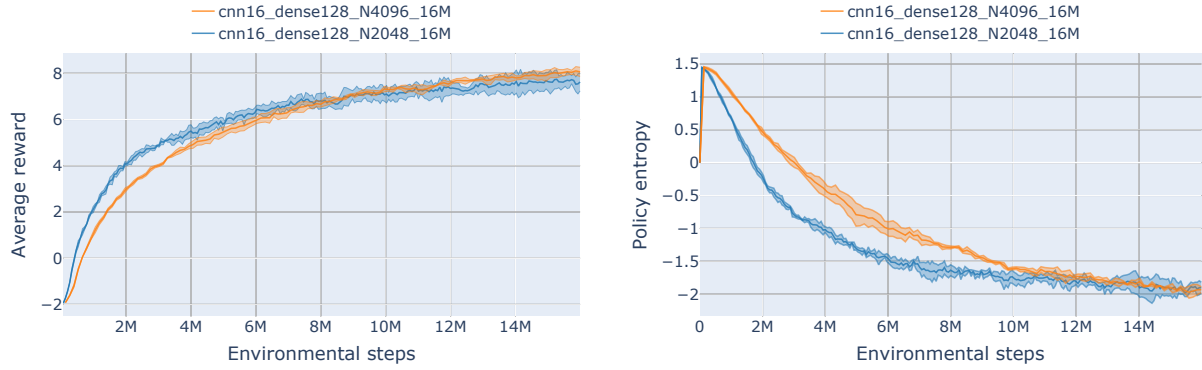
Figure 4.9: History of average reward and entropy during training with different values of N.
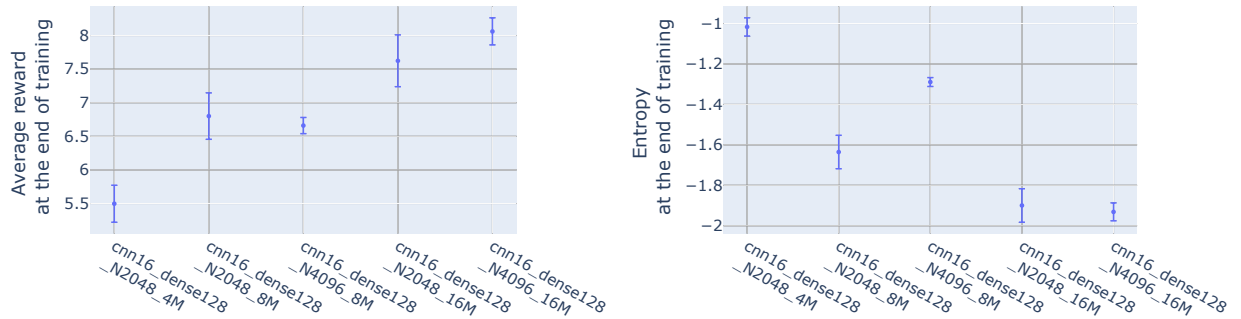
Figure 4.10: Comparison of average reward and entropy at the end of training with different values of N and total training steps.

reward and entropy at different stages of training. Until around 8 million steps, the performance of the policy with $N = 4096$ is poorer, which is likely caused by less frequent iterations between the sample collection and policy update. As the training progresses, the policy trained with $N = 4096$ outperforms the policy trained with $N = 2048$. This observation confirms that a larger buffer size is beneficial in developing a good policy. The best-performing policy from the training with $N = 4096$ is used as the nominal policy for subsequent analyses.

4.3.2   Behavior of the Policy
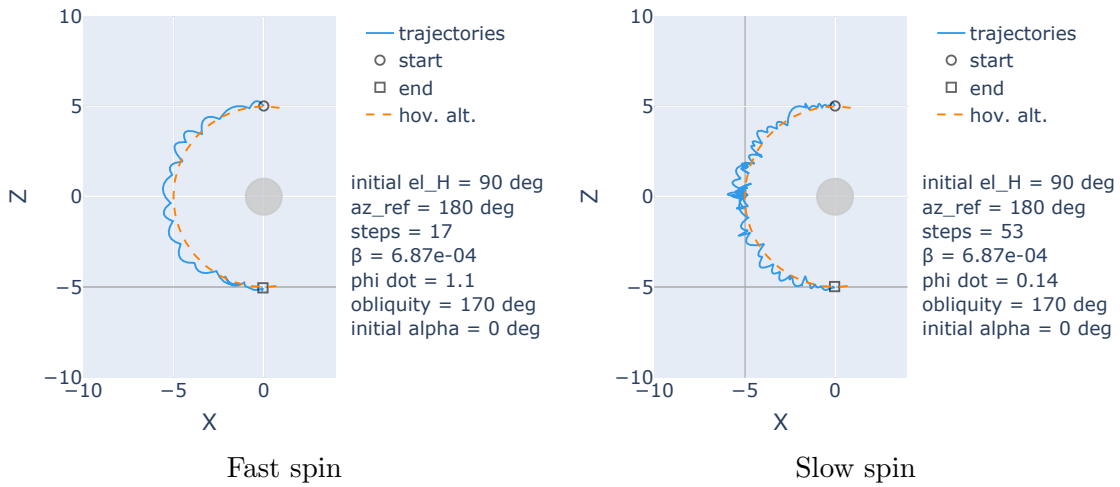
Fast spin   Slow spin

Figure 4.11: Example behavior of the policy with fast and slow spin rate.

The behavior of the best-performing policy is discussed herein. Figure 4.11 shows the trajectories obtained from the same initial condition with different spin rates ($\dot{\varphi} = 1.1$ and $\dot{\varphi} = 0.13$). The trajectories are shown in the Hill frame. When the spin rate is fast, the agent tends to have a larger change in the elevation angle. When the spin rate is slow, the task is more challenging, and the agent cannot often observe the target location in a single hop even if the spacecraft is at the corresponding elevation angle. With the trained policy, the spacecraft maintains the same elevation angle before moving to a different latitude. Figure 4.12 highlights the difference in policy's behavior when the initial pole orientation is different. On the left, the initial pole is defined with $\alpha_p = 0°$, and on the right, it is defined with $\alpha_p = 180°$. The initial pole orientation is plotted as an arrow.
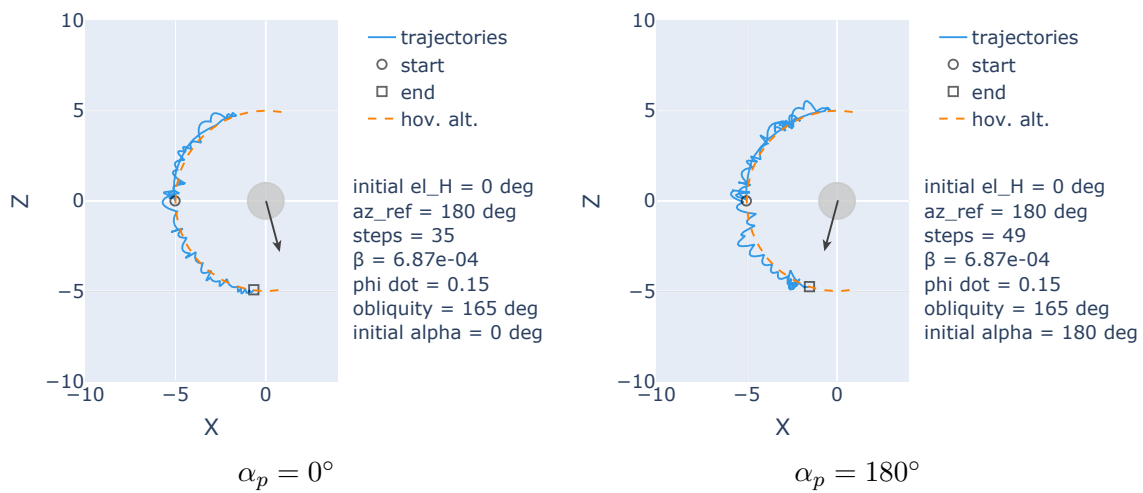
Figure 4.12: Example behavior of the policy with different pole orientations.

We can see that the policy adjusts the locations the spacecraft flies over to account for the shift in the target positions in the Hill frame.

Next, the overall difference in the policy's response when a parameter of the asteroid environment or task context is varied is studied by running Monte Carlo simulations. Initially, the state-action pairs are sampled from the policy. When the state is initialized, the parameter of interest is fixed to the median of the predefined parameter range. Other state elements are sampled according to the initial distribution used during the training. Once 50,000 state-action pairs are sampled, the element of the MDP state that corresponds to the parameter of interest is changed to its upper bound value. Then, the actions for the updated states are recorded. Some parameters are coupled with other state components and cannot be updated individually. In such a case, el_B and $\boldsymbol{b}_2$ are updated while other elements are kept the same. Figure 4.13 shows the histogram of the change in the action. Responses to the changes in $\dot{\varphi}$, $\mathrm{az}_{\mathrm{tgt}}$, $\dot{\varepsilon}$, and β are shown. The plots on the left and right show the changes in $\Delta \mathrm{el}$ and Δt, respectively. The actions are normalized to be in $[-1, 1]$. The histogram is normalized such that the area integral becomes unity. When the value of φ is changed, the resulting changes in the actions are larger, which indicates the spin rate has a significant impact on the action. We can also see the policy is sensitive to the change in $\mathrm{az}_{\mathrm{tgt}}$ and ε. When the target azimuth angle or the obliquity is different, the elevation angles in the Hill frame that the spacecraft needs to have in order to map target locations shift. The spacecraft needs to adjust its position to account for these elevation shifts, which results in changes in the actions. On the contrary, the policy is less sensitive to the SRP change. Similarly, we confirmed that the policy is not sensitive to the change in the mean motion. These observations indicate that some of the task context and environmental parameters have a stronger impact on the decision-making tasks, and the policy successfully learns to respond to such parameters.

In order to assess the robustness of the trained policy, it is of interest to study how well the policy can handle the tasks when there are reality gaps. Since the policy is trained in the simulation environment with various assumptions, it might not perform well in an environment that has a different state transition probability. The performance of the policy is evaluated with

Figure 4.13: Policy's sensitivity to changes in parameters.

an almost identical but modified MDP task. The spacecraft's dynamics are replaced by the test dynamics explained earlier, introducing the elliptic asteroid's orbits and higher-order gravity field of the asteroid. The initial state distribution is also different as the test environment uses a specific set of asteroid parameters. The asteroids Bennu and Itokawa are used as test cases, whose parameters are listed in Table 4.1. Because the test environment is defined for a specific target asteroid, β, $\dot{\varphi}$, n, and ε are not sampled from a distribution. β is updated at each step according to the Sun-asteroid distance. Similarly, n is updated to the asteroid's true anomaly rate at each time step. The asteroid's initial true anomaly is fixed to 0. ε is set to $170°$ for both asteroids. Other MDP state elements are sampled from the same initial distribution as the training environment.
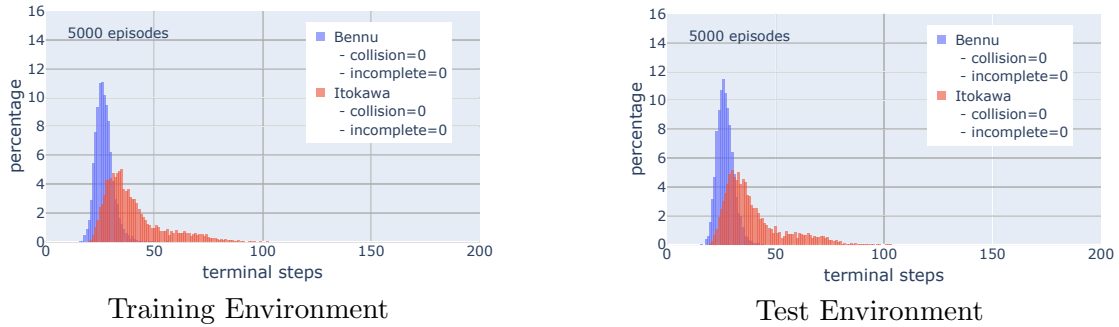
Figure 4.14: Number of steps taken to complete an episode.

We performed 5,000-episode Monte Carlo simulations for each asteroid. Figure 4.14 shows the distribution of the number of steps required to complete each episode for Bennu and Itokawa. The plot on the left is generated with the same spacecraft dynamics as the training environment. Since the spin rate of Itokawa is slower than that of Bennu, the agent requires more environmental steps to reach a successful goal state. The plot on the right shows the distribution from the test environment. The plots on the left and right look similar, and it is confirmed that the policy works well even when the spacecraft's dynamics have biases. Also, no collision or incomplete episode was confirmed for any of the cases, which demonstrates the policy's efficacy.

Next, the policy's performance is analyzed when the environment has a different magnitude of maneuver execution noise. The maneuver execution noise is sampled from a Gaussian distribution
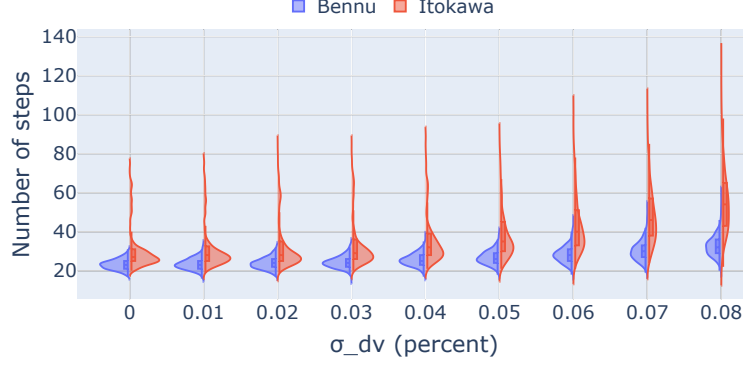
Figure 4.15: Violin plots showing the distribution of the number of environmental steps to complete an episode with different values of maneuver execution noise.

whose noise level is proportional to the maneuver size, namely, $\sigma_{\Delta V,\mathrm{crtl}} = \sigma_{\Delta V,\mathrm{ctrl},p}|\boldsymbol{\Delta V}|$. We performed 5,000-episode Monte Carlo simulations, sampling $\sigma_{\Delta V,\mathrm{crtl},p}$ uniformly from $\sigma_{\Delta V,\mathrm{crtl},p} \in [0, 1, 2, 3, 4, 5, 6, 7, 8]$ percent. Figure 4.15 shows the violin plot of the number of terminal steps for different $\sigma_{\Delta V,\mathrm{crtl},p}$. The left half of the violin is for Bennu, and the right half is for Itokawa. We can confirm that as the noise level decreases, the agent can complete the task with fewer steps. When the noise level is higher than $\sigma_{\Delta V,\mathrm{crtl},p} = 0.05$, which is the value used during the training, the task requires more steps. However, the agent can still complete the task within the maximum step of 200. The result shows that by performing the training with a conservative value of $\sigma_{\Delta V,\mathrm{crtl},p} = 0.05$, the policy works well for a wide range of noise levels.

4.4 Conclusions

This chapter describes the design of the hovering trajectory controller for surface global mapping tasks. The task is formulated as an MDP, and RL is used to solve the problem. Specifically, the PPO algorithm is used to solve the MDP task. The policy is made adaptive by introducing asteroid parameters and task context as part of the MDP state and randomizing them during the training. The training samples are collected in a simulation environment. Hyperparameter studies show that extracting the spatial structure in the MDP state input is important for better training results, and thus using CNNs improves the performance of the policy. By looking at the example

behavior of the trained policy, we confirm that the policy is indeed adaptive, changing the actions depending on the environmental parameters. The study also tests the robustness of the policy by introducing biases in the spacecraft's dynamical interaction with the asteroid. The results of the Monte Carlo runs show that the policy works well even with model discrepancies.

<center>Chapter 5</center>

<center>Simple Covariance Analysis</center>

This chapter provides the covariance analysis for the proposed onboard navigation scheme. This approach uses optical measurements provided by onboard imagers and measurements from onboard accelerometers to estimate the spacecraft's state as well as a target asteroid's parameters. The covariance studies are performed for the asteroid approach trajectory and hovering trajectory. The analysis uses simple dynamical models without model biases to understand the information contents of the measurements in an ideal situation. We first describe the measurement models used in the study. Then, the filtering algorithm used for state estimation is explained. The results of the covariance studies are provided, followed by some concluding remarks.

5.1   Measurement Models

The core of the proposed autonomous trajectory operation is navigation based on optical and ΔV measurements. As for the optical measurements, the angular location and angular size of the asteroid are assumed to be extracted from images taken by the spacecraft's onboard camera.

$$\begin{aligned}
\boldsymbol{Y}_1 &= -\hat{\boldsymbol{r}} \quad \text{(angular location)} \\
Y_2 &= \frac{R}{r} \quad \text{(angular size)}
\end{aligned} \tag{5.1}$$

where R is the asteroid's mean radius. We note that $\boldsymbol{Y}_1$ contains only two independent measurements, although it is a 3x1 vector because there is a constraint $|\hat{\boldsymbol{r}}| = 1$. The filter models the asteroid as a sphere, and a complex shape model is not considered in this study. This is equivalent to assuming that a shape and spin state have been modeled by separate onboard algorithms (for

example, see references [68, 69] for shape estimation). By counting the number of pixels filled by the asteroid in an image, a solid angle $\Omega(t)$ can be obtained as an original measurement. The solid angle can be expressed as $\Omega(t) = A(t)/r^2(t)$, where $A(t)$ is an asteroid's area projected on the sphere centered at the imager with radius r. If the estimates of shape and spin are available, the time-varying area can be computed. The shape construction depends on the range information. Therefore, given poor range accuracy, its scale should also have a large error, which can be estimated in the navigation process. With a projection A_{model} obtained from the asteroid model and a corresponding reference radius R_{model} such as mean radius, the true projection can be written as $A(t) = (R/R_{\mathrm{model}})^2 A_{\mathrm{model}}(t)$, assuming only the scale is erroneous. Thus, the angular size measurement in this study corresponds to $R/r = \sqrt{\Omega R_{\mathrm{model}}^2/A_{\mathrm{model}}}$. As Fig. 5.1 shows, these measurements have scale invariance, i.e., the same measurements could be obtained from different states, making it difficult to uniquely determine the state. If the size of an asteroid is precisely known, the angular size measurement can provide range information; however, this is not the case as the ground-based observation has relatively large size uncertainty. An approach to break the scale invariance is to apply a known maneuver , which is studied for the cases of relative motion between two satellites [70, 71, 72, 73] and for an asteroid flyby scenario [74]. The current work considers the use of such maneuvers for a wider range of proximity operation phases at an asteroid.

Because the measurement functions are nonlinear, we need to linearize them when we utilize the Kalman filter. The partial derivatives of the measurement functions are given as follows.

$$\frac{\partial \boldsymbol{Y}_1}{\partial \boldsymbol{r}} = \frac{1}{r}(\hat{\boldsymbol{r}}\hat{\boldsymbol{r}} - I_{\mathrm{3x3}}) \tag{5.2}$$

$$\frac{\partial Y_2}{\partial \boldsymbol{r}} = -\frac{R}{r^3}\boldsymbol{r} \tag{5.3}$$

$$\frac{\partial Y_2}{\partial R} = \frac{1}{r} \tag{5.4}$$

The optical measurements both have errors associated with the resolution of the onboard camera. When the onboard camera has N_p^2 pixels in a square array, the error is computed as

$$\sigma_\theta = \mathrm{IFOV}\sqrt{1 + (r_{\mathrm{ref}}/r)^2} \tag{5.5}$$

where IFOV is the total field of view (FOV) divided by N_p. Because errors in the angular location measurements come from errors in the detection of the asteroid's center, $\sigma_{Y1} = \sigma_\theta$. Also, $\sigma_{Y2} = \sigma_\theta$ as Y_2 can be only as accurate as the pixel size. The noise σ_θ is scaled according to the distance from the asteroid to account for errors in the asteroid's shape model. The reference distance r_{ref} is chosen such that at $r = r_{\text{ref}}$, the angular error corresponds to 1.5 m size error, namely $r_{\text{ref}}\,\sigma_\theta \simeq$ 1.5 m. Assuming IFOV of $60°/1000$, the corresponding distance is $r_{\text{ref}} \simeq 1$ km. We note that the choice of the shape model error may be too optimistic, and a more sophisticated error model is desirable in future analysis.

angular location

angular size
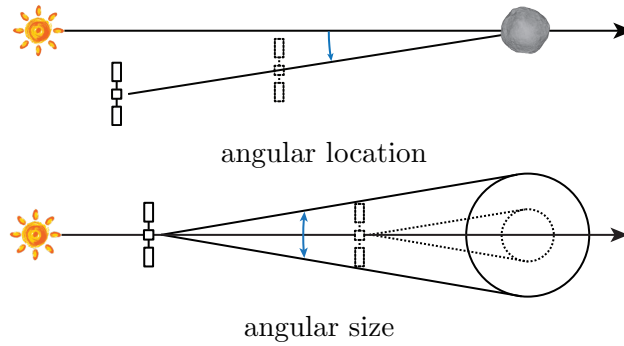
Figure 5.1: Two types of optical information and scale invariance.

We also assume that the asteroid does not fill the FOV of the imager. If the spacecraft is too close to the asteroid, the entire FOV could be covered by the asteroid. The angular location and size cannot be determined in such a case. This requirement means

$$d \tan(\text{FOV}/2) \geq R \tag{5.6}$$

$$\Leftrightarrow \quad d/R \geq 1/\tan(\text{FOV}/2) \tag{5.7}$$

where d is the asteroid-S/C distance. Figure 5.2 shows the minimum distance the spacecraft needs to maintain to obtain the assumed optical measurements. The distance is measured in terms of radius. For example, if the asteroid's radius is 246 meters and FOV is 6 degrees, then the distance must be larger than about 19 R or 4.67 km. If the FOV is 60 degrees, the minimum distance is about 1.7 R or 4.18 km. This study nominally uses $N_p = 1000$ with FOV = $6°$ or $60°$. It would be reasonable to assume that the spacecraft carries two cameras with different FOVs and switches

between them depending on the distance to the asteroid in the same fashion as the Hayabusa-2 spacecraft [75].
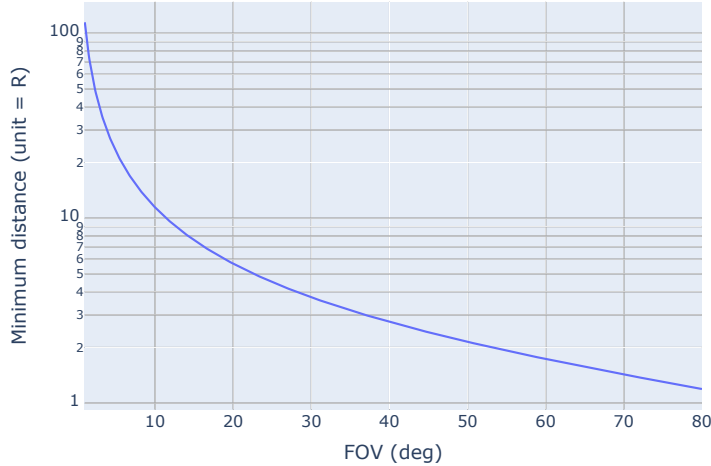
Figure 5.2: Minimum distance required for optical measurements.

To break the scale invariance of the optical measurements, it is assumed that impulsive velocity changes can be measured by onboard accelerometers, which, when integrated, provide absolute information about how the position evolves over time. If the accelerometers are of a static type or capable of measuring the DC component of the acceleration, ideally, they could measure all of the non-gravitational perturbations. This, in turn, could be used to break the scale invariance. However, actual accelerometers have a non-negligible bias that varies from day to day [76]. Removing the bias is a nontrivial task, often involving a precise orbit determination process or onboard calibration. Thus, the direct measurement of non-gravitational accelerations is not considered. Instead, we assume the acceleration from thrusters can be measured to provide $\mathbf{\Delta V}$ estimates because the change in the acceleration is easier to measure. Integrating the accelerometer data provides a measurement of a $\mathbf{\Delta V}$. Measurement noise of an accelerometer is often defined as noise spectral density with a unit of $\mathrm{m/s^2}/\sqrt{\mathrm{Hz}}$. Characteristics of several onboard accelerometers are shown in Table 5.1. If we denote the noise density as σ_{aH}, uncertainty in acceleration measurement

is computed as

$$\sigma_a = \sigma_{aH} \sqrt{\frac{1}{\Delta T}} \tag{5.8}$$

where $1/\Delta T$ is the measurement frequency. Then the measured velocity change can be modeled as $\Delta V = \sum_{i=1}^{N} a_i \Delta T$, and uncertainty in the ΔV can be calculated simply as

$$\sigma_{\Delta V \text{meas}} = \sqrt{\sum_{i=1}^{N} \sigma_a^2 \Delta T^2} = \sqrt{T} \sigma_{aH} \tag{5.9}$$

where $T = N\Delta T$ is the total duration of the maneuver. We assume that noise in the acceleration measurement at each time are uncorrelated. Thus longer maneuver time results in a larger ΔV error. Nominally, $\sigma_{\Delta V \text{meas}}$ is set to 0.1 mm/s. For example, if $T = 100$ s, this noise level is equivalent to $\sigma_{aH} = 10^{-5} \text{m/s}^2/\sqrt{\text{Hz}}$, which is more accurate than an off-the-shelf IMU but much less sensitive than state-of-the-art accelerometers.

Table 5.1: Characteristics of several onboard accelerometers.

Mission	Accelerometer	Noise Density $(\text{m/s}^2/\sqrt{\text{Hz}})$	Freq. Range (Hz)	Bias (m/s^2)
-	LN-200S (IMU) [77]	3.4×10^{-4}	-	2.9×10^{-3}
BepiColombo	ISA [78]	10^{-8}	3×10^{-5} to 10^{-1}	-
CHAMP	STAR [79]	10^{-9}	10^{-4} to 10^{-1}	10^{-5}
GRACE	SuperSTAR [79]	10^{-10}	10^{-4} to 10^{-1}	2×10^{-6}
GOCE	EGG/GRADIO [79, 80]	2×10^{-12}	5×10^{-3} to 10^{-1}	-

In the actual filter implementation, a $\boldsymbol{\Delta V}$ is not handled as a measurement; rather, a measured $\boldsymbol{\Delta V}$ is directly used as an a priori value in the state vector to be estimated, and the knowledge about the $\boldsymbol{\Delta V}$ is incorporated through the system dynamics. In other words, the filter does not maintain a nominal belief of the $\boldsymbol{\Delta V}$ generated by a guidance algorithm or update it by measurement update equations. It is possible to analytically compute how the mean and covariance of a state vector change at the time when an impulsive maneuver is performed. Thus, this formulation enables us to propagate these statistics over an arc that contains a maneuver without requiring a measurement update at the intermediate time step. The detail on the impulsive maneuver effect on the state estimates is given in appendix D.

5.2 Least Squares Algorithm

The state mean and covariance are propagated by dynamics and a set of new observations is processed for measurement update. A state transition matrix (STM) maps a small deviation and associated covariance at the previous epoch to a new epoch.

$$\boldsymbol{x}(t_k) = \Phi(t_k, t_{k-1}) \cdot \boldsymbol{x}(t_{k-1}) \tag{5.10}$$

$$P(t_k) = \Phi(t_k, t_{k-1}) \cdot P(t_{k-1}) \cdot \Phi(t_k, t_{k-1})^T \tag{5.11}$$

The STM is computed by integrating the following ODEs

$$\begin{cases} \dot{\Phi}(t, t_k) = \left. \frac{\partial \dot{\boldsymbol{X}}}{\partial \boldsymbol{X}} \right|_{\boldsymbol{X}^*} \cdot \Phi(t, t_k) \\ \Phi(t_k, t_k) = I_{nxn} \end{cases} \tag{5.12}$$

where $\boldsymbol{X}^*$ is the nominal state at time t. As a set of new measurements is obtained, a new state estimate that maximizes the posterior probability is determined along with a new covariance. For the covariance update, the so-called Joseph formulation is used for numerical stability [81].

To prevent filter saturation and to simulate the effect of unmodeled acceleration errors, process noise is included in the actual time update of the covariance. The state noise compensation (SNC) algorithm with an approximate STM is used to inflate the covariance. The dynamics now have additional acceleration $\boldsymbol{u}(t)$ as Gaussian white noise.

$$\dot{\boldsymbol{X}}(t) = \boldsymbol{F}(\boldsymbol{X}) + B \cdot \boldsymbol{u}(t) \tag{5.13}$$

B is an $nx3$ matrix that maps the noise acceleration into $nx1$ state space. For ease of computation, we treat $\boldsymbol{u}(t)$ as a white random sequence rather than a random process as described in Chapter 4.9 in [81]. The noise acceleration $\boldsymbol{u}(t)$ is piecewise constant between measurement updates. The covariance of this random sequence is given by

$$E[\boldsymbol{u}(t_i)\boldsymbol{u}(t_j)] = Q_i\delta_{ij} = \begin{cases} Q_i & (i = j) \\ 0 & (i \neq j) \end{cases} \tag{5.14}$$

where δ_{ij} is the Kronecker delta. Throughout the study, the covariance Q_i is assumed to be constant, namely, $Q_i = Q$ for all i. Furthermore, Q_i is set to be a 3x3 diagonal matrix whose element is σ_{snc}^2. We note that the covariance Q_i is different from the process noise power spectral density $\mathcal{Q}(t)$ for a random process $\boldsymbol{u}(t)$. If $\boldsymbol{u}(t)$ is a random process, its covariance is represented by $E[\boldsymbol{u}(t)\boldsymbol{u}(\tau)] = \mathcal{Q}(t)\delta(t - \tau)$ where $\delta(t)$ is the Dirac delta. Unlike $\mathcal{Q}(t)$ whose dimension is $(\text{length})^2(\text{time})^{-3}$, the dimension of Q_i is acceleration squared $(\text{length})^2(\text{time})^{-4}$. We set $\sigma_{\text{snc}} = 10^{-12}$ km/s^2 for the covariance study and $\sigma_{\text{snc}} = 10^{-11}$ km/s^2 for the end-to-end simulation presented later. In the end-to-end simulation, the noise is chosen to be roughly 10 percent of the SRP acceleration, while the 10 times smaller value is used in the covariance study to investigate the performance in an ideal situation. The covariance matrix is propagated by

$$P(t_k) = \Phi(t_k, t_{k-1}) \cdot P(t_{k-1}) \cdot \Phi(t_k, t_{k-1})^T + \Gamma(t_k, t_{k-1}) \cdot Q \cdot \Gamma^T(t_k, t_{k-1}) \tag{5.15}$$

where

$$\Gamma(t_k, t_{k-1}) = \int_{t_{k-1}}^{t_k} \Phi(t_k, \tau) \cdot B d\tau \simeq \Delta t \begin{bmatrix} \frac{\Delta t}{2} I_{3\text{x}3} \\ I_{3\text{x}3} \\ 0_{(n-6)\text{x}3} \end{bmatrix}. \tag{5.16}$$

is the process noise transition matrix. Assuming the time step is small, the quadrature is approximated in Eq. (5.16). The details of the simplified process noise transition matrix are given in Appendix E. As white noise is assumed, the process noise does not affect the propagation of the mean.

The state vector is defined as

$$\boldsymbol{X} = [\boldsymbol{r}, \, \dot{\boldsymbol{r}}, \, C_{\text{SRP}}, \, R, \, \mu, \, \boldsymbol{\Delta V}_i, \, \tau_i] \quad \forall i \tag{5.17}$$

where τ_i is the time of the i-th maneuver. In the covariance analysis, all of the planned maneuvers are included in the state for a given trajectory.

5.3   Covariance Analysis

The results of the covariance analysis are presented in this section. The covariance analysis uses the simple augmented Hill three-body dynamics defined in Eq. (2.11). The purpose of the covariance analysis is to investigate the information in the onboard measurements. Therefore, the reference state and dynamics used in the filter are made to be identical to the simulated truth. The values of the true parameters used in the covariance study are listed in Table 5.2. The covariance study uses simulated noisy measurements. Two distinct phases are studied. The first phase corresponds to a near rectilinear motion along the x-axis for the asteroid approach. The second phase corresponds to a close hovering operation. After looking at these different phases in detail, a comprehensive covariance study is performed for a trajectory that encompasses both phases, identifying expected navigation performance for a wide range of measurement noise levels.

Table 5.2: Physical parameters used in the simple covariance analysis as true values.

Symbol	Unit	Description	Value
R	m	Meand radius of the asteroid	246
μ	m^3/s^2	GM of the asteroid	5.2
ρ	-	Surface reflectivity	0.4
M_{SC}/A_{SC}	kg/m^2	Mass-to-area ratio	63
A	AU	SMA of the asteroid's orbit	1.126

5.3.1   Approach Trajectory

The spacecraft is assumed to approach the asteroid from the negative x direction. Because of the Coriolis force, the spacecraft moves away from the x-axis. Thus, a $\boldsymbol{\Delta V}$ in the positive y direction is required to constrain the path around the x-axis. Also, a maneuver is necessary to properly control the approach velocity. While such a maneuver can be designed by the guidance algorithm discussed earlier, for the covariance analysis, arbitrarily defined deterministic maneuvers are used.

The impact of the maneuver can be assessed by following simple analytical calculations. If a spacecraft is placed on the x-axis with distance d, and a ΔV is applied as shown in Figure 5.3, the

angle θ grows with time.

$$\dot{\theta} = \Delta V/d \iff d = \Delta V/\dot{\theta} \tag{5.18}$$

Thus the variation in the distance can be computed as

$$\delta d = \delta \Delta V/\dot{\theta} - \Delta V \delta\dot{\theta}/\dot{\theta}^2 \tag{5.19}$$

Using Eq. (5.18), along with the assumption that $\delta\Delta V$ and $\delta\dot{\theta}$ are uncorrelated, we get

$$(\sigma_d/d)^2 = (\sigma_{\Delta V}/\Delta V)^2 + (\sigma_{\dot{\theta}}/\dot{\theta})^2. \tag{5.20}$$

If we assume two angle measurements are taken over an interval of Δt, such that $\dot{\theta} = (\theta_1 - \theta_2)/\Delta t$, the variance of $\dot{\theta}$ is computed as $\sigma_{\dot{\theta}}^2 = 2\sigma_\theta^2/\Delta t^2$, again assuming that the two angle measurements are uncorrelated. Finally, the error in the distance can be related to the ΔV and angle error as follows.

$$(\sigma_d/d)^2 = (\sigma_{\Delta V}/\Delta V)^2 + 2[\sigma_\theta d/(\Delta V \Delta t)]^2 \tag{5.21}$$

which indicates that a larger ΔV applied at closer range results in smaller uncertainty in the spacecraft's distance.

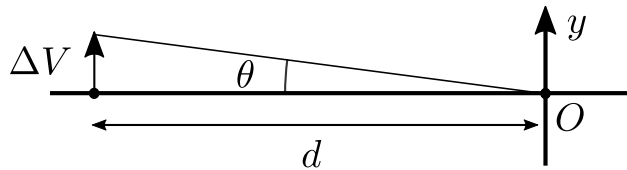Figure 5.3: Simple schematic of approach trajectory.

To further study the information in the optical and ΔV measurements, state uncertainty is computed numerically along example trajectories. The initial position and velocity are set to

$$\boldsymbol{r}(t_0) = [-32, \ -0.1, \ -0.1] \ (\text{km}) \tag{5.22}$$

$$\boldsymbol{v}(t_0) = [10^{-1}, \ -10^{-1}, \ 10^{-2}] \ (\text{mm/s}) \tag{5.23}$$

Table 5.3: Initial uncertainties of the approach trajectory

Type	$\sigma_{rx,ry,rz}$	$\sigma_{vx,vy,vz}$	$\sigma_{C_{\mathrm{SRP}}}$	σ_R
Value	10	0.1	0.5	500
Unit	km	m/s	–	m

There is no strong reason for choosing the specific values; the spacecraft is located about 30 km away from the asteroid with small random position and velocity components. The focus of this analysis is on the phase when the spacecraft is far away from the asteroid, resulting in the dynamics governed by SRP and solar gravity. For the sake of simplicity, the asteroid's gravity is ignored for this analysis, using the Hill three-body equations with $\mu = 0$. The initial uncertainty is defined in Table 5.3. The a priori uncertainties are based on the assumptions made in [18] except for the position accuracy, which is 10 times smaller than their assumption. The spacecraft is placed relatively close to the asteroid at the beginning of the current simulation, which assumes the initial navigation has been partially performed already, allowing the smaller position error. The same assumption is made in the end-to-end simulation. First, the state is propagated for 200 hours, only with optical measurements taken every two hours. We note that we are assuming a conservative measurement frequency, and the spacecraft should be able to make more frequent optical measurements, which allows us to suppress the measurement noise. Figure 5.4 shows the simulated trajectory. The true trajectory and asteroid are plotted along with their shadows. Blue dots indicate the locations of the measurement updates. This case is referred to as 1-A.

The time history of the standard deviation is shown in Fig. 5.5. Different lines correspond to different values of IFOV. The FOV is assumed to be 6 degrees, and the number of pixels is varied among $N_p = 10^2$, 10^3, and 10^4. The result shows that having a higher resolution only helps in reducing uncertainty quickly. The smaller IFOV hardly improves the final uncertainty. The angle measurements contain rich information about y and z position in the scenario considered here, especially when their values are close to zero. Thus the covariance associated with the y and z components of the position and velocity is about 10 to 100 times smaller than those of x components. As for the y components, the dynamics are coupled with the x components. Therefore,
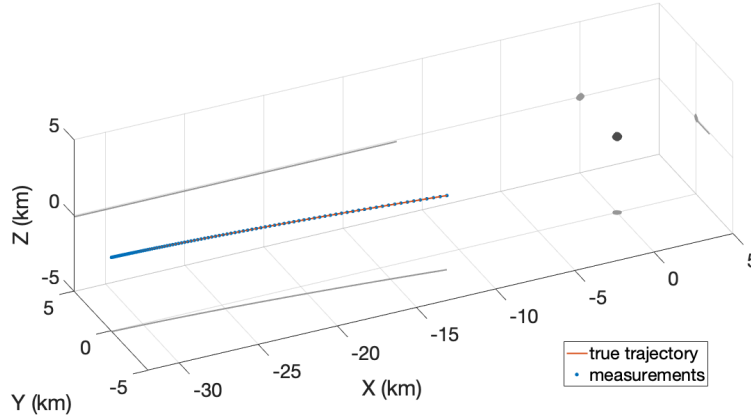
Figure 5.4: Trajectory used in the covariance analysis (case 1-A).

the covariance becomes larger as the spacecraft moves away from $y = 0$. The SRP coefficient can be estimated only up to $\sigma_{C_{\text{SRP}}} = 0.26$. The inclusion of angular size measurements does not improve the navigation solution. Rather, the measurements can be used to estimate the size of the asteroid. The final error in the radius is about 26 percent. The uncertainty of the asteroid's size at $t = 0$ in the simulation result is much smaller than the initial value listed in Table 5.3 because the measurement at $t = 0$ can determine the asteroid's size more accurately than the a priori baseline, given the assumed initial range uncertainty and measurement noise level.

If a better estimate of the SRP coefficient is available, the final covariance of the position and velocity becomes much smaller. Figure 5.6 shows the errors of the final position and velocity as functions of a priori SRP uncertainty. Again, each line corresponds to a different IFOV value. When $\sigma_{C_{\text{SRP}}}$ is large, change in the IFOV does not have any effect. However, as $\sigma_{C_{\text{SRP}}}$ becomes smaller, having a higher resolution becomes more advantageous. The estimate of the target's radius improves as well. The error in the radius is about 1.2 percent if $\sigma_{C_{\text{SRP}}} = 0.01$ and IFOV $= 6°/10^3$. In this case, SRP is acting as a "known" thrust and can help break the scale invariance.

As a next step, we investigate the impact of applying and measuring a maneuver. Two different scenarios are considered. In case 1-B, a ΔV of 10 mm/s is applied in the y-direction at $t \simeq 150$ hours. In case 1-C, a ΔV of 5 mm/s is applied at $t \simeq 100$ hours. Figure 5.7 shows these trajectories. IFOV is fixed to $6°/1000$. The time history of covariance for cases 1-B and
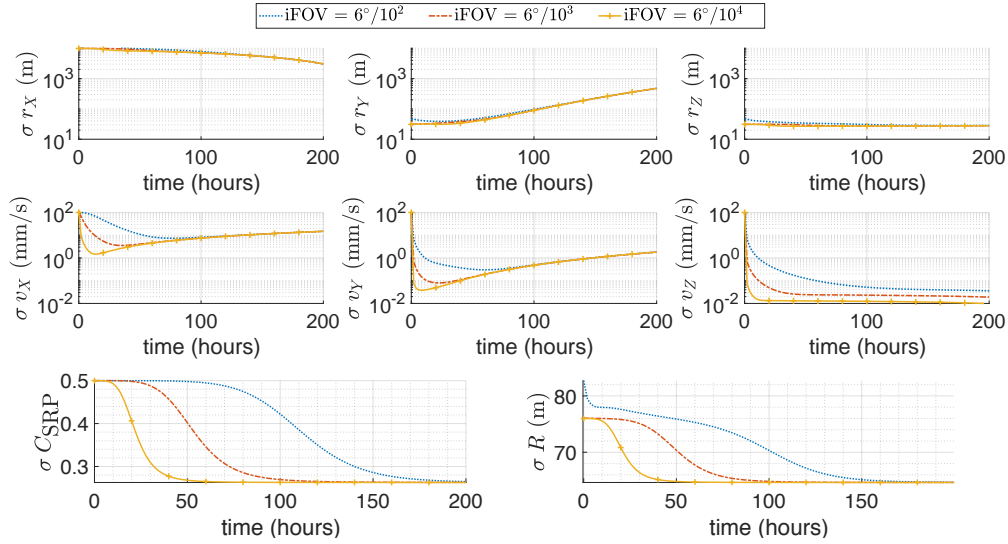
Figure 5.5: Time history of estimated standard deviation (case 1-A).

1-C are shown in Figure 5.8. The dashed and dotted lines correspond to cases 1-B and 1-C, respectively. Two noise levels are considered: $\sigma_{\Delta V} = 10^{-1}$ mm/s (shown as lines with circles) and $\sigma_{\Delta V} = 10^{-3}$ mm/s (shown as lines with plus marks). The result for case 1-A is plotted as a solid line as well. In both cases 1-B and 1-C, the covariance decreases drastically after a maneuver is applied. The resulting SRP error also decreases and is on the order of 10^{-2}. Therefore, even if we have poor prior information about the SRP coefficient, applying and measuring a maneuver can improve the navigation solution. Having 100 times more accurate accelerometers does not result in final uncertainties that are 100 times smaller at the given level of the optical measurement noises. It is confirmed that the baseline assumption of $\sigma_{\Delta V \mathrm{meas}} = 10^{-1}$ mm/s works fine. Another point to note is that, as the simple analytical computation predicts, case 1-B, which has larger ΔV when the probe is closer to the asteroid than case 1-C, results in smaller final uncertainty. Assuming that the velocity change is observed over $\Delta t = 10$ hours with $\sigma_{\Delta V \mathrm{meas}} = 0.1$ mm/s, the distance uncertainty predicted by Eq. (5.21) is $\sigma_d \simeq 280$ m for case 1-B and $\sigma_d \simeq 800$ m for case 1-C. The analytical estimates more or less agree with the numerical results.
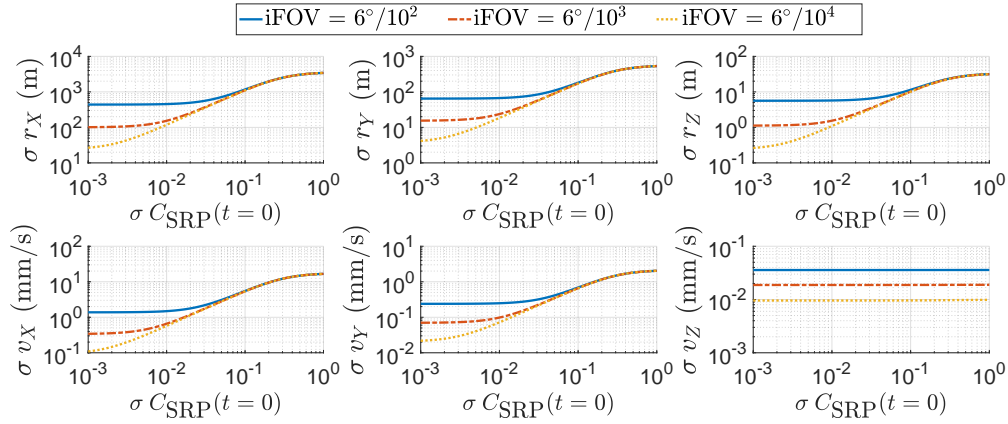
Figure 5.6: Final errors of position and velocity against initial SRP error (case 1-A).

5.3.2   Hovering Trajectory

Numerical covariance analyses with simplified dynamical models are performed for the close hovering trajectories as well. The main focus in this phase is to study the information on the asteroid's mass in the measurement data. Therefore, the augmented Hill three-body dynamics with non-zero μ are used. Two scenarios are considered. In case 2-A, a ΔV is applied every time the spacecraft passes through $x = -4.5$ km such that the x component of the velocity changes its sign, reflecting the motion at the surface. In case 2-B, the same control strategy is adopted except that the altitude at which the maneuvers occur becomes smaller every time a maneuver happens. The maneuvers are applied at $x = -4.5, -3.5, -2.5,$ and -1.5 km. The second case is developed to study the relative advantage of getting closer to the asteroid for mass parameter estimation. Figure 5.9 shows the trajectories for the two cases. In both cases, the initial state is defined as follows

$$\boldsymbol{r}(t_0) = [-6.5, \ -0.2, \ -0.1] \ (\text{km}) \tag{5.24}$$

$$\boldsymbol{v}(t_0) = [10^{-1}, \ -10^{-1}, \ 10^{-2}] \ (\text{mm/s}) \tag{5.25}$$

and the time of flight is 400 hours. The initial uncertainties are defined in Table 5.4. Except for the mass parameter, the initial uncertainties in the close hovering analysis have the same orders of magnitude as the final uncertainties in the approach trajectory with a maneuver. The measurement errors are computed with IFOV $= 30°/1000$.
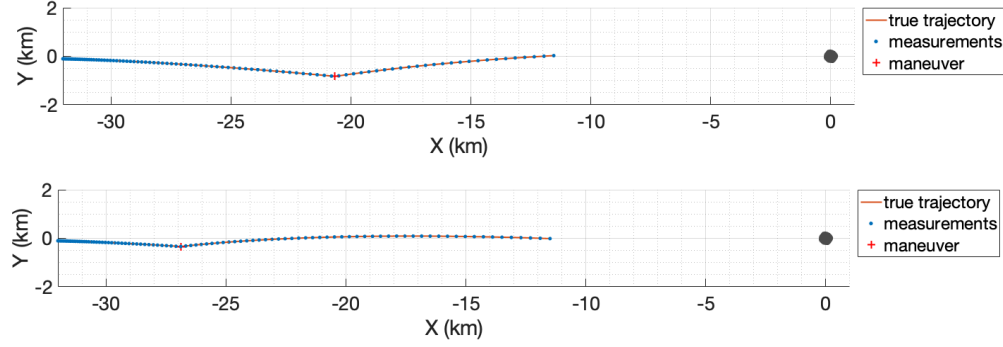
Figure 5.7: Trajectory for covariance analysis. Case 1-B (top) and case 1-C (bottom).

The time histories of standard deviation for position and velocity in cases 2-A and 2-B are shown in Figure 5.10. The plots on the top are for case 2-A and on the bottom for case 2-B. Dashed vertical lines indicate the times when maneuvers occur. In each plot, four different lines are drawn. The dotted lines show the result where only the angle measurements are available. On the other hand, the solid lines with dots correspond to a case where only the angular size measurements are available. The uncertainty in ΔV is 10^{-3} mm/s in both cases. The dashed lines correspond to a scenario with complete optical measurements and $\sigma_{\Delta V} = 10^{-3}$ mm/s. The solid lines show the result for the nominal scenario with complete optical measurements and $\sigma_{\Delta V} = 0.1$ mm/s. The time history of parameter uncertainty is presented in Figure 5.11 in the same way.

Comparing the results with different measurement types, it is clear that both angle and angular size measurements work together to refine the estimates. In the angular size only case, the uncertainty of the y and z components of the position and velocity are much larger than the uncertainty of the x component. The results look reasonable because the directional measurements help determine y and z position with the given geometry. The estimate of the SRP coefficient has larger uncertainty compared to the other cases. On the contrary, when only angular location mea-

Table 5.4: Initial uncertainty for close hovering trajectory

Type	σ_{rx}	$\sigma_{ry,rz}$	σ_{vx}	$\sigma_{vy,vz}$	$\sigma_{C_{\mathrm{SRP}}}$	σ_R	σ_μ
Value	5×10^{-1}	5×10^{-3}	5×10^{-3}	2×10^{-4}	5×10^{-2}	20	10^4
Unit	km	km	m/s	m/s	$-$	m	m^3/s^2
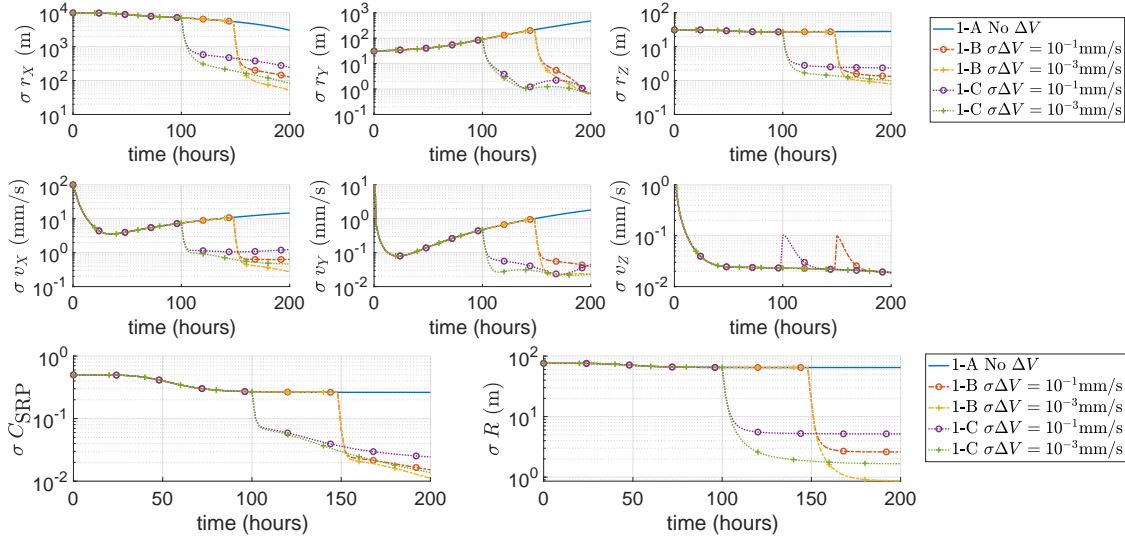
Figure 5.8: Time history of covariance (cases 1-A to 1-C).

surements are available, the uncertainty in the x component of the position and velocity component is larger. While the SRP estimate is better than the angular size only case, the estimate of μ is poorer. To precisely determine μ, the distance from the asteroid must be known well. On the other hand, SRP works uniformly, and measuring drift in y direction caused by SRP seems to lead to a better estimate of C_{SRP}. The best navigation result is obtained when both types of measurements are available.

Another observation to make is the benefit of lowering the altitude. From Figure 5.11, it is confirmed that the estimates of the parameters in case 2-B are better than that in case 2-A. The final uncertainties of the SRP coefficient, radius, and gravitational parameter in case 2-B are $\sigma_{C_{\mathrm{SRP}}} = 1.09 \times 10^{-2}$, $\sigma_R = 3.54 \times 10^{-1}$ m, and $\sigma_\mu = 2.46 \times 10^{-2}$ m^3/s^2 respectively. The SRP estimate in case 2-B is two times more accurate than in case 2-A, and the uncertainties of R and μ are four times smaller.

Even if the error of the ΔV measured by the accelerometers is smaller than 10^{-3} mm/s, it does not improve the navigation solution. The limiting factor here is IFOV. If IFOV is 5 times smaller than the adopted value of $30°/10^3$, the resulting error in μ in case 2-B is $\sigma_\mu = 6.36 \times 10^{-3}$ m^3/s^2 and if IFOV is 10 times smaller than the nominal, the error is $\sigma_\mu = 3.73 \times 10^{-3}$ m^3/s^2. However,
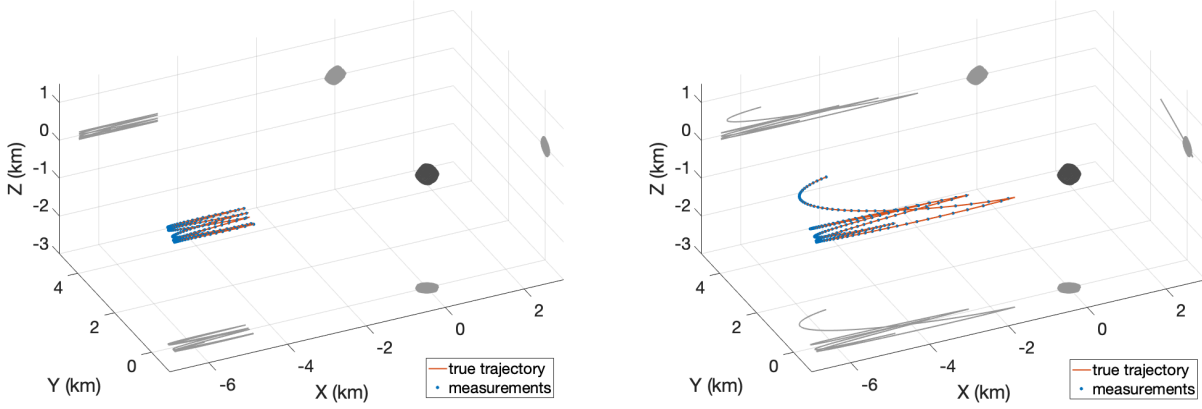
Figure 5.9: Trajectory for covariance analysis. Case 2-A (left) and case 2-B (right).

this tacitly assumes the shape model is also known more precisely.

5.3.3   Comprehensive Measurement Noise Study

The analyses presented so far illustrate how the state uncertainties evolve over time for a given set of measurements in detail. Only specific combinations of measurement types and noise levels are studied there. While such analyses are helpful for understanding the behavior of the navigation system, they do not provide a global picture. A comprehensive study is performed to understand the capabilities of the proposed navigation strategy for a wide range of measurement noise levels. This study uses a trajectory that incorporates both the approach and hovering phases studied above, as shown in Fig 5.12. The initial part of the trajectory is the same as the trajectory from case 1-B in the earlier covariance analysis shown in Fig. 5.7. The same initial condition and initial uncertainties are used. The trajectory is propagated with the augmented Hill three-body dynamics equations in Eq. (2.11) with the non-zero mass parameter. Once the spacecraft reaches $x = -5$ km, it performs hovering control at that distance. A total of 10 hovering maneuvers are applied. The maneuvers occur approximately every two days.

Figure 5.13 shows the state uncertainties at the end of the trajectory for a range of IFOV and $\sigma_{\Delta V}$ values. The final uncertainties for x-, y-, and z-components of the position, SRP coefficient, radius, and mass parameter are shown. The uncertainties for R and μ are relative to
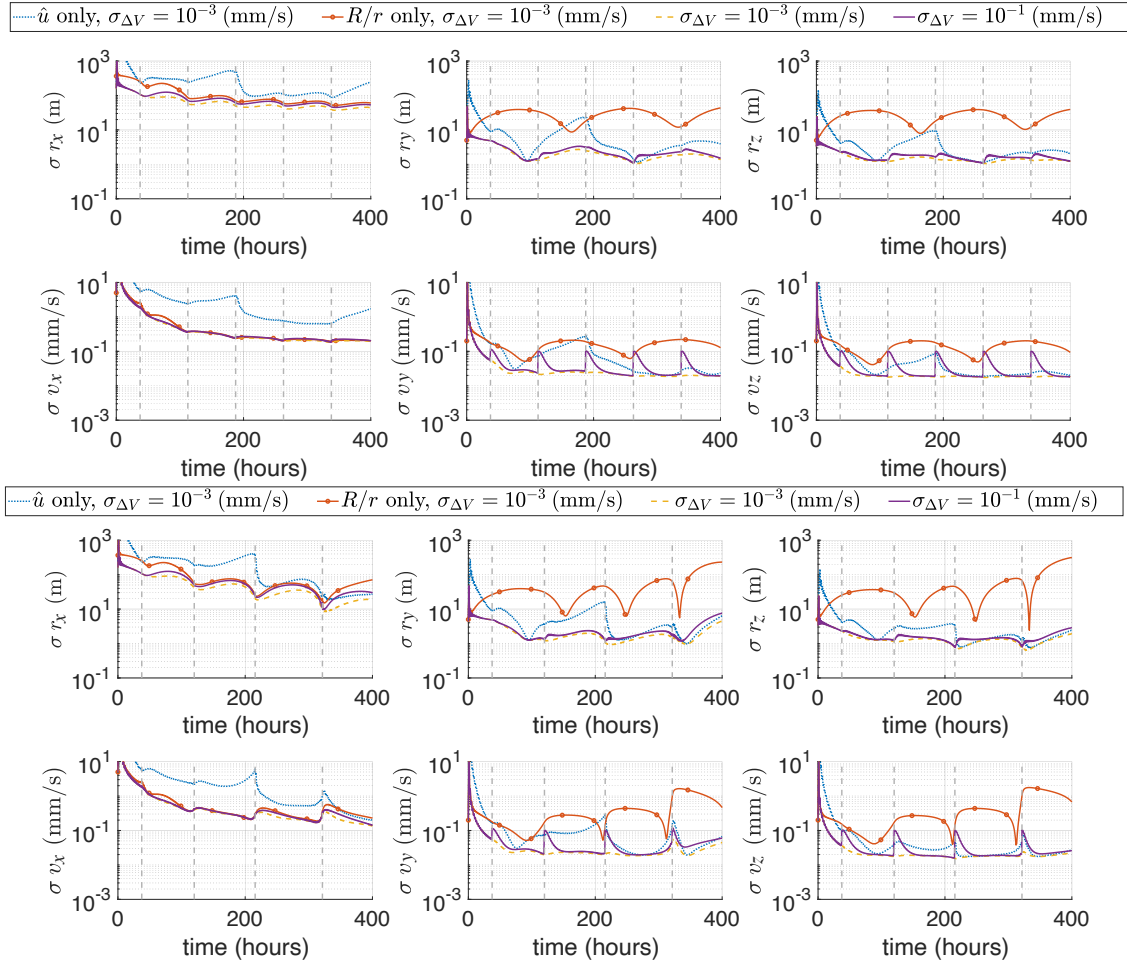
Figure 5.10: Time history of position and velocity errors. Case 2-A (top) and case 2-B (bottom).
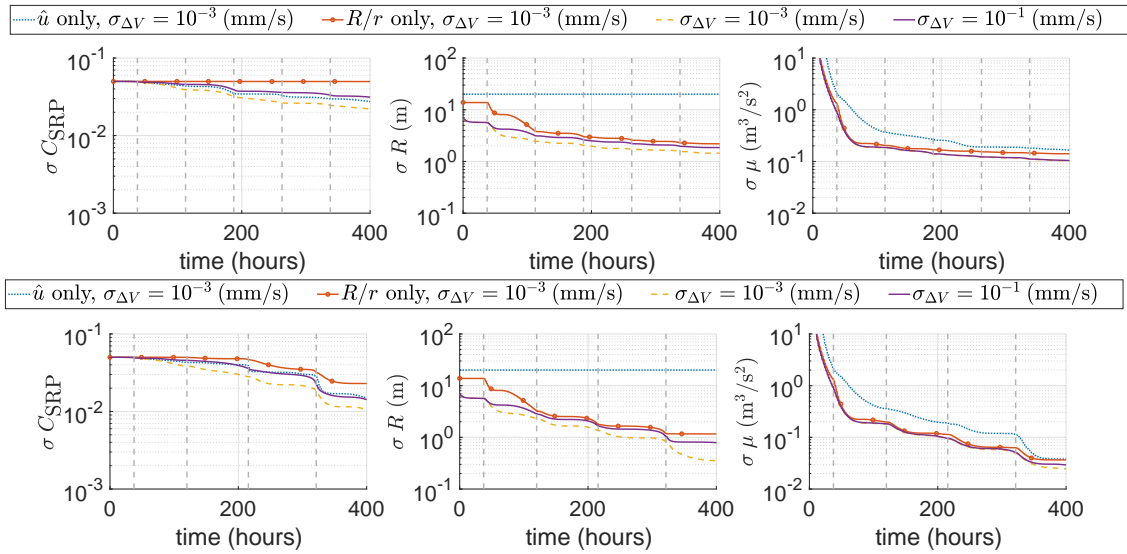
Figure 5.11: Time history of parameter errors. Case 2-A (top) and case 2-B (bottom).
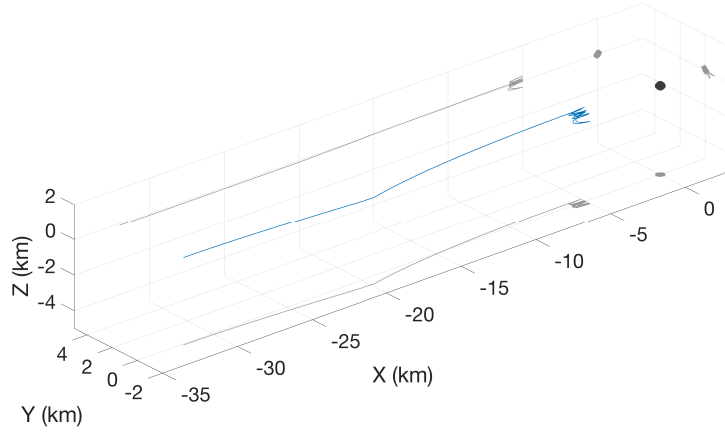
Figure 5.12: A trajectory used in the comprehensive covariance analysis.

the true values. The noise level and measurement accuracies are shown in the log scale with base 10. The plots confirm previous observations for the navigation performance. Namely, the optical measurements have a weaker signal on the range information. We can also observe that when the ΔV measurements are inaccurate, increasing the optical measurements' accuracy does not help reduce the state uncertainties. Similarly, if the optical measurements' accuracy is poor, the precise measurements of ΔVs do not result in accurate state estimation. The plots could be a useful tool in understanding expected state uncertainties for a given set of measurement noise levels.

Figures 5.14 and 5.15 show the same final uncertainty plots when only the directional measurement ($\boldsymbol{Y}_1$) or angular size measurement (Y_2) is available. When only the directional measurements are available, the final state uncertainties become significantly larger compared to the case with both $\boldsymbol{Y}_1$ and Y_2. Also, the size of the asteroid cannot be estimated in such a case. The navigation performance does not seem to degrade as much when only the angular size measurements are available. However, as expected, the measurement accuracy for y- and z-components of the position are poor. As for the SRP estimation accuracy, the directional measurements outperform the angular size measurement except when the measurement noise is minimal.
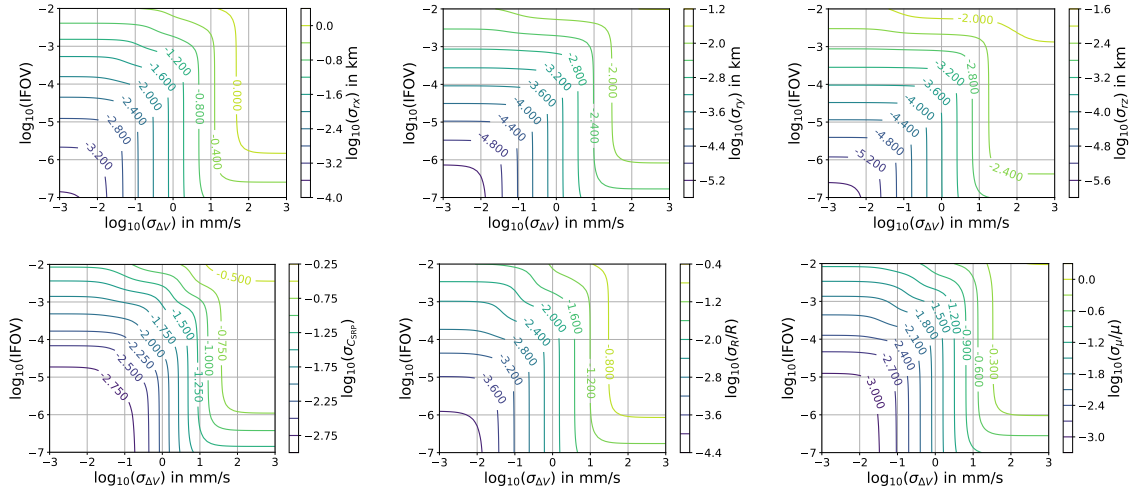
Figure 5.13: Final uncertainty for the trajectory that encompasses both approach and hovering phases for the comprehensive covariance analysis using both optical measurements.
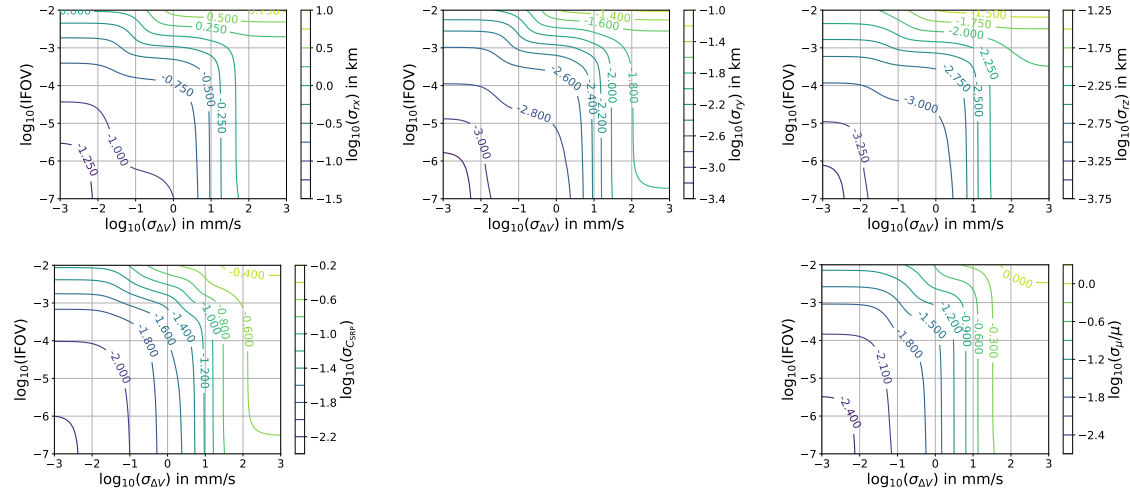
Figure 5.14: Final uncertainty for the trajectory that encompasses both approach and hovering phases for the comprehensive covariance analysis using only the directional measurements.
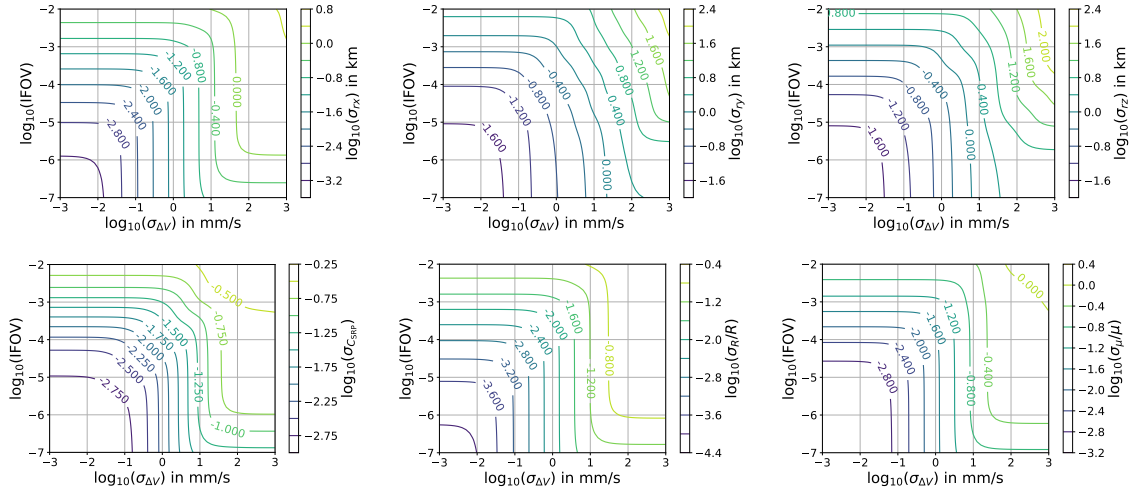
Figure 5.15: Final uncertainty for the trajectory that encompasses both approach and hovering phases for the comprehensive covariance analysis using only the angular size measurements.

5.4   Conclusions

This chapter presents details of the covariance analysis for a spacecraft's navigation relative to an asteroid built around hovering trajectories. It is assumed that onboard optical cameras provide angle and relative size measurements. Two distinct phases are studied in detail. In the first phase, where the spacecraft approaches the target along the Sun-asteroid line, the optical measurements alone cannot determine the state well due to the scale invariance. Applying and measuring a $\boldsymbol{\Delta V}$ can significantly improve the navigation results. We also observe that a small a priori uncertainty of SRP allows the optical measurements to reduce state uncertainty because the SRP acceleration plays the same role as the $\boldsymbol{\Delta V}$ measurements. A simple analytical relationship between the range uncertainty and optical measurement accuracy is derived for the angular direction measurement. The analytical calculation suggests that a larger $\boldsymbol{\Delta V}$ applied at closer distance results in better position estimates. The numerical simulation supports the results. The position error at the end of the arc can be as small as 20 meters. In the second phase, the spacecraft hovers above the asteroid, applying occasional thrusts and measuring its gravitational parameter. In the same way as the initial phase, if we can measure the $\boldsymbol{\Delta V}$ accurately, the maneuvers are helpful in determining μ as well as other parameters. We have further investigated the advantage of getting closer to the asteroid during the hovering phase. In this case, the parameter uncertainty becomes several times smaller than in another scenario simulated where the minimum altitude is kept constant. In the best case, the uncertainty in μ is less than 1 percent. The relationship between the $\boldsymbol{\Delta V}$ uncertainty and accelerometer noise level is discussed. According to the simulation results, it is ideal for the spacecraft to have $\boldsymbol{\Delta V}$ measurement accuracy of $\sigma_{\Delta V} = 10^{-2}$ mm/s or less. This measurement accuracy does not require state-of-the-art accelerometers used in CHAMP, GRACE, or GOCE missions; however, an off-the-shelf IMU may be insufficient.

Finally, a comprehensive covariance analysis is provided for a trajectory that encompasses the approach and hovering phases, running the filter for a range of measurement noise levels. The results show that both the optical and ΔV measurements need to be accurate to achieve a good

navigation performance. The results of the comprehensive covariance analysis help us identify the expected navigation performance for a given measurement capability of the onboard accelerometer and optical imager.

The results in this chapter serve as a foundation for a more detailed analysis. The asteroid model used in this work is simple. The performance of the navigation system under various errors and biases needs to be studied, which is discussed in the next chapter.

Chapter 6

End-to-End Numerical Simulations

This chapter describes the details of the end-to-end numerical study to test the performance of the autonomous small-body exploration scheme based on onboard navigation and trajectory guidance. The purpose of the study is to test the robustness of the proposed navigation and guidance approach when there are various noises and biases.

The thesis first provides a generic description of the filtering and orbit control strategies implemented in the simulation. Then, the results of the analyses for the rendezvous with a heliocentric asteroid are provided. The study uses the asteroid Bennu as an example target. The analyses for the approach trajectory, the event-driven close hovering trajectories, and the global mapping hovering trajectories based on the RL policy described in Chapter 4 are presented. This chapter also provides end-to-end analyses for the rendezvous with temporarily captured orbiters (TCOs), whose dynamics and the spacecraft's relative motion are described in Chapter 2. The asteroid 2006 RH120 is used as an example target in the TCO rendezvous study.

6.1   Filtering and Orbit Control

This section provides a detailed description of the filtering and orbit control schemes proposed for autonomous exploration. For a spacecraft to autonomously carry out exploration, it needs to make decisions and take appropriate actions sequentially. In this study, the action is either taking optical measurements, solving for the current state and prediction, or performing orbit control. Generally, it is assumed that a high-level mission profile is provided to the spacecraft in advance,

specifying events to trigger maneuvers and parameters to design $\Delta \boldsymbol{V}$s such as target positions and transfer time. This section explains both the overall decision-making process and implementations of navigation and guidance algorithms.

6.1.1 Decision-Making Process

In this study, the spacecraft's position is always defined relative to the rotating frame where the Sun and asteroid are fixed. The typical motion of the spacecraft is as follows. The spacecraft is located at a position on the Sun side of the asteroid and experiences accelerations towards the target because of SRP and the asteroid's gravity. When a certain distance is reached as seen by the asteroid or a predefined event surface is crossed, an impulsive maneuver is performed to push the spacecraft back away from the asteroid or to relocate it to a new position. The spacecraft performs a sequence of such maneuvers to accomplish the characterization and observation of the asteroid. We are assuming that once an asteroid is identified for a mission, the asteroid is at least observed by ground-based telescopes and that the uncertainties of the target body's physical parameters, such as its size, shape, spin period, etc, are small enough to allow us to design the large-scale framework of the mission [18].

The level of autonomy considered in this work is such that a certain scenario of the mission operation is specified by the operators on the ground or by other high-level planning algorithms in advance. Specifically, we assume that a sequence of control commands is predefined, which includes conditions for maneuver triggering and necessary actions taken upon such an event detection. The event detection and subsequent maneuver planning are performed by predicting a future state based on the best knowledge as the spacecraft interacts with the environment. As the maneuver design is based on the estimated states, the process can be seen as feedback control.

As for the spacecraft's action upon an event detection, a typical definition is a transfer to a specified target position in a given transfer time. The spacecraft designs a trajectory that connects the predicted position at an event and a target position based on the best knowledge about its environment at the time of planning. The necessary ΔV for such a transfer is computed by the

TPBVP solution method described in Section 2.3. The number of continuation steps in the end-to-end analysis is set to 20. This means the TPVBP is solved 20 times, increasing the parameter by $p/20$ in each iteration. We note that fine discretization for the continuation may not be necessary if the asteroid's gravitational attraction is relatively weak or the transfer time is short. However, when the gravity is strong or the transfer time is long, one must be careful in choosing the step size to trace a specific family of solutions. Due to its nonlinearity, the algorithm might jump to a solution branch that results in multiple revolutions around the asteroid. If there is enough time before the predicted next maneuver occurs, the spacecraft proceeds to measurement updates with optical images.

The condition for maneuver execution is typically specified as an event surface, which is essentially a plane crossing in position space. There are a few different ways to define an event surface, and care must be taken in its definition so that a subsequent crossing is guaranteed to be defined. Three different definitions of such planes are considered in this study. The simplest definition is a fixed plane

$$S_{\text{fixed}}(\boldsymbol{r}; \hat{\boldsymbol{n}}, \boldsymbol{r}_{\text{ref}}) = \hat{\boldsymbol{n}} \cdot (\boldsymbol{r} - \boldsymbol{r}_{\text{ref}}) = 0 \tag{6.1}$$

which contains a point $\boldsymbol{r}_{\text{ref}}$ and has a normal vector $\hat{\boldsymbol{n}}$. For hovering at a specific location $\boldsymbol{r}_{\text{ref}}$, a plane whose normal is aligned with $\boldsymbol{a}_{\text{acc}}(\boldsymbol{r}_{\text{ref}})$, the local acceleration due to SRP and an asteroid's gravity is used.

$$S_{\text{acc}}(\boldsymbol{r}; \boldsymbol{r}_{\text{ref}}) = \hat{\boldsymbol{a}}_{\text{acc}}(\boldsymbol{r}_{\text{ref}}) \cdot (\boldsymbol{r} - \boldsymbol{r}_{\text{ref}}) = 0 \tag{6.2}$$

For a transfer from $\boldsymbol{r}_a$ to $\boldsymbol{r}_b$, a plane that contains both $\boldsymbol{r}_a$ and $\boldsymbol{r}_b$ is used. The normal of the plane is computed as $\arg\max_{\hat{\boldsymbol{n}}}[\hat{\boldsymbol{a}}_{\text{acc}}(\boldsymbol{r}_a) \cdot \hat{\boldsymbol{n}}]$ under the constraints $\hat{\boldsymbol{n}} \cdot (\boldsymbol{r}_a - \boldsymbol{r}_b) = 0$ and $|\hat{\boldsymbol{n}}| = 1$. Thus,

$$S_{\text{transfer}}(\boldsymbol{r}; \boldsymbol{r}_a, \boldsymbol{r}_b) = \hat{\boldsymbol{a}}_{\text{acc}}(\boldsymbol{r}_a) \cdot \left(I - \frac{(\boldsymbol{r}_a - \boldsymbol{r}_b)(\boldsymbol{r}_a - \boldsymbol{r}_b)}{|\boldsymbol{r}_a - \boldsymbol{r}_b|^2} \right) \cdot (\boldsymbol{r} - \boldsymbol{r}_a) = 0 \tag{6.3}$$

Events are detected only when $S(\boldsymbol{r})$ changes from negative to positive. We can also specify a maneuver time directly as an event trigger.

6.1.2 Navigation

The spacecraft nominally takes an optical measurement at a given interval Δt, which is set to 2 hours in this study. As noted earlier, in an actual mission, the spacecraft should be able to make more optical observations to suppress the measurement noise. In this thesis, we are studying the performance of the combined navigation and guidance systems with conservative measurement frequency. The same measurements described in Chapter 5 are used. The measurements are used to update the estimates, and the estimates are then used to predict the next maneuver time. To this end, it is natural to use sequential filters. Because the dynamics and measurements are nonlinear, they are linearized around a reference state, and the deviation from the reference is estimated by a Kalman filter [81]. Primarily, the extended Kalman filter (EKF) is used to update the belief of the state. With EKF, the reference state for linearization is updated discontinuously at every measurement update. Namely, propagating the updated reference state at each measurement step does not result in the same trajectory. A potential issue with the EKF approach is that the filter might be more susceptible to the nonlinearity in the dynamics and measurement models compared to an approach where a consistent reference trajectory for linearization is used to process multiple measurements. To alleviate this issue, another filtering method is implemented.

This second filtering scheme is activated once the next maneuver time is determined, and it processes an arc that contains multiple measurements using a consistent reference trajectory. In the second filtering approach, the estimates at the beginning of the arc are propagated forward in time by regular Kalman filter equations using the same reference trajectory for linearization. Once all of the measurements are used, the information from all the measurements is propagated backward in time by the smoother equations, which gives us the estimate of the state at the beginning of the arc with all measurement information [81]. The reference state for linearization at the beginning can then be updated with the estimate. Because the system is nonlinear, the forward and backward propagations and the subsequent reference update are iterated until the root mean square (RMS) value of the post-fit residuals converges, just as the epoch state estimators or batch estimators do.

In this study, the approach is denoted as the iterative Kalman filter (IKF). If there is no process noise, what the IKF does is identical to processing the arc with the batch estimators. The arc that the IKF processes begins right before the previous maneuver and ends right before the currently planned maneuver. The estimates from the IKF are used to design the $\boldsymbol{\Delta V}$. In other words, the EKF is normally used to detect the next maneuver time, updating the estimates more frequently, and once the maneuver time is determined, the IKF process is turned on to design the $\boldsymbol{\Delta V}$. While the need for the second filter is not evident if the state errors are small, when they are large, we observed that the EKF-only approach could result in a larger bias in the state estimates due to the nonlinearity in the system. Thus, the IKF is used to improve the robustness and accuracy of the navigation process.

The least squares algorithm in Section 5.2 is used to propagate the mean and covariance of the linearized state deviation from the reference trajectory. The state vector is defined in the same way as the simple covariance analysis.

$$\boldsymbol{X} = [\boldsymbol{r},\ \dot{\boldsymbol{r}},\ C_{\mathrm{SRP}},\ R,\ \mu,\ \boldsymbol{\Delta V}_i,\ \tau_i] \tag{6.4}$$

Unlike the covariance analysis, in the end-to-end simulation, the state only includes the last maneuver information. Once a new maneuver $\boldsymbol{\Delta V}_{i+1}$ is performed, the definition of the state vector $\boldsymbol{X}$ is updated such that $\boldsymbol{\Delta V}_i$ and τ_i are replaced by $\boldsymbol{\Delta V}_{i+1}$ and τ_{i+1}.

Figure 6.1 shows how measurements are scheduled before and after a maneuver along with the switch in the definition of a state vector. Assume that at the measurement update with $\boldsymbol{Y}_{j+1}$, EKF predicts that there is a maneuver event at $t = \tau_{j+1}$. As shown in Fig. 6.1, if the current time is close enough to the maneuver time, meaning $\tau_{i+1} - t_{j+1} < \Delta t + 2\delta t$, then the spacecraft prepares for the maneuver, permanently fixing the next maneuver time at $t = \tau_{i+1}$. $\delta t = 30$ min is a small measurement processing margin. Three measurements are scheduled at $t = \tau_{i+1} - 2\delta t$, $t = \tau_{i+1} - \delta t$, and $t = \tau_{i+1} + \delta t$. Once the measurement $\boldsymbol{Y}_{j+2}$ is taken at $t = \tau_{i+1} - 2\delta t$, the IKF process is initiated and the resulting navigation solution is used to design $\boldsymbol{\Delta V}_{i+1}$. The state at $t = \tau_{i+1} - \delta t$ becomes the initial state of the next IKF arc, in which the filter estimates $\boldsymbol{\Delta V}_{i+1}$

and τ_{i+1} instead of $\boldsymbol{\Delta V}_i$ and τ_i. The measurement $\boldsymbol{Y}_{j+3}$ and $\boldsymbol{Y}_{j+4}$ are placed to better constrain the estimate of τ_{i+1} and $\boldsymbol{\Delta V}_{i+1}$ in the next arc. Figure 6.2 summarizes the whole process of the simulation as a flowchart. The left branch corresponds to the normal EKF-based belief update and the right branch, which is entered when the difference between the predicted next maneuver time τ_{next} and current time t is less than $\Delta t + 2\delta t$ describes the navigation process before and after the maneuver.
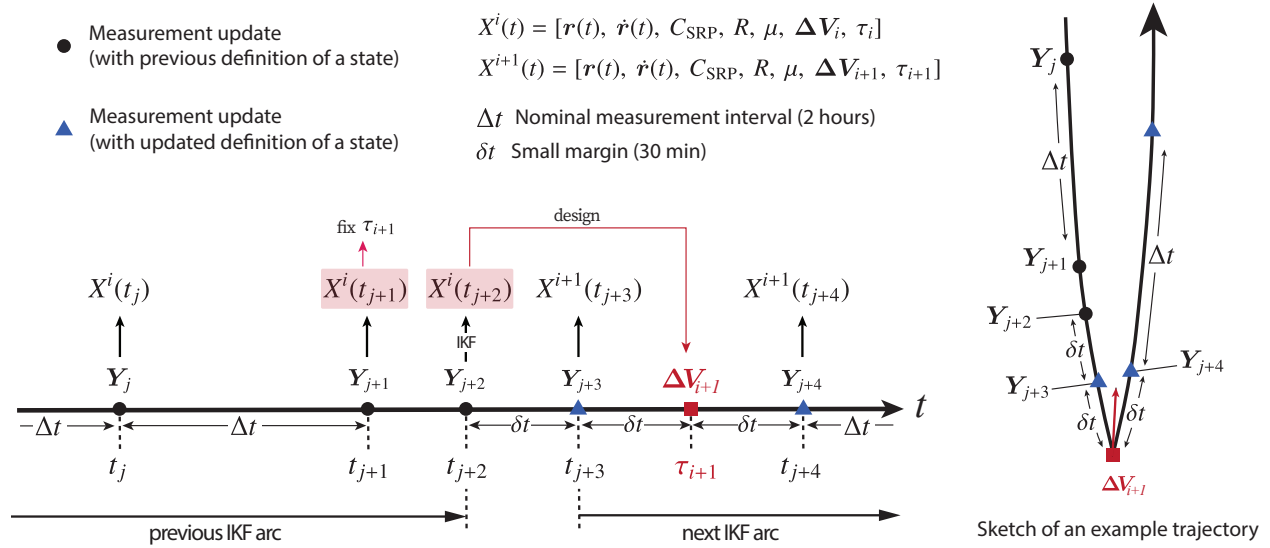
Figure 6.1: Definition of a state vector at each measurement update.

6.2 End-to-End Analysis Results for Heliocentric Asteroid Rendezvous

The thesis first presents the details of the end-to-end numerical analysis for heliocentric asteroid rendezvous scenarios. We first review the dynamical models specific to the end-to-end analysis. The various biases between the truth model and the filter's nominal models are explained. Then the results of the analysis for approach trajectory, close hovering, and RL-based global mapping are presented.
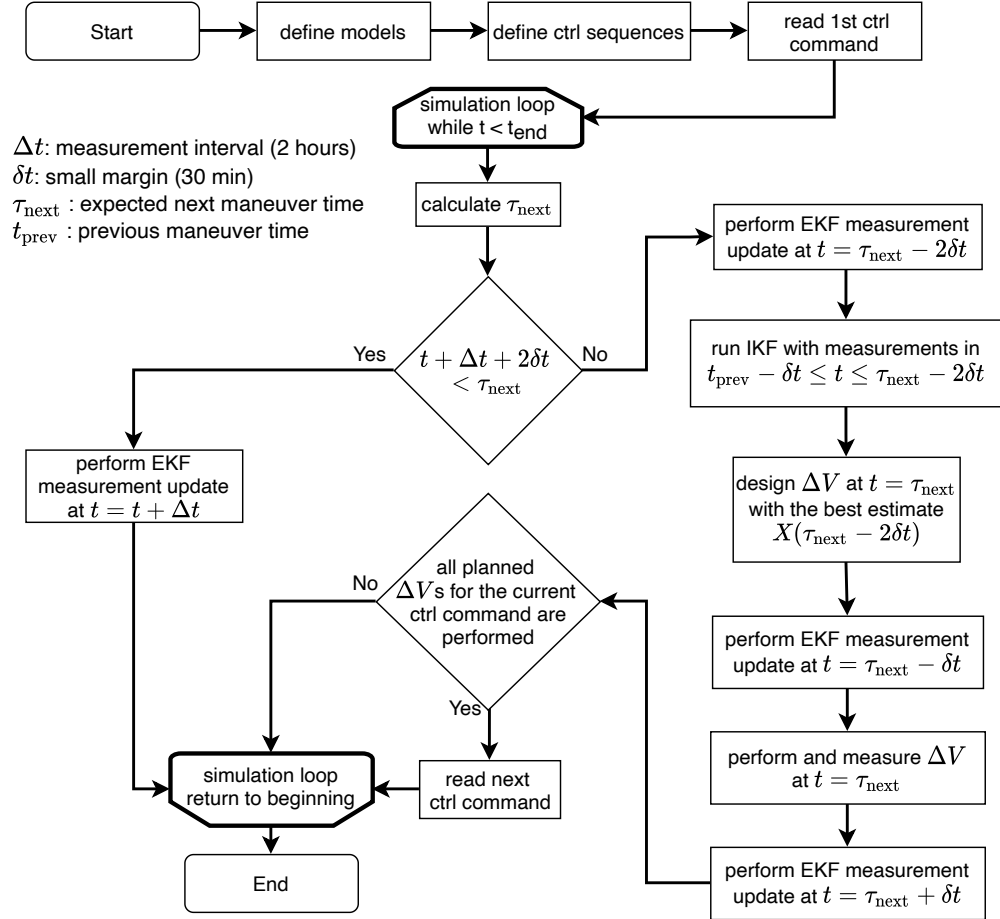
Figure 6.2: Flowchart of the simulation.

6.2.1 Dynamical Models and Biases

The end-to-end study uses the dynamical models described in Chapter 2. However, the models have different fidelities among the truth simulation, filter's nominal belief, and orbit control. The models used in the truth simulation are the most complex. The nominal dynamics used by the navigation filters introduce a few simplifications and thus biases. The models used in the guidance algorithm have the simplest form among all the dynamical models defined in Chapter 2.

The equations of motion for the truth simulation and navigation filter are the elliptic Hill three-body models in Eq. (2.1). The guidance algorithm uses the Hill three-body model in Eq. (2.11) and does not explicitly include the asteroid orbit's ellipticity in its dynamical models. However, in the guidance algorithm, mean motion n and the SRP acceleration are computed using the Sun-asteroid distance at the planning time instead of a semi-major axis, which approximates the elliptic models for a short planning horizon.

As for the gravitational attraction from the target asteroid, the 5x5 spherical harmonics gravity model in Eq. (2.4) is used for the truth simulation. The navigation filter's nominal dynamics and the dynamical models for the TPBPV solver use the simple point mass gravity potential in Eq. (2.5). We intentionally use the simplified dynamical models in the filter and the guidance algorithms so we can study how they perform with model biases.

For the true SRP computation, a hypothetical spacecraft shown in Fig. 6.3 is considered, which has a cubic bus and two solar panels. It is assumed that solar arrays always face the Sun, and thus the acceleration on them is constant. The acceleration for each surface of the bus is computed by the flat-plate model in Eq. (2.10). No self-shadowing is considered. Throughout the thesis, $\rho = 0.4$ is assumed. In this study, total mass-to-area ratio of 63 kg/m^2 is used. For example, for a spacecraft's mass of 50 kg, 300 kg, and 1000 kg, the corresponding total area is about 0.79 m^2, 4.8 m^2, and 16 m^2. The current analysis uses $s = 0.9$ for any of the surface elements. Non-specular reflection is assumed to be Lambertian. The acceleration is set to zero if $(\hat{\boldsymbol{n}}_i \cdot \hat{\boldsymbol{u}}) > 0$. We assume each surface of the box-wing spacecraft model has the same area, including each of the solar panels.
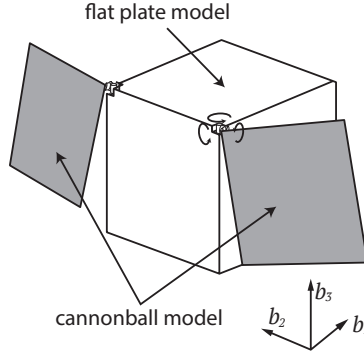
Figure 6.3: Hypothetical spacecraft shape for the true SRP computation.

Thus, for the truth simulation, the cannonball model with the mass-to-area ratio of 42 kg/m^2 and the six-plate model with each plate's mass-to-area ratio of 21 kg/m^2 are used. The spacecraft's attitude is defined such that the first axis of the spacecraft's body frame always points to the asteroid, as illustrated in Fig. 6.4. The attitude of the spacecraft's body frame (S-frame) relative to the asteroid's orbit frame is represented by the DCM: $R_{[SO]} = R_2(\text{elevation}) \cdot R_3(\text{azimuth} - \pi)$. Due to the attitude dependence, the SRP models in the truth and filter dynamics coincide only when the spacecraft is on the x-axis if $s = 1$.

The maneuvers performed by the spacecraft have an execution noise. In general, the study uses the Gates maneuver noise model [82]. With the Gates model, the execution noise is sampled from a spherical Gaussian distribution with zero mean and $\sigma_{\Delta V,\text{crtl}} = \sqrt{\sigma^2_{\Delta V,\text{crtl},c} + (\sigma_{\Delta V,\text{crtl},p}|\mathbf{\Delta V}|)^2}$. In the analyses of the approach trajectory and event-driven hovering trajectory, the maneuver noise is simply sampled from a spherical Gaussian distribution, with $\sigma_{\Delta V,\text{ctrl},p} = 0$. In the analysis with the RL policy, the maneuver execution incorporates a nonzero $\sigma_{\Delta V,\text{ctrl},p}$.

In numerical simulations, model parameters based on OSIRIS-REx measurements of the asteroid (101955) Bennu are nominally used [20, 62, 83, 84]. Table 6.1 shows the pole orientation and asteroid's body parameters [84, 83]. The asteroid's orbit parameters are defined in Table 6.2 [85]. The harmonics coefficients are obtained from [62].

In summary, the truth simulation uses the elliptic Hill three-body model with the 5x5 spherical harmonics asteroid gravity field, flat-plate SRP in Eq. (2.10) and cannonball SRP in Eq. (2.8).
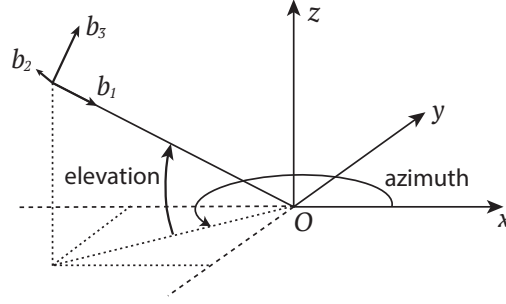
Figure 6.4: Attitude of the spacecraft frame relative to the orbit frame.

Table 6.1: Asteroid's body parameters

Symbol	Description	Value	Unit
μ	gravitational parameter	5.2	m^3/s^2
R	mean radius	246	m
α_p	pole longitude	69	deg
δ_p	pole latitude	-83	deg
–	spin period	4.29	hours

Table 6.2: Asteroid's orbit parameters

Symbol	Description	Value	Unit
A	semimajor axis	1.126	AU
E	eccentricity	0.2	–
–	longitude of ascending node	2	deg
–	inclination	6	deg
–	argument of periapsis	66	deg

The navigation filter uses the elliptic Hill three-body model with a point-mass asteroid gravity and cannonball SRP in Eq. (2.8). The guidance algorithm uses the augmented Hill three-body model defined in Eq. (2.11), assuming a circular asteroid orbit and point mass asteroid gravity.

6.2.2 Approach Phase

First, the study addresses an approach phase leading into the home position hovering at a distance of 10 km from the asteroid's center. The initial position and velocity used by the filter as a nominal state are set to

$$\boldsymbol{r}_0 = [-500, -1000, 0] \text{ (km)}, \qquad \boldsymbol{v}_0 = [0, 2, 0] \text{ (m/s)} \tag{6.5}$$

Although they are not exactly the same, the choice of the initial state is inspired by the Hayabusa-2 approach trajectory, where the spacecraft comes in with a nonzero phase angle (Earth-asteroid-spacecraft) and moves along the sub-Earth line [86]. The nominal parameters and true initial position and velocity are randomly chosen with the standard deviations listed in Table 6.3. The maneuver execution noise is sampled from a fixed spherical Gaussian distribution with $\sigma_{\Delta V \text{ctrl}} = 1$ mm/s, and we assume the accelerometer can reconstruct the net velocity change with an error of $\sigma_{\Delta V \text{meas}} = 0.1$ mm/s. Also, the maneuver timing error of $\sigma_\tau = 60$ sec is introduced. In the approach phase, FOV = 6 deg with $N_p = 1000$ is assumed. The process noise covariance is a diagonal matrix whose elements are σ_{snc}^2 where $\sigma_{\text{snc}} = 10^{-11}$ km/s^2. We note that as described in Section 5.2 and Appendix E, the process noise $\boldsymbol{u}$ in this study is a piecewise constant acceleration sequence, rather than a process, and thus the elements of the process noise covariance has the dimension of acceleration squared.

Table 6.3: Initial uncertainty for approach phase

Type	$\sigma_{rx,ry,yz}$	$\sigma_{vx,vy,vz}$	$\sigma_{C_{\text{SRP}}}$	σ_R	σ_μ
Value	10 (km)	10 (cm/s)	0.5	0.5 (km)	5μ

A simple fixed-time control scheme is implemented, where a total of five $\boldsymbol{\Delta V}$s are performed, one performed every five days with a five-day transfer time. At the i-th maneuver, the guidance

algorithm targets a point on the x-axis such that

$$x_{i+1} = x_i + (x_{\text{goal}} - x_i)/(N - i + 1) \quad (i = 1, 2, \cdots, 5) \tag{6.6}$$

where N = 5 is the number of maneuvers and $x_{\text{goal}} = -10$ km is a target hovering location. Once the spacecraft reaches $x = x_{\text{goal}}$, it transitions to hovering control at the altitude. The interval between the hovering $\boldsymbol{\Delta V}$s is designed to be two days. The simulation terminates at $t = 50$ days, when the spacecraft has performed roughly 10 hovering maneuvers. A simple schematic is shown Fig. 6.5.
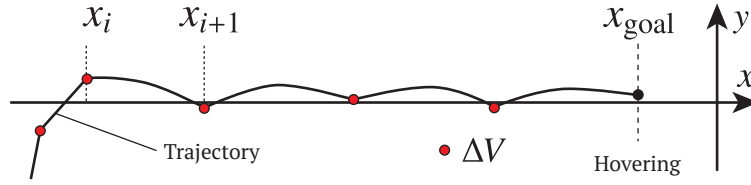
Figure 6.5: Schematic of approach trajectory.

Figure 6.6 shows an example trajectory, and Fig. 6.7 shows the time history of state uncertainties estimated by the filter for the trajectory. The dashed-dotted lines in Fig. 6.7 correspond to the fixed-time $\boldsymbol{\Delta V}$s, and the dashed lines indicate $\boldsymbol{\Delta V}$s for the hovering. The parameter uncertainties are scaled by the true values. We note that $C_{\text{SRP}} = 1$ is used as truth; however, this is only true when the spacecraft is on the x-axis. Otherwise, the cross-section is dependent on position, and the SRP force is not completely aligned with the x-direction. We can confirm that at the first maneuver, the position and velocity uncertainties are reduced significantly. This result demonstrates the efficacy of the ΔV measurements in breaking the scale invariance. Also, due to the scale invariance, errors in the x-component are larger than the y and z components. The mass parameter can be estimated only when the spacecraft comes down to a distance of about 10 km. For this particular case, the mass parameter can eventually be estimated up to a few percent precision.

To test the robustness of the combined implementation of guidance and navigation algorithms, Monte Carlo simulations are performed. Figure 6.8 shows the simulated truth trajectories in the

Distant View   Close-up View
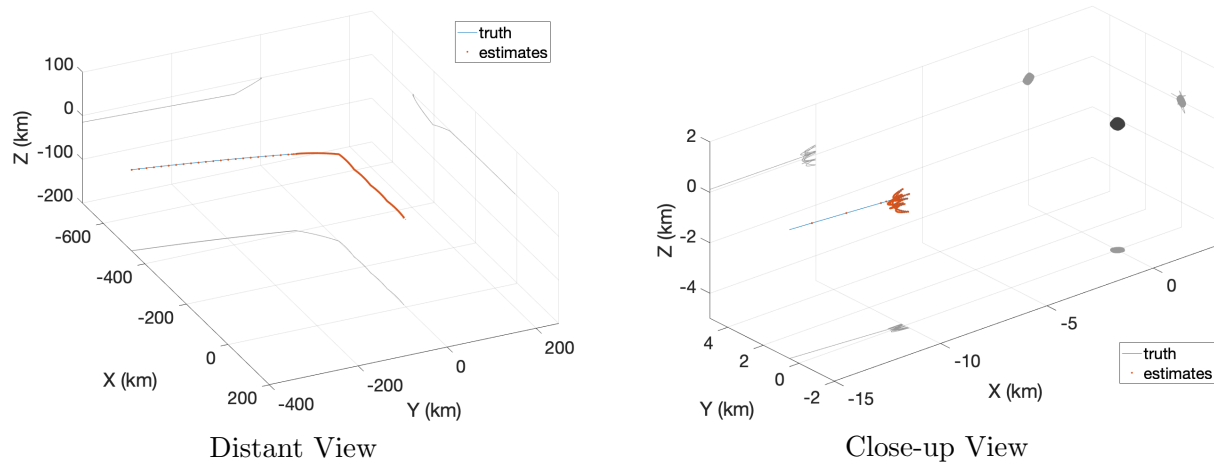
Figure 6.6: Example trajectory for the approach phase.

Position and Velocity Uncertainty

Parameter Uncertainty
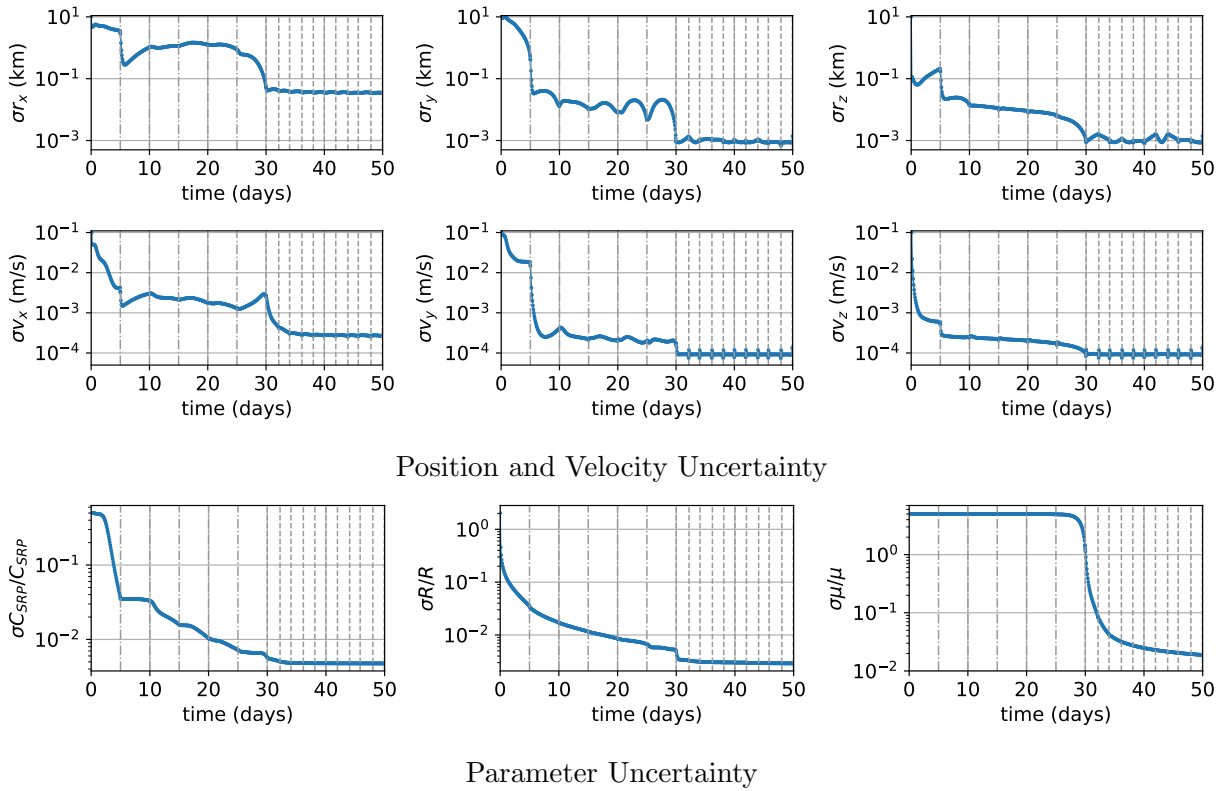
Figure 6.7: Time history of state uncertainty for an example trajectory.

Monte Carlo runs. It is confirmed that the proposed method can contain the trajectory in a reasonably bounded region and that no trajectory fails to transition to the home position hovering. We note that the large dispersion of the trajectories comes from maneuver execution errors rather than navigation errors. Figure 6.9 shows the time history of estimation errors (estimates - true values) of the position and parameters for the 1000 runs. Dashed vertical lines indicate fixed-time maneuvers. The error magnitudes are consistent with the filter's output in the example case shown in Fig. 6.7. The estimation errors of the SRP coefficient have a clear bias toward $C_{\mathrm{SRP}} > 1$ until the spacecraft transitions to the home position hovering at 10 km. The result is reasonable as the cross-section is larger when the spacecraft deviates from the x-axis. During the home position hovering, the position of the spacecraft is more tightly bounded, justifying the small and apparently unbiased errors. The position errors also have a bias, which may be the result of the unmodeled attitude dependence of the SRP force.
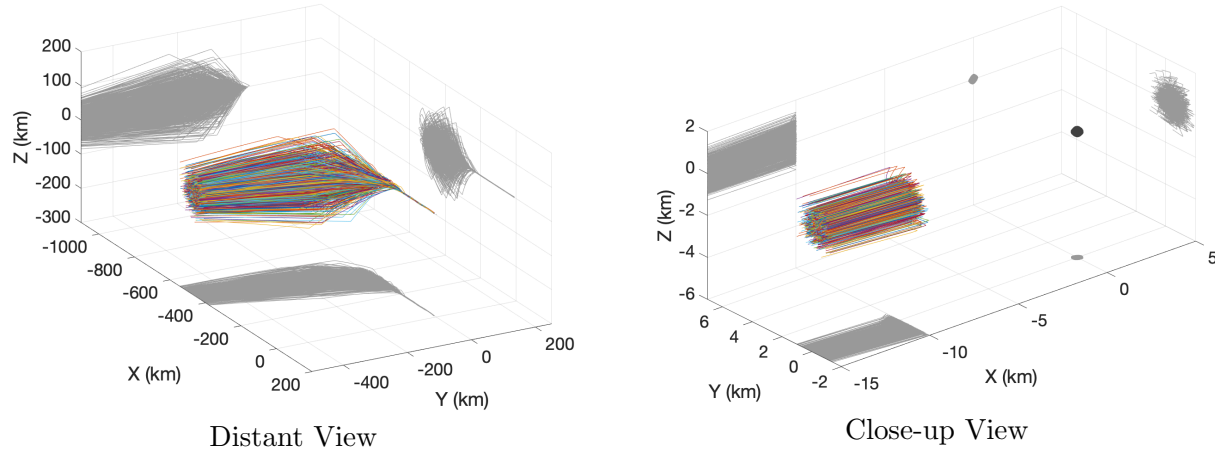
Figure 6.8: Trajectories from 1000 Monte Carlo runs (approach phase).

Another observation is that there are a few cases where the spacecraft misses to detect the surface crossing at $x = 10$ km for the first time it comes down to the surface. The overshoot is caused by the large initial GM (mass parameter) uncertainty. The spacecraft may anticipate that there is enough time before the surface crossing and plan a regular measurement update two hours later when it is, in reality, attracted to the asteroid much more quickly. Depending on the errors in the GM estimation, the spacecraft may have passed the surface already at the measurement update.
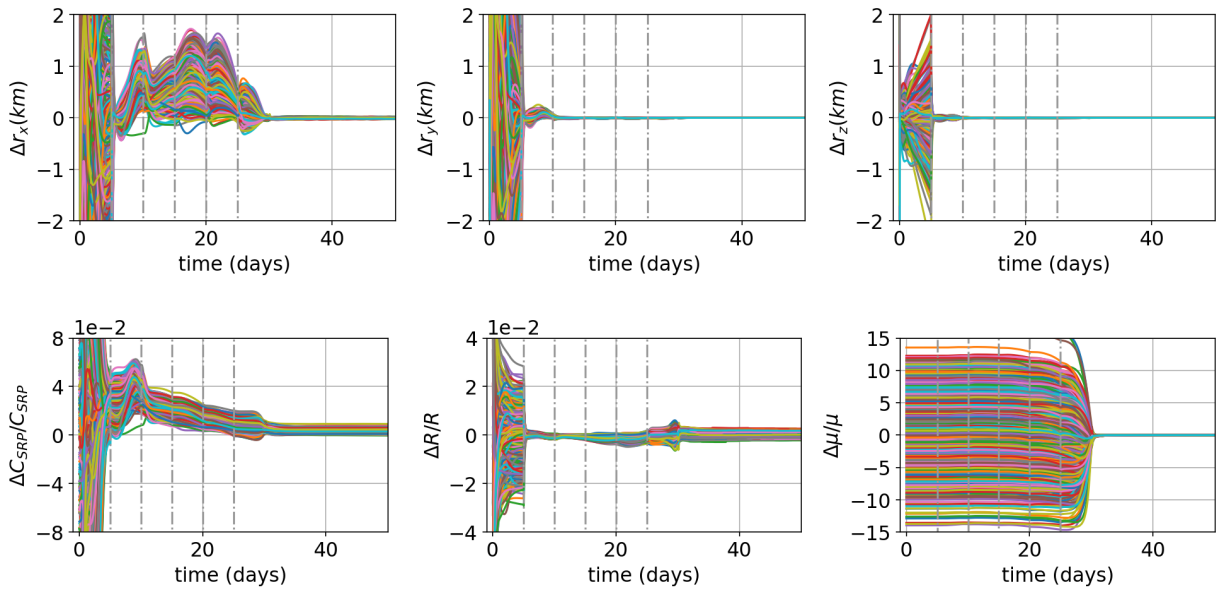
Figure 6.9: Position and parameter errors for the 1000 Monte Carlo runs (approach phase).

The guidance algorithm is designed to immediately plan a maneuver after a measurement update (after 2.5 δt later) if no event is detected. Because the spacecraft can estimate its position up to several dozens of meters even with a large GM error, we confirmed that the contingency maneuver can successfully bring the spacecraft to perform hovering. At this altitude, the measurements have a strong signal of gravitational attraction, which is the cause of the overshoot in the first place; therefore, after a few maneuvers, the GM estimate improves significantly. An alternate option to deal with the overshoot is to use a higher altitude for a home position, where the spacecraft performs hovering.

6.2.3 Event-Driven Close Hovering

As a next step, the same navigation and control algorithms are applied to a mission scenario that includes, gradual descent for GM estimation, transitions between multiple hovering locations, and subsequent terminator orbit insertion. Figure 6.10 shows an example trajectory. The blue line is the simulated truth and the orange dots are position estimates at each measurement update. The simulation of the approach phase ends with the home position hovering. Thus, the final condition for the approach phase can be used as an initial condition for the close-hovering phase. Specifically, the initial position and velocity used by the filter as a nominal state are set to

$$\boldsymbol{r}_0 = [-10.0, 1.44 \times 10^{-1}, -7.64 \times 10^{-2}] \text{ (km)} \tag{6.7}$$

$$\boldsymbol{v}_0 = [-1.08 \times 10^{-2}, -1.55 \times 10^{-3}, -5.39 \times 10^{-5}] \text{ (m/s)} \tag{6.8}$$

The process noise covariance is defined again with $\sigma_{\text{snc}} = 10^{-11}$ km/s^2. True and nominal states are randomly initialized in the same way as the simulations for the approach phase, introducing errors in the true position and velocity and nominal parameters. The initial covariance is given as a diagonal matrix with the values shown in Table 6.4. The initial covariance is slightly inflated from the final covariance of the approach phase. In this phase, IFOV is changed to 60°/1000, assuming the telescopic camera is replaced by a wide-FOV camera. The noise levels of the maneuver execution and measurement are the same as the approach trajectory. Starting from the 10 km home position,

the spacecraft first goes through a series of hovering operations for GM estimation, gradually lowering the altitude. In this phase, the spacecraft performs a 10-day hovering operation at multiple fixed locations, namely, $x = -10, -8, -5$, and -2 km. The interval between the maneuvers for the hovering is designed to be two days, as is the case with any fixed-location hovering in this simulation. After the GM estimation, 30-day hovering at $(r, \phi_o, \lambda_o) = (10 \text{ km}, 120°, 0°)$, $(10 \text{ km}, 120°, -60°)$, and $(10 \text{ km}, 180°, 60°)$ are implemented to test the robustness of the algorithm against the change in acceleration directions. Here, ϕ_o and λ_o are the azimuth and elevation of the position vector relative to the orbit frame. The transfers between different observation geometries are all designed to be 2-day transfers. Finally, the spacecraft performs terminator orbit insertion at its periapsis. When a terminator orbit is targeted, a modified initial condition is used to account for the offset between the mass and orbit centers as detailed in Chapter 3. The semimajor axis of the orbit is chosen to be 1.5 km. Before the orbit insertion, a correction burn is implemented at the surface crossing of $z = 2$ km, followed by a 5-hour free-fall. The correction maneuver is placed to mitigate the position errors caused by the control errors and expanded by the long transfer time. The target terminator orbit is designed onboard using the estimated SRP coefficient and mass parameter. Table 6.5 lists control commands to realize the operation, where r_{TO} is the terminator orbit's periapsis and t_{prev} is the previous maneuver time. The repetition (rep.) indicates how many times the command is used before reading the next command.

Table 6.4: Initial uncertainty for the close-hovering phase

Type	σ_{rx}	$\sigma_{ry,yz}$	σ_{vx}	$\sigma_{vy,vz}$	$\sigma_{C_{\text{SRP}}}$	σ_R	σ_μ
Value	3.16e-2	1e-3	1.41e-2	2e-2	1e-2	7.07e-4	3.85 e-2
Unit	km	km	cm/s	cm/s	–	km	μ

For the GM estimation phase, the conditions of the maneuver triggering are the surface crossings at $x = -10, -8, -5$, and -2 km. For a transfer from a position r_a to another position r_b, the transfer surface $S_{\text{transfer}}(r; r_a, r_b) = 0$ is used to detect the arrival at r_b. For the off x-axis hovering, the spacecraft first checks the crossing with $S_{\text{acc}}(r; r_{\text{target}}) = 0$ where r_{target} is a target hovering location. If no crossing is detected, it uses the transfer surface instead to plan the
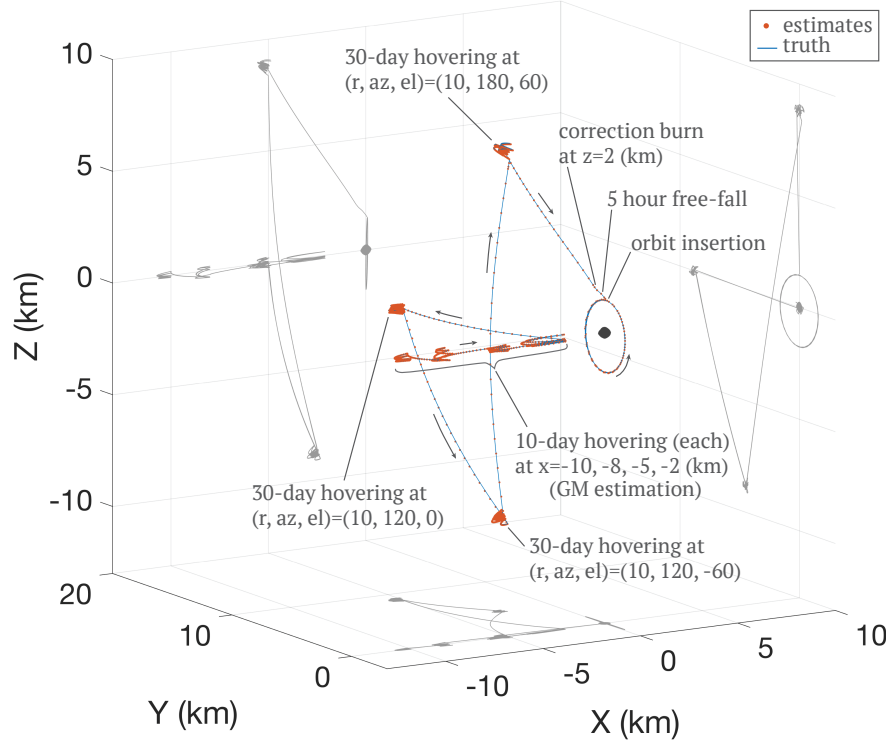
Figure 6.10: Example trajectory for the close-hovering phase.

Table 6.5: Control commands for the event-driven close-hovering phase

#	event conditions	maneuver type	rep.	note
1	$S_{\text{fixed}}(\boldsymbol{r};\ \hat{\boldsymbol{x}}, \boldsymbol{r}_0) = 0$	transfer to $\boldsymbol{r}_0$ with $\Delta T = 2$ days	5	$\boldsymbol{r}_0 = -10\hat{\boldsymbol{x}}$ (km)
2	$S_{\text{fixed}}(\boldsymbol{r};\ \hat{\boldsymbol{x}}, \boldsymbol{r}_0) = 0$	transfer to $\boldsymbol{r}_1$ with $\Delta T = 2$ days	1	$\boldsymbol{r}_1 = -8\hat{\boldsymbol{x}}$ (km)
3	$S_{\text{fixed}}(\boldsymbol{r};\ \hat{\boldsymbol{x}}, \boldsymbol{r}_1) = 0$	transfer to $\boldsymbol{r}_1$ with $\Delta T = 2$ days	5	
4	$S_{\text{fixed}}(\boldsymbol{r};\ \hat{\boldsymbol{x}}, \boldsymbol{r}_1) = 0$	transfer to $\boldsymbol{r}_2$ with $\Delta T = 2$ days	1	$\boldsymbol{r}_2 = -5\hat{\boldsymbol{x}}$ (km)
5	$S_{\text{fixed}}(\boldsymbol{r};\ \hat{\boldsymbol{x}}, \boldsymbol{r}_2) = 0$	transfer to $\boldsymbol{r}_2$ with $\Delta T = 2$ days	5	
6	$S_{\text{fixed}}(\boldsymbol{r};\ \hat{\boldsymbol{x}}, \boldsymbol{r}_2) = 0$	transfer to $\boldsymbol{r}_3$ with $\Delta T = 2$ days	1	$\boldsymbol{r}_3 = -2\hat{\boldsymbol{x}}$ (km)
7	$S_{\text{fixed}}(\boldsymbol{r};\ \hat{\boldsymbol{x}}, \boldsymbol{r}_3) = 0$	transfer to $\boldsymbol{r}_3$ with $\Delta T = 2$ days	5	
8	$S_{\text{fixed}}(\boldsymbol{r};\ \hat{\boldsymbol{x}}, \boldsymbol{r}_3) = 0$	transfer to $\boldsymbol{r}_4$ with $\Delta T = 2$ days	1	$\boldsymbol{r}_4 = [-5.0, 8.7, 0.0]$ (km)
9	$S_{\text{transfer}}(\boldsymbol{r};\ \boldsymbol{r}_3, \boldsymbol{r}_4) = 0$	transfer to $\boldsymbol{r}_4$ with $\Delta T = 2$ days	1	
10	$S_{\text{acc}}(\boldsymbol{r};\ \boldsymbol{r}_4) = 0$	transfer to $\boldsymbol{r}_4$ with $\Delta T = 2$ days	15	
11	$S_{\text{acc}}(\boldsymbol{r};\ \boldsymbol{r}_4) = 0$	transfer to $\boldsymbol{r}_5$ with $\Delta T = 2$ days	1	$\boldsymbol{r}_5 = [-2.5, 4.3, -8.7]$ (km)
12	$S_{\text{transfer}}(\boldsymbol{r};\ \boldsymbol{r}_4, \boldsymbol{r}_5) = 0$	transfer to $\boldsymbol{r}_5$ with $\Delta T = 2$ days	1	
13	$S_{\text{acc}}(\boldsymbol{r};\ \boldsymbol{r}_5) = 0$	transfer to $\boldsymbol{r}_5$ with $\Delta T = 2$ days	15	
14	$S_{\text{acc}}(\boldsymbol{r};\ \boldsymbol{r}_5) = 0$	transfer to $\boldsymbol{r}_6$ with $\Delta T = 2$ days	1	$\boldsymbol{r}_6 = [-5.0, 0.0, 8.7]$ (km)
15	$S_{\text{transfer}}(\boldsymbol{r};\ \boldsymbol{r}_5, \boldsymbol{r}_6) = 0$	transfer to $\boldsymbol{r}_6$ with $\Delta T = 2$ days	1	
16	$S_{\text{acc}}(\boldsymbol{r};\ \boldsymbol{r}_6) = 0$	transfer to $\boldsymbol{r}_6$ with $\Delta T = 2$ days	15	
17	$S_{\text{acc}}(\boldsymbol{r};\ \boldsymbol{r}_6) = 0$	transfer to $\boldsymbol{r}_{\text{TO}}$ with $\Delta T = 2$ days	1	
18	$S_{\text{acc}}(\boldsymbol{r};\ \boldsymbol{r}_7) = 0$	transfer to $\boldsymbol{r}_{\text{TO}}$ with $\Delta T = 5$ hours	1	$\boldsymbol{r}_7 = 2\hat{\boldsymbol{z}}$ (km)
19	$t = t_{\text{prev}} + 5\text{hours}$	terminator orbit insertion	1	

next maneuver. To illustrate the need for the two-factor event definition, consider the operation where the spacecraft transitions from r_3 to r_4 and performs hovering at r_4, i.e., command # 8-10 in Table 6.5. After leaving r_3, a ΔV to target r_4 is applied when the spacecraft crosses $S_{\text{transfer}}(r; r_3, r_4) = 0$ at a location which may not be close to r_4 due to the control errors. The next maneuver is nominally triggered when the crossing with $S_{\text{acc}}(r; r_4) = 0$ is detected. Because the surface normal of $S_{\text{transfer}}(r; r_3, r_4) = 0$ and $S_{\text{acc}}(r; r_4) = 0$ are not necessarily close to each other, the spacecraft may be already inside the next event surface, whose position r satisfying $S_{\text{acc}}(r; r_4) > 0$. Depending on the execution error in the previous maneuver, the spacecraft may never cross $S_{\text{acc}}(r; r_4) = 0$. Because the spacecraft is guaranteed to be outside the transfer surface, having the transfer surface as a backup option is reasonable. Figure 6.11 illustrates a possible failure mode and how the trajectory can be corrected by using the transfer surface as a backup condition. There could be further improvements regarding the definition of event surfaces and contingency plans when no event is detected.
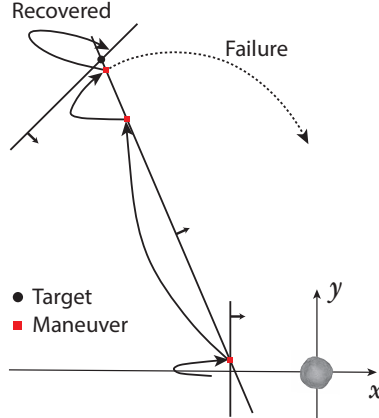
Figure 6.11: A failure mode in an orbit transfer and a recovery option.

Figure 6.12 shows the time history of estimated state errors for the example trajectory along with 3σ bounds. The dashed vertical lines indicate the time when impulsive maneuvers are performed. The errors are inside the 3σ bounds except for the SRP coefficient. Again, the plot of the SRP coefficient shows the deviation from $C_{\text{SRP}} = 1$. During the initial GM estimation operation, the SRP coefficient is close to 1. However, as the spacecraft transitions to hovering at off x-axis

locations, the deviation becomes larger, which is similar to what is observed in the approach phase. Another point to note is that depending on the observation geometry, the covariance envelope of the position and velocity changes its size. The variation of the covariance is indicative of the scale invariance of the optical measurements. While the optical measurements contain rich information for the lateral motion, they have less information for the radial motion.

Randomly introducing noises in the initial states, controls, and measurements, Monte Carlo simulations are performed for the close-hovering phase as well. Figure 6.13 shows truth trajectories from the 1000 Monte Carlo runs. The dispersion of the trajectories is much larger than the estimation errors due to maneuver execution errors. In particular, at the end of a large transfer arc, the trajectories are more dispersed. Because the event surface after such a maneuver is almost parallel to the direction of the spacecraft's motion, small errors in the velocity result in large dispersion of the subsequent surface crossing. The conditions for orbit control could be improved further; however, even with the simple implementation, all of the trajectories eventually converge to the target hovering location. Besides, no trajectory fails to go through a sequence of planned operations: gravity estimation, reconnaissance at various angles, and insertion to a stable orbital platform. Figure 6.14 shows estimation errors (estimates - truth) in the position and parameters. The position errors are consistent with the output from the filter for the example case, and the errors are within the 3σ covariance envelope. There are similar biases in the position and C_{SRP} errors when the discrepancy between the filter's SRP model and true SRP model becomes large because of the off x-axis motion. The filter uses a relatively large process noise covariance of $\sigma_{snc} = 10^{-11}$ km/s^2, which is roughly 10% of the total SRP acceleration. The large process noise prevents the filter from being insensitive to new measurements and helps to maintain reasonable covariance estimates. However, it may be degrading the estimates of other parameters. By applying alternative approaches, such as the dynamic model compensation algorithm, the navigation solution could be improved [81]. Figure 6.15 shows the histogram of total ΔV in the close-hovering phase for the 1000 runs. The mean is 2.759 m/s. Although the maneuvers are not optimized in any way, it seems the total ΔV is not a significant burden, given the corresponding operational period
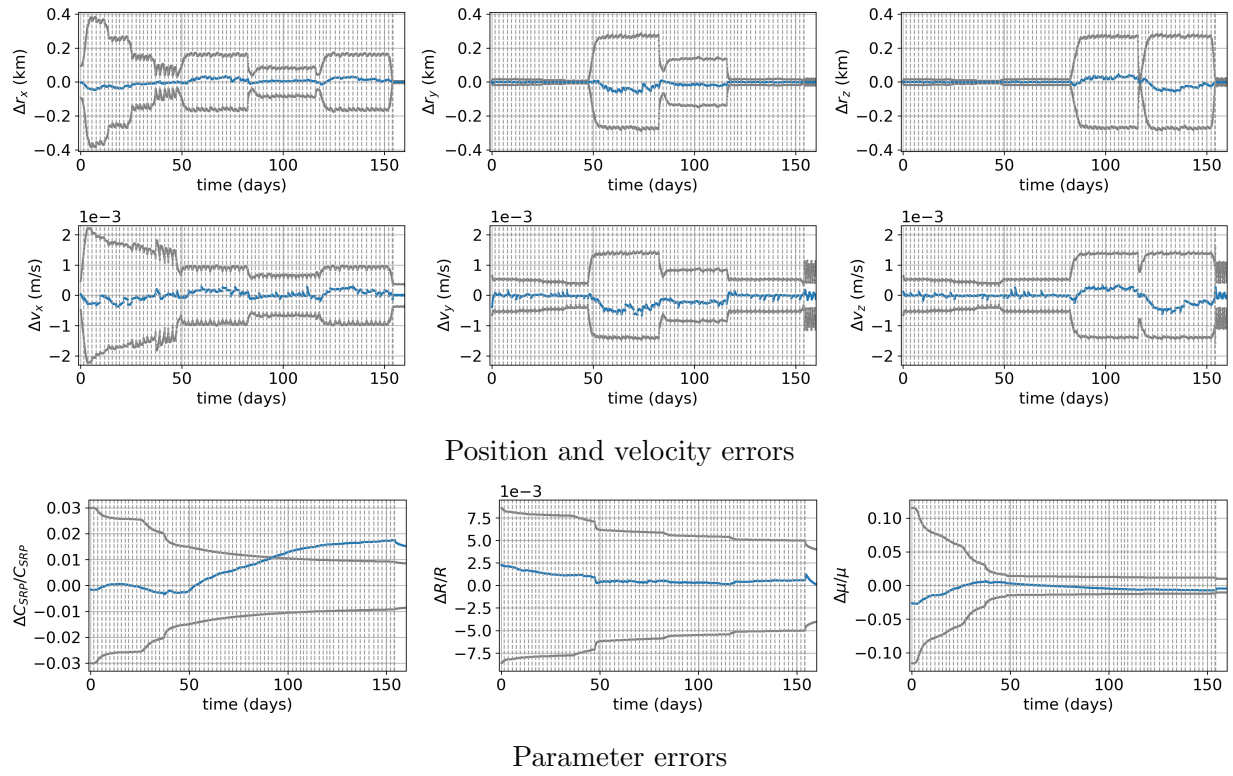
Position and velocity errors

Parameter errors

Figure 6.12: Time history of estimation errors for an example trajectory (close-hovering phase).

is about 160 days.

6.2.4   RL-Based Global Mapping

Next, the end-to-end numerical study is performed, combining the RL-based global mapping policy and the optical and ΔV measurement-based onboard navigation. The introduction of the RL-based policy is an obvious addition. The current analysis also incorporates the maneuver execution noise that is dependent on the ΔV magnitude, as the RL policy is trained to be compatible with the maneuver-dependent execution error. The nominal noise level used in the current analysis is inflated compared to the earlier analyses, allowing us to evaluate the performance of the guidance algorithms in the worst-case scenario. The best performing policy obtained in Chapter 4 is used for the hovering trajectory controller for surface imaging. By using the passage of time from the previous maneuver as an event condition and by translating the RL policy into a $\boldsymbol{\Delta V}$ by solving a TPBVP, the trained RL policy can be integrated into the event-based end-to-end simulation. During the global mapping phase, the spacecraft keeps track of the state of the Markov decision process (MDP) defined in Eq. (4.19). Since the true state is not available to the spacecraft, the latest navigation solution is propagated backward in time right before the decision-making step, which is then used to update the MDP state. The updated MDP state is passed to the policy, which gives us an action. Based on the action, a TPBVP is solved to calculate a $\boldsymbol{\Delta V}$.

The study focuses on the performance of the combined navigation and guidance scheme during the home position hovering at 10 km distance, mass estimation with a gradual descent, global mapping from multiple phase angles with the RL policy, and terminator orbit insertion. Table 6.6 shows the sequence of control commands implemented. Conditions to trigger maneuvers and the types of subsequent maneuvers are listed. The fourth column of the table indicates the number of times the control command is repeated before the next command is executed. For the global mapping phase with the RL policy, the spacecraft keeps repeating the control command until it reaches a successful terminal state or the number of maneuvers exceeds the limit of 200. The global mapping phase is entered once the spacecraft goes through the mass estimation hovering
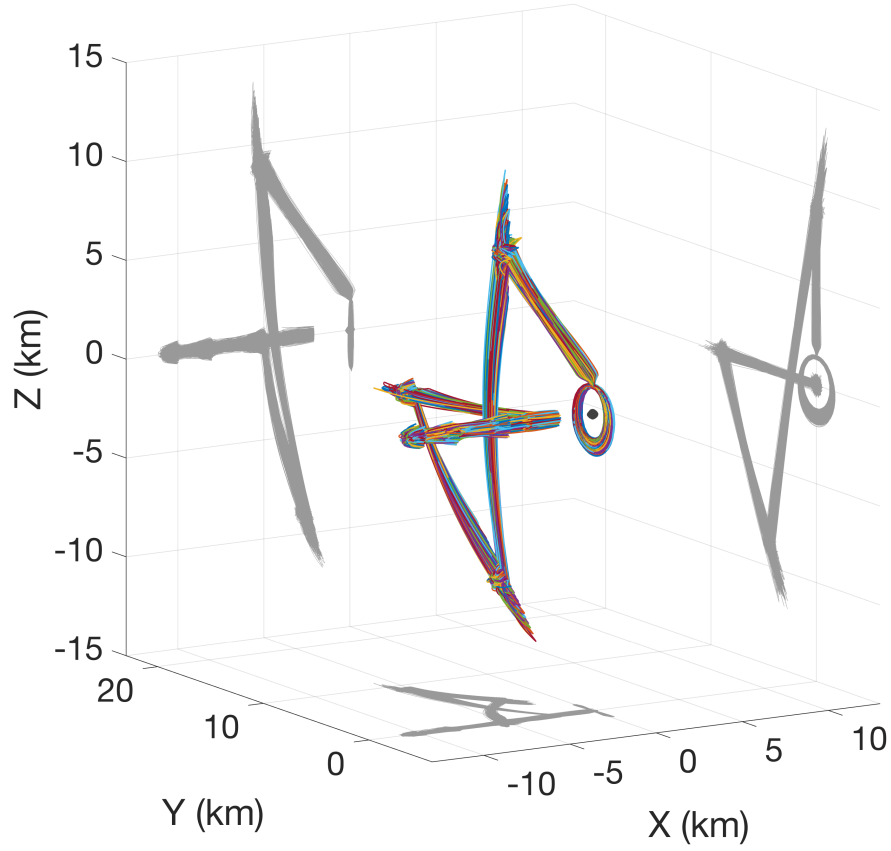
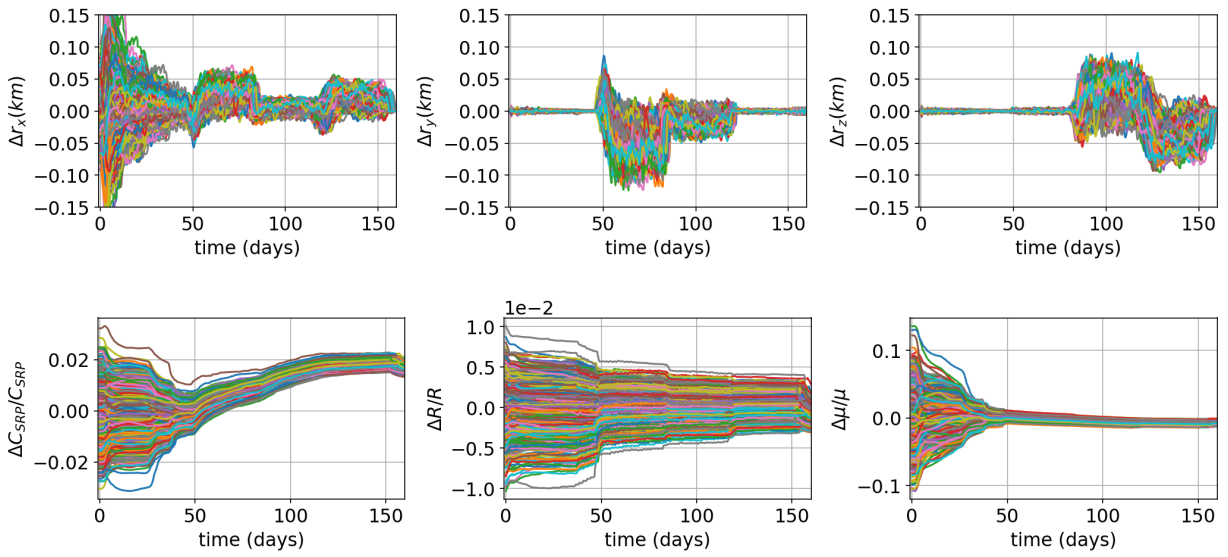Figure 6.13: Trajectories from 1000 Monte Carlo runs (close-hovering phase).

Figure 6.14: Position and parameter errors for the 1000 Monte Carlo runs (close-hovering phase).
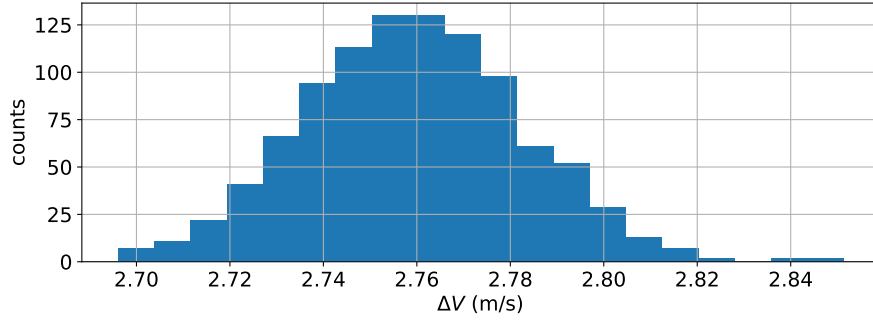
Figure 6.15: Histogram of total ΔV.

Table 6.6: Control commands for the close hovering phase with RL-based global mapping

#	event conditions	maneuver types	rep.	note
1	$S_{\text{fixed}}(\boldsymbol{r};\ \hat{\boldsymbol{x}}, \boldsymbol{r}_0) = 0$	transfer to $\boldsymbol{r}_0$ with $\Delta T = 1$ day	10	$\boldsymbol{r}_0 = -10\hat{\boldsymbol{x}}$ (km)
2	$S_{\text{fixed}}(\boldsymbol{r};\ \hat{\boldsymbol{x}}, \boldsymbol{r}_0) = 0$	transfer to $\boldsymbol{r}_1$ with $\Delta T = 1$ day	1	$\boldsymbol{r}_1 = -8\hat{\boldsymbol{x}}$ (km)
3	$S_{\text{fixed}}(\boldsymbol{r};\ \hat{\boldsymbol{x}}, \boldsymbol{r}_1) = 0$	transfer to $\boldsymbol{r}_1$ with $\Delta T = 1$ day	10	
4	$S_{\text{fixed}}(\boldsymbol{r};\ \hat{\boldsymbol{x}}, \boldsymbol{r}_1) = 0$	transfer to $\boldsymbol{r}_2$ with $\Delta T = 1$ day	1	$\boldsymbol{r}_2 = -6\hat{\boldsymbol{x}}$ (km)
5	$S_{\text{fixed}}(\boldsymbol{r};\ \hat{\boldsymbol{x}}, \boldsymbol{r}_2) = 0$	transfer to $\boldsymbol{r}_2$ with $\Delta T = 1$ day	10	
6	$S_{\text{fixed}}(\boldsymbol{r};\ \hat{\boldsymbol{x}}, \boldsymbol{r}_2) = 0$	transfer to $\boldsymbol{r}_3$ with $\Delta T = 1$ day	1	$\boldsymbol{r}_3 = -4\hat{\boldsymbol{x}}$ (km)
7	$S_{\text{fixed}}(\boldsymbol{r};\ \hat{\boldsymbol{x}}, \boldsymbol{r}_3) = 0$	transfer to $\boldsymbol{r}_3$ with $\Delta T = 1$ day	10	
8	$S_{\text{fixed}}(\boldsymbol{r};\ \hat{\boldsymbol{x}}, \boldsymbol{r}_3) = 0$	transfer to $\boldsymbol{r}_4$ with $\Delta T = 1$ day	1	$\boldsymbol{r}_4 = [-5R, 0, 0]$
9	$S_{\text{fixed}}(\boldsymbol{r};\ \boldsymbol{r}_3, \boldsymbol{r}_4) = 0$	transfer to $\boldsymbol{r}_4$ with $\Delta T = 6$ hours	1	
10	$\begin{cases} \lvert\boldsymbol{r}\rvert - 3R = 0 \text{ or} \\ t = t_{\text{prev}} + \Delta t_{\text{prev}} \end{cases}$	perform an action sampled from the RL policy with $\text{az}_{\text{tgt}} = 180°$		
11	$\begin{cases} \lvert\boldsymbol{r}\rvert - 3R = 0 \text{ or} \\ t = t_{\text{prev}} + \Delta t_{\text{prev}} \end{cases}$	perform an action sampled from the RL policy with $\text{az}_{\text{tgt}} = 135°$	≤ 200	
12	$\begin{cases} \lvert\boldsymbol{r}\rvert - 3R = 0 \text{ or} \\ t = t_{\text{prev}} + \Delta t_{\text{prev}} \end{cases}$	perform an action sampled from the RL policy with $\text{az}_{\text{tgt}} = 225°$	≤ 200	
13	$t = t_{\text{prev}} + \Delta t_{\text{prev}}$	transfer to $\boldsymbol{r}_{\text{TO}}$ with $\Delta T = 6$ hours	1	
14	$t = t_{\text{prev}} + \Delta t_{\text{prev}}$	transfer to $\boldsymbol{r}_{\text{TO}}$ with $\Delta T = 4$ hours	1	Correction burn
15	$t = t_{\text{prev}} + \Delta t_{\text{prev}}$	terminator orbit insertion	1	

phase, gradually approaching the target body. The observations from az $= 180°$, $135°$, and $225°$ are successively performed. During the global mapping phase, the spacecraft nominally plans the next maneuver at the time specified by the RL policy. However, another event condition $|\boldsymbol{r}| - 3R = 0$ is defined to allow the spacecraft to perform a maneuver before reaching the next maneuver time specified by the RL policy. This condition prevents the spacecraft from getting too close to the asteroid. In the table, t_{prev} is the previous maneuver time, and Δt_{prev} is the expected maneuver interval. After the global mapping, the spacecraft is inserted into a terminator orbit. Its semi-major axis is chosen to be 1.5 km, and its orbit normal is chosen to point to the Sun. The insertion location $\boldsymbol{r}_{\mathrm{TO}}$ is either the periapsis or apoapsis, and the spacecraft chooses the closer point when a $\boldsymbol{\Delta V}$ is computed. The simulation time is set to 90 days. The simulation uses the same initial condition and initial covariance as the event-driven hovering analysis. The true position and velocity and nominal parameter values are sampled in the same way as the earlier end-to-end simulations. Nominally, $\sigma_{\Delta V,\mathrm{crtl},c} = 1$ mm/s and $\sigma_{\Delta V,\mathrm{crtl},p} = 0.05$ are used. The same measurement noise levels as the event-drive hovering analysis are used.

The process noise of the navigation filters is set to $\sigma^2 = 10^{-21}$ (km/s^2)^2. One failure mode discovered in the end-to-end analysis is the divergence of the filter that could occur when the spacecraft gets too close to the asteroid. When the distance is too close, the nonlinearity of the gravity and perturbations from the unmodeled gravity field make the filtering more challenging. To prevent the filter saturation and divergence, the process noise is slightly inflated compared to the value of $\sigma^2 = 10^{-22}$ (km/s^2)^2 used in the earlier studies.

An example trajectory from the end-to-end simulations is shown in Fig. 6.16. The blue lines indicate the true trajectory, and the dots correspond to the estimated positions. The projections onto x-, y-, and z-planes are shown in gray. We can see that the spacecraft enters the global mapping hovering after the gradual descent for mass estimation, performing multiple hops from different phase angles in succession.

As for the state estimation errors, the same observations from the earlier end-to-end analyses hold true. The optical measurements have less information about the relative range, and thus the
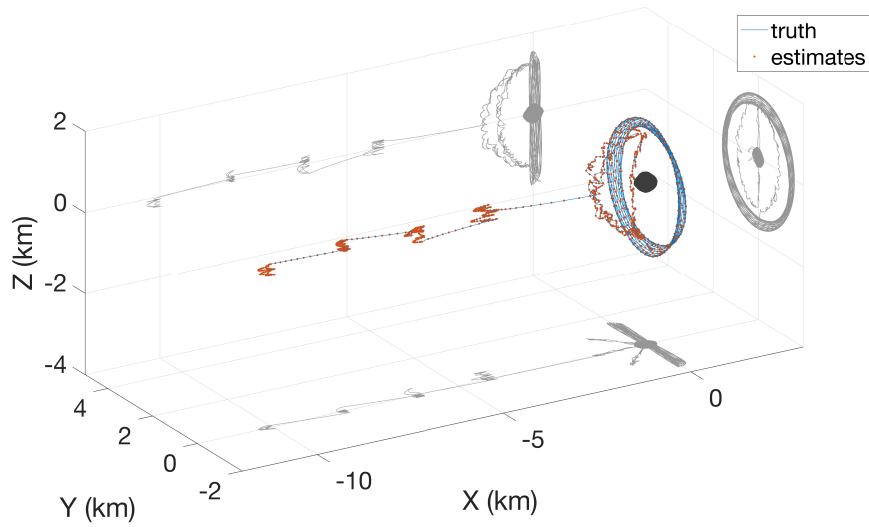
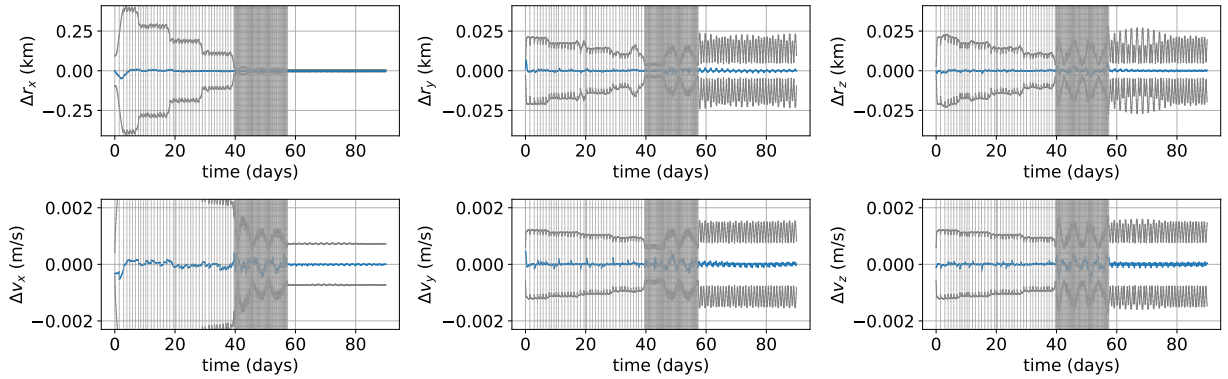Figure 6.16: 3-D plot of an example trajectory from the end-to-end simulation.

Figure 6.17: Position and velocity errors for the example trajectory from the end-to-end simulation.

x-component of the position and velocity errors are larger. The angular size measurements can constrain the range more tightly as the spacecraft approaches the asteroid. Figure 6.17 shows the position and velocity errors with the $3 - \sigma$ covariance estimates for the example trajectory. The vertical dashed lines indicate the maneuver times. What looks like a shaded area in the plot after around 40 days indicates frequent maneuvers in the global mapping phase. The navigation filter can successfully estimate the state even with such frequent maneuvers. We also confirmed that the mass parameter uncertainty could be reduced significantly during the gradual descent and global mapping phase. At the end of the simulation, all of the parameter uncertainties are less than one percent of the true values.

Next, Monte Carlo simulations are performed to test the robustness of the proposed autonomous guidance and navigation scheme in the same way as the earlier analyses. In order to reconfirm that the trained RL policy work without a problem under different state transition dynamics, simulations are performed with two different maneuver noise execution settings. In one case, the nominal values of $\sigma_{\Delta V,\text{crtl},c} = 1$ mm/s and $\sigma_{\Delta V,\text{crtl},p} = 0.05$ are used, which is denoted as a large ΔV case. In another runs, denoted as small ΔV case, $\sigma_{\Delta V,\text{crtl},c} = 0.1$ mm/s and $\sigma_{\Delta V,\text{crtl},p} = 0.017$ are used. The 1000 runs are performed for each of the maneuver noise settings.

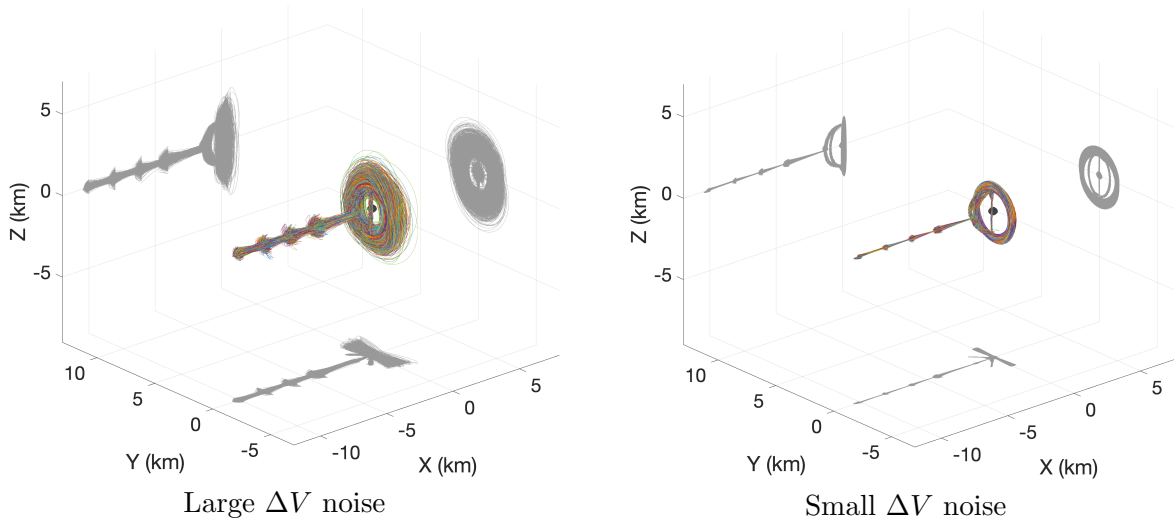Large ΔV noise   Small ΔV noise

Figure 6.18: 3-D plots of trajectories from the end-to-end Monte Carlo simulations.
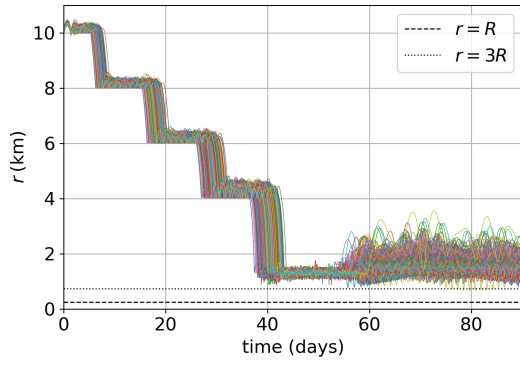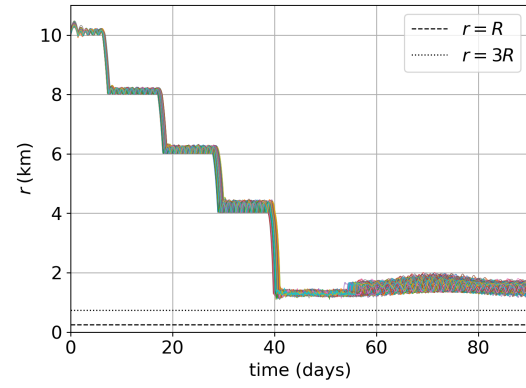
Large ΔV noise

Small ΔV noise

Figure 6.19: Time histories of asteroid relative distance in the end-to-end Monte Carlo simulations.

The trajectories obtained from the Monte Carlo runs are shown in Fig. 6.18. With the larger maneuver execution noise, the trajectories have much larger dispersions. The smaller dispersions from the smaller maneuver execution noise confirm that the navigation filters can accurately track the spacecraft's position and velocity. Figure 6.19 shows the time history of the spacecraft's distance relative to the asteroid. The distance for $r = R$ and $r = 3R$ are shown as references. Even with the larger maneuver execution noise, no collision with the asteroid was observed in the Monte Carlo simulations. However, there were a few cases where the spacecraft detected crossing with $r = 3R$ during the global mapping phase and performed a contingency maneuver as a safety precaution. The spacecraft was then able to continue on the MDP task successfully. The spacecraft can maintain a safe distance from the target when the noise level is low.

Large ΔV noise   Small ΔV noise
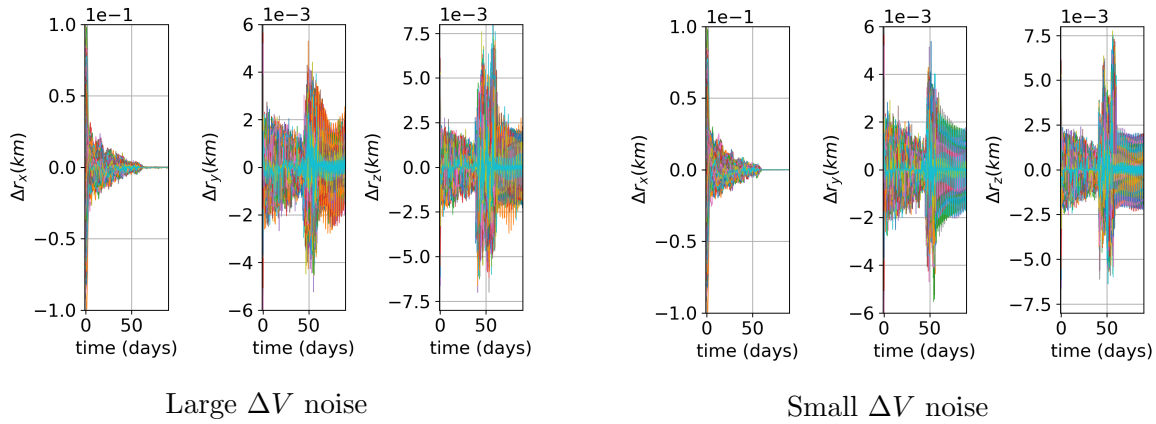
Figure 6.20: Time histories of position errors in the end-to-end Monte Carlo simulations.

Figures 6.20 and 6.21 show the time histories of the estimated position errors and parameter errors in the Monte Carlo runs. It is confirmed that the navigation filters work well regardless of the maneuver execution noise levels. As for SRP, the SRP model used to simulate the truth trajectories depends on the spacecraft's attitude. Thus, there is a bias between the filter's and truth simulation's dynamical models. The spacecraft's attitude depends on its position as we define the spacecraft's attitude such that an axis of the spacecraft's body-fixed frame always points to the asteroid. Therefore, there is a slight difference in the SRP coefficient errors between the large and small ΔV cases. The parameter uncertainties the filters estimate at the end of the simulation are

Large ΔV noise   Small ΔV noise
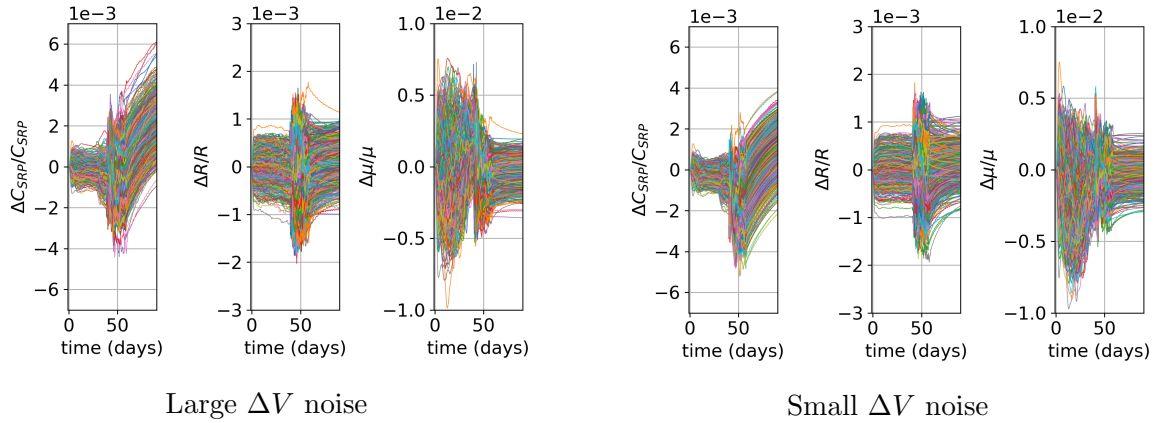
Figure 6.21: Time histories of parameter errors in the end-to-end Monte Carlo simulations.

about 0.6 % for C_{SRP}, 0.1 % for R, and 0.2 % for μ. Thus, the actual errors in the Monte Carlo runs are within the estimated $3 - \sigma$ bounds, and the filter works without being overconfident about the state estimates.

The distribution of the total ΔV in the Monte Carlo runs is shown in Fig. 6.22. The plot is normalized such that the area integral becomes unity. In both maneuver noise settings, the total ΔV is around 6 - 6.5 m/s. With the larger noise, the total ΔV is larger. The larger ΔV might be caused by more frequent maneuvers to correct the spacecraft's location.

Figure 6.23 shows the distribution of the number of steps the spacecraft took to complete a single MDP episode. Again, the plot is normalized such that the area integral becomes unity. As expected from the earlier experiments, the small ΔV noise results in a marginally smaller number of steps to complete the observation task. However, the difference is not significant. In both cases, the RL policy was able to complete the observation task even though the state transition and resulting state distributions are slightly different from the training environment. The results of the Monte Carlo simulations confirm that the trained RL policy is robust.

6.3   End-to-End Analysis Results for TCO Rendezvous

Finally, this section provides the results of the end-to-end numerical simulations for a TCO rendezvous scenario. The goal is to study if the same navigation and control concept can be applied

Large ΔV noise

Small ΔV noise
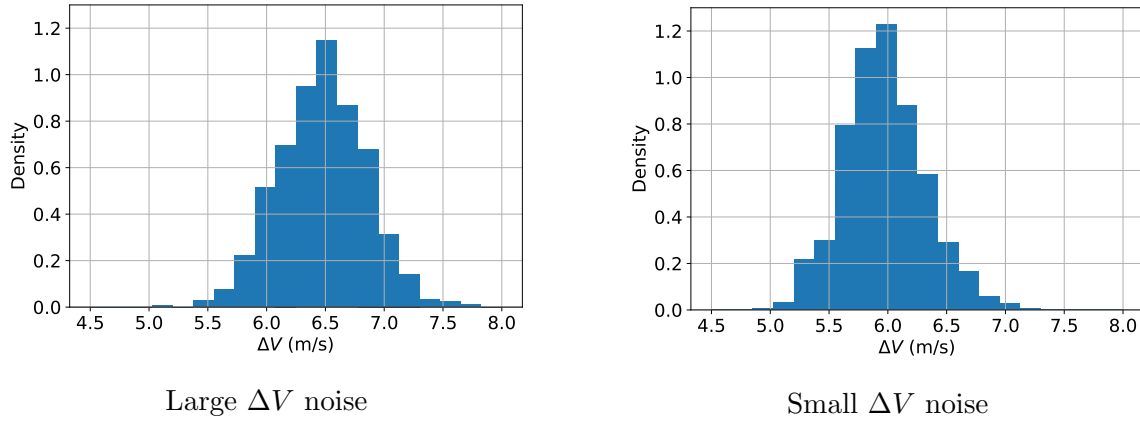
Figure 6.22: Distribution of total ΔV in the end-to-end Monte Carlo simulations.

Large ΔV noise

Small ΔV noise

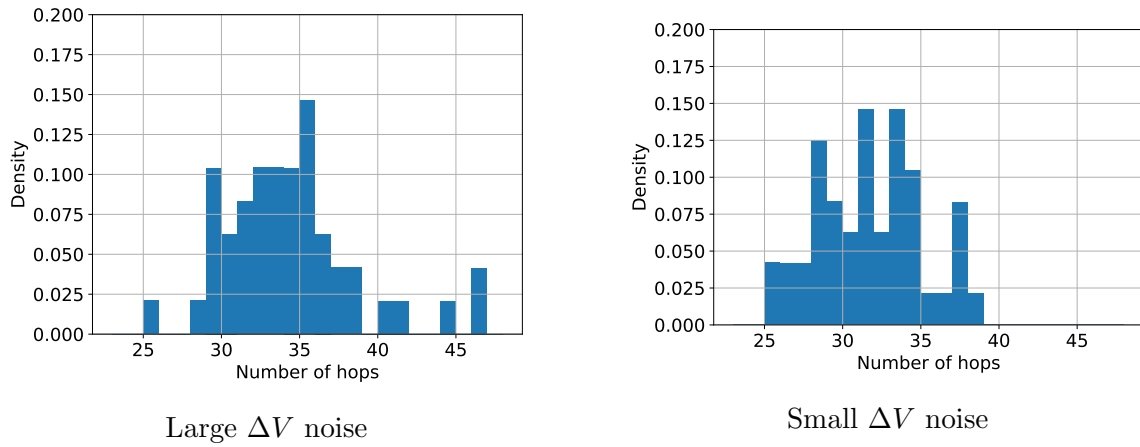Figure 6.23: Distribution of the number of steps required to complete an MDP episode in the end-to-end Monte Carlo simulations.

to the rendezvous with a much smaller asteroid, which also has a different dynamical environment compared to the rendezvous with a heliocentric asteroid.

The models for the relative motion dynamics used in the truth simulation and navigation filter are identical in the TCO rendezvous analysis and are defined by Eq. (2.28). Given the small gravitational attraction from the target asteroid, major model biases would be the SRP error and gravity gradient error due to erroneous ephemeris. Including these biases in the simulation would be a part of future work. The analysis in Chapter 2 shows that the acceleration errors due to ephemeris errors are small when the distance between the hovering location and the asteroid is short. However, studying the effect of the ephemeris errors more in detail is an important aspect as it is expected that there is a significant ephemeris error. Through the gravity gradient term, it might be possible to estimate the ephemeris just by looking at the relative motion dynamics.

The state vector for the navigation filter is identical to the earlier end-to-end analysis for heliocentric asteroid rendezvous. The true parameter values $(C_{\mathrm{SRP}}, R, \mu)$ are fixed, while the nominal parameter values that the filter uses are sampled from Gaussian distributions. The true parameters are defined as

$$C_{\mathrm{SRP}} = 1.0 \tag{6.9}$$

$$R = 2.5 \quad \mathrm{m} \tag{6.10}$$

$$\mu = 8.7366 \times 10^{-15} \quad \mathrm{km}^3/\mathrm{s}^2 \tag{6.11}$$

On the other hand, the nominal position and velocity are fixed, whereas the true position and velocity are sampled from Gaussian distributions. The concrete $1 - \sigma$ values of the Gaussian distributions are described later for each analysis.

The results of the end-to-end simulation are presented herein. Two different analyses are performed: constant altitude hovering and a comprehensive simulation that starts from more than 2,000 km away that ends with a fixed altitude hovering. In both analyses, the simulation period is set to 300 days. Table 6.7 shows common noise parameters used in the end-to-end simulations. As for the maneuver errors, the Gates maneuver model explained earlier is used. The same set of

measurements is used as the heliocentric asteroid rendezvous. The frequency of optical measurements is defined to be every 2 hours ($\Delta t = 2$ hours), which is a rather conservative assumption as mentioned earlier in Chapter 5. The small interval between the time of a maneuver and the subsequent measurement update is set to $\delta t = 30$ minutes. See Figs. 6.1 and 6.2 for details of the measurement scheduling.

Table 6.7: Common noise parameters used in end-to-end simulations for a TCO rendezvous.

Parameter	Unit	Value
IFOV	mrad	$0.105 \ (= 6°/1000)$
$\sigma_{\tau,\text{meas}}$	sec	60
$\sigma_{p,\text{meas}}$	-	0.01
$\sigma_{c,\text{meas}}$	mm/s	0.1
$\sigma_{\tau,\text{ctrl}}$	sec	60
$\sigma_{p,\text{ctrl}}$	-	0.01
$\sigma_{c,\text{ctrl}}$	mm/s	0.1
σ_{snc}	km/s^2	10^{-11}

6.3.1 Analysis 1: Constant Altitude Hovering at a TCO

Initially, the behavior of the navigation and control systems is studied with a simple scenario where the spacecraft performs fixed-altitude hovering. The spacecraft performs a maneuver every day. Three different hovering altitudes are studied: 10 km, 1 km, and 100 m.

The nominal position and velocity at the initial epoch are defined as

$$\boldsymbol{r} = [-d_{\text{hov}}, 0, 0] \quad \text{(km)} \tag{6.12}$$

$$\boldsymbol{v} = [-1, 0, 0] \quad \text{(cm/s)} \tag{6.13}$$

where d_{hov} is the nominal hovering distance. The initial covariance is defined as shown in Table 6.8.

Figure 6.24 shows the trajectories for the fixed altitude hovering. For the 10 km hovering, the dispersion of the trajectory looks larger. A larger range error is likely the cause of the larger dispersion. Table 6.9 shows the total ΔV for the 300 day hovering. The control efforts are made to

Table 6.8: A priori uncertainties used in TCO rendezvous end-to-end analysis 1.

Parameter	Unit	Value
$\sigma_{r,x}$	m	31
$\sigma_{r,y}$	m	1
$\sigma_{r,z}$	m	1
$\sigma_{v,x}$	mm/s	0.14
$\sigma_{v,y}$	mm/s	0.2
$\sigma_{v,z}$	mm/s	0.2
$\sigma_{C_{\mathrm{SRP}}}$	-	0.01
σ_R	R	0.5
σ_μ	μ	5

counteract the SRP at these distances. Therefore, the total ΔVs are more or less the same among the three cases.

Figures 6.25-6.30 show the state errors with $3 - \sigma$ covariance bounds, parameter errors with $3 - \sigma$ covariance bounds, and estimated uncertainty $1 - \sigma$ of the parameters. Compared to the rendezvous with larger asteroids studied earlier, the 10 km hovering has larger range uncertainty. The range error is about 400 meters with 10 km hovering in this study. However, as the hovering distance becomes shorter, the range uncertainty becomes smaller. It seems the angular size measurements are indeed helpful for rendezvous with smaller asteroids in reducing the range error. At 100 meters hovering, the range uncertainty can be as small as 5 meters.

As for the SRP uncertainty, the SRP coefficient can be estimated more accurately when the spacecraft is farther away from the asteroid. This is likely because there is a coupling between the drift along the y-axis and SRP acceleration; the SRP pushes the spacecraft, and the change in the velocity, in turn, results in the y-drift through Coriolis force. The SRP uncertainty can be as small as 0.5 %. The radius estimates are more accurate when the S/C-asteroid distance is smaller. The final radius uncertainty can be as small as 0.3 %. The mass uncertainty cannot be reduced at all, even at 1 km. For 100 meter hovering, the mass uncertainty can be reduced to about 200 %.

case 1: 10 km hovering

case 2: 1 km hovering

case 3: 100 m hovering
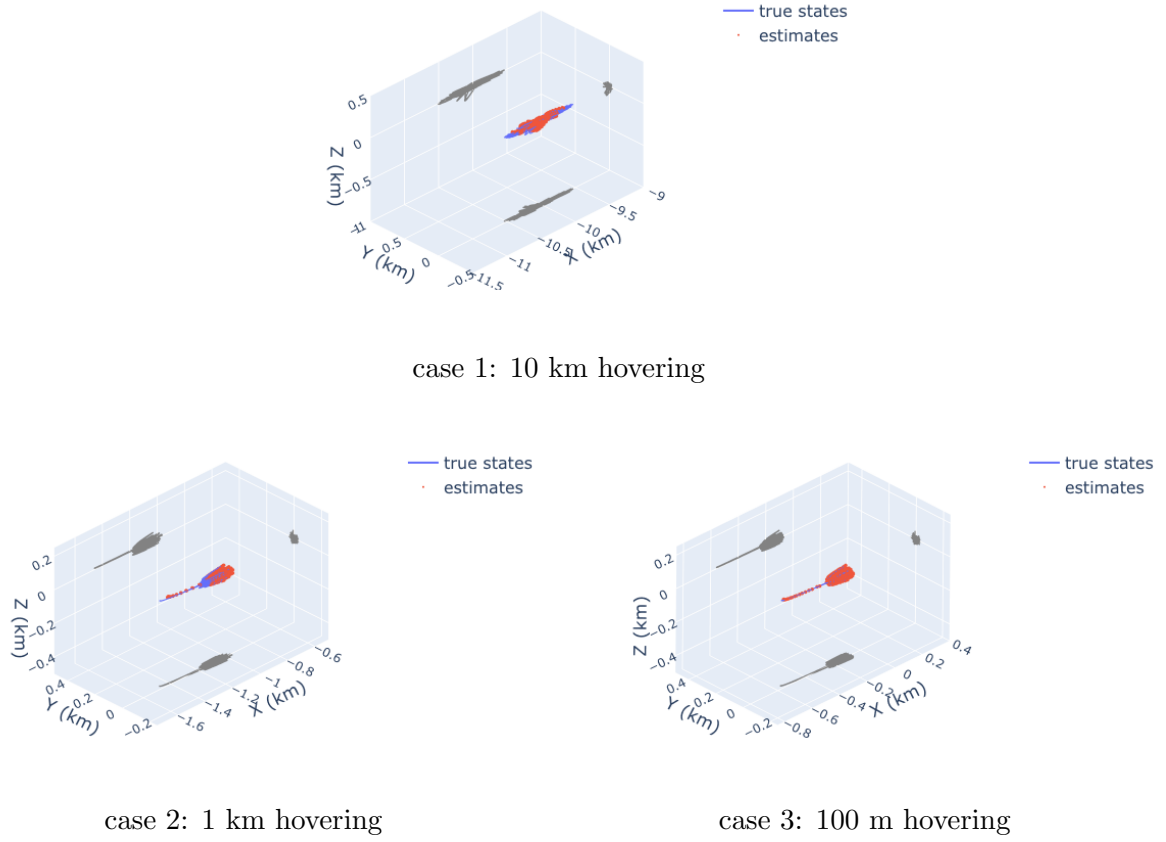
Figure 6.24: Hovering trajectories from TCO rendezvous end-to-end analysis 1 (cases 1-3).

Table 6.9: Total ΔV for 10-month hovering from TCO rendezvous end-to-end simulation analysis 1.

Hovering distance (km)	10	1	0.1
Total ΔV (m/s)	3.3575	3.3104	3.3171

Table 6.10: A priori uncertainties used in end-to-end analysis 2.

Parameter	Unit	Value
$\sigma_{r,x}$	km	0.1
$\sigma_{r,y}$	km	0.1
$\sigma_{r,z}$	km	0.1
$\sigma_{v,x}$	m/s	0.1
$\sigma_{v,y}$	m/s	0.1
$\sigma_{v,z}$	m/s	0.1
$\sigma_{C_{\mathrm{SRP}}}$	-	0.1
σ_R	R	1
σ_μ	μ	5
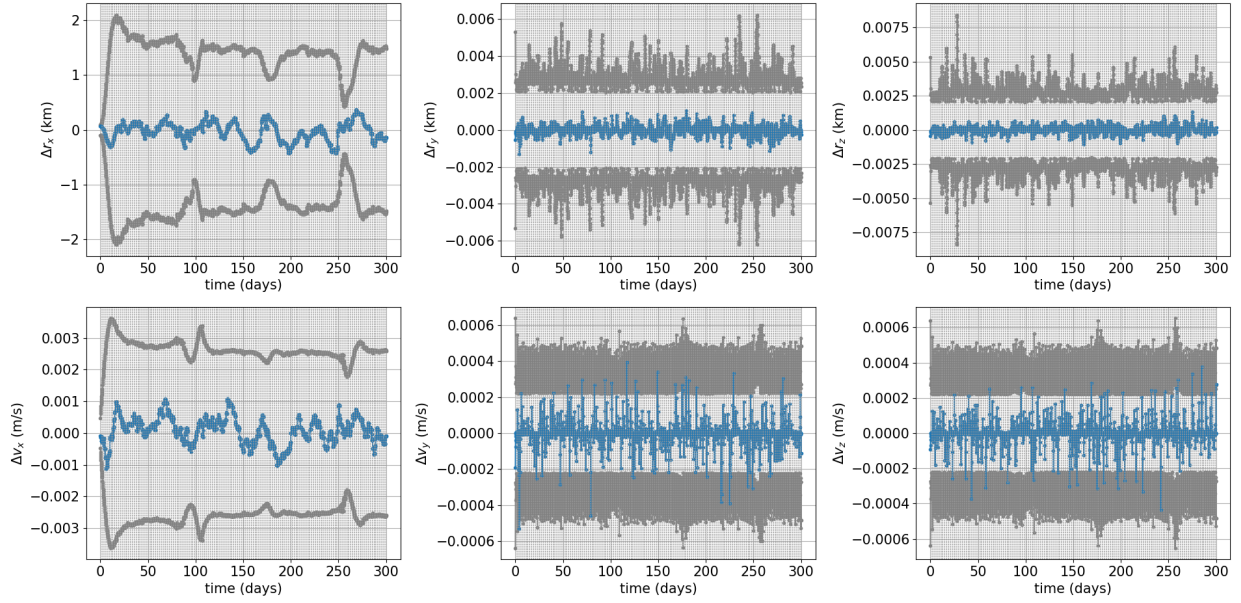
Figure 6.25: Position and velocity errors for analysis 1 case 1 (10 km hovering). Blue lines: estimation errors. Gray lines: $3-\sigma$. Dashed vertical lines: maneuver times.
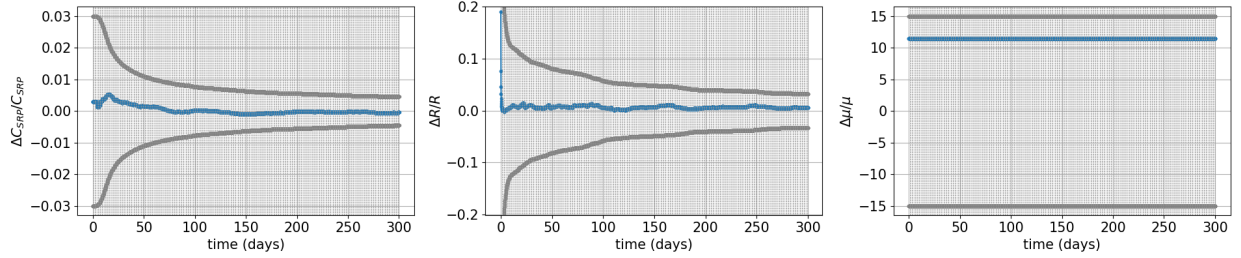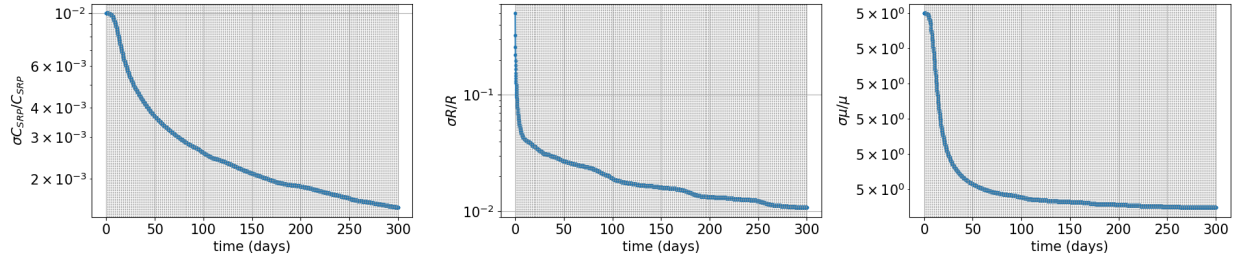
Figure 6.26: Parameter errors for TCO rendezvous analysis 1 case 1 (10 km hovering). Dashed vertical lines: maneuver times.
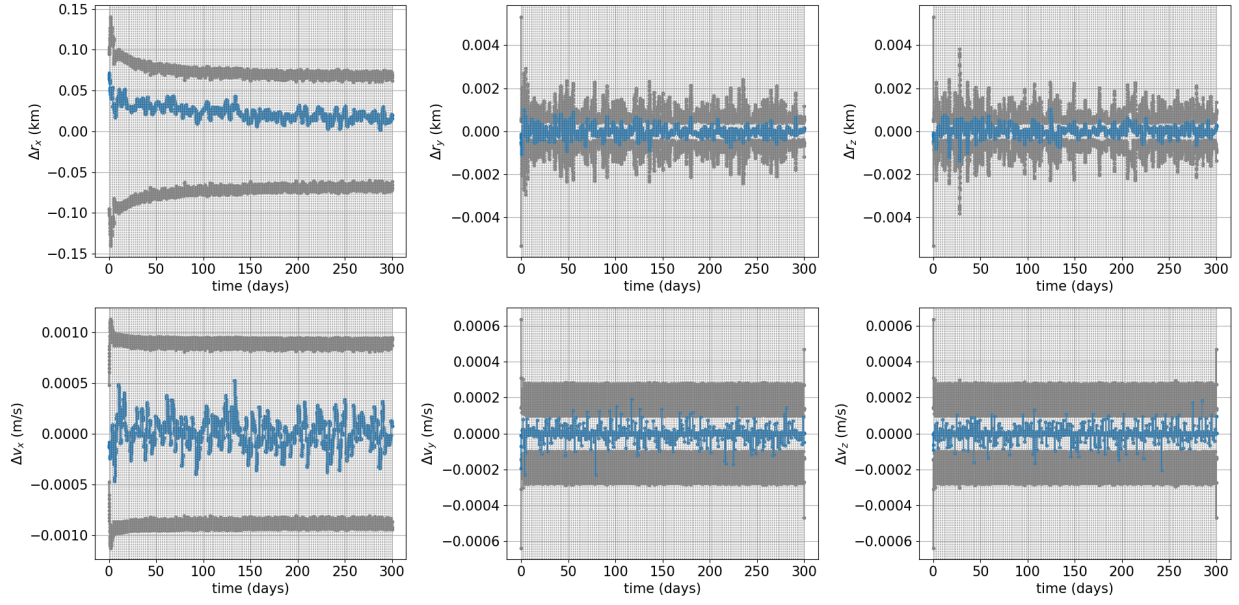
Figure 6.27: Position and velocity errors for TCO rendezvous analysis 1 case 2 (1 km hovering). Blue lines: estimation errors. Gray lines: $3 - \sigma$. Dashed vertical lines: maneuver times.
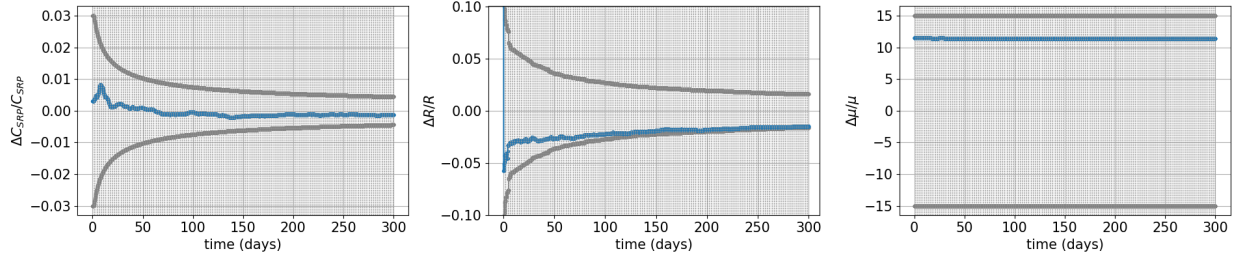
Parameter errors with $3 - \sigma$ bounds
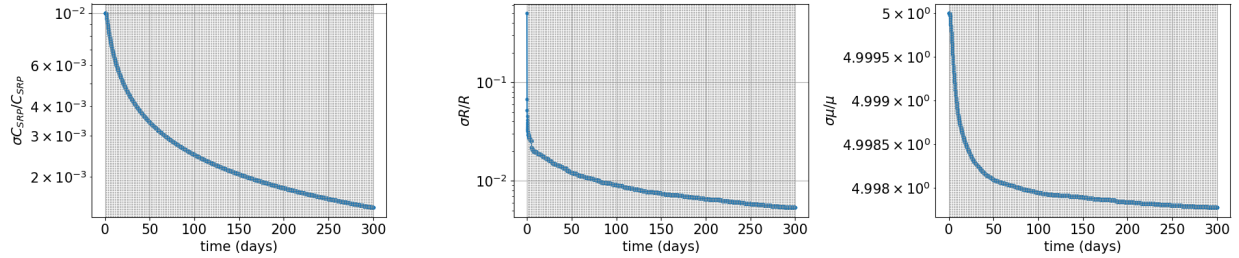
$1 - \sigma$

Figure 6.28: Parameter errors for TCO rendezvous analysis 1 case 2 (1 km hovering). Dashed vertical lines: maneuver times.
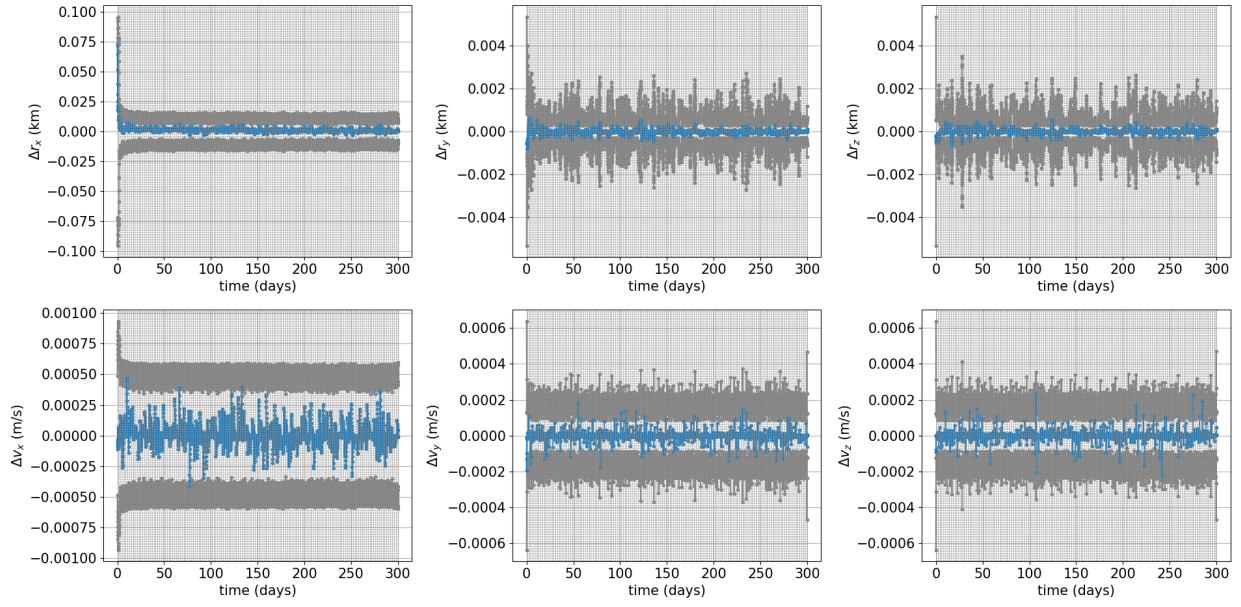
Figure 6.29: Position and velocity errors for TCO rendezvous analysis 1 case 3 (100 m hovering). Blue lines: estimation errors. Gray lines: $3 - \sigma$. Dashed vertical lines: maneuver times.
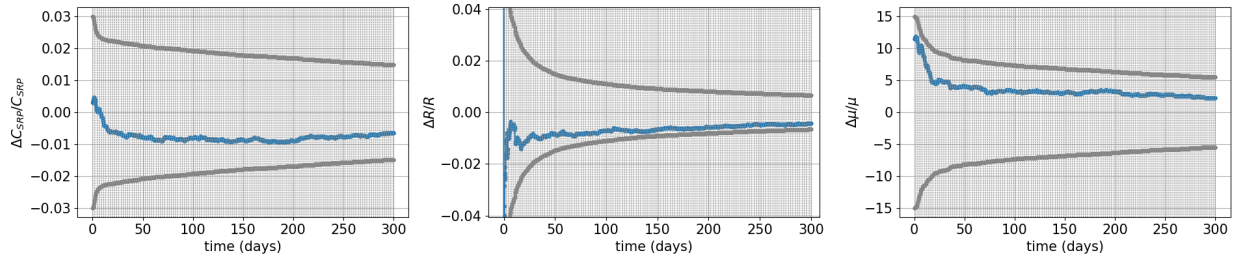
Parameter errors with $3 - \sigma$ bounds
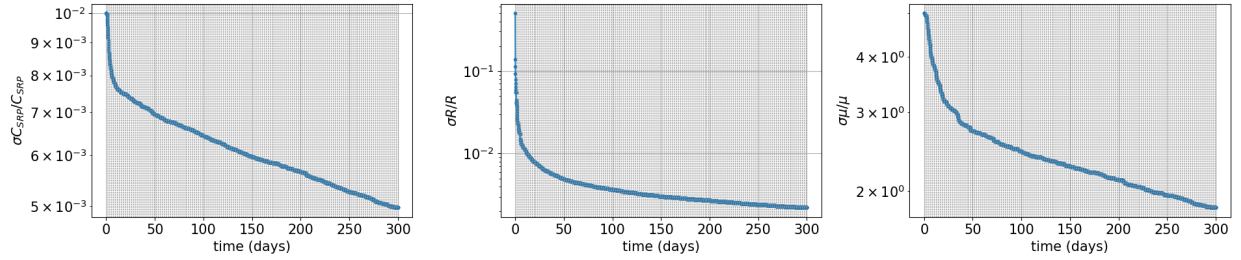
$1 - \sigma$

Figure 6.30: Parameter errors for TCO rendezvous analysis 1 case 3 (100 m hovering). Dashed vertical lines: maneuver times.
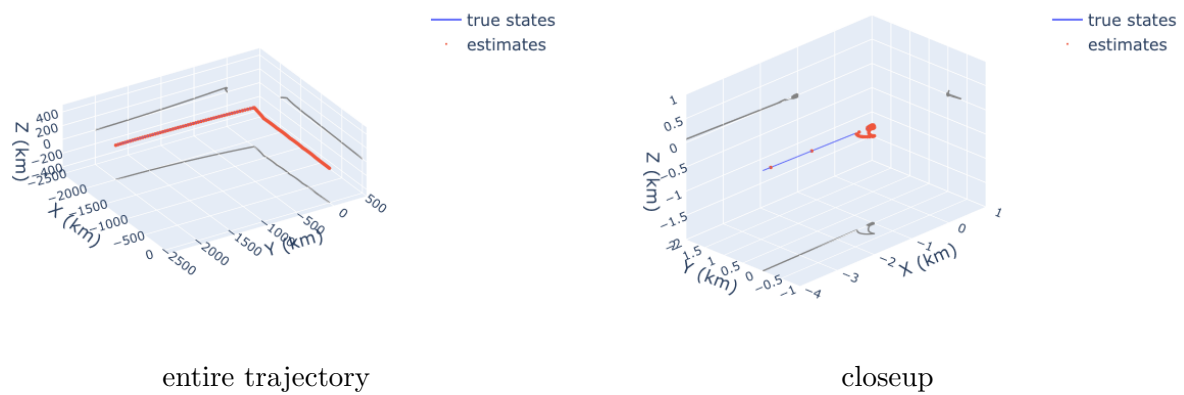
entire trajectory   closeup

Figure 6.31: 3D plots of trajectory from end-to-end analysis 2.

6.3.2   Approach Phase Leading to Constant Altitude Hovering at a TCO

As a more practical scenario, an end-to-end simulation is performed where the spacecraft approaches the asteroid from more than 2,000 km away and transitions to 1 km hovering. The nominal position and velocity at the initial epoch are defined as

$$\boldsymbol{r} = [-2000, -2000, 0] \quad (\text{km}) \tag{6.14}$$

$$\boldsymbol{v} = [0, 5, 0] \quad (\text{m/s}) \tag{6.15}$$

Thus, the spacecraft is moving from the negative y to the positive y direction. The initial covariance is defined as shown in Table 6.10. Once the spacecraft detects $x - z$ plane crossing, a sequence of maneuvers is performed to bring the spacecraft close to the hovering location of $\boldsymbol{r}_{\text{tgt}} = [-1, 0, 0]$ km. Initially, five maneuvers are performed every five days, followed by five more maneuvers performed at a day intervals. Then, another maneuver is applied to put the spacecraft on a six-hour transfer trajectory to the hovering position. Subsequently, the spacecraft transitions to hovering at a distance of 1 km. Every time a crossing with $x = -1$ km is detected, a maneuver is applied to bring the spacecraft back to $\boldsymbol{r}_{\text{tgt}} = [-1, 0, 0]$ km in one day until the simulation is over.

Figure 6.31 shows the trajectories from the end-to-end analysis 2. Figure 6.32 shows the estimation errors of position and velocity for the first 50 days with $3 - \sigma$ bounds and estimated position and velocity uncertainties for 300 days. The vertical dashed lines indicate maneuver times. We can confirm that the estimation errors are within the $3 - \sigma$ bounds. We can also confirm that uncertainties drop significantly during the 1 km hovering. The range error at the end of the 1 km hovering is about 30 meters. Figure 6.33 shows the estimated parameter uncertainties. The SRP uncertainty can be smaller than 0.2 % at the end of the hovering operation. As for the radius uncertainty, it drops significantly during the initial phase of the 1 km hovering. The final size uncertainty is about 0.6 %. The asteroid's mass cannot be estimated at all at 1 km distance, as expected from the acceleration study. These observations suggest that it would be beneficial for the spacecraft to perform a period of fixed altitude hovering to guarantee that the navigation uncertainties reach a steady state before lowering the altitude.
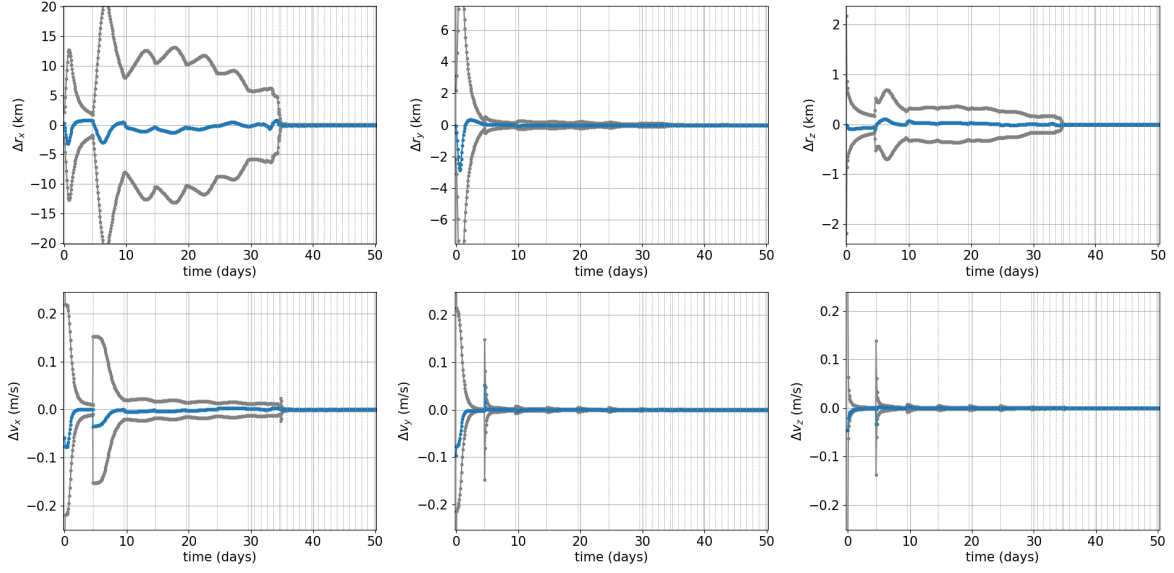
Position and velocity errors with $3 - \sigma$ bounds.
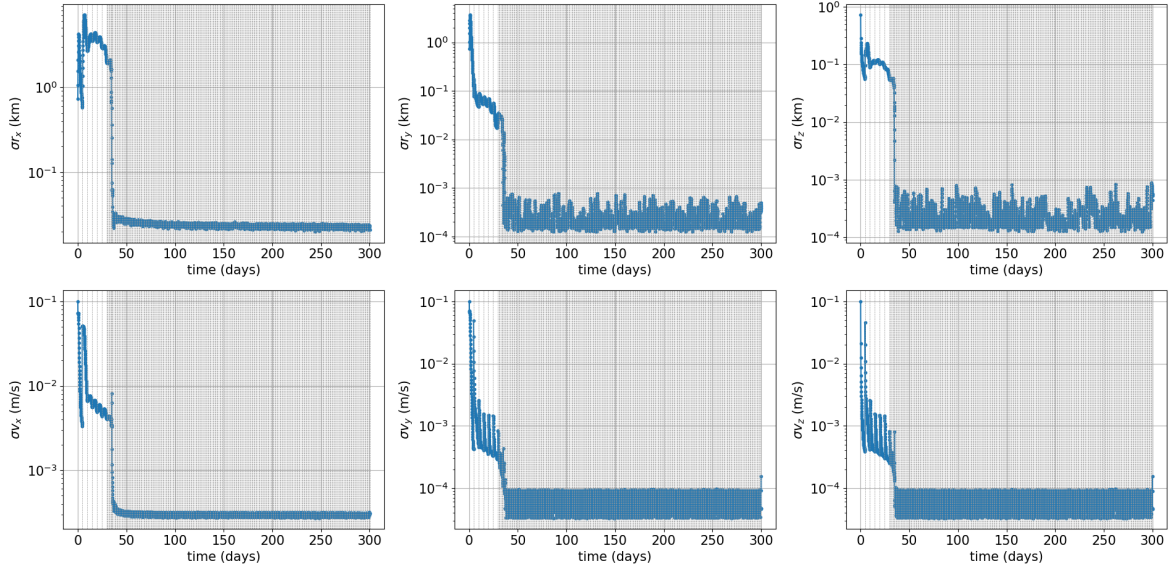
Position and velocity uncertainty (1-σ).

Figure 6.32: Estimation errors (for the first 50 days) and estimated uncertainty (for 300 days) of position and velocity in the end-to-end analysis 2. Dashed vertical lines: maneuver times.
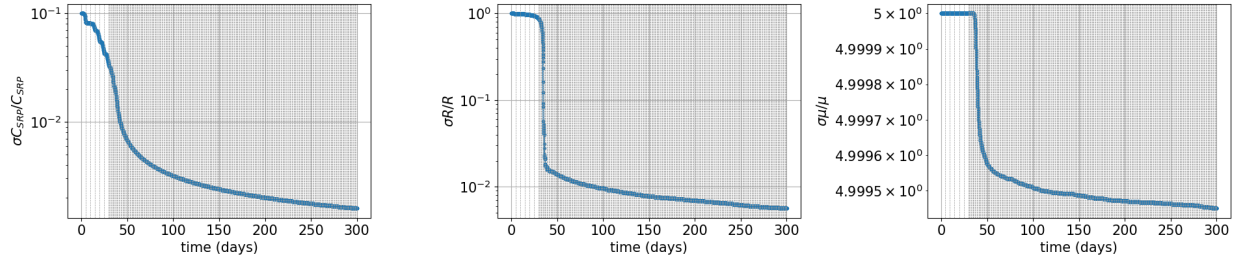
Figure 6.33: Estimated parameter uncertainties (1-σ) in the end-to-end analysis 2. Dashed vertical lines: maneuver times.

6.4   Conclusions

For autonomous exploration, the spacecraft needs to control its trajectory in addition to localizing itself and mapping the orbital environment. End-to-end numerical analyses are performed to evaluate the overall performance and feasibility of the proposed onboard navigation and guidance. The onboard navigation utilizes the optical measurements and ΔV measurements to break the scale invariance of the optical information. As for the trajectory control, an event-driven trajectory control scheme is introduced where the event is typically specified as a surface crossing in position space. Using the best navigation solution at the time of planning, an impulsive maneuver to reach a target position in a given transfer time is computed by solving a TPBVP.

The study first analyzes the navigation and guidance performance for the rendezvous with a heliocentric asteroid, using asteroid Bennu as a test case. The analysis focuses on multiple phases and scenarios. Initially, the asteroid approach phase that ends with a home position hovering is studied. Using the simulation result of the approach phase, the close-hovering phase is analyzed, where detailed reconnaissance of the asteroid is performed. The study also focuses on the global mapping hovering trajectory obtained by running the RL-based policy explained in the earlier chapter. Monte Carlo simulations are performed by introducing noises in the initial state distribution, measurements, and control. It is confirmed that by the end of the close-hovering phase, both the mean radius and mass parameter can be estimated with less than 1% error. The numerical study

also confirms that the accuracy of the position and velocity estimates correlates with the observation geometry due to the scale invariance of the optical measurements. While the filter dynamics assume cannonball SRP, an attitude-dependent SRP model is used for the truth simulation. This unmodeled SRP has a non-negligible effect on filter performance. The SNC algorithm is used to account for the unmodeled accelerations in the filter, setting its noise level as roughly 10% of the total SRP acceleration. With the process nose, the filter returns a reasonable covariance estimate. During the global mapping phase with the RL policy, frequent noisy maneuvering may put the spacecraft too close to the target, which stresses the navigation filter. When the spacecraft is too close to the target, filter divergence could happen. However, we confirm that despite the frequent maneuvering, by using a slightly inflated process noise covariance, the navigation can be performed without an issue.

The second part of the end-to-end analysis focuses on the autonomous proximity operation at a TCO. The TCO is assumed to be a few meters in diameter, which is much smaller than the target asteroid considered in the earlier analysis. The relative motion dynamics are also different from the rendezvous with a heliocentric asteroid. We confirm that navigation with the optical and ΔV measurements works well for such a small asteroid. The end-to-end analysis is performed for the fixed altitude hovering phase and approach phase that leads into a close hovering trajectory. The results show that the spacecraft's relative range uncertainties are an order of magnitude larger than the rendezvous with a larger asteroid at the same distance due to the lack of strong angular size measurements. As the spacecraft approaches the target body, the range estimates become more accurate. These observations suggest that the optical-based navigation is valid for the rendezvous with such a small asteroid and that gradually lowering the altitude is beneficial for obtaining an accurate range estimate.

Chapter 7

Conclusions

The spacecraft's capability to autonomously explore small near-Earth asteroids is an essential aspect for future asteroid exploration missions, where cost-effect spacecraft are distributed to various target bodies for increased scientific and engineering returns. One of the biggest challenges in asteroid exploration is the relatively large a priori uncertainties of the target asteroid's physical parameters, such as its shape, mass, size, and ephemeris. The conventional approach relies heavily on support from the ground stations for orbit control and navigation, which tends to be costly and less responsive. For autonomous exploration, the spacecraft may need the ability to navigate and make plans on its own in the asteroid environment. This study focuses on various phases of proximity operation at NEAs and proposes approaches for onboard orbit design, trajectory control, and navigation.

7.1   Research Goal 1: Frozen Orbit Design

Stable orbit options at small NEAs are limited due to strong perturbations caused by SRP and the irregular gravity field of the asteroid. The averaged analysis tells us that frozen orbits exist, where the contributions of the perturbations cancel out. When the spacecraft is in frozen orbits, the orbit geometry remains unchanged. Terminator orbits are a well-known family of stable frozen orbits that exist under strong SRP. This study proposes higher-order corrections to define the terminator orbits. The proposed corrections are analytical and suitable for onboard computation. When the orbit size is small, the irregular gravity field disturbs the orbits. Focusing on the contributions

from J_2 and J_3 terms, the updated frozen orbit conditions and corrections to the conventional mean orbital elements of the terminator orbits are proposed using Milankovitch orbital element formulation. When the orbit size is large, relatively strong SRP pushes the orbits, causing an offset between the mass and orbit centers. A large offset causes results in bias between the mean and osculating elements. The study proposes an approach to define orbital elements with a position vector measured from an offset. A short-period analysis is performed to obtain an optimal offset. Finally, the behavior of the stable terminator orbits is studied for the cases when the asteroid orbit's eccentricity is nonnegligible. The semi-analytical and numerical studies confirm that the offset corrections are valid for the eccentric asteroid, and they are important to make the spacecraft stay in the vicinity of the asteroid.

7.2   Research Goal 2: Reinforcement Learning Policy for Global Mapping

Due to the lack of a target body's physical information, it may be impractical to design detailed operational plans ahead of time and make the spacecraft follow the nominal trajectory. For an autonomous spacecraft, the capabilities to define such plans and to generate trajectories adaptively after the asteroid arrival may be required. As the control of the spacecraft's trajectory is susceptible to random noises, the adaptive ability of the spacecraft to correct its action based on the current status is all the more important. This study proposes an application of reinforcement learning and function approximations by feedforward neural networks to design an adaptive policy that allows the spacecraft to change its action depending on the target asteroid. The study focuses on the hovering trajectory controller design for surface global mapping tasks. Using the PPO algorithm, the policy is trained in a simulation environment with various asteroid models. The dynamics of the spacecraft's interaction with the asteroid are normalized, identifying key environmental parameters. By including the task context and the environmental parameters as part of the state and randomizing them during the training, the policy is made adaptive. The hyperparameter study shows that extracting spatial structures in the MDP state definition by using CNNs is important for improving the policy's performance. Numerical studies confirm that the obtained

policy is indeed adaptive and also robust to realistic biases in the dynamical models.

7.3   Research Goal 3: Simple Covariance Analysis

An essential capability for an autonomous spacecraft in the proximity operation at NEAs is determining its relative position, velocity, and other environmental parameters. The study considers the use of optical measurements by onboard imagers and the measurements of ΔVs by onboard accelerometers to break the scale invariance of the optical information. The covariance studies are performed for the approach trajectory along the Sun-asteroid line and subsequent hovering trajectory. The results show that the relative range estimation error is less than a hundred meters and the parameter uncertainties are less than a few percent with the ΔV measurement error of $\sigma_{\Delta V \text{meas}} = 0.1$ mm/s. This ΔV measurement capability requires onboard accelerometers that are better than an off-the-shelf IMU. However, they do not need to be as accurate as the state-of-the-art accelerometers used in missions such as CHAMP, GRACE, or GOCE. The study also confirms that for accurate range estimation, angular size measurements are important. For the estimation of the SRP coefficient, the directional measurements are helpful. The analysis with various measurement noise levels for the optical imagers and onboard accelerometers serves as a useful tool to identify expected navigation performance.

7.4   Research Goal 4: End-to-End Numerical Simulations

In order to assess the overall feasibility of the autonomous proximity operation, it is important to perform an error analysis introducing various noises and biases. A framework to evaluate the combined performance of autonomous navigation and trajectory control is introduced. Realistic noises and model discrepancies are incorporated. The end-to-end simulations are performed for both rendezvous with heliocentric asteroids and TCOs. For the analysis of the heliocentric asteroid rendezvous, various modes of operation are considered, including approach trajectory, home position hovering, mass estimation with a gradual descent, hovering at various phase angles, and global mapping hovering using the RL policy introduced in the earlier study. The analyses show that

the combined navigation and guidance work as expected. The end-to-end simulation for the TCO rendezvous shows that the proposed navigation and control scheme works well even when the target body size is as small as a few meters. For the rendezvous with such a small body, the range estimates tend to have a large uncertainty as the angular size measurements do not have rich information about the target body size. We confirm that going through a sequence of fixed altitude hovering and gradually lowering the hovering altitude could allow the spacecraft to keep improving the range estimate and thus safely approach the target.

Bibliography

[1] A. W. Harris and G. D'Abramo, "The population of near-Earth asteroids," Icarus, Vol. 257, 2015, pp. 302–312, `https://doi.org/10.1016/j.icarus.2015.05.004`.

[2] A. Morbidelli, J. Chambers, J. I. Lunine, J. M. Petit, F. Robert, G. B. Valsecchi, and K. E. Cyr, "Source regions and timescales for the delivery of water to the Earth," Meteoritics & Planetary Science, Vol. 35, No. 6, 2000, pp. 1309–1320, `https://doi.org/10.1111/j.1945-5100.2000.tb01518.x`.

[3] D. P. O'Brien, K. J. Walsh, A. Morbidelli, S. N. Raymond, and A. M. Mandell, "Water delivery and giant impacts in the 'Grand Tack' scenario," Icarus, Vol. 239, 2014, pp. 74 – 84, `https://doi.org/10.1016/j.icarus.2014.05.009`.

[4] Center for Near Earth Object Studies, "NEO Basics," `https://cneos.jpl.nasa.gov/about/neo_groups.html`. Accessed: November 22, 2020.

[5] D. Perna, M. Barucci, and M. Fulchignoni, "The near-Earth objects and their potential threat to our planet," The Astronomy and Astrophysics Review, Vol. 21, No. 1, 2013, p. 65, `https://doi.org/10.1007/s00159-013-0065-4`.

[6] Center for Near Earth Object Studies, "Discovery Statistics," `https://cneos.jpl.nasa.gov/stats/totals.html`. Accessed: November 22, 2020.

[7] D. Hestroffer, P. Sánchez, L. Staron, A. C. Bagatin, S. Eggl, W. Losert, N. Murdoch, E. Opsomer, F. Radjai, D. C. Richardson, et al., "Small solar system bodies as granular media," The Astronomy and Astrophysics Review, Vol. 27, No. 1, 2019, p. 6, `https://doi.org/10.1007/s00159-019-0117-5`.

[8] A. S. Rivkin and F. E. DeMeo, "How many hydrated NEOs are there?," Journal of Geophysical Research: Planets, Vol. 124, No. 1, 2019, pp. 128–142, `https://doi.org/10.1029/2018JE005584`.

[9] T. J. Colvin, K. Crane, and B. Lal, "Assessing the economics of asteroid-derived water for propellant," Acta Astronautica, 2020, `https://doi.org/10.1016/j.actaastro.2020.05.029`.

[10] W. W. James, K. Zacny, J. Craft, P. Chu, and M. M. Cohen, "Robotic Asteroid Prospector (RAP) NIAC Phase 1 Results," 7th Symposium on Space Resource Utilization, 2014, p. 0500, `https://doi.org/10.2514/6.2014-0500`.

[11] J. McMahon, S. K. Mitchell, K. Oguri, N. Kellaris, D. Kuettel, C. Keplinger, and B. Bercovici, "Area-of-Effect Softbots (AoES) for Asteroid Proximity Operations," 2019 IEEE Aerospace Conference, IEEE, 2019, pp. 1–16, https://doi.org/10.1109/AERO.2019.8741680.

[12] J. Sercel, "Asteroid Provided In-situ Supplies (APIS): A breakthrough to enable an affordable NASA program of human exploration and commercial space industrialization," NIAC Phase I Final Report, ICS Associates, Lake View Terrace, CA, 2016.

[13] J. C. Sercel, C. E. Peterson, J. R. French, A. Longman, S. G. Love, and R. Shishko, "Stepping stones: Economic analysis of space transportation supplied from NEO resources," 2018 IEEE Aerospace Conference, 2018, pp. 1–21, https://doi.org/10.1109/AERO.2018.8396702.

[14] J. Miller, B. Williams, W. Bollman, R. Davis, C. Helfrich, D. Scheeres, S. Synnott, T. Wang, and D. Yeomans, "Navigation Analysis for Eros Rendezvous and Orbital Phases," Journal of the Astronautical Sciences, Vol. 43, No. 4, 1995, pp. 453–476.

[15] J. Kawaguchi, "Hayabusa, Summary of Guidance, Navigation and Control Achievement in its Proximity Phase," AIAA/AAS Astrodynamics Specialist Conference and Exhibit, 2006, https://doi.org/10.2514/6.2006-6533.

[16] T. Yamaguchi, T. Saiki, S. Tanaka, Y. Takei, T. Okada, T. Takahashi, and Y. Tsuda, "Hayabusa2-Ryugu proximity operation planning and landing site selection," Acta Astronautica, Vol. 151, 2018, pp. 217–227, https://doi.org/10.1016/j.actaastro.2018.05.032.

[17] B. Williams, P. Antreasian, E. Carranza, C. Jackman, J. Leonard, D. Nelson, B. Page, D. Stanbridge, D. Wibben, K. Williams, M. Moreau, K. Berry, K. Getzandanner, A. Liounis, A. Mashiku, D. Highsmith, B. Sutter, and D. S. Lauretta, "OSIRIS-REx Flight Dynamics and Navigation Design," Space Science Reviews, Vol. 214, No. 4, 2018, p. 69, https://doi.org/10.1007/s11214-018-0501-x.

[18] D. J. Scheeres and J. W. McMahon, "Autonomous Architectures for Small Body Exploration," 2019 AAS/AIAA Astrodynamics Specialist Conference, Portland, Maine, 2019. Paper AAS 19-656.

[19] S. Watanabe, Y. Tsuda, M. Yoshikawa, S. Tanaka, T. Saiki, and S. Nakazawa, "Hayabusa2 mission overview," Space Science Reviews, Vol. 208, No. 1-4, 2017, pp. 3–16, https://doi.org/10.1007/s11214-017-0377-1.

[20] S. G. Hesar, D. J. Scheeres, and J. W. McMahon, "Sensitivity Analysis of the OSIRIS-REx Terminator Orbits to Maneuver Errors," Journal of Guidance, Control, and Dynamics, Vol. 40, No. 1, 2017, pp. 81–95, https://doi.org/10.2514/1.G002058.

[21] D. Wibben, A. Levine, S. Rieger, J. McAdams, P. Antreasian, J. Leonard, M. Moreau, and D. Lauretta, "OSIRIS-REx Frozen Orbit Design and Flight Experience," 2019 AAS/AIAA Astrodynamics Specialist Conference, Portland, Maine, 2019. Paper AAS 19-677.

[22] L. E. Cunningham, "On the computation of the spherical harmonic terms needed during the numerical integration of the orbital motion of an artificial satellite," Celestial mechanics, Vol. 2, No. 2, 1970, pp. 207–216, https://doi.org/10.1007/BF01229495.

[23] O. Montenbruck and E. Gill, Satellite Orbits: Models, Methods, and Applications, ch. Force Model, pp. 53–116. Berlin, Heidelberg: Springer, 2000, `https://doi.org/10.1007/978-3-642-58351-3_3`.

[24] D. J. Scheeres, Orbital motion in strongly perturbed environments: applications to asteroid, comet and planetary satellite orbiters. Springer, 2012, `https://doi.org/10.1007/978-3-642-03256-1`.

[25] C. R. McInnes, Solar Sailing: Technology, Dynamics and Mission Applications, ch. Solar radiation pressure, pp. 32–55. London: Springer, 1999, `https://doi.org/10.1007/978-1-4471-3992-8_2`.

[26] R. H. Gooding, "A procedure for the solution of Lambert's orbital boundary-value problem," Celestial Mechanics and Dynamical Astronomy, Vol. 48, No. 2, 1990, pp. 145–165, `https://doi.org/10.1007/BF00049511`.

[27] M. Granvik, J. Vaubaillon, and R. Jedicke, "The population of natural Earth satellites," Icarus, Vol. 218, No. 1, 2012, pp. 262–277, `https://doi.org/10.1016/j.icarus.2011.12.003`.

[28] H. Urrutxua, D. J. Scheeres, C. Bombardelli, J. L. Gonzalo, and J. Peláez, "Temporarily captured asteroids as a pathway to affordable asteroid retrieval missions," Journal of Guidance, Control, and Dynamics, Vol. 38, No. 11, 2015, pp. 2132–2145, `https://doi.org/10.2514/1.G000885`.

[29] M. Granvik, R. Jedicke, B. Bolin, M. Chyba, G. Patterson, and G. Picot, "Earth's Temporarily-Captured Natural Satellites–The First Step towards Utilization of Asteroid Resources," Asteroids, pp. 151–167, Springer, 2013, `https://doi.org/10.1007/978-3-642-39244-3_6`.

[30] Solar System Dynamics, "Horizons System," `https://ssd.jpl.nasa.gov`, February 2022.

[31] M. Giancotti, S. Campagnola, Y. Tsuda, and J. Kawaguchi, "Families of periodic orbits in Hill's problem with solar radiation pressure: application to Hayabusa 2," Celestial Mechanics and Dynamical Astronomy, Vol. 120, No. 3, 2014, pp. 269–286, `https://doi.org/10.1007/s10569-014-9564-5`.

[32] S. B. Broschart, G. Lantoine, and D. J. Grebow, "Quasi-terminator orbits near primitive bodies," Celestial Mechanics and Dynamical Astronomy, Vol. 120, No. 2, 2014, pp. 195–215, `https://doi.org/10.1007/s10569-014-9574-3`.

[33] H. Dankowicz, "Some special orbits in the two-body problem with radiation pressure," Celestial Mechanics and Dynamical Astronomy, Vol. 58, No. 4, 1994, pp. 353–370, `https://doi.org/10.1007/BF00692010`.

[34] D. Scheeres and F. Marzari, "Spacecraft Dynamics in the Vicinity of a Comet," Journal of the Astronautical Sciences, Vol. 50, No. 1, 2002, pp. 35–52, `https://doi.org/10.1007/BF03546329`.

[35] S. M. Byram and D. J. Scheeres, "Stability of Sun-synchronous orbits in the vicinity of a comet," Journal of guidance, control, and dynamics, Vol. 32, No. 5, 2009, pp. 1550–1559, `https://doi.org/10.2514/1.41655`.

[36] F. Mignard and M. Henon, "About an unsuspected integrable problem," Celestial mechanics, Vol. 33, No. 3, 1984, pp. 239–250, https://doi.org/10.1007/BF01230506.

[37] D. J. Scheeres, "Satellite dynamics about small bodies: averaged solar radiation pressure effects," Journal of the Astronautical Sciences, Vol. 47, No. 1, 1999, pp. 25–46, https://doi.org/10.1007/BF03546208.

[38] D. J. Scheeres, "Orbit mechanics about asteroids and comets," Journal of Guidance, Control, and Dynamics, Vol. 35, No. 3, 2012, pp. 987–997, https://doi.org/10.2514/1.57247.

[39] D. Vokrouhlickỳ and D. Čapek, "YORP-induced long-term evolution of the spin state of small asteroids and meteoroids: Rubincam's approximation," Icarus, Vol. 159, No. 2, 2002, pp. 449–467, https://doi.org/10.1006/icar.2002.6918.

[40] W. F. Bottke Jr, D. Vokrouhlickỳ, D. P. Rubincam, and D. Nesvornỳ, "The Yarkovsky and YORP effects: Implications for asteroid dynamics," Annu. Rev. Earth Planet. Sci., Vol. 34, 2006, pp. 157–191, https://doi.org/10.1146/annurev.earth.34.031405.125154.

[41] O. Golubov and D. J. Scheeres, "Systematic structure and sinks in the YORP effect," The Astronomical Journal, Vol. 157, No. 3, 2019, p. 105, https://doi.org/10.3847/1538-3881/aafd2c.

[42] H. Demura, S. Kobayashi, E. Nemoto, N. Matsumoto, M. Furuya, A. Yukishita, N. Muranaka, H. Morita, K. Shirakawa, M. Maruya, et al., "Pole and global shape of 25143 Itokawa," Science, Vol. 312, No. 5778, 2006, pp. 1347–1349, https://doi.org/10.1126/science.1126574.

[43] S. Watanabe, M. Hirabayashi, N. Hirata, N. Hirata, R. Noguchi, Y. Shimaki, H. Ikeda, E. Tatsumi, M. Yoshikawa, S. Kikuchi, et al., "Hayabusa2 arrives at the carbonaceous asteroid 162173 Ryugu—A spinning top–shaped rubble pile," Science, Vol. 364, No. 6437, 2019, pp. 268–272, https://doi.org/10.1126/science.aav803.

[44] D. Lauretta, S. Balram-Knutson, E. Beshore, W. V. Boynton, C. D. d'Aubigny, D. DellaGiustina, H. Enos, D. Golish, C. Hergenrother, E. Howell, et al., "OSIRIS-REx: sample return from asteroid (101955) Bennu," Space Science Reviews, Vol. 212, No. 1-2, 2017, pp. 925–984, https://doi.org/10.1007/s11214-017-0405-1.

[45] D. Lantukh, R. P. Russell, and S. Broschart, "Heliotropic orbits at oblate asteroids: balancing solar radiation pressure and J2 perturbations," Celestial Mechanics and Dynamical Astronomy, Vol. 121, No. 2, 2015, pp. 171–190, https://doi.org/10.1007/s10569-014-9596-x.

[46] R. P. Russell, D. Lantukh, and S. B. Broschart, "Heliotropic Orbits with Zonal Gravity and Shadow Perturbations: Application at Bennu," Journal of Guidance, Control, and Dynamics, 2016, pp. 1925–1933.

[47] S. Kikuchi, Y. Tsuda, M. Yoshikawa, and J. Kawaguchi, "Stability Analysis of Coupled Orbit–Attitude Dynamics Around Asteroids Using Finite-Time Lyapunov Exponents," Journal of Guidance, Control, and Dynamics, Vol. 42, No. 6, 2019, pp. 1289–1305, https://doi.org/10.2514/1.G003879.

[48] S. Kikuchi, Y. Oki, and Y. Tsuda, "Frozen Orbits Under Radiation Pressure and Zonal Gravity Perturbations," Journal of Guidance, Control, and Dynamics, Vol. 44, No. 11, 2021, pp. 1924–1946, https://doi.org/10.2514/1.G005564.

[49] J. McMahon, D. Scheeres, S. Hesar, D. Farnocchia, S. Chesley, and D. Lauretta, "The OSIRIS-REx radio science experiment at Bennu," Space Science Reviews, Vol. 214, No. 1, 2018, p. 43, https://doi.org/10.1007/s11214-018-0480-y.

[50] A. J. Rosengren and D. J. Scheeres, "On the Milankovitch orbital elements for perturbed Keplerian motion," Celestial Mechanics and Dynamical Astronomy, Vol. 118, No. 3, 2014, pp. 197–220, https://doi.org/10.1007/s10569-013-9530-7.

[51] D. A. Surovik and D. J. Scheeres, "Reactive and robust paradigms for autonomous mission design at small bodies," Journal of Guidance, Control, and Dynamics, Vol. 40, No. 2, 2017, pp. 333–343, https://doi.org/10.2514/1.G001902.

[52] J. Schulman, F. Wolski, P. Dhariwal, A. Radford, and O. Klimov, "Proximal policy optimization algorithms," arXiv preprint, 2017, https://doi.org/10.48550/arXiv.1707.06347.

[53] B. Gaudet, R. Linares, and R. Furfaro, "Six degree-of-freedom hovering over an asteroid with unknown environmental dynamics via reinforcement learning," AIAA Scitech 2020 Forum, 2020, p. 0953, https://doi.org/10.2514/6.2020-0953.

[54] B. Gaudet, R. Linares, and R. Furfaro, "Terminal adaptive guidance via reinforcement meta-learning: Applications to autonomous asteroid close-proximity operations," Acta Astronautica, 2020, https://doi.org/10.1016/j.actaastro.2020.02.036.

[55] C. J. Sullivan and N. Bosanac, "Using reinforcement learning to design a low-thrust approach into a periodic orbit in a multi-body system," AIAA Scitech 2020 Forum, 2020, p. 1914, https://doi.org/10.2514/6.2020-1914.

[56] N. B. LaFarge, D. Miller, K. C. Howell, and R. Linares, "Guidance for closed-loop transfers using reinforcement learning with application to libration point orbits," AIAA Scitech 2020 Forum, 2020, p. 0458, https://doi.org/10.2514/6.2020-0458.

[57] J. Schulman, P. Moritz, S. Levine, M. Jordan, and P. Abbeel, "High-dimensional continuous control using generalized advantage estimation," arXiv preprint, 2015, https://doi.org/10.48550/arXiv.1506.02438.

[58] R. S. Sutton, D. McAllester, S. Singh, and Y. Mansour, "Policy Gradient Methods for Reinforcement Learning with Function Approximation," Advances in Neural Information Processing Systems, Vol. 12, MIT Press, 1999, pp. 1057–1063.

[59] J. Schulman, S. Levine, P. Abbeel, M. Jordan, and P. Moritz, "Trust region policy optimization," International conference on machine learning, 2015, pp. 1889–1897.

[60] M. Andrychowicz, A. Raichuk, P. Stańczyk, M. Orsini, S. Girgin, R. Marinier, L. Hussenot, M. Geist, O. Pietquin, M. Michalski, S. Gelly, and O. Bachem, "What matters in on-policy reinforcement learning? a large-scale empirical study," arXiv preprint, 2020, https://doi.org/10.48550/arXiv.2006.05990.

[61] J. Tian and o. contributors, "ReinforcementLearning.jl: A Reinforcement Learning Package for the Julia Language," 2020.

[62] S. R. Chesley, A. S. French, A. B. Davis, R. A. Jacobson, M. Brozović, D. Farnocchia, S. Selznick, A. J. Liounis, C. W. Hergenrother, M. C. Moreau, J. Pelgrift, E. Lessac-Chenen, J. L. Molaro, R. S. Park, B. Rozitis, D. J. Scheeres, Y. Takahashi, D. Vokrouhlický, C. W. V. Wolner, C. Adam, B. J. Bos, E. J. Christensen, J. P. Emery, J. M. Leonard, J. W. McMahon, M. C. Nolan, F. C. Shelly, and D. S. Lauretta, "Trajectory Estimation for Particles Observed in the Vicinity of (101955) Bennu," Journal of Geophysical Research: Planets, Vol. 125, No. 9, 2020, p. e2019JE006363, https://doi.org/10.1029/2019JE006363.

[63] D. Scheeres, R. Gaskell, S. Abe, O. Barnouin-Jha, T. Hashimoto, J. Kawaguchi, T. Kubota, J. Saito, M. Yoshikawa, N. Hirata, T. Mukai, M. Ishiguro, T. Kominato, K. Shirakawa, and M. Uo, "The actual dynamical environment about Itokawa," AIAA/AAS Astrodynamics Specialist Conference and Exhibit, 2006, pp. 1–22. Paper AIAA 2006-6661, https://doi.org/10.2514/6.2006-6661.

[64] M. Innes, E. Saba, K. Fischer, D. Gandhi, M. C. Rudilosso, N. M. Joy, T. Karmali, A. Pal, and V. Shah, "Fashionable Modelling with Flux," CoRR, Vol. abs/1811.01457, 2018, https://arxiv.org/abs/1811.01457.

[65] I. Loshchilov and F. Hutter, "Decoupled Weight Decay Regularization," arXiv preprint, 2017, https://doi.org/10.48550/ARXIV.1711.05101.

[66] X. Glorot and Y. Bengio, "Understanding the difficulty of training deep feedforward neural networks," Proceedings of the Thirteenth International Conference on Artificial Intelligence and Statistics, Vol. 9 of Proceedings of Machine Learning Research, Chia Laguna Resort, Sardinia, Italy, PMLR, 2010, pp. 249–256.

[67] R. Pascanu, T. Mikolov, and Y. Bengio, "On the difficulty of training recurrent neural networks," Proceedings of the 30th International Conference on Machine Learning, Vol. 28 of Proceedings of Machine Learning Research, Atlanta, Georgia, USA, PMLR, 2013, pp. 1310–1318.

[68] D. A. Baker and J. W. McMahon, "Limb-Based Shape Modeling: A Demonstration on Itokawa," RPI Space Imaging Workshop, Troy, New York, 2019.

[69] D. A. Baker and J. W. McMahon, "Limb-Based Shape Modeling and Localization for Autonomous Navigation around Small Bodies," 2020 AAS/AIAA Astrodynamics Specialist Conference, Lake Tahoe, California, 2020. Paper AAS 20-467.

[70] S. E. Hammel and V. J. Aidala, "Observability requirements for three-dimensional tracking via angle measurements," IEEE Transactions on Aerospace and Electronic Systems, No. 2, 1985, pp. 200–207, https://doi.org/10.1109/TAES.1985.310617.

[71] G. Gaias, S. D'Amico, and J.-S. Ardaens, "Angles-only navigation to a noncooperative satellite using relative orbital elements," Journal of Guidance, Control, and Dynamics, Vol. 37, No. 2, 2014, pp. 439–451, https://doi.org/10.2514/1.61494.

[72] D. C. Woffinden and D. K. Geller, "Observability criteria for angles-only navigation," IEEE Transactions on Aerospace and Electronic Systems, Vol. 45, No. 3, 2009, pp. 1194–1208, https://doi.org/10.1109/TAES.2009.5259193.

[73] D. C. Woffinden and D. K. Geller, "Optimal orbital rendezvous maneuvering for angles-only navigation," Journal of guidance, control, and dynamics, Vol. 32, No. 4, 2009, pp. 1382–1387, `https://doi.org/10.2514/1.45006`.

[74] Y. Takahashi and D. J. Scheeres, "Small-body postrendezvous characterization via slow hyperbolic flybys," Journal of guidance, control, and dynamics, Vol. 34, No. 6, 2011, pp. 1815–1827, `https://doi.org/10.2514/1.53722`.

[75] Y. Tsuda, M. Yoshikawa, M. Abe, H. Minamino, and S. Nakazawa, "System design of the Hayabusa 2—Asteroid sample return mission to 1999 JU3," Acta Astronautica, Vol. 91, 2013, pp. 356 – 362, `https://doi.org/10.1016/j.actaastro.2013.06.028`.

[76] K. Vielberg, E. Forootan, C. Lück, A. Löcher, J. Kusche, and K. Börger, "Comparison of accelerometer data calibration methods used in thermospheric neutral density estimation," Annales Geophysicae, Vol. 36, No. 3, 2018, pp. 761–779, `https://doi.org/10.5194/angeo-36-761-2018`.

[77] Northrop Grumman, LN-200S Inertial Measurement Unit (IMU), 2013. Specification Sheet.

[78] V. Iafolla, E. Fiorenza, C. Lefevre, A. Morbidini, S. Nozzoli, R. Peron, M. Persichini, A. Reale, and F. Santoli, "Italian Spring Accelerometer (ISA): A fundamental support to BepiColombo Radio Science Experiments," Planetary and Space Science, Vol. 58, No. 1-2, 2010, pp. 300–308, `https://doi.org/10.1016/j.pss.2009.04.005`.

[79] P. Touboul, B. Foulon, B. Christophe, and J. P. Marque, "CHAMP, GRACE, GOCE instruments and beyond," Geodesy for Planet Earth (S. Kenyon, M. C. Pacino, and U. Marti, eds.), pp. 215–221, Berlin, Heidelberg: Springer, 2012, `https://doi.org/10.1007/978-3-642-20338-1_26`.

[80] M. R. Drinkwater, R. Haagmans, D. Muzi, A. Popescu, R. Floberghagen, M. Kern, and M. Fehringer, "The GOCE gravity mission: ESA's first core Earth explorer," Proceedings of the 3rd international GOCE user workshop, Frascati, Italy, 2007, pp. 1–8. ESA Special Publication, SP-627, `https://doi.org/10.1007/978-94-017-1333-7_36`.

[81] B. D. Tapley, B. E. Schutz, and G. H. Born, Statistical Orbit Determination, ch. Fundamentals of Orbit Determination, pp. 159–284. Burlington: Elsevier Academic Press, 2004, `https://doi.org/10.1016/B978-0-12-683630-1.X5019-X`.

[82] C. R. Gates, "A simplified model of midcourse maneuver execution errors," NASA Technical Report No. 32-504, 1963, pp. 1–4.

[83] J. M. Leonard, J. L. Geeraert, B. R. Page, A. S. French, P. G. Antreasian, C. D. Adam, D. R. Wibben, M. C. Moreau, and D. S. Lauretta, "OSIRIS-REx Orbit Determination Performance During the Navigation Campaign," 2019 AAS/AIAA Astrodynamics Specialist Conference, Portland, Maine, 2019. Paper AAS 19-714.

[84] D. S. Lauretta, D. N. DellaGiustina, C. A. Bennett, D. R. Golish, K. J. Becker, S. S. Balram-Knutson, O. S. Barnouin, T. L. Becker, W. F. Bottke, W. V. Boynton, H. Campins, B. E. Clark, H. C. Connolly, C. Y. Drouet d'Aubigny, J. P. Dworkin, J. P. Emery, H. L. Enos, V. E. Hamilton, C. W. Hergenrother, E. S. Howell, M. R. M. Izawa, H. H. Kaplan, M. C. Nolan, B. Rizk, H. L. Roper, D. J. Scheeres, P. H. Smith, K. J. Walsh, C. W. V. Wolner,

D. E. Highsmith, J. Small, D. Vokrouhlický, N. E. Bowles, E. Brown, K. L. Donaldson Hanna, T. Warren, C. Brunet, R. A. Chicoine, S. Desjardins, D. Gaudreau, T. Haltigin, S. Millington-Veloza, A. Rubi, J. Aponte, N. Gorius, A. Lunsford, B. Allen, J. Grindlay, D. Guevel, D. Hoak, J. Hong, D. L. Schrader, J. Bayron, O. Golubov, P. Sánchez, J. Stromberg, M. Hirabayashi, C. M. Hartzell, S. Oliver, M. Rascon, A. Harch, J. Joseph, S. Squyres, D. Richardson, L. Mc-Graw, R. Ghent, R. P. Binzel, M. M. A. Asad, C. L. Johnson, L. Philpott, H. C. M. Su-sorney, E. A. Cloutis, R. D. Hanna, F. Ciceri, A. R. Hildebrand, E.-M. Ibrahim, L. Bre-itenfeld, T. Glotch, A. D. Rogers, S. Ferrone, C. A. Thomas, Y. Fernandez, W. Chang, A. Cheuvront, D. Trang, S. Tachibana, H. Yurimoto, J. R. Brucato, G. Poggiali, M. Pa-jola, E. Dotto, E. M. Epifani, M. K. Crombie, C. Lantz, J. d. Leon, J. Licandro, J. L. R. Garcia, S. Clemett, K. Thomas-Keprta, S. Van wal, M. Yoshikawa, J. Bellerose, S. Bhaskaran, C. Boyles, S. R. Chesley, C. M. Elder, D. Farnocchia, A. Harbison, B. Kennedy, A. Knight, N. Martinez-Vlasoff, N. Mastrodemos, T. McElrath, W. Owen, R. Park, B. Rush, L. Swan-son, Y. Takahashi, D. Velez, K. Yetter, C. Thayer, C. Adam, P. Antreasian, J. Bauman, C. Bryan, B. Carcich, M. Corvin, J. Geeraert, J. Hoffman, J. M. Leonard, E. Lessac-Chenen, A. Levine, J. McAdams, L. McCarthy, D. Nelson, B. Page, J. Pelgrift, E. Sahr, K. Stakkestad, D. Stanbridge, D. Wibben, B. Williams, K. Williams, P. Wolff, P. Hayne, D. Kubitschek, M. A. Barucci, J. D. P. Deshapriya, S. Fornasier, M. Fulchignoni, P. Hasselmann, F. Mer-lin, A. Praet, E. B. Bierhaus, O. Billett, A. Boggs, B. Buck, S. Carlson-Kelly, J. Cerna, K. Chaffin, E. Church, M. Coltrin, J. Daly, A. Deguzman, R. Dubisher, D. Eckart, D. Ellis, P. Falkenstern, A. Fisher, M. E. Fisher, P. Fleming, K. Fortney, S. Francis, S. Freund, S. Gon-zales, P. Haas, A. Hasten, D. Hauf, A. Hilbert, D. Howell, F. Jaen, N. Jayakody, M. Jenkins, K. Johnson, M. Lefevre, H. Ma, C. Mario, K. Martin, C. May, M. McGee, B. Miller, C. Miller, G. Miller, A. Mirfakhrai, E. Muhle, C. Norman, R. Olds, C. Parish, M. Ryle, M. Schmitzer, P. Sherman, M. Skeen, M. Susak, B. Sutter, Q. Tran, C. Welch, R. Witherspoon, J. Wood, J. Zareski, M. Arvizu-Jakubicki, E. Asphaug, E. Audi, R.-L. Ballouz, R. Bandrowski, S. Ben-dall, H. Bloomenthal, D. Blum, J. Brodbeck, K. N. Burke, M. Chojnacki, A. Colpo, J. Con-treras, J. Cutts, D. Dean, B. Diallo, D. Drinnon, K. Drozd, R. Enos, C. Fellows, T. Ferro, M. R. Fisher, G. Fitzgibbon, M. Fitzgibbon, J. Forelli, T. Forrester, I. Galinsky, R. Gar-cia, A. Gardner, N. Habib, D. Hamara, D. Hammond, K. Hanley, K. Harshman, K. Herzog, D. Hill, C. Hoekenga, S. Hooven, E. Huettner, A. Janakus, J. Jones, T. R. Kareta, J. Kidd, K. Kingsbury, L. Koelbel, J. Kreiner, D. Lambert, C. Lewin, B. Lovelace, M. Loveridge, M. Lu-jan, C. K. Maleszewski, R. Malhotra, K. Marchese, E. McDonough, N. Mogk, V. Morrison, E. Morton, R. Munoz, J. Nelson, J. Padilla, R. Pennington, A. Polit, N. Ramos, V. Reddy, M. Riehl, S. Salazar, S. R. Schwartz, S. Selznick, N. Shultz, and The OSIRIS-REx Team, "The unexpected surface of asteroid (101955) Bennu," Nature, Vol. 568, No. 7750, 2019, pp. 55–60, https://doi.org/10.1038/s41586-019-1033-6.

[85] S. R. Chesley, D. Farnocchia, M. C. Nolan, D. Vokrouhlický, P. W. Chodas, A. Milani, F. Spoto, B. Rozitis, L. A. Benner, W. F. Bottke, M. W. Busch, J. P. Emery, E. S. Howell, D. S. Lauretta, J.-L. Margot, and P. A. Taylor, "Orbit and bulk density of the OSIRIS-REx target Asteroid (101955) Bennu," Vol. 235, 2014, pp. 5–22, https://doi.org/10.1016/j.icarus.2014.02.020.

[86] Y. Tsuda, H. Takeuchi, N. Ogawa, G. Ono, S. Kikuchi, Y. Oki, M. Ishiguro, D. Kuroda, S. Urakawa, S. Okumura, and Hayabusa2 Project Team, "Guidance and Navigation Re-sult of Hayabusa2 Asteroid Rendezvous Operation," 32nd International Symposium on Space Technology and Science, Fukui, Japan, 2019. Paper 2019-d-074.

[87] D. S. Kahan, "NASA Planetary Data System," GRAIL Moon LGRS Derived Gravity Science Data Products V1.0, GRAIL-L-LGRS-5-RDR-V1.0, 2013.

[88] NASA, "NASA's GRAIL Creates Most Accurate Moon Gravity Map," `https://www.nasa.gov/mission_pages/grail/news/grail20121205.html`, 2012. [Online; accessed 27-Jun-2022].

Appendix A

Quadrature of Position Dependent Functions for the Short-Period Analysis

The time integrals used to find the short-period term of an angular momentum vector are listed in this appendix. The symbol E represents eccentric anomaly and subscripts t and 0 indicate values evaluated at an intermediate time t and the initial time t_0 respectively. To evaluate the time integral, known relationships in the two-body problem that are listed in Appendix A in [24] are used.

$$
\begin{aligned}
\boldsymbol{Q}_1 &= \int_{t_0}^{t} \frac{\boldsymbol{R}}{R^3} dt \\
&= \frac{1}{a^2 n (1-e^2)^{1/2}} \left[\left(\frac{\sqrt{1-e^2}\sin E_t}{1-e\cos E_t} - \frac{\sqrt{1-e^2}\sin E_0}{1-e\cos E_0} \right) \hat{\boldsymbol{e}} - \right. \\
&\qquad\qquad \left. \left(\frac{\cos E_t - e}{1-e\cos E_t} - \frac{\cos E_0 - e}{1-e\cos E_0} \right) \hat{\boldsymbol{e}}_\perp \right]
\end{aligned}
\tag{A.1}
$$

$$
\begin{aligned}
\overline{\boldsymbol{Q}_1} &= \frac{1}{T} \int_{t_0}^{t_0+T} \boldsymbol{Q}_1 dt \\
&= \frac{1}{a^2 n (1 - e\cos E_0)} \left(-\sin E_0 \hat{\boldsymbol{e}} + \sqrt{1-e^2}\cos E_0 \hat{\boldsymbol{e}}_\perp \right)
\end{aligned}
\tag{A.2}
$$

$$
\begin{aligned}
\boldsymbol{Q}_2 &= \int_{t_0}^{t} \left(\boldsymbol{R} + \frac{3}{2} a\boldsymbol{e} \right) dt \\
&= \frac{a}{n} \left[\left(-\frac{e}{4}(\sin 2E_t - \sin 2E_0) + \left(1 - \frac{e^2}{2}\right)(\sin E_t - \sin E_0) \right) \hat{\boldsymbol{e}} + \right. \\
&\qquad \left. \sqrt{1-e^2}\left(-(\cos E_t - \cos E_0) + \frac{e}{4}(\cos 2E_t - \cos 2E_0) \right) \hat{\boldsymbol{e}}_\perp \right]
\end{aligned}
\tag{A.3}
$$

$$\overline{\boldsymbol{Q}_2} = \frac{1}{T} \int_{t_0}^{t_0+T} \boldsymbol{Q}_2 dt$$

$$= \frac{a}{n} \left[\left(\frac{e}{4} \sin 2E_0 + \left(\frac{e^2}{2} - 1 \right) \sin E_0 \right) \hat{\boldsymbol{e}} \right.$$

$$\left. + \sqrt{1 - e^2} \left(\cos E_0 + \frac{e}{2} - \frac{e}{4} \cos 2E_0 \right) \hat{\boldsymbol{e}}_\perp \right] \tag{A.4}$$

Appendix B

Spherical Harmonics Gravity Model

B.1   Legendre Polynomial Expansion

The motion of an object under the influence of the higher-order gravity field of the central body can be written as follows [23].

$$\ddot{\boldsymbol{r}} = \frac{\partial U_g}{\partial \boldsymbol{r}} \tag{B.1}$$

$$U_g = G \int \frac{\rho_d(\boldsymbol{s})}{|\boldsymbol{r} - \boldsymbol{s}|} dV \tag{B.2}$$

where $\boldsymbol{s}$ is the location of an infinitesimal mass $\rho(\boldsymbol{s}dV)$. Using the Legendre polynomial expansion, we have

$$\frac{1}{|\boldsymbol{r} - \boldsymbol{s}|} = \frac{1}{r} \sum_{n=0}^{\infty} \left(\left(\frac{s}{r} \right)^n P_{n,0}(\cos \gamma) \right) \quad \text{where} \quad \cos \gamma = \frac{\boldsymbol{r} \cdot \boldsymbol{s}}{rs} \tag{B.3}$$

If we introduce the latitude ϕ and longitude λ relative to the central body to define the position of an object, then

$$x = r \cos \phi \cos \lambda \tag{B.4}$$

$$y = r \cos \phi \sin \lambda \tag{B.5}$$

$$z = r \sin \phi. \tag{B.6}$$

The Legendre polynomials $P_{n,0}$ are expressed in terms of $P_{n,m}$, the associated Legendre polynomial of degree n and order m as

$$P_{n,0}(\cos) = \sum_{m=0}^{n} (2 - \delta_{0,m}) \frac{(n-m)!}{(n+m)!} P_{n,m}(\sin \phi') \cos(m(\lambda - \lambda')) \tag{B.7}$$

where the prime indicates longitude and latitude for the vector $\boldsymbol{s}$. The Legendre polynomials are defined as

$$P_{n,0}(x) = \frac{1}{2^n n!} \frac{d^n}{dx^n} (x^2 - 1)^n \tag{B.8}$$

$$P_{n,m}(x) = (1 - x^2)^{m/2} \frac{d^n}{dx^n} P_{n,0}(x) \tag{B.9}$$

$$P_{0,0}(x) = 1 \tag{B.10}$$

Then, the gravitational potential can be written as

$$U = \frac{\mu}{r} \sum_{n=0}^{\infty} \sum_{m=0}^{n} \left(\frac{R}{r}\right)^n P_{n,m}(\sin\phi) \left(C_{n,m} \cos(m\lambda) + S_{n,m} \sin(m\lambda)\right) \tag{B.11}$$

$$= \frac{\mu}{R} \sum_{n=0}^{\infty} \sum_{m=0}^{n} \left(C_{n,m} V_{n,m} + S_{n,m} W_{n,m}\right) \tag{B.12}$$

where R is the Brillouin radius. The functions $V_{n,m}$ and $W_{n,m}$ are defined by

$$V_{n,m} = \left(\frac{R}{r}\right)^{n+1} P_{n,m}(\sin\phi) \cos(m\lambda) \tag{B.13}$$

$$W_{n,m} = \left(\frac{R}{r}\right)^{n+1} P_{n,m}(\sin\phi) \sin(m\lambda). \tag{B.14}$$

We can confirm that $V_{0,0} = R/r$ and $W_{0,0} = 0$.

The harmonics coefficients have the following properties.

- $C_{0,0} = 1$

- $S_{n,0} = 0$

- $C_{1,0} = C_{1,1} = S_{1,1} = 0$ if the origin is at the center of mass.

The following scaling is often introduced to alleviate the large variation in the magnitude of the coefficients and the associated Legendre polynomials.

$$N_{n,m} = \sqrt{\frac{(n+m)!}{(2 - \delta_{0,m})(2n+1)(n-m)!}} \tag{B.15}$$

$$\begin{pmatrix} \overline{C}_{n,m} \\ \overline{S}_{n,m} \end{pmatrix} = N_{n,m} \begin{pmatrix} C_{n,m} \\ S_{n,m} \end{pmatrix} \tag{B.16}$$

$$\overline{P}_{n,m}, \ \overline{V}_{n,m}, \ \overline{W}_{n,m} = \frac{1}{N_{n,m}} P_{n,m}, \ \frac{1}{N_{n,m}} V_{n,m}, \ \frac{1}{N_{n,m}} W_{n,m} \tag{B.17}$$

B.2 Recursion of $V_{n,m}, W_{n,m}$

The computation of the spherical harmonics gravity potential requires the values of $V_{n,m}$ and $W_{n,m}$. There is a recursive relationship to compute these functions efficiently.

B.2.1 Un-Normalized Recursion

The un-normalized version is as follows.

$$\begin{cases} V_{m,m} = (2m-1)\left(\dfrac{xR}{r^2}V_{m-1,m-1} - \dfrac{yR}{r^2}W_{m-1,m-1}\right) \\[3mm] W_{m,m} = (2m-1)\left(\dfrac{xR}{r^2}W_{m-1,m-1} + \dfrac{yR}{r^2}V_{m-1,m-1}\right) \end{cases} \tag{B.18}$$

$$\begin{cases} V_{m+1,m} = (2m+1)\dfrac{zR}{r^2}V_{m,m} \\[3mm] W_{m+1,m} = (2m+1)\dfrac{zR}{r^2}W_{m,m} \end{cases} \tag{B.19}$$

$$\begin{cases} V_{n,m} = \left(\dfrac{2n-1}{n-m}\right)\dfrac{zR}{r^2}V_{n-1,m} - \left(\dfrac{n+m-1}{n-m}\right)\dfrac{R^2}{r^2}V_{n-2,m} \\[3mm] W_{n,m} = \left(\dfrac{2n-1}{n-m}\right)\dfrac{zR}{r^2}W_{n-1,m} - \left(\dfrac{n+m-1}{n-m}\right)\dfrac{R^2}{r^2}W_{n-2,m} \end{cases} \tag{B.20}$$

B.2.2 Normalized Recursion

The normalized version is as follows.

$$\begin{cases} \overline{V}_{m,m} = \sqrt{\dfrac{2m+1}{m(2-\delta_{0,m-1})}}\left(\dfrac{xR}{r^2}\overline{V}_{m-1,m-1} - \dfrac{yR}{r^2}\overline{W}_{m-1,m-1}\right) \\[4mm] \overline{W}_{m,m} = \sqrt{\dfrac{2m+1}{m(2-\delta_{0,m-1})}}\left(\dfrac{xR}{r^2}\overline{W}_{m-1,m-1} + \dfrac{yR}{r^2}\overline{V}_{m-1,m-1}\right) \end{cases} \tag{B.21}$$

$$\begin{cases} \overline{V}_{m+1,m} = \sqrt{2m+3}\dfrac{zR}{r^2}\overline{V}_{m,m} \\[3mm] \overline{W}_{m+1,m} = \sqrt{2m+3}\dfrac{zR}{r^2}\overline{W}_{m,m} \end{cases} \tag{B.22}$$

$$\begin{cases} \overline{V}_{n,m} = a_{n,m} \dfrac{zR}{r^2} \overline{V}_{n-1,m} - b_{n,m} \dfrac{R^2}{r^2} \overline{V}_{n-2,m} \\[2mm] \overline{W}_{n,m} = a_{n,m} \dfrac{zR}{r^2} \overline{W}_{n-1,m} - b_{n,m} \dfrac{R^2}{r^2} \overline{W}_{n-2,m} \end{cases} \tag{B.23}$$

where

$$a_{n,m} = \sqrt{\frac{(2n-1)(2n+1)}{(n+m)(n-m)}} \tag{B.24}$$

$$b_{n,m} = \sqrt{\frac{(n+m-1)(n-m-1)(2n+1)}{(n+m)(n-m)(2n-3)}} \tag{B.25}$$

B.3 Partial Derivatives of $V_{n,m}, W_{n,m}$

In order to compute the acceleration or dynamics matrix, we need partial derivatives of the functions $V_{n,m}$ and $W_{n,m}$. The recursive formula for the partial derivatives can be found in Cunningham(1970) [22]. If we define

$$v_{n,m} = \begin{cases} \dfrac{1}{R^{n+1}} (V_{n,m} + iW_{n,m}) & (m \geq 0) \\[3mm] \dfrac{(-1)^{-m}}{R^{n+1}} \dfrac{(n+m)!}{(n-m)!} (V_{n,-m} - iW_{n,-m}) & (m < 0) \end{cases} \tag{B.26}$$

then,

$$\frac{\partial^{\alpha+\beta+\gamma}}{\partial x^\alpha \partial y^\beta \partial z^\gamma} v_{n,m} = i^\beta \sum_{j=0}^{\alpha+\beta} \frac{(-1)^{\alpha+\gamma-j}}{2^{\alpha+\beta}} \frac{(n-m+\gamma+2j)!}{(n-m)!} C_{\alpha,\beta,j} v_{n+\alpha+\beta+\gamma,m+\alpha+\beta-2j} \tag{B.27}$$

$$C_{\alpha,\beta,j} = \sum_{k=max(0,j-\alpha)}^{min(\beta,j)} (-1)^k \begin{pmatrix} \alpha \\ j-k \end{pmatrix} \begin{pmatrix} \beta \\ k \end{pmatrix} \tag{B.28}$$

where $\begin{pmatrix} n \\ m \end{pmatrix}$ is the binomial coefficients $_nC_m$. With the formula, we can compute the partial derivatives of the functions $V_{n,m}$ and $W_{n,m}$.

B.3.1   First Order Derivatives (Un-Normalized)

$$\frac{\partial V_{n,m}}{\partial x} = \begin{cases} -\dfrac{V_{n+1,1}}{R} & (m = 0) \\[2mm] \dfrac{1}{2R}\Big((n - m + 2)(n - m + 1)V_{n+1,m-1} - V_{n+1,m+1}\Big) & (m > 0) \end{cases} \tag{B.29}$$

$$\frac{\partial V_{n,m}}{\partial y} = \begin{cases} -\dfrac{W_{n+1,1}}{R} & (m = 0) \\[2mm] -\dfrac{1}{2R}\Big((n - m + 2)(n - m + 1)W_{n+1,m-1} + W_{n+1,m+1}\Big) & (m > 0) \end{cases} \tag{B.30}$$

$$\frac{\partial V_{n,m}}{\partial z} = -\frac{1}{R}(n - m + 1)V_{n+1,m} \tag{B.31}$$

$$\frac{\partial W_{n,m}}{\partial x} = \begin{cases} 0 & (m = 0) \\[2mm] \dfrac{1}{2R}\Big((n - m + 2)(n - m + 1)W_{n+1,m-1} - W_{n+1,m+1}\Big) & (m > 0) \end{cases} \tag{B.32}$$

$$\frac{\partial W_{n,m}}{\partial y} = \begin{cases} 0 & (m = 0) \\[2mm] \dfrac{1}{2R}\Big((n - m + 2)(n - m + 1)V_{n+1,m-1} + V_{n+1,m+1}\Big) & (m > 0) \end{cases} \tag{B.33}$$

$$\frac{\partial W_{n,m}}{\partial z} = -\frac{1}{R}(n - m + 1)W_{n+1,m} \tag{B.34}$$

B.3.2   First Order Derivatives (Normalized)

The normalized version is as follows.

$$\frac{\partial \overline{V}_{n,m}}{\partial x} = \begin{cases} -K_1\dfrac{\overline{V}_{n+1,1}}{R} & (m = 0) \\[2mm] \dfrac{1}{2R}\sqrt{\dfrac{2n + 1}{2n + 3}}\Big(K_2\overline{V}_{n+1,m-1} - K_3\overline{V}_{n+1,m+1}\Big) & (m > 0) \end{cases} \tag{B.35}$$

$$\frac{\partial \overline{V}_{n,m}}{\partial y} = \begin{cases} -K_1\dfrac{\overline{W}_{n+1,1}}{R} & (m = 0) \\[2mm] -\dfrac{1}{2R}\sqrt{\dfrac{2n + 1}{2n + 3}}\Big(K_2\overline{W}_{n+1,m-1} + K_3\overline{W}_{n+1,m+1}\Big) & (m > 0) \end{cases} \tag{B.36}$$

$$\frac{\partial \overline{V}_{n,m}}{\partial z} = -\frac{1}{R}K_4\overline{V}_{n+1,m} \tag{B.37}$$

$$\frac{\partial \overline{W}_{n,m}}{\partial x} = \begin{cases} 0 & (m = 0) \\ \dfrac{1}{2R}\sqrt{\dfrac{2n+1}{2n+3}}\left(K_2\overline{W}_{n+1,m-1} - K_3\overline{W}_{n+1,m+1}\right) & (m > 0) \end{cases} \tag{B.38}$$

$$\frac{\partial \overline{W}_{n,m}}{\partial y} = \begin{cases} 0 & (m = 0) \\ \dfrac{1}{2R}\sqrt{\dfrac{2n+1}{2n+3}}\left(K_2\overline{V}_{n+1,m-1} + K_3\overline{V}_{n+1,m+1}\right) & (m > 0) \end{cases} \tag{B.39}$$

$$\frac{\partial \overline{W}_{n,m}}{\partial z} = -\frac{1}{R}K_4\overline{W}_{n+1,m} \tag{B.40}$$

where

$$K_1 = \sqrt{\frac{(n+2)(n+1)(2n+1)}{2(2n+3)}} \tag{B.41}$$

$$K_2 = \sqrt{\frac{2(n-m+2)(n-m+1)}{2-\delta_{0,m-1}}} \tag{B.42}$$

$$K_3 = \sqrt{(n+m+2)(n+m+1)} \tag{B.43}$$

$$K_4 = \sqrt{\frac{(2n+1)(n+m+1)(n-m+1)}{2n+3}} \tag{B.44}$$

B.3.3   Example Computation of Surface Gravity

The Moon's surface gravity is computed using the equations defined above for verification purposes. The spherical harmonics coefficient data derived from the GRAIL mission (gggrx_0660pm_sha.tab) are used [87]. Figure B.1 shows the surface gravity computed by the author using $n = 200$ and $m = 200$ and the gravity field map obtained from the NASA website [88]. We can confirm that the same patterns of the stronger and weaker local gravity show up, which verifies the implementation.
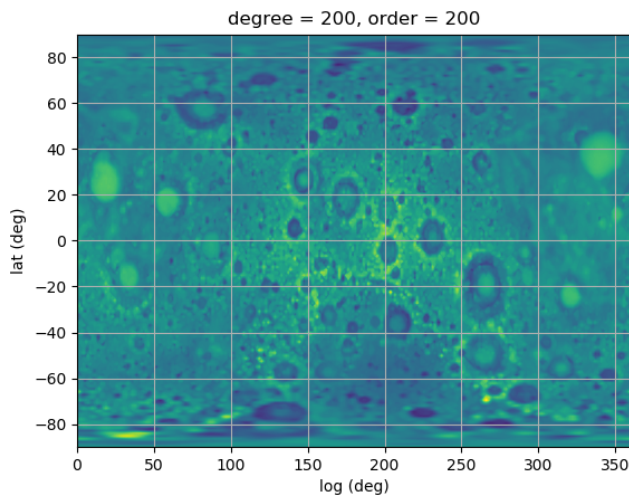
With the author's implementation
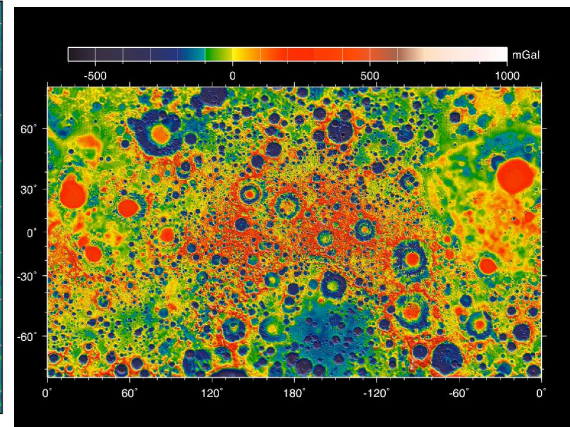
Gravity map from the GRAIL mission [88]

Figure B.1: Comparison of the lunar gravity map.

Appendix C

Computation of the Observability Status of the Asteroid Reconnaissance MDP

The state of the asteroid reconnaissance MDP includes a binary vector $\boldsymbol{b}_2$ that indicates whether each target position can be observed from the current observation geometry. When a target cannot be observed from the given phase angle, the corresponding element of $\boldsymbol{b}_2$ is set to 1, and 0 otherwise. The computation of $\boldsymbol{b}_2$ is explained in this appendix.
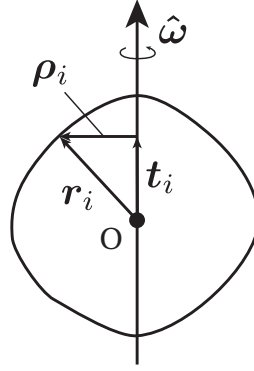
Figure C.1: Vectors to specify an observation target on an asteroid surface.

A target position on the asteroid's surface can be defined as

$$\boldsymbol{r}_i = \boldsymbol{\rho}_i + t_i \hat{\boldsymbol{\omega}} \tag{C.1}$$

where $\hat{\boldsymbol{\omega}}$ is a unit vector in the direction of the asteroid's spin. Figure C.1 visualizes the relationship of $\boldsymbol{r}_i$, $\boldsymbol{\rho}_i$, and $t_i \hat{\boldsymbol{\omega}}$.

We consider necessary conditions that the position of an observation target must satisfy for valid observation. A set of positions $\boldsymbol{r}$ traced by the observation target when the asteroid rotates

is given by the following equations, assuming a fixed pole direction.

$$(\boldsymbol{r} - t_i\hat{\boldsymbol{\omega}}) \cdot (\boldsymbol{r} - t_i\hat{\boldsymbol{\omega}}) = \rho_i^2 \tag{C.2}$$

$$(\boldsymbol{r} - t_i\hat{\boldsymbol{\omega}}) \cdot \hat{\boldsymbol{\omega}} = 0 \tag{C.3}$$

We formulate the MDP such that the observation by the spacecraft is performed from a given target azimuth angle. If we denote the normal of the plane on which the spacecraft needs to perform the observation as $\hat{\boldsymbol{n}}$, then a set of positions $\boldsymbol{r}$ that are in the target plane is given by

$$\boldsymbol{r} \cdot \hat{\boldsymbol{n}} = 0 \tag{C.4}$$

Furthermore, for valid observation, the target position must be on the Sun side. A set of position $\boldsymbol{r}$ that satisfies this condition is given by

$$\hat{\boldsymbol{d}} \cdot \boldsymbol{r} < 0 \tag{C.5}$$

where $\hat{\boldsymbol{d}}$ is a unit vector that points from the Sun to the asteroid.

In the asteroid's body-fixed frame, the necessary conditions for the observation location become

$$\begin{cases} z = t_i \\[6pt] x^2 + y^2 = \rho_i^2 \\[6pt] n_x x + n_y y + n_z t_i = 0 \\[6pt] d_x x + d_y y + d_z t_i < 0 \end{cases} \tag{C.6}$$

where $\boldsymbol{r} = [x, y, z]$, $\hat{\boldsymbol{\omega}} = [0, 0, 1]$, $\hat{\boldsymbol{n}} = [n_x, n_y, n_z]$, and $\hat{\boldsymbol{d}} = [d_x, d_y, d_z]$ in the asteroid's body-fixed frame. If $n_x \neq 0$, then we find from the conditions in Eq. (C.6) that

$$y = \frac{1}{n_x^2 + n_y^2}\left[-n_y n_z t_i \pm |n_x|\sqrt{(n_x^2 + n_y^2)\rho_i^2 - n_z^2 t_i^2}\right] \tag{C.7}$$

Similarly, if $n_y \neq 0$, then

$$x = \frac{1}{n_x^2 + n_y^2}\left[-n_x n_z t_i \pm |n_y|\sqrt{(n_x^2 + n_y^2)\rho_i^2 - n_z^2 t_i^2}\right] \tag{C.8}$$

If we normalize the position vectors such that $r_i^2 = \rho_i^2 + t_i^2 = 1$, along with the fact that $|\hat{\boldsymbol{n}}| = 1$, then we find that

$$(n_x^2 + n_y^2)\rho_i^2 - n_z^2 t_i^2 = 1 - (t_i^2 + n_z^2) \tag{C.9}$$

Thus, the steps to determine the observability of a target can be summarized as follows, assuming the position vectors are normalized.

- Check the sign of $1 - (t_i^2 + n_z^2)$

  If the sign is negative, no location satisfies the target observation phase angle constraint for the target position $\boldsymbol{r}_i$.

- Otherwise, compute the following quantities.

  If $n_x \neq 0$

$$\begin{cases} y = \left[-n_y n_z t_i \pm |n_x|\sqrt{1 - (t_i^2 + n_z^2)}\right] / (n_x^2 + n_y^2) \\ x = -(n_y y + n_z t_i)/n_x \\ z = t_i \end{cases} \tag{C.10}$$

  If $n_y \neq 0$

$$\begin{cases} x = \left[-n_x n_z t_i \pm |n_y|\sqrt{1 - (t_i^2 + n_z^2)}\right] / (n_x^2 + n_y^2) \\ y = -(n_x x + n_z t_i)/n_y \\ z = t_i \end{cases} \tag{C.11}$$

- Check the lighting condition.

  If at least one of the solutions satisfies the following condition, the target position is observable.

$$xd_x + yd_y + t_i d_z < 0 \tag{C.12}$$

Appendix D

The Effects of ΔVs on the State Mean and Covariance

Upon an impulsive maneuver at $t = \tau_i$, the state and covariance change discontinuously. During a maneuver, the position stays the same while the velocity is increased by $\boldsymbol{\Delta V_i}$. The discontinuous change in the covariance is represented by the STM. When the i-th maneuver happens between $t = t_k$ and $t = t_{k+1}$, the STM can be decomposed as

$$\Phi(t_{k+1}, t_k) = \Phi(t_{k+1}, \tau_i^+) \cdot \Phi(\tau_i^+, \tau_i^-) \cdot \Phi(\tau_i^-, t_k) \tag{D.1}$$

where $\Phi(\tau_i^+, \tau_i^-) = \partial \boldsymbol{X}(\tau_i^+)/\partial \boldsymbol{X}(\tau_i^-)$ defines the mapping of states right before and after the maneuver. To compute $\Phi(\tau_i^+, \tau_i^-)$, the STM is integrated around $t = \tau_i \pm \varepsilon$ where $\varepsilon << 1$ following Eq. (5.12). Because the interval of the integration is very small, the time evolution of the components that do not involve the delta function can be ignored. In other words, they stay the same as the initial condition. Assuming a state vector consists of $\boldsymbol{X} = [\boldsymbol{r}, \boldsymbol{v}, \boldsymbol{\Delta V_i}, \tau_i]$, the differential equations for the STM can be written as follows. We note that the following discussion holds true even when

we have additional constant parameters in the state vector.

$$
\dot{\Phi} =
\begin{bmatrix}
\partial\dot{\boldsymbol{r}}/\partial\boldsymbol{r} & \partial\dot{\boldsymbol{r}}/\partial\boldsymbol{v} & \partial\dot{\boldsymbol{r}}/\partial\boldsymbol{\Delta V}_i & \partial\dot{\boldsymbol{r}}/\partial\tau_i \\[4pt]
\partial\dot{\boldsymbol{v}}/\partial\boldsymbol{r} & \partial\dot{\boldsymbol{v}}/\partial\boldsymbol{v} & \partial\dot{\boldsymbol{v}}/\partial\boldsymbol{\Delta V}_i & \partial\dot{\boldsymbol{v}}/\partial\tau_i \\[4pt]
\partial\boldsymbol{\Delta V}_i/\partial\boldsymbol{r} & \partial\boldsymbol{\Delta V}_i/\partial\boldsymbol{v} & \partial\boldsymbol{\Delta V}_i/\partial\boldsymbol{\Delta V}_i & \partial\boldsymbol{\Delta V}_i/\partial\tau_i \\[4pt]
\partial\tau_i/\partial\boldsymbol{r} & \partial\tau_i/\partial\boldsymbol{v} & \partial\tau_i/\partial\boldsymbol{\Delta V}_i & \partial\tau_i/\partial\tau_i
\end{bmatrix}
\cdot \Phi
\tag{D.2}
$$

$$
=
\begin{bmatrix}
0_{3\text{x}3} & I_{3\text{x}3} & 0_{3\text{x}3} & 0_{3\text{x}3} \\[4pt]
\frac{\partial\dot{\boldsymbol{v}}}{\partial\boldsymbol{r}} & \frac{\partial\dot{\boldsymbol{v}}}{\partial\boldsymbol{v}} & \delta(t-\tau_i)I_{3\text{x}3} & \boldsymbol{\Delta V}_i\frac{\partial\delta(t-\tau_i)}{\partial\tau_i} \\[10pt]
\multicolumn{4}{c}{0_{4\text{x}10}}
\end{bmatrix}
\cdot
\begin{bmatrix}
\Phi_{\boldsymbol{rr}} & \Phi_{\boldsymbol{rv}} & \Phi_{\boldsymbol{r\Delta V}_i} & \Phi_{\boldsymbol{r}\tau_i} \\[6pt]
\Phi_{\boldsymbol{vr}} & \Phi_{\boldsymbol{vv}} & \Phi_{\boldsymbol{v\Delta V}_i} & \Phi_{\boldsymbol{v}\tau_i} \\[6pt]
\Phi_{\boldsymbol{\Delta V}_i\boldsymbol{r}} & \Phi_{\boldsymbol{\Delta V}_i\boldsymbol{v}} & \Phi_{\boldsymbol{\Delta V}_i\boldsymbol{\Delta V}_i} & \Phi_{\boldsymbol{\Delta V}_i\tau_i} \\[6pt]
\Phi_{\tau_i\boldsymbol{r}} & \Phi_{\tau_i\boldsymbol{v}} & \Phi_{\tau_i\boldsymbol{\Delta V}_i} & \Phi_{\tau_i\tau_i}
\end{bmatrix}
\tag{D.3}
$$

where $\Phi_{\boldsymbol{rr}} = \partial\boldsymbol{r}(t)/\partial\boldsymbol{r}(\tau_i^-)$ and so on, where $\tau_i^- \leq t \leq \tau_i^+$. From the equations above, we can see that the following submatrices have zero time rate of change and thus stay constant.

$$
\Phi_{\boldsymbol{\Delta V}_i\boldsymbol{r}}(t) = \Phi_{\boldsymbol{\Delta V}_i\boldsymbol{v}}(t) = 0_{3\text{x}3}
\tag{D.4}
$$

$$
\Phi_{\boldsymbol{\Delta V}_i\tau_i}(t) = \boldsymbol{0}_{3\text{x}1}
\tag{D.5}
$$

$$
\Phi_{\tau_i\boldsymbol{r}}(t) = \Phi_{\tau_i\boldsymbol{v}}(t) = \Phi_{\tau_i\boldsymbol{\Delta V}_i}(t) = \boldsymbol{0}_{1\text{x}3}
\tag{D.6}
$$

$$
\Phi_{\tau_i\tau_i}(t) = 1
\tag{D.7}
$$

$$
\Phi_{\boldsymbol{\Delta V}_i\boldsymbol{\Delta V}_i}(t) = I_{3\text{x}3}
\tag{D.8}
$$

Eventually, it is necessary to integrate only the following two sets of differential equations for submatrices, as we focus only on the evolution of the STM over a short interval of time.

$$
\begin{cases}
\dot{\Phi}_{\boldsymbol{r\Delta V}_i} = \Phi_{\boldsymbol{v\Delta V}_i} \\[6pt]
\dot{\Phi}_{\boldsymbol{v\Delta V}_i} = \delta(t-\tau_i)I_{3\text{x}3}
\end{cases}
\tag{D.9}
$$

$$
\begin{cases}
\dot{\Phi}_{\boldsymbol{r}\tau_i} = \Phi_{\boldsymbol{v}\tau_i} \\[6pt]
\dot{\Phi}_{\boldsymbol{v}\tau_i} = \boldsymbol{\Delta V}_i\dfrac{\partial\delta(t-\tau_i)}{\partial\tau_i} = -\boldsymbol{\Delta V}_i\dfrac{\partial\delta(t-\tau_i)}{\partial t}
\end{cases}
\tag{D.10}
$$

The results are

$$\Phi_{\boldsymbol{v}\boldsymbol{\Delta V}_i}(\tau_i^+, \tau_i^-) = I_{3\mathrm{x}3} \int_{\tau_i-\varepsilon}^{\tau_i+\varepsilon} \delta(t' - \tau_i)dt' = I_{3\mathrm{x}3} \tag{D.11}$$

$$\Phi_{\boldsymbol{r}\boldsymbol{\Delta V}_i}(\tau_i^+, \tau_i^-) = I_{3\mathrm{x}3} \int_{\tau_i-\varepsilon}^{\tau_i+\varepsilon} \int_{\tau_i-\varepsilon}^{t'} \delta(t'' - \tau_i)dt''dt' = \varepsilon I_{3\mathrm{x}3} \to 0_{3\mathrm{x}3} \ (\varepsilon \to 0) \tag{D.12}$$

$$\Phi_{\boldsymbol{v}\tau_i}(\tau_i^+, \tau_i^-) = -\boldsymbol{\Delta V}_i \int_{\tau_i-\varepsilon}^{\tau_i+\varepsilon} \frac{\partial \delta(t' - \tau_i)}{\partial t'} dt' = 0_{3\mathrm{x}1} \tag{D.13}$$

$$\Phi_{\boldsymbol{r}\tau_i}(\tau_i^+, \tau_i^-) = -\boldsymbol{\Delta V}_i \int_{\tau_i-\varepsilon}^{\tau_i+\varepsilon} \int_{\tau_i-\varepsilon}^{t'} \frac{\partial \delta(t'' - \tau_i)}{\partial t''} dt''dt' = -\boldsymbol{\Delta V}_i. \tag{D.14}$$

Therefore, $\Phi(\tau_i^+, \tau_i^-)$ has the above submatrices as well as unity diagonal elements that come from

the initial condition.

Appendix E

Derivation of the Simplified Process Noise Transition Matrix

The least squares algorithm described in section 5.2 uses an approximated process noise transition matrix $\Gamma(t_k, t_{k-1})$ to inflate the state covariance. This appendix explains its derivation.

For simplicity, we assume the state is $\boldsymbol{X} = [\boldsymbol{r}, \boldsymbol{v}]$ without loss of generality. Then the linearized differential equations for the state deviation can be written as follows, assuming the process noise is only added to the acceleration.

$$\dot{\boldsymbol{x}}(t) = A(t) \cdot \boldsymbol{x} + B \cdot \boldsymbol{u}(t) \tag{E.1}$$

where

$$B = \begin{bmatrix} 0_{3\text{x}3} \\ I_{3\text{x}3} \end{bmatrix} \tag{E.2}$$

As described in section 5.2, the noise acceleration is considered to be a piecewise constant white random sequence whose covariance is a constant 3x3 matrix Q such that

$$E\left[\boldsymbol{u}(t_i)\boldsymbol{u}(t_j)\right] = Q\delta_{ij} \tag{E.3}$$

By variation of parameters, the solution of the differential equations is given as

$$\boldsymbol{x}(t_k) = \Phi(t_k, t_{k-1}) \cdot \boldsymbol{x}(t_{k-1}) + \Gamma(t_k, t_{k-1}) \cdot \boldsymbol{u}_{k-1} \tag{E.4}$$

where

$$\Gamma(t_k, t_{k-1}) = \int_{t_{k-1}}^{t_k} \Phi(t_k, \tau) \cdot B d\tau \tag{E.5}$$

is the process noise transition matrix. Then, the state covariance estimate $P(t_k)$ can be propagated as follows [81].

$$P(t_k) = \Phi(t_k, t_{k-1}) \cdot P(t_{k-1})\Phi(t_k, t_{k-1})^T + \Gamma(t_k, t_{k-1}) \cdot Q \cdot \Gamma(t_k, t_{k-1})^T \tag{E.6}$$

The study uses an approximation of the STM in Eq. (E.5) to get an analytical expression of $\Gamma(t_k, t_{k-1})$. The integrand of Eq. (E.5) can be written as

$$\Phi(t_k, \tau) \cdot B = \begin{bmatrix} \Phi_{\boldsymbol{rr}}(t_k, \tau) & \Phi_{\boldsymbol{rv}}(t_k, \tau) \\ \Phi_{\boldsymbol{vr}}(t_k, \tau) & \Phi_{\boldsymbol{vv}}(t_k, \tau) \end{bmatrix} \cdot \begin{bmatrix} 0_{3\text{x}3} \\ I_{3\text{x}3} \end{bmatrix} \tag{E.7}$$

$$= \begin{bmatrix} \Phi_{\boldsymbol{rv}}(t_k, \tau) \\ \Phi_{\boldsymbol{rv}}(t_k, \tau) \end{bmatrix} \tag{E.8}$$

Assuming the time interval (t_{k-1}, t_k) is short, we make the following constant velocity approximation to the dynamics.

$$\boldsymbol{r}(t_k) = \boldsymbol{r}(\tau) + \boldsymbol{v}(\tau)(t_k - \tau) \tag{E.9}$$

$$\boldsymbol{v}(t_k) = \boldsymbol{v}(\tau) \tag{E.10}$$

Then, the STM becomes

$$\Phi_{\boldsymbol{rv}}(t_k, \tau) = (t_k - \tau)I_{3\text{x}3} \tag{E.11}$$

$$\Phi_{\boldsymbol{rv}}(t_k, \tau) = I_{3\text{x}3} \tag{E.12}$$

By evaluating Eq. (E.5) with the approximated STM, the process noise transition matrix can be derived as follows.

$$\Gamma(t_k, t_{k-1}) = \Delta t \begin{bmatrix} \frac{\Delta t}{2} I_{3\text{x}3} \\ I_{3\text{x}3} \end{bmatrix} \tag{E.13}$$

where $\Delta t = t_k - t_{k-1}$. Then, the contribution of the process noise that shows up in the covariance propagation becomes

$$\Gamma(t_k, t_{k-1}) \cdot Q \cdot \Gamma(t_k, t_{k-1})^T = \Delta t^2 \begin{bmatrix} \frac{\Delta t^2}{4}Q & \frac{\Delta t}{2}Q \\ \frac{\Delta t}{2}Q & Q \end{bmatrix} \tag{E.14}$$

We note that the approximation to the STM is only used in the derivation of this simplified $\Gamma(t_k, t_{k-1})$, and numerically integrated STMs are used in place of $\Phi(t_k, t_{k-1})$ in Eq. (E.6).